High Resolution Microscopy Studies of the Architecture of Sites of Hepatitis C Virus RNA Replication

Christopher J. Hinds

A thesis presented for the degree of Doctor of Philosophy

College of Medical, Veterinary and Life Sciences

University of Glasgow

MRC-University of Glasgow Centre for Virus Research

Institute of Infection Immunity and Inflammation

Church Street

Glasgow

G11 5JR

June 2014

Table of Contents

Abstract

Hepatitis C Virus (HCV) is a major cause of chronic liver disease, with an estimated 170 million people worldwide currently infected with the virus. Infection leads to chronicity in the majority of cases, resulting in fibrosis, cirrhosis and hepatocellular carcinoma. It is now the leading cause of liver transplantation in developed countries. HCV, a member of the *Flaviviridae* virus family, has a single stranded, positive sense, RNA genome encoding a unique polyprotein of 3000 amino acids in length.

Genome replication of all positive-strand RNA viruses occur in association with the cytoplasmic surface of host cell membranes. Expression of the viral non-structural proteins induces complex structural changes within the membrane forming a framework for replication of the RNA genome. Expression of the isolated HCV non-structural protein 4B has been shown to induce specific alterations to the endoplasmic reticulum (ER) membrane, recruiting a number of host factors including lipid droplets, double and single membrane vesicles.

Until recently HCV genome replication was thought to occur in structurally complex ER membrane invaginations into the lumen of the organelle, in a manner similar to the other members of the *Flaviviridae* family such as dengue virus. However a growing body of evidence suggests that such membrane alterations protrude into the cytoplasm of the cell connected by a thin neck like structure. Using a number of novel optical and electron microscopy imaging techniques, this study sought to investigate the interaction and architecture of the viral replication complex with the host membrane through both qualitative and quantitative methods.

Using the increased resolution of the OMX structured illumination microscopy (SIM) system, this study examined the interaction of multiple components of the viral replication complex (RC). Utilising the Huh-7/SGR-JFH1 and Huh-7/SGR-JFH1$_{NS5AGFP}$ cell line, a previously sub-resolution hollow structure formed by the NS5A protein harbouring the dsRNA replication intermediate was identified. The structure, interaction and intracellular location of these viral components are indicative of the viral RCs common to all positive-strand RNA viruses.

During this investigation it was noted that two distinct NS5A populations were apparent within the cell; a small population of 300nm barrel structures identified as putative replication foci and a larger population of smaller diameter indistinct objects. Utilising the quantitative modeling capabilities of the Imaris software package, these objects were

identified, filtered for diameter and the individual populations quantified. However limitations in the object identification algorithms constrained accurate quantification of the two populations.

Efforts to develop the comparative colocalisation as a quantitative methodology identified issues with OMX channel alignment affecting correlation values. Correction of this alignment issue increased coefficient values but contrary to expectation these values were found to be inversely correlated to microscope resolution. Following an in-depth investigation and comparison of the CLSM and OMX image capture technologies and colocalisation methodologies a number of factors affecting correlation values were identified. Through this process it became apparent that the differences in correlation coefficient values between the two imaging systems were not necessarily a decrease in colocalisation of the target proteins but an inherent variation of the imaging technology combined with the correlation algorithms.

Following accurate characterisation of the OMX microscopy datasets, the study went on to examine the interaction of the hollow barrel-shaped RC structures with the surface of the ER membrane. Utilising the GFP tagged peripheral ER protein Sec61β representative of the membrane surface, the viral RC was identified in a location distal to the membrane surface, residing as a spherule within the cytoplasm connected by a small membrane "neck". This result supports the recently published evidence suggesting that the HCV replication foci mirror the membrane protrusions found in poliovirus rather than the other members of the flavivirus family.

The data processing pipeline developed throughout the study was used to provide quantitative analysis of the correlation between two forms of NS5A from different cistrons in subgenomic replicon. Through this analytical process it was shown that the NS3-4B proteins were required for targeting and integration of the NS5A protein into the viral RC. The application and validation of such statistical methods of colocalisation analysis provided a platform for a more robust and non-subjective test of correlation.

Alongside the development of super resolution microscopy in this study, a novel method for bridging the resolution gap between optical and electron microscopy was investigated. A number of correlative light and electron microscopy (CLEM) techniques were assessed to provide the optimal balance of optical immunofluorescence specificity with the ultrastructural detail provided by transmission electron microscopy (TEM).

The high quantum yield and electron dense core make quantum dots an ideal novel dual modality probe for CLEM. Despite a number of failed attempts to develop an accurate probe conjugate and staining methodology, recent advances in probe conjugation methods

alongside access to a highly purified primary antibody allowed production of a novel probe specific for the viral NS5A protein. Using the QD-NS5A antibody probe it was possible to correlate replication sites imaged through CLSM with the ultrastructural micrograph generated through TEM. These images revealed that regions of high intensity fluorescence mapped to a complex region of ER membrane interwoven throughout a number of lipid droplets and vesicles.

Parallel to the above imaging studies, proteomic analysis was conducted on Huh-7 and Huh-7.5 cells to try to determine whether the greater permissiveness of Huh-7.5 cells for viral replication was a result of differential protein expression. Utilising a SILAC labeling methodology, cell line proteomes were isotopically labeled following development of a specific protocol for stable growth and replication. Although preliminary screening of fractionated proteome samples failed to identify any significant differences between cell lines, the development of a successful maintenance protocol provides the opportunity for further analysis of cell lines and organelle proteomes.

List of Figures, Equations and Accompanying Material

Chapter 1 Figures

Chapter 1 Figures

Chapter 3 Figures

Chapter 4 Figures

Chapter 5 Figures

Chapter 6 Figures

Equations

Accompanying Material

CD containing electronic copies of figures and tomography tilt series

Acknowledgements

Many thanks to:
My supervisor, Dr. John McLauchlan for providing me with the opportunity to undertake my PhD at the Centre for Virus Research and the considerable guidance and support needed to complete what has been an ambitious and decidedly unusual PhD.

Dr Mark Robinson for his invaluable guidance, support and coffee.

I would also like to thank all the members, past and present of lab 416, for the time spent both in the lab and outside.

All of my friends and colleagues within the CVR, especially my fellow inmates of room 524, for their support throughout my PhD.

Alec for his support and invaluable beer and bike related diversions!

Last but by no means least I would like to thank my family, Deb, Martyn, Mag, Alastair and my partner Karly, for their love, encouragement, support and bankrolling! Without you all I would never have made it as far as I have.

Authors Declaration

This work was completed at the University of Glasgow between October 2009 and January 2013 and has not been submitted for another degree. All work presented in this thesis was obtained by the author's own efforts, unless otherwise stated.

Abbreviations

^{o}C	degrees Celsius
%	percentage
2-D	2-Dimensional
2-DE	2-Dimensional Electrophoresis
3-D	3-Dimensional
AFS	Automatic Freeze Substitution
ALT	Alanine Transaminase
CID	Collision Induced Dissociation
CLEM	Correlative Light and Electron Microscopy
CLSM	Confocal Laser Scanning Microscope
CMV	Cytomegalovirus
DMEM	Dulbecco's Modified Eagle Medium
DMV	Double Membrane Vesicle
DNA	Deoxyribonucleic Acid
EDTA	Ethylenediaminetetraacetic acid
ELISA	Enzyme-Linked Immunosorbent Assay
EBV	Epstein-Barr Virus
EM	Electron Microscopy
ER	Endoplasmic Reticulum
ESI	ElectroSpray Ionisation
ET	Electron Tomography
FACS	Fluorescent Activated Cell Sorting
FCS	Foetal Calf Serum
FIB	Fast Ion Bombardment
FLM	Fluorescent Light Microscopy
FMDV	Foot and Mouth Disease Virus
FRET	Fürster Resonance Energy Transfer
FT-ICR	Fourier Transform-Ion Cyclotron Resonance
FWHM	Full Width Half Maximum
GFP	Green Fluorescent Protein
GLA	Glutaraldehyde
HAV	Hepatitis A Virus
HBV	Hepatitis B Virus

HCC	Hepatocellular Carcinoma
HCV	Hepatitis C Virus
HDL	High Density Lipoprotein
HPF	High Pressure Freezing
HVR	Hyper Variable Region
ICAT	Isotope Coded Affinity Tag
IFN	Interferon
IRES	Internal Ribosome Entry Site
IRF	Interferon Regulatory Factor
LC	Liquid Chromatography
LDL	Low Density Lipoprotein
LN_2	Liquid Nitrogen
LVP	LipoViral Particle
MALDI	Matrix Associated Laser Desorption Ionisation
MAVS	Mitochondrial Antiviral Signalling protein
MS	Mass Spectrometry
MOC	Manders Overlap Coefficient
NA	Numerical Aperture
NANBH	Non-A, Non-B Hepatitis
NK	Natural Killer
OMX	Optical Microscopy eXperimental
ORF	Open Reading Frame
OTF	Object Transfer Function
PBS	Phosphate Buffered Saline
PCC	Pearsons Correlation Coefficient
PEG	Pegylated
PFA	Paraformaldehyde
PSF	Point Spread Function
QD	Quantum Dot
RC	Replication Complex
RF	Radio Frequency
RI	Replication Intermediate
RT-PCR	Reverse Transcription-Polymerase Chain Reaction
RNA	Ribonucleic Acid
ROI	Region of Interest

RTS	Rapid Transfer System
SEM	Scanning Electron Microscope
SILAC	Stable Isotope Labelling by Amino acid Composition
SIM	Structured Illumination Microscopy
SMV	Single Membrane Vesicle
STORM	STochastic Optical Reconstruction Microscopy
S/NR	Signal/Noise Ratio
TAH	Transmission Associated Hepatitis
TEM	Transmission Electron Microscopy
TM	Transmembrane
TOF	Time of Flight
UHV	Ultra High Vacuum
UrAc	Uranyl Acetate
UTR	Untranslated Region
UV	UltraViolet
VLDL	Very Low Density Lipoprotein

1. Introduction

The Introduction to this thesis is presented in four separate sections. Three of these sections describe the history, principles and recent applications of methodologies that are relevant to the studies conducted (Optical Imaging – Section 1.1; Electron Microscopy – Section 1.2; Proteomics – Section 1.3). The final section (Section 1.4) is a description of the clinical and molecular characteristics of hepatitis C virus (HCV) infection, the model system examined in the study using the applications described in Sections 1.1-1.3.

1.1. Optical Imaging

1.1.1. Introduction to Biological Imaging and Microscopy

The discovery of a 3000 year old polished rock crystal lens in the Assyrian palace of Nimrud in modern day Iraq is the earliest documented evidence of an optical lens (The British Museum.,2012b). The development of the art of lens grinding in 14th century Italy for spectacles led to the invention of the first microscope in 1590 by the Dutch lens grinders Hans and his son Zacharias Janssen (Shmaefsky,2006). The Janssen compound microscope comprised of two brass drawtubes with ebony discs holding a lens at each end, providing a 9x magnification (Davidson,2003). In 1665, Robert Hooke first utilised microscopy to describe biological organisms in his work Micrographia, coining the term "cell" in the process (Fara,2009).

Antonie van Leeuwenhoek used his knowledge of glass processing to develop extremely high quality single lens microscopes. Unlike the Janssen and Hooke compound microscopes, Van Leeuwenhoek's design used a single drawn glass bead as it's optical system, more akin to a very powerful magnifying glass than today's compound microscopes. The high optical quality of his drawn lens beads compared to the compound microscopes of the time allowed him to achieve magnification of approximately x200, ten times that of contemporary systems. With this leap in magnification, van Leeuwenhoek produced the first visual description of "animalcules" which are now known as micro-organisms (Ford,1996).

1.1.2. Development of Achromatic Lenses

One of the problems encountered with early compound microscopes was the distortion of the image due to the inability of the lens, or lenses, to focus light of all colours to the same

convergence point. This is an effect of the of the increasing refractive index of light as an inverse function of the wavelength travelling through the medium, a phenomenon known as chromatic aberration (Nuttal,1974). This difference in focal plane manifests itself as coloured fringes, most apparent in high contrast situations; the colour of the fringing is dependent on the wavelength for which the lens system is focused (Flynn et al,2012).

Chromatic lens correction was first attempted through the 18th century where a number of pioneers, including Joseph Lister and Givoanni Amici worked on the problem. The solution is most often credited to the Englishman Chester Moore Hall who produced the first achromatic doublet (Daumas,1989). By combining lens elements manufactured from both crown glass and flint glass, which have different refractive indices, it was possible to bring both the blue rays and red rays to a common focus, close but not identical to the mid-spectrum green (Flynn et al,2012). By using a negative element of flint glass, which has approximately double the refractive index of crown glass, combined with a positive crown element, the combined refraction is equal but opposite, therefore cancelling colour spread. Modern microscopy systems take this concept a stage further by utilising triplet lens combinations to produce objective lenses that are achromatised at three wavelengths (Flynn et al,2012).

1.1.3. Spherical Aberration of the Optical Lens

The perfect optical system can be thought of as one in which every point of a sample object corresponds precisely to a point in the image, connected by rays travelling through all points of an optical system. However, this is impossible in all but the simplest optical systems. Scottish theoretical physicist James Clerk Maxwell postulated that the magnification of a perfect optical system can only be equal to the ratio of the refractive indices of image and object space. Assuming that both object and space are in similar medium, the magnification may only be unity (Smith et al,2001).

With greater understanding of the principles governing optical systems in microscopy, it became obvious that increasing lens power led to a decrease in image quality, much of which came from spherical aberration due to lens quality. Spherical aberration is observed when light rays passing through the outside of a lens undergo greater refraction than rays passing through, or close to the optical axis of the lens. The aplantic point of a lens, the region which suffers no spherical aberration, is limited to the radius of the sphere divided by the refractive index of the lens. The simplest method to overcome this problem utilised multiple lower-powered lens combinations to achieve the same magnification. More

complex lens shapes allow the correction of aberration by changing the refracting surface of the lens, most simply by using surfaces with different radii of curvature (Smith et al,2001).

1.1.4. Defining Lateral Resolution in Optical Systems

Even with a theoretically perfect optical system, the resolution of an optical microscope is limited to approximately half the wavelength of the light used. Within the visible spectrum this means a practical resolution limit of approximately 200-300nm (Schermelleh et al,2010). Discovered by Ernest Abbe in 1873, it was shown that with a point light source of wavelength λ, an observable feature with a resolved radius in the XY plane is defined by:

$$Resolution = \lambda/2NA$$

Equation 1. Definition of Abbe Limit

Where the numerical aperture (NA) of the lens, is defined by:

$$NA = nsin\theta$$

Equation2. Definition of Numerical Aperture

Where n is the refractive index of the medium in which the lens is operating and sinθ the half angle of the maximum light cone that may enter the lens. The majority of modern diffraction limited microscopes will offer high numerical aperture lenses providing a brighter image with shallow depth of field. There are a number of methods for defining resolution criteria, including Full Width Half Maximum (FWHM), Sparrow and Rayleigh criterion which give roughly similar limits. With current lens designs having an approximate NA of 1.4, blue light has a resolution limit of 200nm, increasing to 250nm for green and approximately 300nm for red (Ball et al,2012). Beyond these limits it becomes impossible to distinguish the two points from a single, system-defined, point spread function (PSF). This PSF is formed by the diffraction of light through a circular aperture, resulting in a bright centre region, known as an Airy Disk, surrounded by concentric bright rings known as an Airy Pattern. Using the Rayleigh criterion, a point can be defined as resolved when the principal diffraction maximum of one PSF coincides with the first minimum of the other (Born et al,1999).

1.1.5. Optical Imaging Techniques

1.1.5.1. Microscopy Techniques for Imaging of Live Cells

While fixed biological samples have provided a highly detailed view into the function and interaction of proteins, lipids and nucleic acids within cells, they only provide a static snapshot of intracellular events. The addition of a temporal dimension, through the observation of live cells, gives a further understanding to cell function and kinetics. The most common method for studying dynamic cellular processes is live cell fluorescent microscopy (Stephens et al,2003).

One of the most important considerations for live cell microscopy is the maintenance of a suitable extracellular environment during imaging. Many modern microscopy systems include some environmental controls, ranging from heated collars and stages to fully enclosed units allowing control of CO_2, humidity and temperature. Maintaining a constant stable temperature is important both for the health of the cell and to prevent focal plane drift during long term imaging (Swedlow et al,2002). Photodamage to cells during imaging is a critical factor in the success of an experiment. The photobleaching of fluorophores during imaging results in the production of free radicals which have a deleterious effect on the cell. By minimising the intensity and duration of exposure of the cell to the excitation light, free radical production can be limited, allowing cellular free radical scavenging systems to reduce their concentration between exposures (Swedlow et al,2002).

1.1.6. Confocal Microscopy

1.1.6.1. Principles and Development

Perhaps one of the greatest leaps in microscopy techniques was the development of the confocal microscope. From the 16^{th} century until the release of the first commercial platforms in 1987, microscopy within the biological sciences relied upon widefield imaging techniques. In widefield fluorescence microscopy, the specimen is evenly illuminated using Kohler illumination, a method of generating an even illumination of the sample through defocusing of the light source. This illumination method prevents the formation of an image of the light source in the same plane as the sample image.The result is an excitation of all fluorophores within the optical path. The resulting fluorescence, both in focus and out of focus is collected by the microscopes' imaging sensor (Pawley,2006). The resulting image therefore contains three dimensional (3-D) data captured in a two dimensional (2-D) format with extremely low axial resolution (Pawley,2006).

The axial resolution of a microscope, that perpendicular to the focal plane of the optical system, is defined using the 3-D diffraction image of a point source formed at the focal plane. The periodicity shown by the point spread function in the XY plane is also mirrored along the optical axis (Linfoot et al,1952). Similar to the Rayleigh criterion for lateral resolution, the axial resolution can be defined as the minimum distance between two point light sources that can be achieved along the axis of the microscope (Pawley,2006). The axial point spread function results in the generation of a cone of light both above and below the focal plane resulting in reduced contrast, and an apparent depth of field far greater than the theoretical depth of field (Pawley,2006).

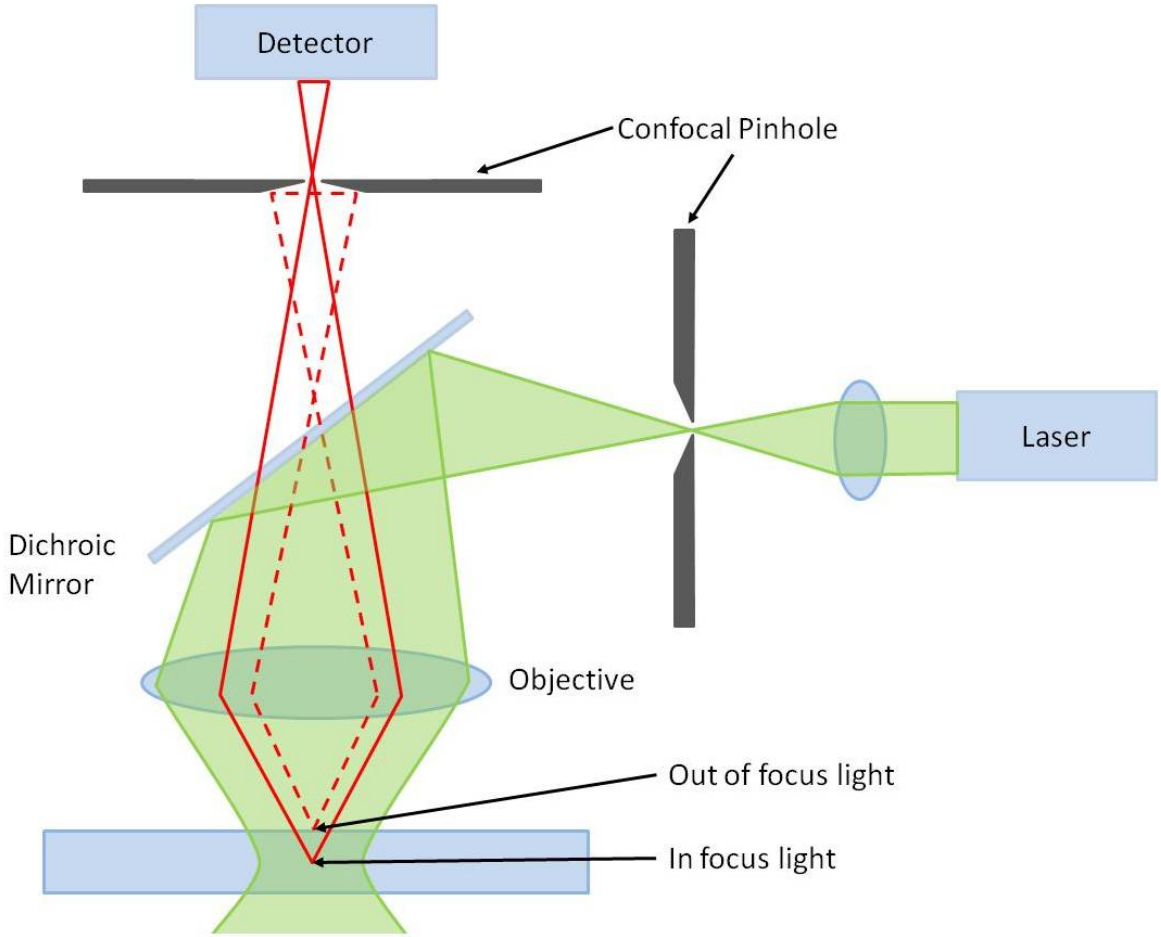

Figure 1. Optical path of confocal microscope showing exclusion of out of focus light using a pinhole arrangement

In 1957 Marvin Minsky, researching neuronal tissue realised that this limitation to traditional microscopy techniques prevented the imaging of densely packed 3-D cells beyond a meaningless blur. He considered that the best method to prevent scattered light was to prevent it being collected. In an ideal situation, the microscope would measure each point of the specimen individually, removing all scattered light from points other than that being imaged. By introducing a pinhole aperture in front of the light source as shown in

Figure 1, only the region of interest is illuminated. The addition of a pinhole at the exit side of the optical path in the image plane that lies beyond the objective lens would then reject all out of focus scattered light (Minsky,2011). By moving the specimen relative to the optical pathway, a rasterised image can be generated with a far thinner optical section and clarity than that afforded by widefield. By moving the specimen on the optical axis of the microscope and compiling the generated images, a 3-D image of the sample could be generated showing the location of subcellular components with far greater accuracy than previous systems (Wilson,1989).

1.1.6.2. Confocal Laser Scanning Microscope

The first confocal microscopes utilised a moving stage to raster scan the specimen through the optical path using two vibrating tuning forks driven by electromagnets (Minsky,2011). With the development of the laser in the 1960's, a number of advances utilising the narrow beam spread and monochromaticity of this novel technology culminated in the modern Confocal Laser Scanning Microscope (CLSM). Using this new technique, the specimen itself was held stationary and the laser was raster scanned using servo-controlled mirrors. This approach results in far lower reaction latency and more flexible scan speeds allowing for optimisation of signal to noise ratio (Pawley,2006;Carlsson et al,1985). The physical movement of the vibrating stage scanning can result in problems with biological samples, usually bathed in a liquid medium that suffer from the inertial effects of the method (Pawley,2006).

1.1.7. Sub-Diffraction Imaging by Structured Illumination Microscopy

Despite the improvements in axial resolution afforded by confocal microscopy, in practice the lateral resolution of confocal methods, including CLSM are at best marginal (Gustafsson,2000). The reason for this is the limited detection of extended resolution information using confocal technology and the sub-Airy disk pinhole size required to do so (Gu et al,1992). Unfortunately using such a small pinhole size to increase lateral resolution discards most of the in-focus light required to form an accurate image. The weak fluorescence produced by most biological samples prohibits the aperture size required to achieve any meaningful increase in lateral resolution (Gustafsson,2000). It is possible to overcome the diffraction limits of most optical microscopes using laterally structured illumination in a widefield non-confocal manner. By applying a lateral modulation to the illuminating beam, the range of measurable spatial frequencies is expanded, rendering

normally inaccessible information visible in the form of moiré fringes (Heintzmann et al,1998;Gustafsson,2000).

The moiré effect is a well understood concept where the superposition of two fine patterns results in the generation of a beat pattern product known as moiré fringes (Gustafsson,2000). With Structured Illumination Microscopy (SIM), one of the patterns used in the superposition is the unknown sample structure or spatial distribution of the fluorescent probe (Figure 2[A]). The other is a deliberately modulated, structured illumination light pattern(Figure 2[B]) (Gustafsson,2000)The resultant moiré fringes can be substantially coarser than either of the two patterns. Collection of a series of the resultant patterns at various angles allows a high resolution reconstruction of the sample.

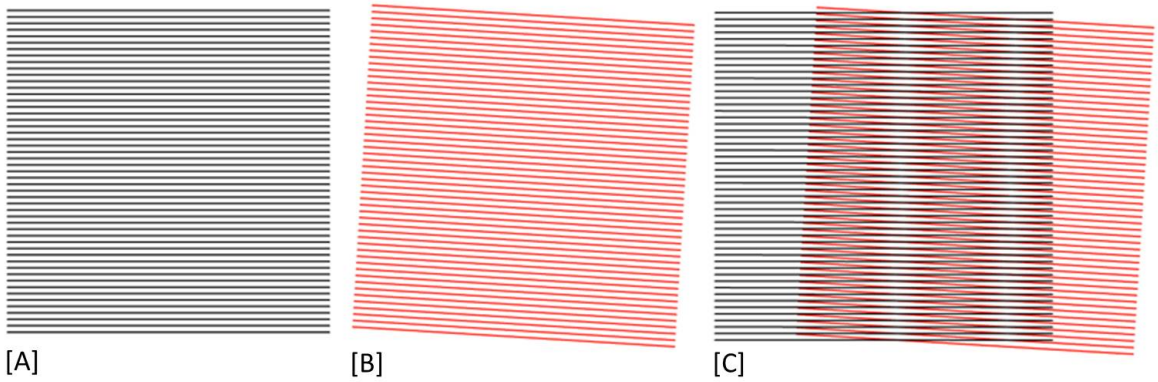

Figure 2 Use of moiré pattern to generate low frequency beat pattern

When the sample is illuminated with a sinusoidal pattern, the observed image contains, in addition to the normal image, moiré fringes corresponding to high resolution data which is offset at a distance and direction defined and proportional to the direction and line spacing of the illuminating pattern (Figure 2[C]) (Gustafsson,2000). Using a sequence of such images with illumination patterns at different orientation and phase, an area twice the size of the normal observable region can be covered, allowing information from outside this region to be collected and processed (Gustafsson,2000).

1.1.7.1. Signal to Noise Ratio and Photobleaching

One of the major drawbacks to SIM as a super-resolution technique is the photobleaching limits imposed upon the sample. To perform 3D SIM, at least five illumination phases must be recorded at three different angles, resulting in a minimum of 15 images for each optical section reconstruction (Dobbie et al,2011). This can cause substantial photobleaching and photodamage of the sample during acquisition. To overcome the problems of working at a photon-limited level, any additional background and noise, such

as stray light and camera electronics must be properly addressed and limited. The microscope utilised in this study, the DeltaVision API OMX (Optical Microscope eXperimental) was specifically designed to overcome this problem (Smith et al,2001). The microscope itself uses a fixed optical path and objective, with focusing and position change of the sample achieved through piezo electric control of the stage and sample. The optical path is optimised to collect emitted fluorescent light, at the expense of excitation light. There are no binoculars and the microscope is kept in a clean air, temperature regulated dark room, separate from the user (Dobbie et al,2011) helping to limit non-poisson noise within the system.

1.1.7.2. Prevention of Photobleaching Using Antifade Reagents

As photobleaching and damage occur as a function of the intensity and duration of the excitation beam, techniques such as SIM require careful sample preparation to prevent irreversible damage during imaging (Giloh et al,1982;Tsien et al,2006). Unfortunately, photochemical damage is one of the least understood yet most important aspects of fluorescence microscopy within biology (Tsien et al,2006). The extent of light-induced damage to fluorophores is heavily dependent on the presence of molecular oxygen within the sample. Photochemical activation during imaging of the kinetically non-reactive triplet state O_2 to the strongly oxidizing singlet state results in damage to the fluorophore (Tsien et al,2006). Reducing the partial pressure or concentration of oxygen within the sample can greatly increase the longevity of fluorophores within chemically fixed samples (Tsien et al,2006;Vaughan et al,1970). This is achieved through the addition of antioxidants and free radical scavengers such as *n*-propyl gallate, hydroquinone or p-phenylenediamine to the mounting media, extending fluorescence lifetimes by a factor of 10 (Tsien et al,2006;Giloh et al,1982). The effects of these antifade reagents may go beyond removing oxygen from the sample, proving more effective than thorough deoxygenation of samples. Indeed it has been hypothesised that polyphenols such as *n*-propyl gallate may limit fluorophore free radical formation (Tsien et al,2006;White et al,1987).

1.1.8. Stochastic Optical Reconstruction Microscopy (STORM)

To avoid the photodamaging effects of OMX imaging, other methods of sub-diffraction limit imaging have been developed. The use of single molecule detection within a sample can provide imaging resolution theoretically limited only by the number of photons collected (Rust et al,2006). STORM-based techniques utilise a number of methods to activate or quench subsets of the fluorophore population in a sample allowing an optically

resolvable subset to be imaged. By imaging discrete non-overlapping fluorophore PSFs, it is then possible to find the centroid position and deconvolve the individual PSF to its original source. By repeatedly activating and deactivating different subsets of fluorophores in an iterative manner it is possible to localize the majority of fluorophores, allowing the construction of a sub-diffraction limited image (Rust et al,2006;Flors et al,2009).

A number of methods exist for stochastic switching between fluorophore excitation states, either using multiple laser lines to excitate specifically designed photoactivatable fluorophores or through the control of electron transfer within traditional fluorophores by deoxygenation of the sample via chemical means (Flors et al,2009;Steinhauer et al,2008). There is a severe disadvantage to systems relying on photoactivatable or switchable fluorophores due to their limited general applicability, multiplexing capability and equipment requirements (Steinhauer et al,2008). The use of engineered dark states through electron transfer modulation allows a number of traditional fluorophore classes to be utilised. The resolution of this technique is essentially limited by photon statistics and the statistical noise of the system. By collecting and processing several thousand images, a focal plane resolution of approximately 30nm can be achieved (Schermelleh et al,2010). The use of Total Internal Reflection Fluorescence Microscopy reduces background signal by limiting excitation of fluorophores to only those within 1-2 microns of the coverslip (Reck-Peterson et al,2010). A consequence of this illumination technique is the extremely limited optical sectioning that is achieved compared to conventional CLSM as only cellular components and processes close to the cell membrane can be effectively imaged.

1.1.9. Image Analysis and Processing of Captured Data

In recent years the biological sciences have come to rely heavily upon imaging techniques for progress, with a shift in emphasis from comparable qualitative assessments to statistically meaningful quantitative analysis (Fricker et al,2006;Meijering et al,2007). With the increasing power and imaging efficiency of modern microscopy systems, biological data sets have grown rapidly both in terms of size and data complexity. Manual measurement and analysis is becoming increasingly untenable due to labour intensity, inaccuracy and poor reproducibility. Computerised image analysis is required to handle the higher volumes of data acquired and to process them with an accuracy and sensitivity to match that of the modern microscope (Murphy et al,2005).

Digital images are mathematically defined as *n*-dimensional matrices, where *n* can represent a number of parameters including, *xyz* coordinates, wavelength and time (Chen et

al,1995). A number of steps are required for successful analysis of the generated image, i) processing to optimise the data set, ii) extraction of object features from the processed image and iii) generation of a reconstruction to facilitate a better understanding of multidimensional data (Meijering et al,2007).

The acquisition process itself may result in degradation of image quality due to effects such as chromatic aberration or spatial distortions as previously mentioned. Combined with the signal-dependent noise generated by any fluorescent sample, which is governed by Poisson statistics and the inherent noise within the electronics of the acquisition system, typically Gaussian in nature, there is a significant negative effect on image quality (Meijering et al,2007;Spring et al,2013). A number of methods of reducing this noise are available during preprocessing of an image. Uniform or Gaussian convolution filters may be utilised as a crude method of improving signal-to-noise ratio (SNR) but their global effect results in blurring of structures of interest alongside noise. Median filtering provides an effective way of removing shot noise from individual bright or dark pixels but may have a negative effect when investigating smaller objects within a sample (Meijering et al,2007). More sophisticated techniques such as non-linear diffusion filtering can be applied to the image. By embedding the original image in a family of derived images obtained through convolution of the original image with a Gaussian kernel of variance t, it is possible to smooth and reduce noise while preserving sharpness at object edges within the image (Perona et al,1990).

The kernel, typically a 3x3 matrix of pixels within an image, is generated by applying a Gaussian function to the weights of neighbouring pixels against a centre pixel. The product of this Gaussian function applied against the weight of each pixel value is then summed to generate a new value for the central pixel (Ludwig,2007). An iterative application of this locally derived function to the image, preserves and enhances the edges found within an image while eliminating noise (Perona et al,1990).

One of the most frequent questions posed in modern microscopy is to what degree two or more cellular components, such as proteins interact with each other or colocalize within a sample. By using different coloured probes for each species being investigated, multicolour fluorescent images can be acquired for analysis (Manders et al,1993). Colocalization analysis in digital images is a “dual-image pixel point” process between at least two input images to generate a single colocalization map (Shotton,1993). One of the most critical aspects of this type of experiment is sufficient separation of emission spectra

and correct filter selection to prevent spectral bleed through or Förster Resonance Energy Transfer (FRET) (Bolte et al,2006).

A number of steps are involved in the colocalization mapping process. Firstly, a threshold intensity value is defined, separating regions of interest from the background noise of the image in each channel. The next process generates a binary output image, segmenting voxels that fail to reach the specified intensity by setting their value to zero and colour coding all those that pass the threshold using a look up table. Computation of quantitative data using a preferred method can then be performed. Finally, this data can be displayed as a 2D histogram of colocalization with intensities of each channel as the x and y axis or used to overlay on the original dataset as a separate channel, usually a maximum intensity additive pseudocolour of both channels (Landmann et al,2004).

One of the most common methods in pattern recognition for determining a quantified measure of the degree of overlap for two separate signals is the Pearson correlation coefficient (PCC). This provides data on the degree of covariance between two sample patterns without regard to the intensity of the image (Manders et al,1993). It is worth noting that the PCC ranges from 1 to -1, 1 being perfect correlation, 0 being no correlation, and -1 being perfect inverse correlation. Variances in fluorescence intensity can lead to the PCC value shifting towards 0 despite complete colocalization of cellular structures (Landmann et al,2004;Manders et al,1993;Bolte et al,2006). A negative PCC value is a good indication for real exclusion of signals (Bolte et al,2006). However, the PCC is difficult to interpret with its positive and negative values, and is greatly affected by the addition of non-colocalizing signals such as background noise (Bolte et al,2006). Of greater concern is the sensitivity of PCC to differences in signal intensity between the channels of an image, which can occur due to the different stoichiometry of fluorochromes and primary antibodies, as well as differences in channel background bleaching rates (Manders et al,1993).

The Manders' overlap coefficient is a variation of the PCC but with the removal of the average intensity values from the equation. This coefficient is also more easily understood, since it's values range from 0, (non correlation of the image), to 1, (equating to perfect correlation). The value M1, is defined as the ratio of "the summed intensities of pixels from the green image for which the intensity in the red channel is above zero" to the "total intensity in the green channel". M2 is defined conversely for red (Bolte et al,2006). The ability to measure signal coincidence independent of channel intensities is extremely useful when comparing fluorophores with different quantum yields. The Manders coefficient is

however, exquisitely sensitive to noise. This difficulty can be circumvented by setting a threshold background limit to each channel as opposed to zero (Bolte et al,2006). Quantitative colocalization analysis as a tool is extremely sensitive to background offset and noise, especially with the high background signals generated by confocal acquisition systems, requiring careful image restoration to prevent false positive counts. Deconvolution, especially within 3-D samples, is the most effective way of improving colocalisation analysis (Landmann,2002).

The relationship between the specimen and the generated image is defined by a mathematical operation known as convolution. This operation describes the spread of light from a point as it travels through the optical system to form the characteristic PSF of the system {Agard, 1989 502 /id}. Once the PSF of the microscope is known the way in which any arbitrary image is distorted can be predicted from this function. Deconvolution is the reversal of this process to recover an estimate of the original image from the degraded data. In most modern imaging software systems this is carried out in a blind *a priori* manner using iterative improvements to the PSF approximation to converge on the best function{Campisi, 2007 366 /id}. For two dimensional datasets the light forming the secondary maxima of the airy disc seen can be computationally restored to the centroid region of the disc. Successful deconvolution of the dataset results in lower background signal and therefore higher signal to noise ratio by returning out of focus light forming the background of the image to the object source from which it initially arose.

The Costes approach introduces a level of statistical significance to the determination of colocalization using a two step process based upon the PCC (Costes et al,2004). Initially the correlation of different regions of the image is evaluated to generate an automatic threshold from which a PCC of the image is calculated. The automatic threshold is determined through an iterative process of maximising signal intensity for each channel followed by rounds of decremented intensity and concomitant recalculation of the PCC in an iterative manner. The final thresholds are then set to values that minimise the contribution of noise (Bolte et al,2006). Having calculated a PCC value for the image, the Costes' approach introduces a statistical analysis based on image randomization and evaluation of this value. As mentioned previously, a single digital image represents the distribution of particles of interest at the optical resolution of the imaging system, appearing as a collection of pixels related to their neighbour. The PSF of this optical system defines the intensity distribution recorded in these pixels, allowing approximation of the particle size based on the Full Width Half Maximum (FWHM) of the intensity

curve. The FWHM defines the region of spread for the signal from a single particle. The Costes' method generates 200 randomized images, created from the shuffling of pixel blocks with sizes defined by the FWHM of the green channel of the original image. For each image, a PCC is generated between the randomised green channel and original red channel. By comparing the PCC of the non randomized image against that of the randomised images, the statistical significance can be calculated in the form of a *p*-value. This *p*-value is inversely correlated to the probability of obtaining the defined PCC by chance. If 95% of the random images correlate worse than the real image then the correlation coefficient can be considered significant (Bolte et al,2006;Costes et al,2004).

With the increase in imaging resolution and data complexity there is a need for more sophisticated visualisation methods to present and explore higher dimensional data (Meijering et al,2007). Beyond slice by slice analysis, which provides only a limited insight as to the relation of objects in 3-D space, visualisation provides a more effective method of representing higher-dimensional data. The powerful information processing steps used in the generation of visualisation models can be easily misused to greatly alter the final results.

Surface rendering is one technique utilised by modelling software such as Imaris (Bitplane) to generate visualisations of multidimensional data. This is carried out through a mathematical description of the surface as a series of geometrical shapes (Meijering et al,2007). Identification of surfaces belonging to an object is performed by comparison of the grey value of the voxel in question to that of it's neighbour. Voxels above a user defined threshold grey value are defined as part of an object while those lower than the threshold are regarded as background. Surface voxels are defined as those belonging to an object above threshold whose neighbouring voxel is less than threshold (Zeigler,2008).

1.1.10. Immunofluorescence Microscopy

1.1.10.1. Principles of the Fluorescence Phenomena

Fluorescence is a luminescence phenomenon caused by the absorption of electromagnetic radiation of one wavelength, resulting in the excitation of an orbital electron of a molecule from a ground state to a higher quantum state, followed by the near immediate return to a ground state with the concurrent emission of a photon. Some of the absorbed energy is lost to rotational or vibrational changes to the orbital electron. Due to this loss of energy, the emitted photon is of a lower energy and therefore longer wavelength than the absorbed photon. The difference between the excitation wavelength maximum and emission

wavelength maximum of the same electron transition is known as the Stokes shift (Mullins,1995). Fluorescence is distinguished from other forms of luminescence by the immediate return of the excited electron to a ground state, typically ~10^{-8} seconds, in contrast to phosphorescence where the excited state may persist for a period before photon emission.

1.1.10.2. Green Fluorescent Protein

The discovery in 1962 of Green Fluorescent Protein (GFP) in *Aequorea victoria* jellyfish by Shimomura et al has become a major contributor to the study of living cells as both a marker for gene expression and protein target for imaging analysis (Misteli and Spector 1997;Shimomura et al. 1962;Tsien 1998). The aptly named protein was found to be responsible for the majority of the *A. victoria* jellyfish luminescence, with an emission spectra centred at 508nm (Johnson et al,1962).

GFP is unique among fluorescent proteins due to the lack of cofactors or substrates required by the protein to generate green light. In *A. Victoria,* GFP is indirectly activated in a calcium-dependent manner when Ca^{+} binds another chemoluminescent protein, aequorin, which transfers energy indirectly to GFP, triggering the release of green light (Prasher,1995). This energy transfer can be mimicked experimentally by exposure of GFP to long-wave ultraviolet (UV) light. The absence of required cofactors was proven conclusively when a cDNA encoding GFP was expressed in both prokaryotic, *E.coli,* and eukaryotic *C.elegans,* organisms, emitting a bright green fluorescence signal when illuminated with blue light (Chalfie et al,1994).

GFP has been used extensively as a protein tag to examine and monitor protein localization and dynamic processes within the living cell. Through standard subcloning techniques, fusion of GFP and any protein of interest can be generated and introduced into an organism for transient or stable expression (Misteli et al,1997). One of the most important features of GFP tagging is the freedom afforded from fixation and permeabilisation procedures, reducing processing artefacts during imaging. The barrel structure of GFP helps to protect the conformation of the original protein, even for large protein moieties. One disadvantage of GFP is it's relatively large size (27kDa) which can affect the function of target proteins (Zimmer,2001;Misteli et al,1997).

1.1.10.3. Organic Fluorophores

Fluorophores are small organic molecules, typically 200-1000Da in size, that exhibit fluorescent properties upon excitation with a specified wavelength of light. Most are based around a synthetic aromatic chemical structure. A series of different molecular families has been developed for fluorescence microscopy, with an array of spectral characteristics (Dean,1992).

Upon the excitation of an electron to an energetically excited state a number of processes may occur, resulting in a loss of energy and return of the electron to the ground state. This may arise through fluorescence emission or internal conversion and vibrational relaxation in the form of heat (Horiba,2013). The quantum yield of a fluorophore is the ratio of photons absorbed by the molecule to photons emitted through fluorescence, a range of between 0 and 1. Modern probe molecules now range from extremely low quantum yield values (0.05) through to almost unity (Lippincott-Schwartz et al,2013).

1.1.10.4. Quantum Dots as a Novel Family Fluorophore

With the improved resolution, sensitivity and versatility of modern microscopy techniques, a clearer understanding of cell structure, dynamics and protein interaction is now possible. Two major drawbacks associated with traditional organic fluorophores are the relatively short fluorescent lifespans and limited excitation and emission wavelengths (Jaiswal et al,2002).

Advances in the manufacture, commercialisation and biofunctionalisation of colloidal semiconductor nanocrystals or quantum dots, has spurred an interest in their use for biological imaging (Medintz et al,2005). Compared to traditional organic fluorophores, nanocrystal probes exhibit 20x brighter quantum yields with a 100-fold increase in photostability that would be expected from a solid state fluorophore (Deerinck 2008;Resch-Genger et al. 2008;Walling et al. 2009). Their electron dense nature combined with their robust fluorescent properties make them ideal as probes for correlative microscopy, in which a target of interest is identified through CLSM followed by characterisation of ultrastructure at high resolution through Transmission Electron Microscopy (TEM) using accelerating voltages in the range of 60keV to 400keV without the need for contrast agents (Nisman et al,2004;Deerinck,2008). Quantum dots for the biosciences are crystalline nanometer-sized particles of periodic group II-VI elements (e.g. CdSe) overcoated with a passivating layer of ZnS, preventing oxidisation of the core

surface and leeching of the CdSe core. This passivating layer also significantly improves the quantum yield over CdSe-only crystals (Dabbousi et al,1997). Quantum dots themselves have a radius smaller than the exciton Bohr radius, residing in a class of materials between molecular and bulk matter (Dabbousi et al,1997).

First discovered in the 1980's as a quantum effect within a glass matrix by the formation of CuCl during exposure to high temperatures, the nanometer sized crystals exhibited quantum confinement effects due to their size relative to the electron wave function (Ekimov et al,1981). The characteristics of many materials exhibit mesoscopic physical phenomena when their physical size is in the nanoscale range, (1-100nm) which cannot be attributed to either bulk or molecular systems (Murray et al,2000). When the physical size of a semiconductor crystal is restricted below the critical Bohr Radius of the exciton electron-hole pair, the Pauli exclusion principle prevents these electrons from sharing the same energy levels which results in quantum confinement within the particle. In this instance, the crowding of the three dimensionally constrained electrons (Excitons) within the nanocrystal results in splitting of the original energy levels into smaller quantised levels. Nanocrystals with sizes larger than the exciton Bohr radius are said to be in the weak confinement regime and do not show size-dependent optical properties. Those with sizes smaller than the Bohr radius, typically sub-10nm, are said to be in a strong confinement regime and have electronic transitions which shift to higher energies with decreasing size. Therefore, there is a direct link between size and optical properties, with a blue shift in fluorescence as the size of the particle decreases (Khare et al,2011;Norris et al,1996).

Synthesis of quantum dots typically occurs in non-polar organic solvents, which are generally incompatible with the aqueous polar solvents used in most immunofluorescence procedures. To allow solubilisation under polar conditions, hydrophobic surface ligands are replaced with amphiphilic ligands. This can be carried out in a number of ways, such as surface group replacement with thiol groups, peptides or encapsulation with an inert polymer such as silica (Michalet et al,2005). To provide quantum dots with target specificity for immunofluorescence, some form of targeting moiety must be attached to their surface. For immunostaining procedures, an antibody is usually bound using thiol-derivatised quantum dots to form a disulphide bridge with the thiol groups of the antibody (Walling et al,2009).

Antibody quantum dot conjugates exhibit modest sample penetration in the range of microns, more efficient than equivalent immunogold particles in fixed and permeabilised

cells. However, secondary antibody conjugates exhibit significantly less penetration properties than their organic fluorophore counterparts, most likely down to differences in size (Deerinck,2008;Giepmans et al,2005). Penetration of probes is inversely proportional to the ultrastructural preservation of the sample. Therefore, sample preparation becomes a trade off between sufficient probe penetration and preservation of cell structure for imaging (Giepmans et al,2005). A number of factors can influence this process, including choice of permeabilisation technique, cell type and cell substrate.

Functionalisation and encapsulation of biocompatible quantum dots can increase the size of the probe from 4-8nm up to 20-30nm, while this increase is still smaller than most mammalian cells it may limit the intracellular mobility of the probe{Medintz, 2005 243 /id}. Depending on probe conjugation the smallest available size is similar to that of GFP (4nm) and nanogold (1nm), however this is heavily dependent on encapsulation and functionalisation conditions{Hink, 2000 504 /id}.

1.2. Electron Microscopy

1.2.1. Increasing Resolution Using Electron Microscopy

The resolution of optical microscopes is limited by the wavelength of visible light and the finite aperture of microscope objectives as discussed above. Any attempts to increase the resolution of such a system would either require an increase of the numerical aperture of the objective lens or a decrease in the wavelength of the excitation beam (Masters,2009).

By using a beam of electrons to illuminate the sample instead of visible light the wavelength can be decreased from hundreds of nanometres down to 1-2 angstroms, the wavelength of electrons. A microscope using this method of illumination can therefore have a far higher resolution than even the highest quality optical microscopes (Masters,2009).

1.2.2. Development of the Electron Microscope

The development of the Geissler cathode tube provided the first piece of equipment for the effective study of electrons within a vacuum. Geissler's exceptional technical skills enabled a tolerable vacuum to be maintained while applying a high potential between a cathode and anode sealed into the glass. This resulted in the appearance of a curious greenish glow on the glass walls of the tube which was attributed to cathode rays, the ambiguous title given to the as yet undiscovered electron (Mulvey,1962).

Hertz was the first to show that cathode rays could be deflected using a magnetic field. His inability to cause beam deflection using electrostatic plates was most likely down to the low quality vacuum tubes available at the time. He postulated that cathode rays were not a material particle as such but a form of motion in the "ether" (Hertz,1883). It was discovered that within a vacuum, accelerated electrons behaved much like light travelling in straight lines and exhibited wave-like properties. Considerable development on the technology required for the generation, focusing and manipulation of an electron beam led to the invention of the cathode ray tube in 1897 (Braun,1897).

Einstein's 1905 postulate on wave particle duality suggested that light could exhibit both wave- and particle-like properties and be examined as such, but not simultaneously. A year later, Louis De Broglie proposed that it was not just photons but all matter, including electrons, which could exhibit wave-particle duality (Greiner,2001). De Broglie also showed the inverse relationship between particle momentum and wavelength, an important principle for increasing the resolution of later microscopes (de Broglie,1925). The invention of the iron shrouded magnetic coil, the precursor to the modern magnetic lens, along with Busch's seminal work on electron optics, showed that a short magnetic field could converge an electron beam in the same manner as glass lens-focused light (Mulvey,1962).

The first functional Transmission Electron Microscope (TEM), was developed in 1931 in Berlin by Knoll and Ruska, a two stage microscope using two magnetic coils, shrouded in a later iteration, as lenses to generate a modest magnification of 17.5x (Ruska,1986). Further development and improvement of the initial design led to an increase in resolution, finally suprassing that of the light microscope (Masters,2009). The final version comprised of 3 magnetic lenses, i) a condenser lens used to concentrate and focus the electron beam for even illumination of the sample, ii) the objective lens to gather the transmitted electrons through the sample, focusing them to produce an image, iii) a projection lens to magnify the specimen for viewing on a phosphor screen (Ruska,1980). A camera outside of the vacuum system could capture images projected on the viewing screen. The incorporation of new lenses resulted in an increase of magnification to 10,000x giving the microscope a resolution limit of 50nm using an accelerating voltage of 75keV (Mulvey,1989).

1.2.3. Resolution Limits of Electron Microscopy

The easiest manner to consider TEM resolution is in terms of the classic Rayleigh criterion used for light microscopy. This states that the smallest distance that can be resolved using a

given system *d* is defined in a similar manner to the optical microscope shown in Eqn 1. Where λ is the wavelength of the objective radiation, *n* is the refractive index of the medium and α is the half-angle of the objective lens $nsin\alpha$ is the Numerical Aperture (NA) of the system which for most modern systems will have a value close to 1. From this, it is relatively easy to see that the resolution is equal to approximately half the wavelength of light. Using green light as a mid-spectrum example with a λ of 550nm, the resolution of the best light microscope is 300nm. de Broglie's theory on the wave particle duality of matter meant that a beam of electrons can be made to behave in the same wave-like manner as photons and electronmagnetic radiation. The wavelength of an electron λ_e is inversely dependent on it's kinetic energy *E*. Therefore by accelerating the beam of electrons across a high electrical potential it is possible to increase the kinetic energy of the electron and decrease its wavelength. The near speed of light, *c*, velocities acquired by the electron mean that a correction for relativistic effects is required

$$\lambda_{e} \approx \frac{h}{\sqrt{2m_0E(1+\frac{E}{2m_0c^2})}}$$

Equation 2. de Broglie Wavelength (Corrected for Relativistic Effects)

where *h* is Planck's constant, m_0 is the rest mass of an electron and *E* is the energy of the accelerated electron (Champness,2001;Buseck et al,1988). For a 100-keV microscope, this results in an electron wavelength of λ=0.037Å, substantially less than the diameter of atoms, usually in the order of 1 to 2 Å (Buseck et al,1988). As of 2008, it has been possible to image the lightest of atoms such as Carbon and even Hydrogen adsorbed onto graphene substrates (Meyer et al,2008).

A significant difference between optical and electron microscopy lies in the relative quality of the lenses used in both systems. While the optics of light microscopes can achieve a resolution matching the theoretical limits of the system (a diffraction limited system), the electromagnetic and electrostatic lenses used in electron microscopy are significantly poorer (Buseck et al,1988). It is fundamentally impossible to manufacture a perfect lens in electron optics. Since the invention of the first TEM system in 1932, the aberration effects of electron lenses have been extensively studied. Unfortunately, there are no effective ways to correct spherical aberrations in the same multicomponent manner as optical systems. Scherzer showed that round electron lenses suffer from inherent aberration which scale with the aperture size of the lens, α^3 plus higher order terms, resulting in smaller lens

designs and a saturation in magnetic field strength (Buseck, Cowley, & Eyring 1988;Freitag et al. 2005;Scherzer 1936).

Scherzer developed a number of systems to avoid the chromatic and spherical aberration that plagued spherical lenses. He developed an alternative to the rotationally symmetric magnetic coil lens, improving spherical aberration using an arrangement of non-rotationally symmetric lenses in a four quadrupole and three octopole configuration (Scherzer,1947;Anon.,2012a). Although the mechanical and electrical instability of early designs limited the effectiveness of the quadrupole/octopole lens system, it provided the basis for modern non-symmetric hexapole lenses. The shift from quadrupole lens (four electromagnetic coils at the vertices of a square), to hexapole lens (six coils at the vertices of a hexagon), allowed an improvement in lens magnetic field symmetry which in turn decreased chromatic aberration within the system (Freitag et al,2005).

1.2.4. Anatomy of the Transmission Electron Microscope

Broadly speaking an electron microscope is composed of four main components, an electron emission source, vacuum system, lens configuration and a method of display, usually containing an image capture device.

The electron gun is used to generate and accelerate a beam of electrons with a high, precise, kinetic energy. Electrons can be emitted through two processes. Thermionic emission utilises a heated source, either a finely drawn tungsten filament or a sharpened point of LaB_6. If enough heat is applied to this source, 2000^{o}C and above, the work function of the material is overcome and electrons are released into the vacuum (Williams et al,1996). Field emission sources utilise a fundamentally different process than thermionic emission. If a voltage is applied to a sharp point then the electric field strength will be considerably higher than that of a planar surface. With a high enough voltage, the work barrier can be lowered sufficiently to allow tunnelling of electrons from the source into the vacuum (Williams et al,1996). Field emission sources must be kept scrupulously clean, either through operation under Ultra High Vacuum (UHV) conditions at ambient temperature or with a poorer vacuum at higher temperatures.

The next stage of the electron gun, the Wehnelt cylinder, operates at a higher negative charge than the emitting cathode. The electrons which exit the filament in a divergent manner are finely focussed by the repulsive electrostatic field of the Wehnelt cylinder. The focussed beam of electrons is accelerated towards the extraction anode at earth potential

where they pass through a hole in its centre into the microscope (Williams et al,1996;Anon.,2006).

The wave-like behaviour of electrons is only applicable within a vacuum, requiring a large mean free path for electron/gas interaction, with vacuum pressures typically ranging from 10^{-4} Pa for standard TEM to 10^{-9} Pa for high-voltage TEM. At atmospheric pressure, strong scattering of electrons occurs preventing the transmission of a coherent, controlled emission beam from the electron gun. By operating the microscope at low pressures it is possible for electrons to travel the length of the microscope free from interaction with gas molecules in the beam path. The UHV of high-voltage TEMs prevent generation of an electrical arc at the electron gun cathode (Williams et al,1996).

To maintain the high vacuum of TEM systems a number of pumps are utilised at different pressures. Roughing pumps, usually mechanical rotational vane pumps, are used to generate a low or "rough" (10^{-1}Pa) vacuum at which high vacuum pumps such as diffusion or turbomolecular pumps can begin to function to achieve correct operating pressures (Williams et al,1996). To maintain such low pressures during operation, samples are transferred in and out of the microscope using an airlock system, allowing evacuation of the chamber before insertion to the specimen stage (Williams et al,1996).

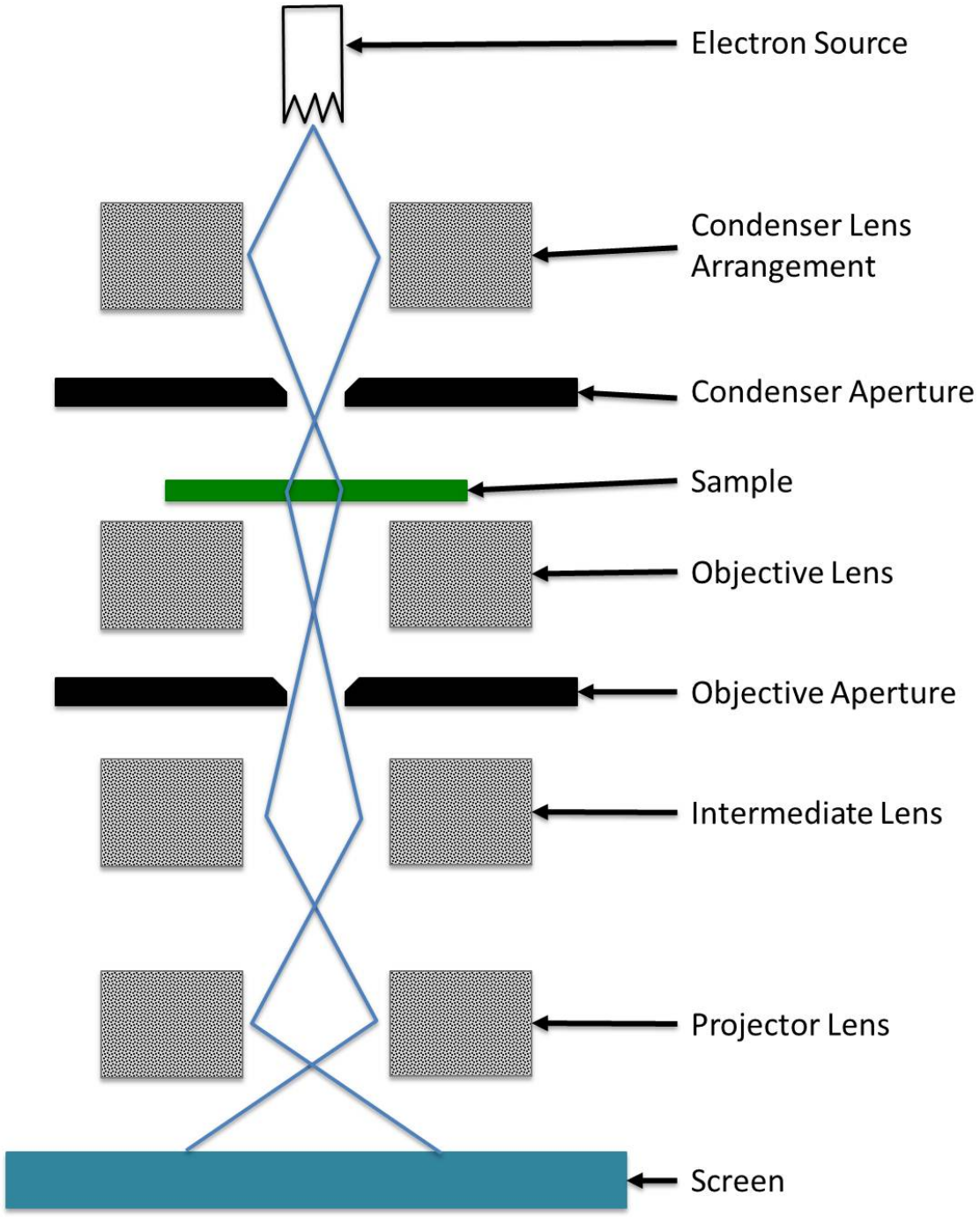

Figure 3. Arrangement of lenses in Transmission Electron Microscope (TEM)

Electron lenses are designed in a manner to emulate the function of an optical lens. Lens yokes and polepieces are manufactured from materials such as iron, and iron cobalt alloys due to their low hysteresis and high magnetic permeability. The magnetic field is generated by coils located within the lens yoke surrounding the polepiece. Modulation of the magnetic field, which allows focusing of the electron beam, is achieved through variation of the lens coil current (Goldstein et al,1986). The arrangement of electron lenses within a microscope is similar to that of an optical microscope. Condenser lenses are responsible for primary beam formation, generating an even parallel beam of electrons for illumination of

the sample. Electrons travelling through the sample are focused through the objective lens to illuminate the sample, generating a primary image which is then expanded onto the phosphorscreen or photographic film for viewing using the projector lens as seen in Figure 3 (Anon.,2006;Williams et al,1996).

1.2.5. Use of Electron Microscopy in Biological Sciences

The electron microscope has allowed biologists to image the fine ultrastructural details of the cell. The first published electron micrographs of intact cells were reported in the seminal 1945 paper, "A Study of Tissue Culture Cells by Electron Microscopy", using chicken embryo fibroblasts grown on a polyvinyl film, fixed with osmium tetroxide and imaged at 1600x magnification. The images clearly showed mitochondria, Golgi and a new structure that would later be recognised as the endoplasmic reticulum (Porter et al,1945;Masters,2009). It was Helmut Ruska, medical doctor and brother of Ernst Ruska, inventor of the first electron microscope who recognised the potential of electron microscopy for the investigation of viruses (Roinegeard,2008;Ruska et al,1939). Ruska would be the first to visualise a virus (tobacco mosaic virus), eight years after developing the first EM (Goldsmith et al,2009;Kausche et al,1939).

Electron microscopy rapidly led to the characterisation and discovery of a number of viral pathogens through the 1940's and 50's. 1948 saw comparisons between the causative agents of smallpox and chickenpox, the first images of polio were taken in 1952 and the interaction between host and viral pathogen began to be investigated by EM in the mid 1950's (Friedlander et al. 1955;Morgan et al. 1954;Nagler and Rake 1948;Reagan and Brueckner 1952).

The low atomic number and density of biological samples frequently made discerning structural inhomogeneities, such as viral particles, extremely difficult. The development of negative staining in 1958 provided a method for adding contrast to difficult to stain samples. In this method, the stain is not absorbed by the viral particles, which remain light, but by darkening the background of the sample to provide contrast {Brenner, 1959 501 /id}.

Until 1968, standard high resolution TEM micrographs only had a projection of several thousand angstroms, providing only a flattened 2-D superposition of 3-D data. To overcome the limitations of standard TEM, de Rosier and Klug developed a method of computational reconstruction using micrographs to produce a 3D model of objects of

interest termed Electron Tomography (ET). By taking a number of images of the object (bacteriophage T4 tail in this instance) and examining the optical density of the structure, it was then possible to use Fourier synthesis to computationally reconstruct the original structure into a 3-D model. de Roisier and Klug also went on to suggest a method of 3D reconstruction based on multiple projections of the object in a tilt series which would ultimately result in the modern methodology of 3D tomography (Rosier et al,1968).

One of the biggest problems encountered when imaging biological specimens by EM is the damage incurred during irraditation with the electron beam. While methods such as dehydration, water substitution and heavy metal staining help to mitigate damage during imaging, they are also responsible for sample distortion and the introduction of artifacts (Masters,2009). The introduction of cryopreservation and cryo-electron microscopy in the 1980's was a breakthrough in biological sample preservation. The specimen is embedded in water or aqueous buffer solution by rapid freezing using liquid nitrogen cooled liquid ethane. The greatest challenge in cryopreservation techniques is the rapid transition between freezing and recrystallisation points to prevent ice crystal formation. A number of factors affect this, including surface heat transfer, heat capacity and conductance within the specimen. The major limiting factor however is the low heat conductance of water within biological samples, bringing cooling rates within the sample below those required for vitrification{Moor, 1980 517 /id}. Cryoprotectants such as glycerol and dimethylsulfoxide can be used to decrease the freezing point, limiting crystal growth but also bring with them a number of deleterious effects, introducing artefacts of their own{Plattner, 1972 518 /id}. One method to overcome the use of cryoprotectants is the application of pressure during the freezing process. Pressures in the range of 2,100 bars have an effect similar to that of a 20% concentration of cryoprotectant{Riehle, 1973 519 /id}. The instantaneous freezing results in the formation of vitreous ice, preventing crystallisation which would otherwise damage the fragile cellular membranes and structures {Dubochet, 1981 286 /id;Adrian, 1984 290 /id;Moor, 1980 517 /id}. This technique allows samples to be imaged in their native state. The method can also be combined with ET to image cellular components and viral particles at molecular resolution (Gruska et al,2008). One limitation of cryofixation techniques is the need to carry out all further processes such as microtomy and microscopy at temperatures below which secondary ice crystals grow (approx -70^{o}c). Freeze substitution is one such method to overcome this limitation is to dissolve the ice within the frozen specimen using an organic solvent at low temperature, usually in the presence of a secondary fixative {Simpson, 1941 521 /id}{Feder, 1958 520 /id}. Once substitution is complete, samples can be warmed up

without recrystallisation due to the absence of water from the sample for further processing.

1.2.6. Fixation and Staining of Samples for Electron Microscopy

One of the most important factors involved in collecting high resolution micrographs is appropriate sample fixation and staining prior to imaging. Every step of the procedure will affect the quality of the final micrograph (Bozzola et al,1999). Fixation has two main functions; firstly it is an attempt to quickly arrest biological activity within the sample, generating a freeze frame of cellular processes and interactions. Secondly, it helps to stabilise the cellular components of the sample, preventing distortion of the conformational and spatial relationships between constituents (Dykstra,1993). Although the term fixation is thought of as both fixing and killing cells it is worth considering that they are not one and the same process. Standard aldehyde fixatives can undergo physiological and physical changes before cell death occurs. In these cases, killing of cells, using osmium tetroxide fumes for instance, may be more appropriate (Hopwood,1967;Dykstra,1993). Cryofixation techniques such as High Pressure Freezing (HPF) occur with such rapidity as to be considered instantaneous (Adrian et al,1984).

A number of cryofixation techniques have been developed for the vitrification of biological samples, however many are limited by the inability to freeze aqueous samples which are not thicker than 10-20μm.

Chemical fixatives are utilised to transform the aqueous colloidal protoplasm of the cell into a cross-linking stabilised sample capable of withstanding the rigors of washing with aqueous and organic solvents, resin embedding and polymerisation via heat or ultraviolet radiation (Dykstra,1993). An ideal fixative should maintain the spatial relationships between organelles and cell structure, prevent the solubilisation of cell components and maintain the antigenic properties required for immunohistochemistry. It should be noted that any method of fixation will introduce some form of artefact into the final sample. Selection of a specific fixation technique depends on the ultrastructural features intended to be preserved (Bozzola et al,1999).

Osmium tetroxide was the first fixative utilised in EM, either through exposure of the sample to osmium vapors or through immersion of the sample (Claude,1948). It was not until 1963 that the currently popular gluteraldehyde-osmium protocol was introduced, that is gluteraldehyde as a primary fixative followed by postfixation exposure to osmium

tetroxide (Sabatini et al,1963). A number of variations of this protocol were subsequently developed, such as the addition of low concentration (4%) formaldehyde to the primary gluteraldehyde fixative. The faster tissue penetration rate of formaldehyde allows for more rapid fixation of tissue (Karnovsky,1965).

Formaldehyde is the simplest of the aldehydes. At room temperature, when dissolved in water, it rapidly hydrates to form glycol. The equilibrium of this reaction lies so far in favour of methylene glycol that at any time only a small percentage of formaldehyde is present. When used as a fixative, the tissue is rapidly penetrated by methylene glycol and a fraction of formaldehyde. The formation of covalent bonds within the tissue utilises the free formaldehyde resulting in the dissociation of methylene glycol back to formaldehyde. This explains the rapid penetration of formaldehyde (methylene glycol) but slow fixation (formaldehyde) (Fox et al,1985). Fixation of tissues results from bridging of biological macromolecules such as proteins and nucleic acids, through crosslinking of reactive groups such as thiols and primary amines to less reactive groups such as primary amides and tyrosine rings (Fraenkel-Conrat et al,1948).

Glutaraldehyde is a five carbon dialdehyde compound with terminal reactive groups. It's attributes as a fixative lie with the two terminal aldehyde groups which are able to cross link primary amino groups more effectively than the single aldehyde group of formaldehyde (Bozzola et al,1999). Glutaraldehyde also has the benefit that most of the aldehyde groups are not bound up as glycols allowing significantly greater cross-linking than formaldehyde. It's higher molecular weight however, three times that of formaldehyde/methylene glycol, significantly limits the rate of penetration into tissue (Bozzola et al,1999;Fox et al,1985).

Osmium tetroxide is a symmetrical molecule containing four double-bonded oxygen molecules attached to a central osmium molecule which provides the electron density required for an EM contrast agent (Bozzola et al,1999;Porter et al,1952). Fixation through exposure to osmium tetroxide is thought to proceed through the attack of unsaturated oleic acid substrates within the sample (Schröder,1980;Korn,1967). When introduced into tissue, osmium tetroxide is reduced by unsaturated fatty acids within biological membranes and vesicles, the 4 reactive oxygen molecules ensuring cross-linking within the membrane, which results in the sample assuming a dark brown to black colour (Schröder,1980;Bozzola et al,1999).

Uranyl acetate is a common negative stain in EM, used to increase the contrast of low contrast biological specimens, which can limit the achievable resolution of the microscope. It provides a non-specific background stain, adsorbing well to most biological material (Watson,1958).

1.2.7. Combining Light and Electron Microscopy

One of the most important uses of microscopy within cell biology is in understanding the specific location of biomolecules within the cell, and their interaction with each other (Nisman et al,2004). A number of different techniques, each with their own unique benefits and capabilities, have been developed to provide information on structure and localization, however no single method is capable of providing all of the required information (Plitzko et al,2009). The ideal technique provides information across a broad range of spatial scales combined with labelling specificity and simultaneous detection of multiple antigens. Correlative Light and Electron Microscopy (CLEM) integrates the synergistic capabilities of Fluorescent Light Microscopy (FLM) and EM, bridging the gaps between specificity and resolution of the respective techniques (Cortese et al,2009).

The original use of CLEM as an application in the biological sciences was in the correlation of conventional light microscopy of immunohistological staining of secretory granules within different cell types (Kobayashi et al,1978). Indirect detection has also been applied using two secondary probes, one conjugated to a fluorochrome , the other to an electron dense gold nanoparticle, easily visible by EM (van Dam et al,1991). With the development of GFP, attempts were made to study the transport of a GFP-tagged tube-like protein along the neuronal axon using FLM. The area of this axon was then imaged using EM and found to contain tubular structures. Unfortunately this technique did not allow for the visualisation of exactly the same structure at both resolutions (Nakata et al,1998). CLEM studies have also shown the dangers in relying on single imaging techniques, seemingly similar fluorescent signals when imaged using ImmunoEM have been shown to localise to very different cellular organelles (Mironov et al,2000).

Immunofluorescence/gold techniques can be combined with a number of different preparative methods dependent on specific requirements and targets. Pre-embedding techniques require permeabilisation of the cell membrane to allow access of immunolabels to the intracellular environment. These allow high labelling densities of targets and preservation of antigenic structure. However, the permeabilisation step may result in loss of ultrastructural detail, especially with regards to membrane structure.

Immunofluorescence may also be affected by post-labelling techniques such as dehydration or UV polymerisation. This step can be avoided using post-embedding immmunolabelling techniques on ultrathin sections of embedded cells or tissue, preserving fine structural details. However, the harsh treatments involved in embedding techniques may reduce the antigenicity of specific targets. The embedding media may also prevent ingress of larger nanoparticle probes (Oorschot et al,2002;Giepmans et al,2005).

Although there are a number of different methods for CLEM analysis, there are some key steps that are required to generate correlative images. Samples are prepared through the chosen method and mounted on EM finder grids bearing spatial coordinates. These indexed grids are marked with a series of letters and numbers, providing a "grid reference" to allow exact determination of the position of cellular structures when transferred from the fluorescent microscope to the EM. In CLSM, the grid-mounted sample can be scanned for regions of interest before capture of z-stacks. The grid reference of these captured images can then be used to locate the same region by EM. Through visual comparison of identifiable structures at both EM and FLM levels the two images can be relocated to develop overlays of both images (Sartori et al,2007).

The above methodology describes the use of TEM as the ultrastructural imaging modality however a number of methods utilise Scanning Electron Microscopy (SEM), removing the necessity for sectioning steps prior to imaging. Scanning methods use a tightly focused beam of electrons to raster scan across the specimen block face surface while secondary or backscattered electrons are detected{Denk, 2004 505 /id}. As SEM techniques only provide information on the surface of the sample, three dimensional analysis requires the sequential removal of material from the block face prior to further imaging allowing a number of serial images to be reconstructed to provide a three dimensional model of the sample{Merchan-Perez, 2009 506 /id}. Imaging of the block face itself avoid the deformation and damage to the sample that is common during sectioning while allowing a depth of field only limited by the depth of the block.

Removal of material itself can be carried out in a number of ways, either through serial sectioning by diamond knife in a manner similar to TEM methodologies or by Fast Ion Bombardment (FIB) to ablate the surface between imaging steps{Denk, 2004 505 /id}{Langford, 2006 507 /id}. Following capture of the fluorescent component of the image by CLSM, FIB-SEM can then be carried out to produce the reconstructed volume. One of the major benefits of the FIB-SEM methodology lies in its ability to be fully automated, allowing higher throughput of samples {Lucas, 2014 508 /id}.

1.3. Proteomics

The latter half of the 20th century saw a shift in the research methodologies within the biosciences, moving away from the traditional hypothesis-driven analysis of single molecule studies to the "discovery science" of systems biology (Williams,1999). The basic premise behind this is that for any biological system the number of possible biomolecules, protein, DNA, metabolites etc, and their organisation within pathways is a large, but finite dataset, a comprehensive description of which would allow in-depth understanding of the organism (Patterson et al,2003). A number of fields sprung from this new research concept: i) genomics, the study of the whole genetic complement of the cell, ii) metabolomics, the study of the chemical products of cellular processes and, iii) proteomics, the entire set of proteins expressed by a cell or organism. The term proteome itself was coined by Marc Wilkins in 1994 as a portmanteau of proteins and genome, to describe the entire complement of proteins (Wilkins,2009).

The genesis of proteomics in terms of global protein analysis lies in the combination of two-dimensional gel electrophoresis (2DE) and mass spectrometry (MS). Initial protein sequencing was carried out using 2DE to separate complex protein mixtures followed by immobilisation of peptides on a solid substrate and Edman degradation sequencing. The N-terminal amino acid can then be removed by cleavage and identified through chromatography/autoradiography (Gevaert et al,2000). This methodology was low throughput and time-consuming with relatively low sensitivity (Bandeira et al,2008).

1.3.1. Anatomy of the Mass Spectrometer

One major drawback to the initial use of MS techniques for proteomic analysis was the necessity to ionise the sample in the gas phase for transfer into the high vacuum system of the instrument (Patterson et al,2003). Large molecules such as proteins and peptides are notoriously difficult to ionize without excessive sample degradation using traditional electron or photon ionization. Two major developments in the 1980's overcame these initial limitations, Electrospray ionization (ESI) and matrix-assisted laser desorption ionization (MALDI). ESI utilises a charged (usually several kilovolt) and heated needle through which analyte, dissolved in an appropriate solvent, is passed. Surrounded by a cylindrical electrode, the electric field at the tip of the needle charges the surface of the emerging liquid, resulting in it's dispersion through coulombic forces into an inert sheath gas. The heated needle combined with the sheath gas hasten the evaporation of solvent from each droplet as they drift towards the entrance to the mass spectrometer. The

evaporation of solvent leads to a decrease in the diameter of the droplet which in turn leads to an increase in it's charge density. This continues until the Coulomb repulsion equals the surface tension of the droplet at which point the unstable droplet undergoes a "Coulomb explosion", destroying the original droplet and creating a number of smaller daughter droplets. This process repeats itself, resulting in ever smaller droplets until the charge density on the small droplets is enough to desorb ions from the droplet to the ambient gas (Fenn et al,1989). It is worth noting that the actual mechanics of ion desorption have not been proven (Fenn et al,1989).

MALDI offers an alternative "soft" ionisation technique for the production of ions from large biomolecules such as proteins and peptides without the range of multiple charged ions generated through ESI. However, the ionization processes involved in MALDI are still poorly understood. Samples to be analysed are mixed with an appropriate matrix material before being spotted onto a metal target plate and allowed to dry, resulting in co-crystallisation of analyte and matrix. Matrix compounds have several fundamental properties, a low molecular weight to aid in vaporisation, strong absorption of UV light to allow efficient energy transfer for ablation, generally acidic to encourage proton transfer to the analyte and functionalised with a polar group to allow use with aqueous samples (Zenobi et al,1998;Knockenmuss,2006).

MALDI occurs as a two step process, the sample spot to be analysed is illuminated by a UV laser, the energy from which is absorbed by the matrix, resulting in ablation of the matrix/analyte mixture in the form of a hot plume of particles. During this process the matrix component is thought to transfer protons to the analyte molecule, resulting in the formation of ions. The removal and transfer of positively-charged ions is aided by the use of an extraction grid with -20kV charge relative to the MALDI plate. Positive ions are pulled during ablation and accelerated through the grid before transfer into the mass spectrometer (Watson et al,2008).

The basic function of the mass spectrometer is to analyse the mass-to-charge ration (*m/z*) of gas-phase ions. Therefore the mass analyser is the critical component of the mass spectrometer, separating ions by their mass-to-charge ratio and manipulating their movement through magnetic and electric fields to either eject ions from the system or direct them to a detector (Yates,2004). As soft ionisation techniques, MALDI and ESI both generate ions that are imparted with low energy and therefore undergo little fragmentation. While it is easy to accurately measure the mass-to-charge ratio of these intact ions, very little information regarding covalent structure is available using this technique. To

determine the amino acid sequence of proteins and peptides, as is required for proteomics, ions must be isolated, fragmented and analysed to determine the mass-to-charge ratio of the daughter fragments (Yates,2004). Four types of analyser are commonly used within proteomics research, varying in their physical principles and performance (Han et al,2008).

1.3.1.1. Linear Ion Traps

Quadrupole ion traps have been a mainstay mass spectrometer within the proteomics field. Using a 3-D trap, ions are isolated in the centre of the analyser before being scanned from the trap to the detector. However there are a number of limitations associated with 3-D traps. There is a finite limit to the number of ions that can be stored at any one time within the device, limiting sensitivity. Transfer of ions from trap to detector results in a 50% loss of ions due to ejection of ions from both ends of the trap (Jonschen et al,1997). To overcome these issues 2-D quadrupole ion traps, also known as linear ion traps have been developed with an ion capacity 10 times that of the 3-D traps leading to an increase in sensitivity and accuracy in ion statistics (Schwartz et al,2002). Linear quadrupole ion traps comprise of a ring electrode with two endcap electrodes. Using an oscillating Radio Frequency (RF) electric potential applied to the ring electrode a parabolic electric field is generated forcing ion trajectories to collapse into the centre of the trap (Jonschen et al,1997). Ions are both injected and ejected via a single end cap, allowing the use of two detectors due to the equal radial ejection through the exit slots, doubling the ion current collected during *m/z* range scanning (Schwartz et al,2002;Senko et al,2013). Another benefit of the linear ion trap is the increased scan speed, 15000 AMU/s versus 5500AMU/s, allowing increased data collection during Liquid Chromatography (LC) analysis (Yates,2004). There are certain limitations to 2-D ion traps; increases in resolution require a decrease in scan speeds which results in space charging within the trap. This physical phenomena, caused by forcing similarly charged ions close together, results in perturbation of ideal ion motion within the trap that can only be prevented by decreasing the mass range used (Yates,2004).

1.3.1.2. Time of Flight Analyser

Time-Of-Flight (TOF) mass spectrometry determines the mass to charge ratio through the length of time taken for an ion of known kinetic energy to travel a known distance. Ions transferred from the source are accelerated through an electric field of known strength. The electric field is pulsed to compensate for temporal, spatial and kinetic energy distributions within the ion population, accelerating them into an electric-field-free flight tube

orthogonal to their original trajectory (Wiley et al,1955). The kinetic energy and therefore velocity provided to each ion is a function of it's charge, and the mass of the ion (Chernushevich et al,2001). Ions with larger charges will have a higher potential energy, which is translated to higher velocities for lighter ions and lower velocities for heavier ions. TOF mass separation occurs within the field-free drift tube towards the detector. By recording the time taken for ions to travel through the drift tube, the mass-to-charge ratio can be deduced. Low *m/z* ions will take less time to travel this distance than high *m/z* ions (Domon et al,2006).

The major limitation of the TOF analyser lies in its inability to perform true MS/MS experiments due to the lack of fragmentation capabilities. This is usually overcome through the use of two quadrupole ion traps preceeding the TOF analyser, which enables selection of the precursor ion in the first quadrupole. Fragmentation through Collision Induced Dissociation (CID) (using an inert gas) is carried out in the second quadrupole and the products are analysed by TOF (Domon et al,2006;Yates,2004). The major benefits of TOF mass spectrometry for proteomics research are an "unlimited" *m/z* range and the ability to simultaneously observe the entire mass spectrum without scanning. Developments such as reflecting electrostatic fields to improve mass resolution and orthogonal injection provide both TOF and MS/MS-TOF with the high mass accuracy and resolution required for determination of the charge state and unambiguous assignment of signal peaks (Domon et al,2006).

1.3.1.3. Fourier Transform-Ion Cyclotron Resonance Analyser

Fourier Transform-Ion Cyclotron Resonance Mass Spectrometry (FT-ICR MS) is an extremely high resolution method of mass analysis. Two of the most important parameters in proteomic mass spectrometry are mass resolution and mass accuracy. Mass resolution enables discrimination of ion charge states and isotopic distributions, while mass accuracy enables narrower peak spread and therefore more accurate peak centroid calculation. FT-ICR provides the highest mass accuracy and resolution of any analyser (Yates,2004;Marshall et al,1998).

Ion cyclotron frequency, radius, velocity and energy occur as a function of ion mass and ion charge within a spatially uniform static magnetic field (Marshall et al,1998). FT-ICR operates by transferring ions into a cell where they become trapped in a static magnetic field. Within the magnetic field ions exhibit cyclotron motion, orbiting about the *z* direction within the cell, the frequency of which can be used to determine the *m/z* of the

ions. A RF electronic pulse can be applied orthogonal to the magnetic field within the cell to excite and induce coherence within the orbiting ion population, increasing the cyclotron radius of the ion packet. The in-phase packet of ions induces a charge on a pair of electrodes within the cell as they pass close to them. Ion packets begin to degrade in a mass dependent manner to a smaller radius, incoherent cyclotron motion which does not induce a current across the electrodes. This orbital decay can be recorded as a free induction decay signal in the form of a superposition of sine waves. Fourier transforms of this signal allows extraction of the *m/z* (Marshall et al,1998;Comisarow et al,1974).

The FT-ICR has a number of advantages over other forms of mass analyser. Its extremely high resolution is ideal for separating complex mixtures, detecting ions with similar mass-to-charge ratios as distinct peaks within the spectra (Sleno et al,2005). The high resolution is also ideal for studying large biomolecules such as proteins and peptides which can obtain multiple charge states during Electrospray Ionization. Large molecules such as these contain a distribution of isotopes that result in a number of peaks extremely close together on the *m/z* axis. The resolution of FT-ICR allows a distinction to be made between these peaks that would otherwise be lost in other systems (Solouki et al,1995). This ability to resolve closely related *m/z* ions is also valuable as a method of identifying protein post-translational modifications (Kelleher et al,1997).

1.3.1.4. Orbitrap Analyser

The newest development in mass analyser technology is the orbitrap, which is capable of producing similar mass accuracy and resolution as FT-ICR technology but without the economic and space operating costs of running a superconducting magnet (Domon et al,2006). Developed by Makarov in 1999 it was not until 2005 that it was first used as a tool for proteomic research (Makarov,2000;Hu et al,2005).

Based on the ion trap developed by Kingdon in the 1920's, the orbitrap is composed of an outer barrel-like electrode, comprised of two symmetrical components, surrounding a central coaxial spindle-shaped electrode across which an electrostatic field is maintained (Kingdon,1923). A static applied voltage results in the formation of an electric field with radial logarithmic potential between the electrodes. To introduce ions into the trap, the field strength is reduced before ion packets are injected tangentially into an orbit around the central electrode. The field strength is gradually increased through an increase in the voltage between the electrodes, compressing the ion orbits towards the central electrode until the desired orbital radius is achieved at which point the voltage is maintained at a

static value. Each ion packet injected into the trap is composed of ions having a variety of different velocities orbiting the spindle electrode with different rotational frequencies. However, those with the same *m/z* ratio will oscillate axially with the same frequency resulting in a number of ion packet rings oscillating independently along the inner spindle (Makarov,2000). Axial Oscillations between the two parts of the external barrel electrode generate an image current through a differential amplifier connecting them. The frequency of oscillation for each ion ring within a specified electric field can be used to determine the *m/z* in a similar manner to the rotational frequency detection of FT-ICR through a Fourier transform of the time domain (Han et al,2008;Makarov,2000).

1.3.2. Quantitative Mass Spectrometry for Analysis of the Cellular Proteome

One of the most important yet technically challenging questions in proteomics research is the quantification of proteins within a sample and changes in expression under different conditions. Traditional proteomic techniques such as differential gel staining or Western blotting using fluorophores or radioisotopes have provided sensitivity, linearity and dynamic range. However, they are limited by two important factors. Firstly the high resolution separation required for such methods, typically through 2-D gel electrophoresis, limits their use for highly abundant or highly soluble proteins, with a bias against membrane-associated classes. Furthermore, detection and quantification using this method does not provide information regarding the identity of the unidentified protein of interest (Ong et al,2005;Bantscheff et al,2007).

Liquid Chromatography (LC) separation methods linked to MS/MS analysis can be used to overcome the problems associated with gel separation and identification methods. Standard proteomics workflows utilise site-specific proteolytic enzymes such as trypsin to generate a pool of peptides. These peptides can then be fragmented within the mass spectrometer to generate a mass spectra from which the corresponding peptide sequences can be identified from a database (Ong et al,2005). Proteins can be easily identified, usually requiring only two unique peptide matches for confirmation (Ong et al,2005). However, lack of detection does not denote absence of a protein from a sample, since peptides may exist at concentrations below the detection threshold of the mass spectrometer.

The present/not present binary nature of standard MS proteomics gives a limited view of protein regulation and abundance within a biological system. Bypassing gel separation prevents quantification of protein abundance prior to mass analysis, data which is one

necessary to understand the changing proteome landscape of biological systems under different conditions. Protein abundance can be quantified in one of two ways, the absolute amount of protein within a single sample, or the relative change in a protein between two separate states (Ong et al,2005). In MS, absolute quantification is achieved by spiking the analyte sample with a known amount of a synthetic, isotopically labelled reference peptide. Isotopically labelled peptides are chemically identical to non-labelled counterparts but can be easily identified by their known mass shift during analysis (Bantscheff et al,2007). By comparing the signal intensity or peak size of this known reference peptide against the signal intensity of an endogenous peptide of interest, the exact concentration of the original protein can be calculated (Brönstrup,2004). Relative quantification defines the amount of a peptide by its signal intensity relative to another measurement of that same peptide under different conditions. In reality, absolute quantification encompasses both forms, if two absolute values for a peptide are known then the relative change can be easily determined (Ong et al,2005).

1.3.2.1. Isotope Coded Affinity Tag (ICAT)

One method of chemical modification developed by Gygi *et al* is Isotope-Coded Affinity Tagging (ICAT) (Gygi et al,1997). Using this approach an isotopically-labelled reagent is attached to specific amino acids within the peptide through modification of a defined side chain, such as iodoacetamide modification of cysteine residues. The isotope-coded reagent functions as a linker, binding the modified side chain to an affinity purification tag such as biotin. For comparison of two proteomes, this method is carried out in tandem, however the samples are linked with two iosotopically distinct labels, one being a light isotope, the other heavy. To minimize experimental error both samples are mixed and digested before being affinity purified, simplifying the peptide mixture and isolating tagged peptides from the untagged population. These tagged and purified peptides can then be analysed using LC-MS to generate mass spectra. Comparison of isotopic peaks allows relative quantification of individual peptides and therefore proteins within the two proteomes (Gygi et al,1997;Ong et al,2005). This method can be applied to any proteome from both living and dead tissue, including body fluids and biopsy samples (Mann,2006).

1.3.2.2. Stable Isotope Labelling by Amino acid Composition (SILAC)

There are a number of problems regarding the accuracy of chemical labelling methods, for example derivitization of labelled tags may result in incomplete coverage or result in the formation of secondary products during modification. Any sample loss that occurs before

mixing will adversely affect the relative quantification results. One way to overcome this limitation is metabolic labelling of proteins during growth; both heavy and light samples can be immediately mixed before undergoing further processing, ensuring that any loss which occurs during fractionation and purification applies equally to both samples, thereby reducing quantification errors (Mann,2006). In recent years, Stable Isotope Labelling by Amino acid in Cell culture (SILAC) has become the most popular method for metabolic labelling of proteomes from mammalian cells.

Cell lines are grown in suitable media deficient in two essential amino acids, which is then supplemented through the addition of non-radioactive, isotopically-labelled forms of those amino acids, typically deuterated forms of lysine (Lys-d3) and arginine (Arg-d3). As cells grow and divide, the heavy labelled amino acids are incorporated into proteins within the cell. Typically after five doublings, the unlabelled amino acids from the parent cells have been replaced by those in the deuterated SILAC media. Protein populations from both the heavy-labelled experimental samples and non-labelled control samples are then mixed directly after harvesting before undergoing digestion and purification before analysis through LC-MS. The pairs of chemically identical peptides can be identified by peak shifts within the mass spectra due to their mass differences. These peaks can then be compared and their intensities used to generate a relative abundance ratio for the parent protein (Ong et al,2002).

For accurate measurement of relative change, sources of unlabelled amino acids within the experimental media must be eliminated to ensure complete incorporation. The addition of biological mammalian serum as a growth supplement is the largest source of unlabelled amino acids and as such must be dialysed thoroughly to prevent contamination. This requires adaptation of the cell line to dialysed serum which may prove difficult with certain cell lines (Mann,2006).

1.4. Hepatitis C Virus

1.4.1. Discovery of Hepatitis C Virus

Although early epidemiology studies failed to provide evidence for more than the already known two viral hepatitis agents, hepatitis A virus (HAV) and hepatitis B virus (HBV) (Krugman,1975), an increasing number of post-transfusion hepatitis cases with incubation periods intermediate to both HAV and HBV had begun to appear by the mid 1970's (Mosley,1975). The serendipitous discovery of hepatitis B surface antigen (HB_sAg) in 1963 from the serum of an Australian Aborigine (Alter et al,2008;Lee,1977) led to the

development of a sensitive enzyme-linked immunosorbent assay (ELISA) nearly a decade later. Following the discovery in 1975 of HAV (Feinstone et al,1973), backdated analysis of stored post-transfusion hepatitis sera uncovered a number of samples that tested negative for both HAV, HBV and other hepatropic viruses such as cytomegalovirus (CMV) and Epstein-Barr Virus (EBV), resulting in the designation by exclusion of Non-A, Non-B Hepatitis (NANBH) (Feinstone et al. 1975;Kuo et al. 1989). At this time the causative agent or agents was associated with 90% of all Transfusion Associated Hepatitis (TAH) cases occurring in 10% of total transfusions (Kuo et al,1989)

The infectious nature of the NANBH agent was demonstrated through a series of chimpanzee transmission studies (Tabor et al,1978;Alter et al,1978). Inoculation of chimpanzees with plasma or serum from NANBH human patients resulted in persistent elevated serum alanine aminotransferase (ALT) levels indicative of hepatocellular injury. As in humans , 50% of the infected chimps went on to develop chronic NANBH following inoculation (Bradley et al,1981). The transmission of both acute and chronic hepatitis from patient samples suggested that the agent responsible for NANBH was a transmissible agent capable of i) sustaining a chronic carrier state and, ii) remaining infectious for long periods of time (Alter et al,1978). Treatment of known infectious human serum samples with chloroform before inoculation into chimpanzees prevented infection, suggesting that the agent was susceptible to lipid solvent (Feinstone et al,1983). Further work passaging infectious serum through 80nm filters provided more evidence that the cause of NANBH was a small enveloped virus (He et al,1987). Narrowing of the taxonomic range of possible viral agents responsible raised the possibility that the NANHB agent may well be a flavivirus (Bradley et al,1985). Most significantly, follow up of study patients showed that NANHB was generally a persistent infection progressing to cirrhosis in 20% of cases (Berman et al,1979).

Despite evidence of the NANBH agent being a small enveloped virus, the failure of conventional immunological methods to identify specific viral antibodies and antigens prevented the identification of the causative agent for over a decade (Shih et al,1986). Speculating that this failure was due to insufficient antigen as opposed to a lack of viral antibody, Houghton *et al* sought to increase antigen concentrations using a cDNA library derived from known infectious materials using bacteriophage λgt11 in a blind immunoscreening approach (Choo et al,1989). Serum taken from a diagnosed chronic NANBH patient was used to screen and identify one viral cDNA clone (termed 5-1-1) from a library of one million cDNAs. Hybridisation of this cDNA clone to both human and

chimpanzee DNA by Southern blot analyses proved that the clone was not derived from the host genome, instead binding a large RNA molecule of approximately 10,000 nucleotides in length which was found only in NANBH infectious material (Choo et al. 1989).The authors went on to show that this clone was derived from a positive-strand RNA encoding a large polyprotein of approximately 3000 amino acids with distant sequence identity to members of the Flaviviridae family (Choo et al,1989;Kato et al,1990). NANBH was therefore identified as hepatitis C virus (HCV) using direct molecular cloning of the viral genome with limited knowledge of the nature of the causative agent (Houghton,2010).

Further investigation of the HCV genome highlighted organisational similarities to both the flavivirus and pestivirus genomes, which are members of the Flaviviridae family (Choo et al,1989;Miller et al,1989). Although it shared some sequence homology with the non-structutral 3 (NS3) region of dengue type 2 virus, HCV was sufficiently unique to result in its classification as a novel hepacivirus genus within the Flaviviridae.

1.4.2. Classification and Genotypes of HCV

Within the hepacivirus genus, HCV exhibits broad genetic diversity at a variety of levels. From phylogenetic analysis of isolates, HCV has been classified into 7 genotypes differing by 31-34% at the nucleotide sequence level and by approx 30% of their amino acid sequence (Pawlotsky,2004;Smith et al,2013). The 7 genotypes can be further divided into subtypes based on nucleotide differences of 20-23%. The genetic divergence of the main HCV genotypes is frequently linked to distinct geographical distribution and associated with particular risk groups Finally, there exists a number of measurably different but closely related “quasispecies” within infected individuals (Martell et al,1992;Houghton et al,1991). Comparative sequence analysis of different HCV isolates show that nucleotide variability is unevenly distributed throughout the genome with areas of high conservation and areas of high genetic variability (Martell et al,1992).

1.4.3. HCV Epidemiology and Transmission

HCV is a worldwide problem affecting 3% of the global population, which equates to 170 million chronically infected individuals, and 3-4 million new cases annually. With 70-80% of new cases progressing to chronic disease it has become a leading cause of liver disease (World Health Organisation,2000;Berenguer et al,1999). Within the UK, it is estimated that approximately 215,000 individuals aged 15-59 are infected with the virus

(Costella,2008). Developing countries such as Africa, parts of Asia and South America exhibit far higher infection rates with some areas close to 10% (Wasley et al,2000). The country with the highest prevalence is Egypt with almost 15% of the population chronically infected with the virus (Alter,2007).

The majority of HCV transmission occur through purcutaneous exposure to infected blood through three main routes, the transfusion of blood products from infected donors, non-sterile therapeutic injections and intravenous drug use {Shepard, 2005 522 /id}. Introduction of nucleic acid and antibody screening of donated blood has virtually eliminated new cases of transfusion associated HCV infection in developed countries. However this mode of transmission is still a significant problem in countries lacking developed screening practices{Lemon, 2007 523 /id}. Unsafe medical practices in general account for a large number of new HCV infections. One study estimated that for the year 2000, 2 million cases of HCV infection worldwide were the result of contaminated medical injections{Hauri, 2004 524 /id}. The majority of new acquired HCV infections in developed countries are the result of intravenous drug use{Thomson, 2009 525 /id}. In Scotland alone 90% of those diagnosed in 2003 were found to have injected drugs{Hutchinson, 2005 526 /id}.

.Certain genotypes of HCV (types 1, 2 and 3) show a broad worldwide distribution especially countries in the western hemisphere, whereas others such as genotypes 5, (found mostly in South Africa) and 6, (in Southeast Asia), display tight geographical constraints (Nguyen et al,2005;Alter,2007). Understanding these distribution patterns requires knowledge of routes of transmission within risk groups and historical data over previous decades and centuries, but very little is known outside of specifically surveyed countries (Simmonds,1995).There does exist several discernible routes of genotype distribution which have been identified within countries that have undertaken in-depth studies. Blood donors and chronic hepatitis patients in Western Europe and the United States show frequent infection with genotypes 1a, 1b, 2a, 2b and 3a (Simmonds et al,1993). In a number of European countries genotypic distribution varies with age, highlighting the rapidly changing genotypic distribution within a geographical area with time (Simmonds,1995).

The high level of viral heterogeneity within an individual is in keeping with Batschelet *et al*'s pioneering study showing that such diversity is a consequence of high error rates in RNA replication due to a lack of the elaborate proof-reading ability found during DNA transcription and the inherent instability of RNA compared to DNA (Batschelet et

al,1976;Steinhauer et al,1987). HCV circulates within the body as a heterogeneous mixture consisting of a "master" (most common) sequence and an array of mutants, the full complement of which is known as a quasispecies (Steinhauer et al,1987;Martell et al,1992). The quasispecies model confers a significant evolutionary advantage due to the simultaneous existence of multiple variant genomes, which allows for rapid selection of higher fitness mutants under environmental selective pressure. In the absence of selective pressure, a quasispecies will remain in stable equilibrium with little change to the master sequence (Domingo,1989). Such quasispecies models pose numerous complications with regard to treatment and immune response including vaccination failure through antibody escape mutants, resistance to antiviral agents and changes in cell tropism and virulence (Domingo et al,1985).

1.4.4. Clinical Features of HCV Infection

The liver is the focal point of HCV infection and replication. The virus is a major cause of hepatocellular carcinoma (HCC), and is now a common indication for liver transplantation (Sharma &Lok, 2006). The acute phase of HCV infection is frequently followed by the establishment of a chronic phase. Both phases are described below.

1.4.4.1. Acute HCV Infection

Acute HCV infection follows initial exposure to the virus. In a minority of cases (20%), individuals will present with fatigue, malaise and jaundice, although in the majority of cases (~80%) this is asymptomatic (Pawlotsky,2004). Exposure to the virus rapidly triggers a non-specific immune response principally involving type I IFN secretion and NK cell activation. Type I IFN secretion however does not effectively inhibit viral replication (Thimme et al,2001). It has been suggested that binding of the HCV glycoprotein E2 to the host cell receptor CD81 may inhibit initial NK cell activities, such as proliferation, cytotoxic granule release and cytokine production, as well as post-activation IFN-γ production (Tseng et al,2002). Various HCV proteins also inhibit intracellular anti-viral functions such as the JAK-STAT pathway, RNA-dependent protein kinase (PKR) and IFN regulatory factor-3 (IRF-3) (Katze et al,2002). This manipulation of host innate and adaptive responses by the virus is assumed to result in dampening of the CD4+ and CD8+ T-cell responses leading to the development of a chronic infection (inability to clear the virus after 6 months) in 80-85% of infected individuals (Pawlotsky,2004;Dienstag,1983).

1.4.4.2. Chronic HCV Infection

Once established, chronic HCV infection is rarely cleared without therapy. Although this chronic state can remain asymptomatic for up to 35 years, ~20% of chronically infected individuals do develop hepatic and non-hepatic disease. Chronic infection with HCV will typically induce injury and inflammation of the liver, which in turn results in progressive fibrosis. Fibrosis functions as a non-specific response to injury in the liver, depositing extracellular matrix within the hepatic parenchyma, believed to limit the extent of inflammatory damage (Marcellin et al,2002;Pawlotsky,2004). However, in a sustained hepatropic infection, the irreversible nature of fibrosis leads to widespread hepatic fibrosis and eventually cirrhosis. This pathology is the main cause of morbidity and mortality in chronic HCV infection (Pawlotsky,2004). The damage caused during infection can also be exacerbated by environmental co-factors such as viral co-infection (e.g. HIV) and alcohol intake (Peters et al,2002;Hezode et al,2003). Cirrhosis is characterised by serious liver dysfunction, patients often present with ascites, hepatorenal syndrome, and hepatic encephalopathy which can result in confusion, altered consciousness, coma and if untreated, death (Thomson et al,2005). Although the majority of liver damage caused during HCV infection is due to localised non-specific immune responses, there is growing evidence that steatosis may be a direct cytopathic effect of infection with genotype 3 infections (Kumar et al,2002). Following cirrhosis, a further 1-4% of infected patients will go on to develop hepatocellular carcinoma (HCC) (Fishman et al,1996;Fishman et al,1996).

1.4.5. Treatment of Infection by IFN-α and Ribavirin Combination Therapy

There are currently no vaccines available for HCV, which is the most likely effective method of controlling and possibly eradicating the virus given its global prevalence (Forns et al,2002). Current treatment is more effective in infections with genotypes 2 and 3, where up to 70-80% of patients respond. In those infected with genotype 1, the most prevalent in the western world, up to 65% of patients will clear the virus (Manns et al,2001) although response rates are typically below 50%. Neither the disparity in therapeutic response between genotypes nor the high efficacy (~98% success) of treatment when initiated in the acute phase is properly understood (Jaeckel et al,2001). Until recently, therapy consisted of a combination of pegylated interferon alpha (PEG-IFN-α), injected intramuscularly once weekly and daily administration of the gaunosine analogue Ribavirin (1-β-$_D$-ribofuranosyl-

1,2,4-triazole-3-carboxamide) (Afdhal,2002). The side effects of this therapeutic regime are debilitating, the major types include myalgia, fatigue, influenza-like symptoms, hematologic complications and neuropsychiatric disturbances (Fried,2002). IFN-α is a 19.5kDa glycoprotein cytokine signalling molecule released by lymphocytes in response to the presence of pathogens such as bacteria and viruses, leading to the activation of immune cells such as NK cells and macrophages which exhibit anti-viral activity. Early treatments utilising IFN-α monotherapy were quickly replaced due to the high rates of relapse after 48 weeks of treatment (McHutchison et al,1998). The use of IFN-α combined with Ribavirin proved more effective in maintaining a sustained virological response in 40% of patients, but was associated with breakthrough infections (Zeuzem et al,1996). In order to maintain constant pressure on the virus and increase the half-life of interferon, polyethylene glycol (PEG) was added to IFN-α, modifying the protein to slow its clearance from the blood (Lindsay et al,2001). Ribavirin acts alongside IFN-α; it is a nucleoside analogue which is capable of being incorporated into the viral RNA during replication to prematurely terminate synthesis of the viral genome.

Although, the precise anti-viral function associated with Ribavirin is not fully understood there are a number of postulated modes of action, such as modulation of host T-cells. The phenotype of the host T-cell response may have a significant effect on the outcome of infection, T helper 1 Th1 response is associated with clearance of HCV infection while T helper 2 Th2 may predispose to a chronic course of infection.{Rehermann, 2005 527 /id}. Treatment with Ribavirin and interferon-α has been shown to induce stronger HCV specific T-cell responses compared to monotherapy with interferon-α, correlating with increased SVR rates{Cramp, 2000 528 /id}. One other long held theory for Ribavirin action is in the competitive inhibition of the cellular enzyme inosine monophosphate dehydrogenase (IMPDH), an essential enzyme in the metabolic pathway for the *de novo* synthesis of the purine guanosine, required for viral RNA replication{Streeter, 1973 529 /id}. One other possible mode of action relies on Ribavirins ability to behind equally well to both uracil and cytosine, resulting in hyper mutation of the viral genome. Antiviral effect has been shown to do correlate directly with mutation activity suggesting that Ribavirin forces the virus into a state of error catastrophe, resulting in a rapid drop in viability{Crotty, 2000 531 /id}{Crotty, 2001 530 /id}..

Progression of pathology to end-stage liver disease can only be treated through liver transplantation. However, 90% of transplanted livers become immediately infected due to HCV circulating in the periphery (Gane et al,1996).

1.4.6. Molecular Characteristics of Hepatitis C Virus

1.4.6.1. The HCV Virion

The HCV virion is considered to be a particle 55-65nm in diameter with a host derived lipid bilayer envelope to which virus-encoded glycoproteins E1 and E2 are anchored. The nucleocapsid is comprised of multiple copies of core protein forming the internal structure, of spherical or icosahedrons shape surrounding the genomic RNA {Ishida, 2001 532 /id}(Penin et al,2004b). The infectious unit of HCV harbours not only viral but also host components, circulating in the serum of the infected host as a lipoviral particle (LVP) (Nielsen et al,2006;Thomssen et al,1992;Andre et al,2002). The majority are bound to very low density lipoprotein (VLDL) and low density lipoprotein (LDL), with a size range of 30-80nm constituting the infectious fraction. The influence of bound lipoproteins and their biosynthetic pathways on HCV infectivity, virion internalisation and virion assembly highlights the importance of lipids to every aspect of the viral lifecycle (Bradley et al,1991;Catanese et al,2013;Bartenschlager et al,2011;Benga et al,2009).

1.4.6.2. Viral Genome

The viral genome is a single-stranded, positive-sense RNA molecule, of 9.6kB in length. It contains two highly conserved untranslated regions (UTRs) at the 5' and 3' termini flanking a single large open reading frame encoding a ~3000 amino acid polyprotein (Okamoto et al,1991). The 5' and 3' UTRs are 341 and 230 nucleotides in length respectively, both of which contain *cis*-acting elements required for initiation of genome replication (Friebe et al,2001). The 5' UTR is comprised of four domains, I-IV, domains II-IV together with the first 24 to 40 nucleotides of the core-encoding region comprise the Internal Ribosome Entry Site (IRES). Binding of the ribosome to the viral genome occurs a few nucleotides upstream of the AUG triplet that acts as the translation initiation codon (Penin et al,2004b;Tsukiyama-Kohara et al,1991). The 40s subunit of the ribosome is positioned in contact with the AUG initiation codon by means of domains II and III of the 5' UTR (Penin et al,2004b).

The 3' UTR consists of a variable 40 nucleotide sequence with an internal poly U tract, followed by a 98-nucleotide sequence that is highly conserved between genotypes containing stable stem-loop structures which are thought to be important in initiating genome replication (Shi et al,2001).

The polyprotein encoded by the ORF can be divided into two parts, a) the structural proteins, (core, E1, E2) and p7 (which may or may not be a component of virions) found within the first third from the N-terminus and b) the remainder of the polyprotein encoding the non-structural (NS) proteins. The polyprotein is co- and post-translationally cleaved by host and viral proteases to produce the mature structural and NS proteins.

1.4.6.3. Core Protein

During translation of the viral polyprotein, it is targeted to the host ER membrane for translocation of the E1 ectodomain into the ER lumen. This process is mediated by an internal signal sequence that lies at the C-terminal end of core which is cleaved by host signal peptidase to produce the immature core protein (21kDa) (Penin et al,2004b;McLauchlan et al,2002). Further processing at the ER membrane by host signal peptide peptidase produces the mature form of core (19 kDa) (McLauchlan et al,2002). Most of the core protein is targeted to lipid droplets (Hope et al,2000). The N-terminal 120 amino acids constitute a hydrophilic domain with a high basic amino-acid content, while the C-terminal region is mainly hydrophobic and is required for lipid droplet association (Hope et al,2000;Boulant et al,2007). Multiple copies of core are considered to form the viral capsid.

1.4.6.4. E1 and E2 Proteins

The E1 and E2 envelope glycoproteins are critical in host cell entry, binding to cell membrane receptors, and inducing fusion with the surface of target cells (Penin et al,2004b). The E1 and E2 proteins are type-I transmembrane proteins with an N-terminal ectodomain and a short C-terminal transmembrane domain of hydrophobic stretches separated by highly conserved, polar residues (Dubuisson et al,2002;Op De Beeck et al,2001). During synthesis, the ectodomains of the glycoproteins are targeted to the ER lumen where they undergo modification by N-linked glycosylation at a number of sites. E1 and E2 combine to form non-covalent heterodimers that are likely to be the prebudding form of the complex which will eventually play a role in binding and entry of the mature virion to the host cell (Op De Beeck et al,2001). Both glycoproteins have important roles in virus entry, with glycosylation playing a major role in protein folding and virion entry (Goffard et al,2005). E2 contains two hypervariable regions, HVR1 and HVR2. HVR1 is located in the N-terminal 27 amino acids of E2 and is the most variable region of the HCV genome (Penin et al,2004b). HVR1 is thought to evolve rapidly during infection in

response to antibody-mediated immune responses resulting in a number of escape variants (Mondelli et al,2003).

E2 is thought to be a class II fusion protein, comprised of three domains including a large ectodomain and virtually no cytoplasmic tail. Domain II contains a putative fusion loop, while the CD81 tetraspanin binding domain can be found at the domain II and III interface (Krey et al,2010). A three-fold reduction of CD81 cell surface expression through small interfering RNA (siRNA) has been shown to abrogate infection by HCV pseudo particles (HCVpp) highlighting its importance in viral entry (Zhang et al,2004). Alongside CD-81, a number of cellular HCV receptors have been identified including SR-BI and occludin (Liu et al,2009;Scarselli et al,2002).

1.4.6.5. p7

p7 is a small 63aa intrinsic membrane polypeptide with a double membrane-spanning topology. The transmembrane domains TM1 and TM2 are predicted to form α-helices linked by a charged cytoplasmic loop, with the C-terminal region functioning as an internal signal-like peptide. Amino acid sequence analysis shows highly conserved helix faces suggesting that both TM domains are involved in helix-helix interactions (Carrere-Kremer et al,2002;Perez-Brena et al,2008). While most cleavage events in the HCV polyprotein occur during or immediately after translation, the cleavage of E2/p7 and p7/NS2 by the ER signal peptidase is delayed, suggesting that it is released in a regulated manner (Dubuisson et al,1994). From its conserved structure and characteristics, p7 is considered to belong to the viporin family of proteins, forming hexameric homo-oligomers that affect membrane permeability which are important for viral assembly and release (Carrasco 1995;Griffin et al. 2003;Pavlovic et al. 2003). The hexameric ring structure formed by p7 functions as a membrane pore, preferentially allowing the passage of calcium ions (Griffin et al,2003). The administration of the antiviral agent amantadine, which acts against influenza A virus replication by blocking M2 ion channel formation inhibits p7 activity (Griffin et al,2003). These factors make p7 an attractive choice for novel antiviral drugs.

1.4.6.6. NS2

The NS2 protein is a 23kDa cysteine protease integral membrane protein, responsible for autocatalytic cleavage of the NS2/NS3 junction (Santolini et al,1995;Jones et al,2007). The N-terminus of NS2 consists of one or more transmembrane domains while the C-terminal domain of NS2 couples with the N-terminus of NS3 to form the NS2-3 protease. NS2

functions as a metalloproteinase requiring zinc to maintain its autoproteolytic activity. Addition of a metal chelating agent such as EDTA inhibits protein function, while the addition of $ZnCl_2$ leads to an increase in cleavage activity (Pieroni et al,1997). Site-directed mutagenesis has shown that two amino acids, histidine-143 and cysteine-184, are essential for catalytic activity, however the complete protein is required for efficient function (Grakoui et al,1993a). The NS2 protein is not essential for viral RNA replication *in vitro.*

1.4.6.7. NS3

NS3 is a 72kDa protein with a serine protease domain of 189 amino acids at the N-terminus and a 442 amino acid NTPase-RNA helicase motif at its C-terminus. Following the autoproteolytic cleavage of NS2/3, NS3 mediates cleavage at the boundaries between the remaining downstream NS proteins (NS3/NS4A, NS4A/NS4B, NS4B/NS5A and NS5A/NS5B. Cleavage of NS3-NS4A and NS4B-NS5A boundaries and accelerated cleavage of the NS5A-NS5B site requires a C-terminal 33aa region of NS4A, which acts as a cofactor in NS3 cleavage (Lin et al,1994;Failla et al,2013). Sequence analysis of several HCV isolates has shown that NS3 contains 3 highly conserved residues, histidine-1083, aspartic acid-1107 and serine-1165, which form a serine protease catalytic triad whose function can be abrogated by site-directed mutagenesis (Miller et al,1989;Grakoui et al,1993b). As NS3 is unable to target and bind ER membranes, it must first associate with the central domain of NS4A to stabilize and activate the complex via β-strand, β-barrel association and localise to the ER before cleavage of the downstream junctions (Penin et al,2004b). In the absence of NS4A, NS3 loses its ER localisation, becoming distributed throughout the cytoplasm (Wolk et al,2000). The NS3-4A serine protease is a key target for the direct-acting antiviral (DAA) compounds telaprevir and boceprevir, which are now licensed for therapeutic use in combination with PEG-IFNα and ribarvirin (Lamarre et al,2003;Kwong et al,2008).

The NTPase and helicase activities of NS3 within its C-terminal region are far less well characterised than the protease function. It is a member of the superfamily-2 helicases and appears to have similar properties to RNA helicases of other positive-strand RNA viruses (Suzich et al,1993). The viral RNA helicases are involved in strand separation during replication and transcription and possibly in resolving RNA secondary structure during translation. Most helicases intrinsically hydrolyse nucleoside triphosphates, providing the energy required to unwind nucleic acid sequences in the 3’ to 5’ direction (Tai et al,1996;Major et al,1997). The NS3-4A protease complex also contributes to the immune

evasion strategy of the virus, promoting establishment of a chronic infection through cleavage of the mitochondrial antiviral signalling (MAVS) (Meylan et al,2005). Cleavage of MAVS by the viral protease results in dislocation of the N-terminal fragment from the mitochondrial outer membrane, a location critical for activation of the NF-κβ and IRF-3 upstream of the interferon signalling pathway (Li et al,2005).

1.4.6.8. NS4A

NS4A is a 54 amino acid, 6kDa protein with a hydrophobic N-terminal region followed by a hydrophilic C-terminus which, as mentioned previously is a cofactor for NS3. The region required for NS3 activation resides within the central hydrophobic portion of the protein between amino acids 21-34. This sequence interacts with a β-sheet of the enzyme core, significantly altering the structure of NS3 and is important for enzyme activity and stability (Kim et al,1996).

1.4.6.9. NS4B

NS4B is a 27kDa hydrophobic integral membrane protein that co-translationally associates with the ER membrane, and is the least well characterised of the HCV proteins (Penin et al,2004b). Prediction algorithms suggest that it contains between 4 and 6 TM domains (Hugle et al,2001). The protein has a N-terminal amphipathic α-helix, which is critical for integration with the ER membrane. Mutants with an intact N-terminus region but no TM domains retain the ability to target the protein to the ER while disruption of the N-terminal region abrogates membrane association (Elazar et al,2004).

Expression of NS4B induces the formation of the membranous web structure within the ER membrane that is thought to harbour replicating viral RNA (Egger et al,2002). It is capable of interacting with the ER membrane with or without the presence of the other HCV NS proteins. Therefore, it is possible that NS4B functions as a scaffold, inducing membrane alterations for the formation of the viral replication complex (Gosert et al,2003). The role of NS4B within the replication complex is still unknown although a single amino acid substitution within NS4B has been shown to ablate the activity of a single amino acid change within NS5B that is normally associated with higher replication efficiency. This suggests that the function of NS4B is tightly coupled to the viral RNA polymerase at some stage in the replication cycle (Lohmann et al,2001). In addition, individual mutations within the protein can abolish HCV RNA replication, and, indeed prevent formation of foci indicative of the membranous web (Jones et al,2009;Paul et al,2011). Moreover, mutations

in NS4B affect the phosphorylation status of NS5A, again highlighting the close interaction between the protein and other viral components (Jones et al,2009).

Membrane alterations induced by NS4B have been imaged using electron microscopy and closely resemble the altered membrane structures found in the livers of HCV-infected chimpanzees (Pfeifer et al,1980). Further colocalisation studies using immunogold-tagged NS proteins showed that these structures are indeed multiprotein complexes (Gosert et al,2003). Expression of NS4B in the absence of any other HCV proteins induces membrane changes indistinguishable from those in cells harbouring replicating viral RNA (Egger et al,2002). The discovery that synthesised RNA colocalises with the NS5A protein within these complexes provides further evidence that these are sites of viral replication (Gosert et al,2003).

1.4.6.10. NS5A

NS5A is a membrane-associated phosphoprotein which has a number of functions. Within infected cells, it exists in two states, a basally (p56) phosphorylated form of 56kDa and a hyperphosphorylated (p58) form of 58kDA. Phosphorylation occurs on multiple serine residues through cellular kinases such as casein kinase II (Kim et al,1999). The N-terminal domain of NS5A has an amphipathic α-helix that is critical for mediating membrane association (Penin et al,2004a;Brass et al,2001). The helix itself is highly conserved across isolates and is extremely sensitive to disruption, especially the hydrophobic face region, which results in a loss of membrane association and a drop in replication efficiency (Elazar et al,2003). Coupled with the ability of adaptive mutations in NS5A to stimulate HCV replication in cell culture, this indicates that the protein plays an important role in viral replication (Blight et al,2000)

NS5A is comprised of three domains, the N-terminal domain (Domain I) includes the membrane-binding helix region and coordinates a single zinc atom per molecule of NS5A. Any mutations to the anchor or zinc binding region proves lethal to viral replication (Tellinghuisen et al,2005). Following the helix region, Domain I can be separated into two subdomains IA and IB. IA contains the four cysteine residues that are responsible for binding the single zinc atom which is proposed to aid maintenance of the protein's stable fold (Tellinghuisen et al,2005). Two possible structures for Domain I have been identified by X-ray crystallography. Firstly, a dimeric arrangement forming a positively-charged cleft of sufficient dimensions to bind single- or double-stranded RNA, possibly aligning the molecule for further processing in Domains II and III (Tellinghuisen et al,2005). An

alternative configuration shows an absence of the cleft with the proposed RNA-binding residues exposed and distributed between two remote surfaces (Love et al,2009). It has been suggested that the two configurations may enable switching between genome replication and lipid droplet association/particle assembly (Tellinghuisen et al,2005;Love et al,2009). The structures of Domains II and II remain unknown.

NS5A preferentially binds RNA sequences that are rich in both uracil and guanine which includes the 5' UTR containing the IRES. It is probable therefore that NS5A may bind the viral IRES during translation, blocking ribosome entry and forcing a switch from translation to replication (Huang et al,2005).

To further understand the formation and turnover of replication complexes, Moradpour *et al* used transposon-mediated mutagenesis to identify sites within the NS5A protein that could tolerate insertion of exogenous sequences. It was found that two sites within the C-terminal region of domain III were unexpectedly flexible and capable of harbouring GFP allowing direct visualisation of putative replication sites (Moradpour et al,2004). Only replicons with the GFP sequence inserted after amino acid 418 were viable and capable of conferring colony resistance to the antibiotic G418. Replication with the NS5A-GFP protein was 10-fold lower than that of the wild type replicon but had no effect on polyprotein processing as detected by Western blot analysis (Moradpour et al,2004).

The numerous interactions of NS5A with the host cell during infection suggests that its role extends beyond that of genome replication. Studies have shown that Domain III is a key element in infectious virion assembly, specifically the recruitment of core-coated lipid droplets, necessary for assembly and release (Tellinghuisen et al,2008;Appel et al,2008). One possible regulator of NS5A function switching has been identified as a serine residue within domain III, the deletion of which abrogates virion production. Phosporylation of this residue through casein kinase II is critical for production of infectious particles. Therefore, it has been suggested that domain III also harbours a molecular switch, governing the various functions of NS5A during replication and assembly (Appel et al,2008;Tellinghuisen et al,2008).

1.4.6.11. NS5B

NS5B is a 66kDa tail-anchored protein that acts as the virus-encoded RNA dependent RNA polymerase (RdRp). The 21 amino acid C-terminal α-helix post-translationally targets the protein to the ER membrane, allowing a cytosolic orientation of the functional protein domain (Wattenberg et al,2001). The protein itself is highly conserved across all HCV genotypes exhibiting the classical "fingers", "palm" and "thumb" subdomains of all single chain polymerases as defined by the Klenow fragment of *E.coli* DNA polymerase I (Ollis et al,1985). One unique feature of NS5B is that the fingers' subdomain contains an extension sequence that interacts with the thumb domain to restrict mobility of the subdomains with respect to one another, creating a fully enclosed active site allowing NTP molecules to bind easily with no further rearrangement of the domains (Penin et al,2004b). The conserved 'C motif' within the palm subdomain contains the GDD sequence essential for chelating the magnesium cations required for polymerase function. The finger and thumb domains encircle the palm to create a groove into which the template RNA binds leading to entry of NTPs into the active site from the opposing side through a "tunnel" created within the structure (Penin et al,2004b;Lesburg et al,1999). Like all RdRps, NS5B has no proofreading capability which results in the large numbers of quasispecies found within a single host (Simmonds,2004). It is thought that NS5B may play a part in regulation of HCV translation as mutations disabling the active polymerase site within NS5B results in an increase in translation from input transcript RNA. It has been suggested that this may be due to the RdRP interacting with the IRES of the transcript, blocking ribosome entry and function (McCormick et al,2006).

1.4.7. Model Systems for Studies on the HCV Life Cycle

Research into the three stages of the viral life cycle, i) binding and entry of virus to target cells, ii) translation followed by replication of the viral genome, iii) virion assembly and egress has been hampered by a lack of reliable cell culture and readily accessible animal model systems. The discovery in 2003 of a HCV genotype 2a strain, JFH-1, capable of replicating in human hepatocyte-derived cells (Huh-7) without the need for adaptations provided the first robust system for investigation of the complete viral lifecycle (Kato et al,2003;Wakita et al,2005;Zhong et al,2005). These seminal studies found that transfection of *in vitro* transcribed RNA from a cloned cDNA copy of the complete JFH-1 genome into Huh-7 cells produced virus particles capable of infecting naive cells. Forerunners of this system were surrogate models such as pseudoparticles (Section 1.4.7.2) and subgenomic

replicons (Section 1.4.7.3) were used for investigating virus entry and RNA replication respectively.

1.4.7.1. Production of Infectious Virus

Despite the existence of cloned genomes that were capable of establishing infection in chimpanzees, the only robust animal model for examining HCV (Yanagi et al,1997;Kolykhalov et al,1997), molecular research into HCV prior to 2005 was hampered by the inability to reliably produce infectious virions to enable studies on the complete virus life cycle. Initial attempts used primary human foetal hepatocytes to establish HCV infection were able to detect positive-strand of viral RNA through RT-PCR (Iacovacci et al,1997). Low level replication was achieved after infection with patient sera, releasing HCV for at least 2 months with HCV core protein and negative strand RNA detected in infected cells (Ashfaq et al,2011;Ito et al,1996). The capacity for JFH-1 to produce infectious virus from Huh-7 cells and its derivatives such as Huh-7.5 cells (termed HCVcc for cell culture-derived HCV) has enabled unprecedented insight into the assembly of infectious virions (Wakita et al,2005;Zhong et al,2005). The ability of JFH-1 to replicate HCV RNA to high levels has also led to the development of chimeric constructs that also produce infectious virus. These chimeras include a J6/JFH-1 construct that gives higher yields of infectious virus compared to JFH-1 (Lindenbach et al,2005) as well as other chimeras with varying capacity to produce virions (Pietschmann et al,2006).

1.4.7.2. HCV Pseudoparticles

Before the development of an effective system for infectious virus production, methods for analysing viral binding and cell entry were limited. Initial studies utilised a recombinant baculovirus construct containing DNA of the HCV structural proteins grown in insect cells allowing production of 'virus-like particles' (Baumert et al,1998). Alternative methods utilised vesiculovirus or influenza virus particles modified with HCV E1 and E2 glycoproteins containing transmembrane domain alterations (Bartosch et al. 2003a;Flint et al. 1999b;Lagging et al. 1998). However lack of infectivity and inconsistency in results prevented their use in subsequent investigations of HCV cell entry (Bartosch et al,2003a). Using retroviral and lentiviral core particles Bartosch *et al* were able to display unmodified HCV glycoproteins, generating HCV pseudo-particles (HCVpp) with high infectivity *in vitro* (Bartosch et al,2003a). HCVpp were found to be neutralised by sera from HCV-infected patients and certain anti-E2 antibodies. The addition of GFP as a marker gene

packaged within the HCVpp provides an accurate and reliable method to determine infectivity (Bartosch et al,2003a).

1.4.7.3. HCV Subgenomic Replicons

Prior to the development of the HCVcc system, molecular studies of HCV RNA replication relied on studies of self-replicating, subgenomic fragments of the HCV genome (Lohmann et al,1999;Blight et al,2000). Replication relied largely on the use of Huh-7 cells, which were isolated in response to a lack of human hepatoma cell lines capable of growth in chemically-defined medium. Beforehand, hepatic cell lines such as HuH-6, Hep 3B and Huh-1 required the addition of serum or other undefined substances to the growth medium (Nakabayashi et al,1982). Huh-7 cells were able to grow continuously under defined conditions while still exhibiting liver specific enzyme function and release of plasma proteins (Nakabayashi et al,1982). Improved levels of HCV RNA replication (approx 3-fold) are possible in Huh-7.5 cells, which were generated by prolonged treatment of Huh-7 cells harbouring a subgenomic replicon with IFN-α (Blight et al,2002). Huh-7.5 cells contain a dominant negative mutation in the CARD domain of the RIG-I protein, which has been proposed to account for the added permissiveness of the cell line to viral RNA replication (Sumpter et al,2005) although alternative explanations have been given for the increased competence for HCV genome synthesis in other Huh-7 clones (Binder et al,2007a).

The first subgenomic replicon was based on sequences derived from the Con-1 (gt1b) strain (Lohmann et al,1999). This report demonstrated that expression of the NS proteins, NS3, NS4A, NS4B, NS5A and NS5B, along with the 5' and 3' UTR regions of the genome were sufficient for HCV RNA replication. Cells that constitutively replicated this sub-genomic replicon could be selected by co-expressing an antibiotic gene from the same RNA as the NS proteins. However, persistent replication required evolution of adaptive mutations in the NS proteins (Lohmann et al,2001;Krieger et al,2001). Subsequently, it became possible to replicate sub-genomic replicons from the H77 strain (gt1a) of the virus (Blight et al,2003). More recently, subgenomic replicons have been described for genotype 3 and 4 strains (Saeed et al,2012;Saeed et al,2013).

1.4.8. Life Cycle

1.4.8.1. Binding and Entry

As obligate intracellular parasites, successful binding and entry of the HCV virion into permissive cell types is critical to survival of the virus. Entry begins with a highly coordinated process of binding between multiple host cell factors and the HCV envelope glycoproteins E1 and E2. The role of E1 in the entry process is still not fully understood. However, several E2 domains have specific roles in entry, binding to the cell receptors CD-81 and scavenger receptor class B type I (SR-BI). For example, the HVR-1 region of E2 is likely involved in SR-BI-mediated entry (Bartosch et al,2003b). During infection *in vivo,* HCV enters the liver through the sinusoidal blood where it is probably captured by liver sinusoidal cells which may facilitate viral infection of neighbouring hepatocytes (Zeisel et al,2010). This uptake is thought to be regulated by Dendritic Cell-Specific Intercellular adhesion molecule-3-Grabbing Non-integrin (DC-SIGN), expressed on Kupffer cells in close proximity to liver sinusoidal endothelial cells (LSEC) and hepatocytes (van Kooyk et al,2003). Both DC-SIGN and Lectin Specific Intercellular adhesion molecule-3-Grabbing Non-integrin (L-SIGN) have high binding affinity to the viral E2 glycoprotein (Gardner et al,2003). In a manner similar to dengue virus, heparan sulphate glycosaminoglycans represent the first attachment sites for HCV to hepatocytes, allowing further interaction with other host cell factors to initiate viral entry (Koutsoudakis et al,2006).

CD81 is a ubiquitously expressed 25kDa tetraspanin, containing small and large extracellular loops (LEL). It was the first molecule identified as a receptor that interacted with a soluble form of E2 and is now recognised as a critical factor in virus entry (McKeating et al,2004;Zeisel et al,2010). The LEL is thought to be a major component in viral entry, since a soluble form of the CD81 LEL interacts with E2, inhibiting HCVpp and HCVcc infection (Flint et al,1999;Zhang et al,2004).

SR-BI is an 82kDa glycoprotein which is highly expressed within the hepatic environment, interacting with a variety of lipoproteins, including HDL and LDL and is involved in the bi-directional transport of cholesterol across the cell membrane (Krieger,2001). The SR-BI extracellular loop interacts with the HVR-1 of E2 and is thought to play a role in both binding and post-binding steps (Catanese et al,2010). The interaction between SR-BI, HCV and lipoproteins suggests a complex interplay between the three components during viral binding and entry (Zeisel et al,2010).

Another factor critical in viral binding and cell entry is Claudin-1 (CLDN1), a 23kDa protein containing four transmembrane domains. Claudin proteins are critical in the formation of intercellular tight junctions and cell polarity. HCV is thought to interact with non-junctional CLDN1 (Evans et al,2007;Furuse et al,1998). CLDN1 also associates with CD81 in a number of cell types and the formation of CLDN1-CD81 complexes is essential for productive HCV infection (Harris et al,2008).

Occludin (OCLN) is another late stage host cell factor vital for HCV entry (Ploss et al,2009). Although there is no evidence to-date of direct interaction with HCV, it is thought that OCLN is one of the two host factors responsible for species-specificity. Expression of human OCLN and CD81 in transgenic mouse cell lines can confer HCV permissivity (Ploss et al,2009).

The recruitment of so many host factors suggests that HCV entry may be mediated through a highly orchestrated virus-induced entry complex at the plasma membrane (Zeisel et al,2007). The precise sequence of events from interaction of the virus with the cell surface, through viral fusion and internalisation to translation and then replication remain poorly understood. However, HCVpp studies have shown that entry into human hepatocyte cell lines is dependent on clathrin-mediated endocytosis and that clathrin-actin associations are required for efficient HCV uptake (Blanchard et al,2006;Coller et al,2009). Clathrin-mediated endocytosis of HCV particles results in the transport of virus and cell membrane receptors to both early and late stage endosomes (Marsh et al,2006). The change to an acidic pH within the endosome is thought to form a vital cue for penetration and uncoating of the virion (Smith et al,2004).

1.4.8.2. Translation and Replication of Viral RNA

After release of the genome from virions, translation of viral RNA occurs in a cap-independent manner with the ribosome directly interacting with the internal ribosome entry site (IRES) in the 5' UTR (Shih et al,2008). The HCV IRES can directly recruit the 40S ribosomal subunit without the need for initiation factors or unwinding of RNA secondary structure (Shih et al,2008). Eukaryotic initiation factor 2 (eIF2) then places the initiating tRNA for methionine on the surface of the 40S subunit and this complex is stabilised by eIF3 (JI et al,2004). Thereafter, the 60S ribosomal subunit attaches to generate a 80S complex that initiates translation. Translation proceeds without the need for any viral proteins, giving rise to the HCV polyprotein, which is cleaved by host and viral proteases to yield the mature polypeptides.

Like all positive-strand RNA viruses, replication of the HCV genome occurs in the cytoplasm of infected cells, closely associating with cellular membranes and a number of host factors and viral proteins (Lindenbach,2011). RNA replication is thought to take place within an ER membrane-derived structure called the membranous web (Moradpour et al,2007). The partial resistance of proteins and RNA to protease and nuclease treatment respectively suggests that replication sites form invaginations, which isolate replication complexes from recognition by cellular processes (Quinkert et al,2005).

While the process of membranous web formation has yet to be fully elucidated, NS4B has been identified as capable of inducing membrane alterations similar to the membranous web when expressed individually (Egger et al,2002). This membrane formation bears similarities to the "sponge-like inclusions" found within the liver of HCV-infected chimpanzees (Egger et al,2002;Pfeifer et al,1980). These replication sites were thought to form invaginations at the cytoplasmic surface of the ER membrane, enhancing immune evasion during replication (Quinkert et al,2005). More recent studies of the membranous web utilising immunofluorescence and EM-based methods has suggested an alternative protruding membrane arrangement bearing greater similarity to the picorna- and coronaviruses, than the closely-related flaviviruses (Merz et al,2013;Ferraris et al,2010). From these studies, it would appear that the main constituents of the membranous web are single- and double-membrane vesicles, induced respectively by NS4B and NS5A expression, suggesting that formation of the fully functional replication complex requires the combined function of several NS proteins (Welsch et al,2009).

Following formation of a functional replication complex, genome synthesis is instigated by the viral RNA-dependent, RNA-polymerase protein NS5B (Moradpour et al,2007;Binder et al,2007b). From the positive-strand genome, NS5B generates a negative-strand RNA template that is then utilised for the production of positive-strand molecules. Positive-strand genomes are produced in excess to negative strands (Quinkert et al,2005) and are released from replication sites for both translation of viral proteins and encapsidation into virions.

HCV RNA replication is possible in several cell lines of both hepatocyte and non-hepatocyte origin (Jones et al,2010;Kato et al,2005) and also can be achieved in cells of non-human origin (Long et al,2011). Nonetheless, replication is highly dependent on a wide spectrum of host cell factors (Binder et al,2013).

1.4.8.3. Assembly and Release

At present there is a limited understanding of the molecular events involved in the assembly and release of infectious virions from infected cells. HCV assembly appears to be closely interlinked with lipid droplets, cytoplasmic storage organelles which accumulate core protein on their surface during productive infection (Boulant et al,2007). In addition to lipid droplets, there seems also to be an intimate connection between virus assembly and VLDL production. A number of host factors involved in the assembly of VLDLs are thought to play a critical role in the release of virions, with substantial evidence supporting key roles for the lipid binding proteins (apolipoproteins), apoE and apoB as viral infectivity factors. Indeed, depletion of these proteins adversely affects the production of infectious virions (Shulla et al,2012;Benga et al,2009;Chang et al,2007). Anti-apoB and anti-apoE antibodies can immunoprecipitate HCV from infectious serum (Nielsen et al. 2006) and apoE has been detected on the surface of affinity-purified HCVcc (Merz et al. 2011), further emphasising the close interaction between HCV virions and VLDL components.

As well as the HCV structural proteins and components of the VLDL pathway, the viral NS proteins also play a part in assembly. Mutations in p7 can both inhibit and enhance virus production (Jones et al,2007;Steinmann et al,2007;Russell et al,2008) Moreover, NS2 appears to play a critical role in the latter stages of virion assembly (Yi et al,2009). Mutations in both NS3 and NS4B have also been identified that enhance HCV infectivity (Han et al,2009;Jones et al,2009). Finally, as described above, Domain III of NS5A is essential for virion production (Tellinghuisen et al,2008;Appel et al,2008). Thus, virus assembly and release is a complex process involving interplay between most of the viral proteins and host factors engaged in VLDL production.

AIMS

The major aim of this project was to develop and apply novel imaging methods using the sites of HCV RNA replication as a model system. The objective was to employ Structured Illumination Microscopy (SIM) to determine whether it was possible to enhance our understanding of the architecture of foci where viral RNA replication takes place given the predicted increase in resolution that new light microscopy methods can apparently now achieve. Moreover, much of the current literature on the cell biology of HCV infection does not assess the distribution of viral proteins by rigorous statistical approaches, which may influence data interpretation. Therefore, an ancillary aim was to explore the limits of

data analysis using images collected by confocal and super-resolution microscopy. In parallel with application of super-resolution microscopy, the project set out to develop the potential for using QDs as a means to probe sites of RNA replication by correlative light and electron microscopy (CLEM). The ambition was to determine whether it may be feasible to utilise such probes under conditions that limit the introduction of artefacts inherent in most microscopy methods and describe putative replication sites by 3-D tomography. Finally, a smaller study set out to examine whether quantitative labelling methods could be deployed for identifying changes in the proteome of cells that differ in their capacity to replicate HCV RNA.

2. Materials and Methods

2.1. Materials

2.1.1. Kits and Enzymes

2.1.1.1. Kits

Kit	Source
Purelink HiPure plasmid midi prep kit	Invitrogen
RNeasy mini kit	Qiagen
T7 RiboMAX Express Large Scale RNA Production System	Promega
RNeasy mini kit	Qiagen
Taqman kit	Applied Biosciences
Qdot 605 ITK Streptavidin Conjugate Kit	Molecular Probes
Qdot 585 Antibody Conjugation Kit	Molecular Probes
BCA Protein Assay Kit	Pierce

2.1.1.2. Enzymes

Restriction enzymes	NEB/Roche
Mung bean Nuclease	NEB
Taq Polymerase	Applied Biosciences
Multiscribe RT	Applied Biosciences

2.1.2. Cells

Cells	Description	Source
Huh-7 cells	Human hepatoma cell line	John McLauchlan [CVR]
Huh-7.5 cells	Human hepatoma clonal cell line derived from Huh-7 cells	Charles Rice [Rockefeller University]
Huh-7/SGR-JFH1 cells	Human hepatoma cell line harbouring the JFH1 subgenomic replicon	John McLauchlan [CVR]

2.1.3. Transfection and Transformation Reagents

Reagent	Source
Lipofectamine 2000	Invitrogen
Opti-mem-I	Gibco

2.1.4. Cell Culture Growth Medium

Component	Source
Dulbecco's Modified Eagles Medium (DMEM)	Gibco (Invitrogen Life Technologies)
10% Foetal Calf Serum (FCS)	Gibco (Invitrogen Life Technologies)
100 units/ml Penicillin/Streptomycin	Gibco (Invitrogen Life Technologies)
100µg/ml G418 Sulphate	Melford
1x Trypsin (10x Stock)	Sigma
PBS	Gibco (Invitrogen Life Technologies)

2.1.5. Antibodies

2.1.5.1. Primary Antibodies

Antibody	Species	Source
Anti-NS5A	Sheep Polyclonal	Mark Harris and Steve Griffin, [University of Leeds]
Anti-NS5A (9E10)	Mouse Monoclonal	Tim Tellinghuisen [Scripps, Florida]
Anti-NS4B	Rabbit Polyclonal	Sarah Gretton [University of Leeds] and Graham Hope [MRC Virology Unit]
Anti-NS3 #337	Mouse Monoclonal	Twincore
Anti-dsRNA J2	Mouse Monoclonal	English & Scientific Consulting [Hungary]
Anti-FLAG (ECS)	Rabbit Polyclonal	Bethyl Laboratories
Anti-HA	Mouse Monoclonal	Sigma
Anti-c-Myc	Rabbit Polycloncal	Sigma

2.1.5.2. Secondary Antibodies

Antibody	Species	Source
Anti-mouse-Alexa-488nm (FITC)	Donkey Polyclonal	Invitrogen
Anti-mouse-Alexa-350nm	Donkey Polyclonal	Invitrogen
Anti-sheep-Alexa-488nm (FITC)	Donkey Polyclonal	Invitrogen
Anti-sheep-Alexa-594nm (TRITC)	Donkey Polyclonal	Invitrogen
Anti-rabbit-Alexa-594nm (TRITC)	Donkey Polyclonal	Invitrogen
Anti-mouse-Atto-425nm	Goat Polyclonal	Rockland

2.1.6. Nucleic Acid Probes

Oligo Name	Sequence	Tag	Supplier
5' UTR probe	GUCUACGAGACCUCCCGGG[Btn]	Biotin	Sigma

2.1.7. Animal Sera

Species	Abbreviation	Manufacturer
Mouse	-	Sigma
Donkey	-	Sigma
Sheep	-	Sigma
Bovine Serum Albumin	BSA	Sigma
Foetal Calf Serum	FCS	Gibco

2.1.8. Electron Microscopy

2.1.8.1. Embedding Media

Reagent	Supplier
Epon 812	TAAB Laboratories
Lowicryl HM20	TAAB Laboratories

2.1.9. Commonly Used Chemicals

Chemical	Abbreviation	Source
2-Amino-2-(hydroxymethyl)-1,3-propanediol	TRIS	BDH
2-Mercaptoethanol	β-ME	Sigma
4',6-diamidino-2-phenylindole	DAPI	Promega
Acetonitrile	AcN	Sigma
Agarose	-	Melford
Ammonium Carbonate	-	Sigma
Ammonium Persulphate	APS	Bio-RAD
Ampicillin	Amp	Melford
Arginine	Arg	Thermo
Boric Acid	-	Sigma
Bromophenol Blue	BPB	BDH
Chloroform	-	Sigma
Digitonin	-	Sigma
Ethylenediaminetetraacetic acid	EDTA	Sigma
Ethanol	EtOH	Fischer Scientific
Ethidium Bromide	EtBr	Sigma
Formic Acid	-	Fischer Scientific
Glutaraldehyde	GTA	Sigma
Hydrochloric Acid	HCl	Fisher Scientific
Poly-L-Lysine	P-Lys	Sigma
Magnesium Chloride	MgCl	Sigma
Methanol	MeOH	BDH
N,N,N',N'-Tetramethylethylene-diamine	TEMED	Sigma
Neomycin phosphotransferase	G418	Melford
Osmium Tetroxide	OsTet	TAAB
Paraformaldehyde	PFA	Sigma
Potassium Acetate	-	Sigma
Phenol	-	Sigma
Propan-2-ol	IPA	Fischer Scientific
Sodium Acetate	-	Sigma
Sodium Chloride	NaCl	BDH

Sodium dodecyl sulphate	SDS	BDH
Sodium Hydroxide	NaOH	BDH
Sucrose	-	BDH
Triton X-100	TX-100	Sigma
Uranyl Acetate	UrAc	Agar Scientific

2.1.10. Clones

Clone	Details	Source
pSGR-JFH1	Subgenomic replicon	Takaji Wakita [National Institute for Infectious Disease, Japan]
pSGR- $JFH1_{NS5AGFP}$	Subgenomic replicon harbouring GFP-tagged NS5A protein	Daniel M. Jones [CVR]
pSGR- $JFH1_{NS5AFLAG}$	Subgenomic replicon harbouring FLAG-tagged NS5A protein	Christopher McCormick [University of Southampton]
pGFP-Sec61β	GFP tagged ER membrane protein Sec61β	Tom Rapoport [Harvard Medical School]

2.1.11. Bacterial Expression

Solution	Components
L-Broth	170mM NaCl, 10g/l Bactopeptone, 5g/l yeast extract
L-Agar	L-Broth plus 1.5% (w/v) agar

2.1.12. DNA Manipulation & Purification

Solution	Components
Equilibration buffer (EQ1)	0.1M sodium acetate (pH 5.0),0.6M NaCl, 0.15% (v/v) Triton X-100
Cell Resuspension buffer (R3)	50mM Tris-HCl (pH 8.0), 10mM EDTA, 100µg/ml RNase A
Lysis buffer (L7)	0.2M NaOH, 1% (w/v) SDS
Precipitation buffer (N3)	3.1M potassium acetate (pH5.5)
Wash buffer (W8)	0.1M sodium acetate (pH 5.0), 825mM NaCl
Elution buffer (E4)	100mM Tris-HCl (pH 8.5), 1.25M NaCl
TE buffer	10mM Tris-HCl (pH 8.0), 0.1mM EDTA
Agarose gel loading	5x TBE, 50% sucrose, 1µg/ml BPB

buffer	
TBE (10x)	0.9M Tris-HCl, 0.9M boric acid, 0.02M EDTA

2.1.13. SDS-PAGE

Component	Supplier
NuPage Sample Buffer	Life Technologies
NuPage MOPS SDS Running Buffer	Life Technologies
MiniProtean TGX 4-20% Bis-Tris 10 Well Gel	BioRad
SimplyBlue SafeStain	Life Technologies

2.1.14. Tissue Culture

Solution	Components
Trypsin	0.25% (w/v) Gibco Trypsin dissolved in PBS

2.2. Methods

2.2.1. Tissue Culture Maintenance

Both Huh-7 and Huh-7.5 cell lines were cultured in DMEM, supplemented with 10% FCS, at 37^{o}c in a 5% CO_2, humidified atmosphere. Cells harbouring the neomycin resistance gene as part of a HCV SGR were cultured with G418 at a concentration of 100µg/ml. Cells were routinely cultured in 160cm^2 Nunclon tissue culture flasks. At approximately 90% confluency, cells were removed through trypsinisation followed by resuspension in 10ml of $DMEM_{COMPLETE}$ for use in experiments or reseeding into fresh flasks and media.

2.2.2. DNA Manipulation

2.2.2.1. DNA Restriction Enzyme Digestion

DNA digestion was performed at 37^{o}c typically as a 50µl reaction comprised of 10 units of restriction enzyme per 0.5µg DNA/hr. All reactions were carried out using the appropriate supplier-specified buffer.

2.2.2.2. Transformation of Competent Bacteria

Transformation was carried out using chemically competent *E. coli* DH5α from lab stocks. 100µl of DH5α cells were thawed on ice before 1µg of plasmid was added to the cells and incubated on ice for 30mins. This was followed by heating to 42^{o}C for 2 minutes followed

by 1 minute on ice. 300µl of L-broth was added to cells followed by incubation for 30-45mins at 37^{o}C. Bacteria were then plated on L-agar plates and incubated overnight.

2.2.2.3. Small-Scale DNA Purification (Minipreps)

Single colonies of transformed bacteria were used to inoculate 2ml of L-Broth which was incubated overnight at 30^{o}C, shaken at 180rpm and in the presence of the appropriate selective antibiotic. 200µl of overnight culture was mixed with an equal volume of lysis buffer, briefly vortexed and incubated for 5 minutes at room temperature. A 200µl volume of precipitation buffer was then added to the lysis mixture and vortexed briefly. Samples were centrifuged at 15000x g for 2 minutes to pellet cellular debris before the supernatant was removed and added to 600µl of isopropanol to precipitate plasmid DNA. Samples were centrifuged again at 15000x g for 5 minutes to pellet DNA followed by washing with 70% ethanol and further centrifugation at 15000x g for a further 5 minutes. The supernatant was removed and the pellet allowed to air dry. The pellet was then resuspended in an appropriate volume of ddH_2O for analysis by restriction enzyme digest.

2.2.2.4. Large-Scale DNA Purification (Midipreps)

Single colonies of transformed bacteria were used to inoculate 150ml of L-Broth which was incubated overnight at 30^{o}C, shaken at 180rpm and in the presence of the appropriate selective antibiotic. Cultures were pelleted by centrifugation at 4000x g for 10 minutes at 4^{o}C before removal of supernatant. DNA purification was carried out using the PureLink HiPure plasmid midiprep kit (Invitrogen). Bacterial pellets were resuspended in 4ml of buffer R3 (cell resuspension buffer) through pipetting. 4ml of L7 (lysis buffer) was added to the suspension and gently mixed by inversion followed by incubation at room temperature for 5 minutes. Buffer N3 (precipitation buffer) was added followed by further inversion mixing; centrifugation at 6500x g for 10 minutes at room temperature was used to pellet cellular debris. Supernatant, containing plasmid DNA, was gravity filtered through an equilibrated Hipure Midi column (Invitrogen). Plasmid DNA was bound to the column during filtration of the supernatant, where it was washed twice with 8ml of buffer W8 (wash buffer), filtered by gravity. Plasmid DNA was then eluted by adding 5ml of buffer E4 (elution buffer) and gently mixed with 3.5ml of isopropanol resulting in precipitation of plasmid DNA. DNA was pelleted through centrifugation of samples at 6500x g for 15 minutes at 4^{o}C. Supernatant was removed and pellets washed with 70% ethanol and centrifuged at 6500x g for 5 minutes at 4^{o}C. Again the supernatant was

removed and allowed to air dry before being resuspended in TE buffer, typically to a final concentration of 0.5µg/µl.

2.2.2.5. Linearisation of HCV SGR and HCV genomic plasmid DNA

Plasmid DNA was linearised in a 50µl reaction using the restriction enzyme *XbaI* with the appropriate buffer. Post-linearization purification was carried out using a QIAquick spin column followed by the addition of 2 units of Mung Bean Nuclease (MBN). This reaction was incubated at 30^{o}C for 30 minutes to remove overhanging ends generated by the restriction digest. Linearised DNA was then purified using phenol/chloroform extraction before resuspension in an appropriate volume of TE buffer.

2.2.3. Isolation and Purification of DNA

2.2.3.1. Agarose Gel Electrophoresis

DNA fragments were resolved and isolated using agarose gel electrophoresis produced by restriction enzyme digest. DNA fragments larger than 500bp were separated using 1% agarose gels (120mm x 90mm), while those smaller than 500bp were separated using 2% agarose. Agarose gels were prepared using 0.5x TBE buffer with a final ethidium bromide concentration of 1µg/ml. Gels were run at 150V immersed in 0.5xTBE buffer to separate fragments. DNA fragment size was determined using 1kbp or 100bp ladders (NEB) run in parallel with samples. Fragments were then visualised and imaged using a BioRad gel documentation system illuminated with short wavelength UV.

2.2.3.2. Phenol Chloroform Extraction

Linearised DNA was purified through the addition of an equal volume of 1:1 phenol/chloroform proceeded by aggressive vortexing. The solution was then subjected to centrifugation at 15000x g for 1 minute, separating the protein containing organic layer from the nucleic acid containing aqueous layer. The upper aqueous layer was removed to a fresh tube and an equal volume of chloroform was added followed by further vortexing. Centrifugation at 15000x g was used to separate the aqueous and organic layers and again the aqueous phase was transferred to a fresh tube. DNA was obtained from the aqueous layer through ethanol precipitation.

2.2.3.3. Ethanol Precipitation

Precipitation of DNA from solution was initiated through the addition of 5M sodium chloride to a final concentration of 250μM and the addition of 2.5 volumes of 100% ethanol. DNA was pelleted by centrifugation at 15000x g for 5 minutes followed by washing with 70% ethanol and repeat centrifugation. Supernatant was then removed and the pellet air dried before being resuspended in an appropriate volume of ddH_2O to a concentration of approximately 1μg/μl.

2.2.4. RNA Manipulation

2.2.4.1. *In Vitro* RNA Transcription

In vitro transcription reactions were carried out using T7 RiboMAX Express Large Scale RNA Production System (Promega). Reactions were comprised of 10μl of T7 RiboMAX 2x Buffer, 1μl of linearised template DNA, 2μl of T7 RiboMAX Enzyme Mix and made up to 20μl with dH_2O. Reaction mixtures were incubated for 1 hour at 37^oC. Transcribed RNA quality and yield was determined by gel electrophoresis prior to transfer into cells by electroporation.

2.2.4.2. RNA Extraction and Purification

RNA extraction was carried out using the RNeasy Mini kit (Qiagen) from cells harvested from a 160cm^2 cell culture flask. Trypsinised cells suspended in PBSA were pelleted by centrifugation at 300x g for 5 minutes. Following aspiration of the supernatant, cells were disrupted through the addition of 600μl of buffer RLT, vortexed and incubated for 2 minutes at room temperature. The lysate was then transferred to a QIAshredder spin column placed in a collection tube and centrifuged at 15000x g for 2 minutes and the supernatant recovered. A volume of 70% ethanol was added to the homogenised lysate and mixed by pipetting. Samples were transferred to an RNeasy spin column and centrifuged for 15 seconds at 15000x g. Flow-through from the column was discarded. 700μl of buffer RW1 (wash buffer) was added to the column and was again centrifuged for 15 seconds at 15000x g and the flow-through discarded. 500μl of buffer RPE (wash buffer with ethanol) was then added to the column and centrifuged at 15000x g for 2 minutes. The column was transferred to a fresh collection tube and centrifuged at 15000x g for 1 minute. The column was again transferred to a fresh collection tube and 30-50μl of RNase free water added. RNA was then eluted through centrifugation at 15000x g for 1 minute. Purified RNA was stored at -70^oC.

2.2.4.3. RNA Electroporation of Eukaryotic cells

After resuspension following trypsinisation, cells were enumerated and the appropriate number was centrifuged at 500x g for 5 minutes at room temperature. Media was removed and cells were washed in PBSA by resuspension followed by further centrifugation at 500x g for 5 minutes at room temperature. Cells were then resuspended in an appropriate volume of PBSA to give a final cell concentration of $4x10^6$ cells/ml for electroporation. 800µl of suspended cells were transferred to a cuvette (4mm gap) along with 10µg of *in vitro* transcribed RNA. Cells were electroporated at 0.36kV, 950µF using a BioRad Gene Pulser II. Electroporated cells were transferred into an appropriate volume of $DMEM_{COMPLETE}$ and the cuvette rinsed. Cells were mixed thoroughly by pipetting, transferred to 90mm dishes and incubated at 37°C.

2.2.5. DNA Transfection

After resuspension following trypsinisation, cells were enumerated and 12-well cell culture dishes seeded at $1x10^5$ cells/well in 1ml of $DMEM_{COMPLETE}$. Cells were incubated and allowed to settle for 24 hours at 37°C prior to transfection. 1.6µg of DNA and 4µl Lipofectamine 2000 (Invitrogen) were diluted in 100µl of Opti-mem-I (Gibco) and incubated at room temperature for 5 minutes. The diluted DNA and Lipofectamine 2000 were combined and incubated for a further 20 minutes at room temperature before being added to the plated cells and incubated at 37°C for 16-20 hours.

2.2.6. Assessment of HCV RNA replication

2.2.6.1. qRT-PCR

qRT-PCR experiments were carried out in two stages. During the first stage cDNA was generated from purified cellular RNA which was transcribed using the Taqman Kit (Applied Biosciences), typically in a final reaction volume of 20µl. Reactions comprised of 1µl of cellular RNA, 2.5µM random hexamers, dNTPs, 1x RT buffer, 5.5µM $MgCl_2$, 8 units of RNase inhibitor and 25 units of Multiscribe RT. Reactions were made up to a final volume of 20µl with dH_2O. A ThermoHybaid PX2 Thermal Cycler was used to perform Reverse Transcription in the following manner: (i) primer annealing at 25°C for 10 minutes (ii) strand elongation at 37°C for 1 hour (iii) RT inactivation at 90°C for 5 minutes. The second stage utilised the transcribed cDNA from stage one to perform Real Time PCR. Reactions were comprised of the following, 900nM forward and reverse primers, 250nM FAM JFH1 probe, 1x Taqman Fast Universal Mix and 2µl of cDNA Template and made

up to a final volume of 20µl using dH_2O. Primers and probe were complementary to sequences in the 5' UTR of the JFH1 genome. Reactions were performed using an Applied Biosciences 7500 Fast Real-Time PCR System. Samples were heated to 95°C for 20 seconds to denature cDNA. PCR was then carried out in the following manner: (i) dsDNA strand separation at 95°C for 3 seconds (ii) primer annealing and strand elongation at 60°C for 30 seconds. Both steps were repeated sequentially 40 times. All qRT-PCR reactions were performed in triplicate. Cellular GAPDH controls were determined using the above protocol, using GAPDH specific primers.

2.2.7. Light Microscopy

2.2.7.1. Coverslip Preparation

15mm diameter No.1.5 coverslips (VWR) were separated and added to a covered glass beaker containing 1M HCl, and left overnight at 50°C with gentle agitation. Coverslips were allowed to cool and then washed thoroughly using dH_2O. Coverslips were then rinsed in 100% ethanol for 5 minutes before being left to dry on Type 105 Lens Cleaning Tissue (Whatman) in a sterile tissue culture dish. Manipulation of coverslips was carried out using sterile tweezers within a clean air hood.

2.2.7.2. poly L-lysine coating

Acid washed, sterile coverslips were separated and placed in a 15cm tissue culture dish. 10-15ml of sterile filtered 1mg/ml poly L-Lysine solution (Sigma) was added to the dish and incubated with rocking for a minimum or 30 minutes. The polyamino acid was removed and the coverslips washed in dH_2O a minimum of 6 times to remove the cytotoxic unbound poly L-lysine. Coverslips were then washed in 100% ethanol and dried in an open tissue culture dish in a clean air hood. Manipulation of coverslips was carried out using sterile tweezers.

2.2.7.3. Sample Fixation

Prior to fixation, growth media was aspirated and cell-coated coverslips were washed once in PBSA. Depending on the experiment, cells were fixed with either methanol, paraformaldehyde (PFA) or a paraformaldehyde/gluteraldehyde (PFA/GTA) mix. Coverslips undergoing methanol fixation were submerged in 100% methanol at -20°C for 10 minutes. 4% PFA was freshly prepared through dilution in PBSA from methanol-free, Ultra Pure 16% formaldehyde stored in the dark. For PFA fixation, coverslips were

immersed to a depth of 2-3mm for 15 minutes at room temperature. PFA/GTA fixation utilised 2% PFA, diluted in the same manner as 4% PFA combined with Electron Microscopy grade glutaraldehyde (Sigma) to a final concentration of 0.1%. Coverslips were immersed in the PFA/GTA fixative at 37^{o}C and transferred directly to ice for 15 minutes.

2.2.7.4. Antigen Retrieval

Following fixation, coverslips were washed once in PBSA, transferred to a microwave proof container and immersed in sodium citrate buffer (pH6.0). Samples were centred in a microwave oven set to high power and heated for 2-8 minutes or until the buffer started to boil. This was repeated several times, dependent on antibody. The volume of the buffer was observed and refilled as necessary. Coverslips were allowed to cool for 20 minutes then washed three times for 2 minutes with PBSA.

2.2.7.5. Permeabilisation of Cells

Fixed cells were permeabilised using either Triton X-100 or Digitonin depending on the nature of the experiment. Triton X-100 was prepared as a 0.5% solution in PBS, supplemented with either 5% serum from the same species as the secondary antibody or 5% BSA for blocking of non-specific binding sites. Digitonin permeabilisation was carried out using a variety of buffer agents, PBS, PHEM and Opti-MEM-I (GIBCO). Cells were incubated with digitonin at a concentration of 40µg/ml for 15 minutes. Live cells were permeabilised on ice while fixed cells were permeabilised at room temperature.

2.2.7.6. Indirect Immunofluorescence

Following permeabilisation and blocking, coverslips were washed three times with PBSA. Primary antibody was diluted to the appropriate working concentration in PBSA supplemented with 1% BSA and 0.3% Triton X-100 to reduce non-specific staining through hydrophobic interactions. 200µl of diluted antibody was added to cells and incubated for 1 hour at room temperature. Cells were washed 3 times with PBSA. Secondary antibody was diluted to a working concentration in PBSA supplemented with 1% BSA and 0.3% Triton X-100, 200µl of this solution was added to cells and incubated in the dark for 1 hour at room temperature. Cells were once again washed 3 times with PBSA. If appropriate cell nuclei were stained by the addition of DAPI at 1/2000 dilution and incubated at room temperature for approximately 30 seconds. Cells were once again washed 3 times in PBSA.

2.2.7.7. Mounting of Coverslips

Coverslips were washed in dH_sO to remove residual salt and excess liquid was removed through gentle contact with blotting paper. Coverslips stained with organic fluorophores were mounted using ProLong Gold (Invitrogen) and sealed with nail varnish. Coverslips stained using quantum dots were mounted using 1:9 PBS:Glycerol solution and sealed using nail varnish.

2.2.8. Quantum Dot Procedures

2.2.8.1. Quantum Dot/RNA Probe

RNA probes were conjugated to Qdot ITK 605nm Streptavidin (Invitrogen) quantum dots at varying ratios, at a volume of 200µl/coverslip in the presence of Qdot incubation buffer at room temperature for 1 hour. Probes were diluted to the appropriate concentration using PBSA. Post fixation and permeabilisation blocking was carried out on coverslips using Endogenous Avidin/Biotin Blocking Kit (Invitrogen). PBSA was aspirated from coverslips in a 12 well tissue culture plate and 2 drops (50µl) of reagent A (Avidin solution) were applied followed by incubation at room temperature for 10 minutes. Coverslips were then washed thoroughly in PBSA before the addition of 2 drops (50µl) of reagent B (Biotin solution) and again incubated at room temperature for 10 minutes. Coverslips were washed thoroughly and 200µl of conjugated probe added to each well followed by incubation at room temperature for 1 hour. Coverslips were then aspirated and washed 3 times for 10 minutes with PBSA.

2.2.8.2. Quantum Dot Antibody Conjugation

The following method was used for both NS5A 9E10 antibody (provided by T. Tellinghuisen) and anti-FLAG ECS antibody (Bethyl) using the Qdot 585nm Antibody Conjugation Kit (Invitrogen). Antibodies were prepared in 300µl of PBS to a concentration of 1mg/ml prior to conjugation. 1 vial of SMCC (component B) was thawed to 37^{o}C at least 15 minutes prior to use and 40µl of distilled water added to dye label marker (component G) and mixed through vortexing.

14µl of thawed SMCC was added to a fresh eppendorf tube along with 125µl of Qdot nanocrystals (component A) and incubated for 1 hour at room temperature to allow activation of quantum dots (QDs). At 30 minutes during the activation process, 300µl of the antibody solution was added to a fresh eppendorf tube and mixed with 6.1µl of DTT

solution (component C) and briefly mixed followed by incubation at room temperature for 30 minutes.

Desalting columns were prepared prior to the end of QD activation and antibody reduction steps. The top and bottom caps from two desalting columns were removed and the storage buffer allowed to drain through the column. As the liquid reached the top of the column gel bed, 10 ml of exchange buffer (component E) was added and allowed to flow through the column. When the liquid level was just above the gel bed the column was recapped until needed.

500µl of water was added to an eppendorf tube and the level of the meniscus marked on the tube. A further 500µl was added and again the meniscus marked; the water was then discarded.

Upon completion of the antibody reduction step, 20µl of dye-labelled marker was added to the antibody solution. One of the desalting columns was uncapped and the remaining exchange buffer allowed to drain from the column. As soon as the liquid entered the gel bed, the dye-labelled, reduced antibody was added to the column. Once the reduced antibody had fully entered the gel bed, 1ml of exchange buffer was added to the column to completely elute the antibody. Antibody was collected from the column when the first coloured drop eluted. Desalted antibody was collected in the marked eppendorf tube, collecting no more than 500µl.

Upon completion of the QD activation step, the other desalting column was uncapped and remaining exchange buffer drained from the column. As soon as the liquid entered the gel bed, the activated QD solution was added to the column. Once the activated QD solution had fully entered the gel bed, 1ml of exchange buffer was added to the column to completely elute the nanocrystals. 500µl of coloured material, eluted from the column, was collected in the eppendorf containing the reduced and desalted antibody. Upon collection the solution was mixed and incubated at room temperature for 1 hour.

A 10mM working solution of quenching reagent was freshly prepared prior to use through the addition of 3µl of 2-mercaptoethanol to 4ml of distilled water. 10µl of working solution was added to the conjugation reaction mixture after 1 hour and incubated for a further 30 minutes.

A separation column was marked at two points, the first 45mm above the top of the frit, the second 55mm above the frit. Separation media (component F) was resuspended through

gentle mixing and added to the 55mm mark on the separation column, 0.5 ml of distilled water was added to the column without disturbing the gel bed. A syringe (component H) was attached to the separation column via tubing (component J) and the plunger slowly withdrawn, extracting the solvent from the column. As solvent was removed from the separation media, the column was filled with PBSA to prevent dehydration of the gel bed. This was drawn through the column using the syringe and repeated twice. On the last PBSA fill, the liquid was drained to a level 2-3mm above the settled gel bed, the syringe and tube were removed and the separation column recapped.

At this point the quenched conjugation reaction volume was split equally into two ultrafiltration devices (component K) and centrifuged at 4000x g for approximately 10 minutes until the volume in each filtration unit was approximately 20µl.

The separation column was uncapped and the remaining PBS allowed to elute by gravity. Upon the meniscus reaching the top of the gel bed, both volumes (approx 40µl) of the concentrated conjugation reaction were added to the separation column. This was allowed to enter the gel and 50µl of PBSA gently added to the gel bed. The reservoir above the top of the gel bed was then filled with PBSA and the sample allowed to elute by gravity. The dead space between the frit and the column tip was monitored as the coloured material passed through the column. When colour appeared in the dead space the first 10 drops of material were collected in a fresh eppendorf tube. No more than 10 drops were collected to prevent contamination of the conjugated probe with unbound antibody. Purified probe was stored at 4^{o}C.

2.2.9. Confocal Microscopy

Coverslips were examined in either a Zeiss LSM 510 Meta or LSM 710 Meta confocal microscope. The following laser and filter sets were utilised for the corresponding fluorophore:

Fluorophore	**Laser**	**Filter Set**
DAPI	Diode	BP 420-480
Alexafluor 350	Diode	BP 420-480
Atto 425	Diode	BP 420-480
Alexafluor 488	Argon	BP 505-550
Alexafluor 594	HeNe	LP-560
QD 585nm	Diode	Spectral Array
QD 605nm	Diode	Spectral Array

Channels were scanned sequentially at optimal resolution of 1 Airy unit and an image size of 1024x1024; averaged over 4 times. Datasets were collected using a 34 channel Quasar multichannel photomultiplier detection unit using LSM 510 software or Zeiss Zen 2011 prior to exporting to AutoQuant for deconvolution and image analysis. The Quasar/PMT arrangement is shown in Figure 1.

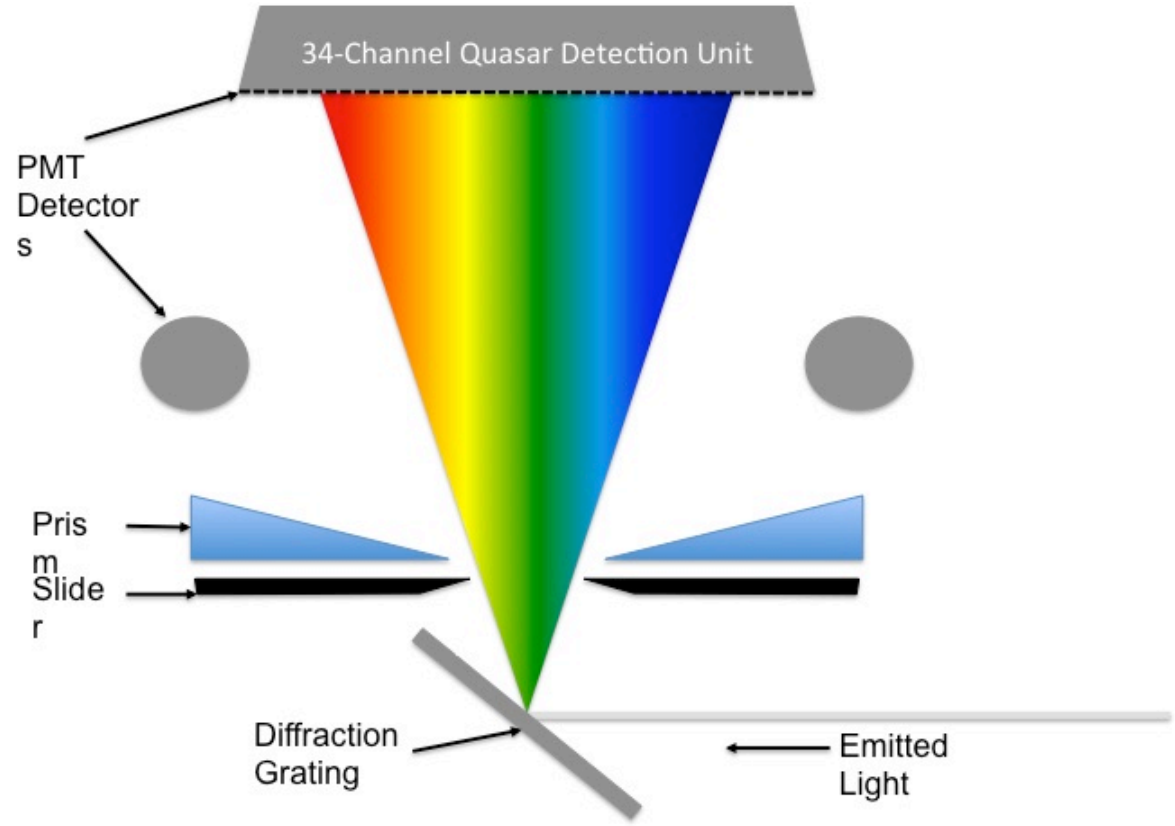

Figure 1. PMT Arrangement within LSM

2.2.10. OMX Structured Illumination Microscopy (SIM)

Samples for SIM were analysed at the SULSA OMX facility, University of Dundee using a Deltavision OMX Imaging System, Version 3. The microscope was operated in SIM mode using 3 solid state laser lines, 405, 488, and 568nm. SIM images were captured using 3 channel dedicated back-illuminated 16-bit EMCCD cameras with a 512x512 chip size (Cascade II, Photometrics). Mounting media (ProLong Gold, Invitrogen) matching the refractive index of the objective lens (Olympus UplanS Apo 100x 1.42NA) was used in conjunction with the appropriate Applied Precision immersion oil. Field of view was 40x40µm for SIM imaging.

2.2.10.1. Target Location

To identify cells of interest, samples were first imaged using a dedicated conventional Deltavision wide field fluorescent microscope designated Low Magnification Microscope (LMX). Using the high range of working distance and precision motorised stage, images from Regions Of Interest (ROI) were captured and the stage coordinates recorded. Numerous ROI were selected at this point before transfer of the sample to the OMX. During transfer, care was taken to maintain the same orientation of the slide between

microscopes. Cross indexing between OMX and LMX stage controllers allowed sharing of coordinates between the two systems to evaluate preselected low magnification ROI to be rapidly acquired using DVpoints.

2.2.10.2. Image Acquisition

All OMX image acquisition procedures were carried out remotely through a Linux controller running Deltavision softWoRx. The OMX system itself operates in a isolated, temperature controlled clean room environment. The desired cameras were activated in the necessary channels, and Electron Multiplication (EM) mode was selected for each camera. EM mode utilises the solid state multiplication register built into the end of the normal chip readout register to multiply weak signals without the addition of noise from the output amplifier. This is achieved using a higher clock voltage across hundreds of stages within the register to multiply the original electron through the phenomenon of impact ionization. Following an initial image acquisition step to confirm correct ROI, microscope settings were optimised for the individual image. Minimum, maximum and mean pixel intensity values were displayed and used to adjust the relative signal levels of each channel. Ideally the maximum pixel count was 2000 higher than user identified background. Typically laser intensity was set between 0.1-1%, with EMCCD sensitivity set to 3000 using 100ms exposure to provide a raw image of 16-bit dynamic range with the minimum laser intensity possible to minimize photobleaching. Sample thickness was measured and Z-stack parameters adjusted accordingly; stack heights were limited to 30µm. The light path was set to Structured Illumination mode. Samples were illuminated using a coherent scrambled laser light source passed through a diffraction grating to generate a 3D sinusoidal illumination pattern with a line spacing of 0.2µm. This pattern was shifted laterally through 5 phases and 3 rotational shifts of 60^{o} for each z step. During imaging simultaneous acquisition of 488 and 568nm channels was applied. Samples were subsequently imaged using 405nm laser excitation to limit photobleaching caused by the higher energy of this laser. Pixel binning was set to 1x1. Camera background was set using the Dark Image tool, mean pixel counts were approximately 50-100. SI acquisition was then initiated, typically capturing approximately 3000 individual images.

2.2.10.3. Image Reconstruction

Images were reconstructed offline using a separate softWoRx work station using the SI reconstruction function. The acquired SI images were selected as the input file, output file names were created by default. Object Transfer Function (OTF – the fourier transform of

the PSF) files were selected for each channel and the chosen objective before the SI image reconstruction was allowed to proceed. OTF files were generated prior to imaging through imaging of single 100nm fluorescent beads.

Following SI image reconstruction, both the 405nm and 488/593nm image files were merged to create one three channel image file before undergoing alignment to correct for non-zero lateral displacement between the three separate EMCCD cameras. To initiate alignment the merged image file was used as input for the OMX Image Alignment tool, the Image Source Drawer was set to Standard and the alignment run.

2.2.11. Live Cell Microscopy

All live cell imaging was carried out using 35mm live cell dishes (MatTek Cultureware). Cells were incubated overnight and allowed to settle at 5% CO_2 and 37^{o}C. Washing and permeabilisation of cells was carried out using either PHEM buffer or Opti-Mem-I warmed to 37^{o}C. Further incubations or imaging were carried out with the addition of DMEM lacking phenol red. Microscopy was carried out using a ZEISS LSM510 Meta confocal microscope, fitted with an enclosed stage heated to 37^{o}C with a 5% supply of CO_2.

2.2.12. Electron Microscopy Techniques

2.2.12.1. High Pressure Freezing

High Pressure Freezing (HPF) was carried out using a Leica EM PACT2 system. Prior to use the system Dewar was filled with Liquid Nitrogen (LN_2) and the valve to the sample bath opened and allowed to fill. The sample freezing process was run three times with an empty holder to ensure the hydraulic system was free of air bubbles.

Samples were prepared in one of two ways. Cells were grown on 100% ethanol-sterilised Sapphire discs placed within a 35mm live cell dish to which cells, resuspended in $DMEM_{COMPLETE}$, were added and allowed to settle overnight at 37^{o}C with a 5% supply of CO_2. Discs were then removed and excess media blotted before being transferred to a specimen carrier which was in turn mounted into a bayonet pod loading device. Cells were resuspended in a number of different cryoprotectants, DMEM, 20%BSA, 20% dextran or 10% Ficol, transferred to a sample carrier and again mounted into a bayonet pod and RTS.

Mounted samples were transferred into the HPF system and the chamber locked. Upon initiation of the HPF process, samples were frozen at a rate of between 16,000^{o}C/s and 18,000^{o}C/s before being automatically ejected into the LN_2 filled sample bath. All further

manipulations were carried out under LN_2. Samples were removed from bayonet pods and transferred to long term storage under LN_2 at -196^{o}C.

2.2.12.2. Freeze Substitution

Automatic Freeze Substitution (AFS) was carried out using a Leica EM AFS2. Prior to freeze substitution the AFS dewar was filled with LN_2 and the system initiated to allow cooling of the Freeze Substitution (FS) chamber down to an operating temperature of -80^{o}C. Reagent containers were filled and inserted into the chamber and allowed to cool prior to use. Uranyl Acetate (UrAc) was dissolved in acetone to a concentration of 0.2% with 2% dH_2O. Samples were transferred with cooled forceps to a flow-through ring, 0.2% UrAc was added to the sample bath and allowed to immerse the samples, followed by incubation at -85^{o}C for 48 hours. The temperature was gradually increased over a 10 hour period to -50^{o}C and the samples were washed twice in acetone for 1 hour.

Following washing with acetone, 25% HM20 diluted in acetone was added to the samples and incubated for 4 hours at -50^{o}C. This was repeated sequentially with increasing concentrations of HM20, 50%, 75% and 100%. 100% HM20 step was incubated for 8 hours before being replaced with fresh 100% HM20 and incubated for a further 10 hours at -50^{o}C. The chamber window was replaced with a LED UV lamp and sample polymerisation initiated by irradiation for 48h at -50^{o}C. UV polymerisation continued with a 4 hour temperature gradient increasing from -50^{o}C to +20^{o}C followed by 8 hours at +20^{o}C. Samples were then removed from the flow-through ring by scalpel.

2.2.12.3. Sectioning

Embedded samples were sectioned using a Leica EM UC7 ultramicrotome. Samples were trimmed using a glass knife before sections were cut using a diamond blade in a number of thicknesses, ranging from 100nm to 500nm and collected on water. Section tension was eased through the application of chloroform vapour above the samples before being collected on copper grids.

2.2.13. Proteomics and Mass Spectrometry

2.2.13.1. Media Preparation

Dialysed FCS was prepared from Gibco stock used for tissue culture maintenance. 50ml of FCS was split between two 25ml 3.5kDa Slide-A-Lyzer (Thermo Pierce) cassettes and then submerged into 6L of PBSA at 4^{o}C. The dialysis media was changed three times: after

1 hour, 3 hours, 9 hours and then left overnight. Dialysed FCS was then filtered into a 50ml Falcon tube using a 45µm filtration unit and stored at -20^{o}C.

SILAC growth media was prepared using 2x 500ml bottles of SILAC DMEM (Thermo), deficient in Lysine and Arginine. Bottles were either labelled "Heavy" or "Light", 50ml of DMEM was removed from both bottles and replaced with 10% dialysed FCS and 100 units/ml penicillin/streptomycin; L-Proline (Sigma) was added to excess at 200mg/ml. The heavy labelled bottle was also supplemented with 50mg of 13C6 15N2 L-Lysine-2HCl (Cambridge Isotope Laboratories), 50mg of 13C6 15N4 L-Arginine-HCl (Cambridge Isotope Laboratories). The light labelled bottle was supplemented with 50mg of L-Lysine-2HCl (Sigma) and 50mg of L-Arginine-HCl (Sigma).

2.2.13.2. Cell culture maintenance

Cell lines grown for SILAC analysis were cultured in either SILAC DMEM "heavy" or "light" media at 37^{o}C in a 5% CO_2 atmosphere. Cells harbouring a neomycin resistance gene as part of the HCV SGR were cultured with G418 at a concentration of 100µg/ml. Cells were routinely cultured in 160cm^2 Nunclon tissue culture flasks. At approximately 90% confluency cells were removed using Cell Dissociation Buffer [enzyme-free] (Invitrogen, Life Technologies) followed by resuspension in 10ml of appropriately labelled SILAC DMEM. To ensure incorporation of isotopically labelled amino acids, cells underwent a minimum of 5 doublings followed by incorporation analysis by mass spectrometry.

2.2.13.3. Preparation of Mammalian Cell Extracts for SDS-PAGE Fractionation

Following the appropriate period of isotope incorporation cells, were dissociated as described in section 2.2.13.2. From this point onwards all steps were carried out in a keratin-free environment. Both heavy- and light-labelled cells were counted and transferred to two 50ml Falcon tubes and cells pelleted through centrifugation at 500x g for 5 minutes. Supernatant was removed from both tubes and the cells washed with 5 pellet volumes of PBS before further centrifugation at 500x g for 5 minutes. Supernatant was again removed from both tubes and cells were lysed on ice using a minimal volume of RIPA Lysis buffer (Pierce Biotechnology) to obtain protein concentrations of 2-10mg/ml. Cell debris was removed by centrifugation at 14,000x g for 5 minutes and the supernatant

was removed to fresh tubes. Protein concentration was determined in triplicate by Bradford assay compared to a BSA standard curve.

Equal quantities of protein from both heavy and light lysate was added to a fresh eppendorf tube and diluted to 2mg/ml with NuPAGE LDS Sample Buffer (Invitrogen). Samples were then boiled for 5 minutes and clarified by centrifugation at 14,000x g for 1 minute. 50-100µg (25-50µl) of clarified sample was loaded into one well of a MiniProtean TGX 4-20% Bis-Tris 10 Well Gel (BioRad). Electrophoresis was performed at 120V until the desired protein separation had been achieved. The gel was then stained using SimplyBlue SafeStain (Invitrogen). Protein bands were excised from the lane by cutting 8-12 gel slices using a fresh scalpel and transferring them into fresh centrifuge tubes.

2.2.13.4. In-gel Protein Digestion

All solutions in the following method were added at a volume to sufficiently cover excised gel pieces. Excised gel slices were destained at room temperature using In-gel destain solution comprised of 1:1 solution of dH_2O: Acetonitrile (Sigma). Samples were immersed in destain solution and shaken for 15 minutes at 800rpm. Washing was repeated to ensure complete destaining of gel slices. Destain solution was then aspirated from gel slices and the samples equilibrated by immersion in 100mM NH_4HCO_3. Following a 5 minute equilibration, an equal volume of 100% acetonitrile was added to each gel slice and incubated for 15 minutes with shaking at 800rpm.

The equilibration solution was then aspirated prior to the addition of In-gel reduction solution (comprised of 10mM DTT (Sigma) dissolved in 100mM NH_4HCO_3). Samples were then incubated for 45 minutes at 56^{o}C with shaking at 800rpm. In-gel reduction solution was removed and replaced with In-gel alkylation solution comprised of 55mM iodoacetamide dissolved in 100mM NH_4HCO_3. Samples were then incubated for 30 minutes at room temperature in the dark with shaking at 800rpm.

Samples were washed with 100mM NH_4HCO_3 followed by an equal volume of 100% acetonitrile, this step was repeated twice. Gel slices were then dehydrated through immersion in 100% acetonitrile and dried in a vacuum centrifuge at room temperature until shrunken and white in appearance.

In-gel digestion solution was freshly prepared and comprised of 12.5ng/µl modified trypsin (Promega) dissolved in 50mM NH_4HCO_3. Sufficient In-gel digestion solution was added to cover the gel pieces, and samples were incubated on ice for 30 minutes to allow

rehydration. Excess In-gel digestion solution was removed and the rehydrated gel pieces covered with 50mM NH_4HCO_3 followed by overnight digestion at room temperature.

The first In-gel peptide extraction solution was prepared as a 1:1 solution of NH_4HCO_3:acetonitrile. Gel slices were immersed in this solution and incubated for 10 minutes at room temperature with shaking at 800rpm. After 10 minutes the supernatant was aspirated and transferred to a 600µl Maxymum Recovery microtube (Axygen). Gel slices were then incubated with shaking at 800rpm for a further 10 minutes at room temperature, with the second In-gel peptide extraction solution comprised of 1:1 5% Formic acid:acetonitrile. This step was repeated and the supernatant pooled. Samples were then dried to completion in a vacuum centrifuge at room temperature. Samples were stored at -20^{o}c.

3. Comparative Analysis of HCV RNA Replication Sites by CLSM and OMX Microscopy

3.1. Introduction

In recent years a number of methods for overcoming the ~λ/2 resolution limit, collectively known as super resolution microscopy, has been developed (Section 1.1.7). Among these different approaches, Structured Illumination Microscopy (SIM) and the OMX system provide a novel platform to increase the resolving power of fluorescence light microscopy without loss of the principal advantages over EM (Dobbie et al,2011). The use of a coherent, sinusoidal illumination pattern allows the extraction of additional information encoded in the fluorescent emissions which can then be resolved using post acquisition analysis (Gustafsson,2000;Schermelleh et al,2008). This technique leads to a doubling in both lateral and axial resolution while maintaining the depth of information required for more detailed study of the structure and localisation of intracellular organelles. In the context of viruses, which are obligate cellular parasites, super-resolution microscopy offers unique opportunities to explore virus-host interactions at greater resolution and deliver more detailed information about novel structures generated by infection. The aim of the following study was to apply OMX techniques to the structural analysis and localisation of HCV replication complexes (RCs) in order to achieve a greater understanding of this stage of the virus lifecycle compared to previous studies using Confocal Laser Scanning Microscopy (CLSM).

The mechanisms involved in HCV RNA replication are largely unknown. Similar to other positive-strand RNA viruses, genome replication is thought to occur through remodelling of the ER membrane, forming structures known as the membranous web (Gosert et al,2003). Confocal microscopy-based visualisation of cells harbouring replicating HCV RNA reveal punctate foci containing viral non-structural proteins and viral RNA closely associated with the surface of the ER (Targett-Adams et al,2008). Such foci are likely to represent RCs, which provide the scaffold for *de novo* synthesis of viral RNA. Investigation of such sites is possible by using cell lines that harbour self-replicating HCV RNA that encodes the viral proteins, which are necessary and sufficient for RNA synthesis (referred to as subgenomic replicons, Section 1.4.7.3).

EM visualisation of predicted replication sites revealed clusters of heterogeneously-sized vesicles of 70-400nm embedded within a membranous matrix, a morphology similar to that of other positive-strand RNA viruses (Egger et al,2002;Miller et al,2008). While EM

provides the ultrastructural detail of predicted RCs, it lacks the specificity and depth of information provided by immunofluoresence microscopy. However the size and spacing of these vesicles and structures of interest are at or below the limits of spatial resolution ($D_{x,y}$ =180-250nm, ~D_z = 500-700nm) afforded by traditional optical techniques, limiting their use in structural studies.

The following study set out to utilise findings from earlier reports as a benchmark from which to examine the benefits and limitations of both CLSM and OMX techniques alongside a detailed evaluation of software to process the digital images generated by the two light microscopy methods. From this evaluation it was possible to investigate the structure of predicted replication sites in far greater detail than had previously been achieved. To limit observational bias during data analysis, a number of standardised colocalisation methodologies were applied to the datasets to provide an accurate measure of the relative distribution of viral components.

With a better understanding of the effects of increased resolution on colocalisation variables it was then possible to investigate the relationship between HCV RCs and host membrane surfaces. This revealed unexpected findings, which bring into question the validity of some of the currently held paradigms based on RNA replication of related flaviviridae.

3.2. Strategy for Comparative Analysis of HCV RNA Replication Sites by CLSM and OMX Microscopy Approaches

The studies in this chapter combine use of different microscopy methods and software packages that have distinct analytical principles, which are applied to a model for examining HCV RNA replication. For ease of presentation, most sections are organised as a combination of results and discussion. In addition, the data and analysis are presented in the following order:

a) Construction of cells that constitutively replicate HCV subgenomic RNA
b) Selection of optimal parameters for CLSM
c) Deconvolution of CLSM imaging data
d) Comparison of 3D Models generated by Autoquant and Imaris software
e) Optimisation of OMX microscopy parameters
f) Interaction of NS5A with dsRNA at putative HCV replication sites
g) Automated quantification of putative replication sites using Imaris

h) The affect of channel alignment on statistical colocalisation
i) Quantification of colocalisation data
j) Analysis of colocalisation results
k) Interaction of replication sites with the ER membrane

It should be noted that the overall intent was to progressively refine the process of data analysis, ultimately leading to a less biased and more statistically robust approach to determining the colocalisation between viral and host components.

3.3. Construction of Cells Harboring JFH-1 Subgenomic Replicon

Colocalisation between the HCV dsRNA genomic intermediate and viral NS proteins has been shown previously, alongside the relative location and position of RCs to subcellular organelles (Targett-Adams et al,2008;Merz et al,2013;El-Hage et al,2003). Prior to using super resolution methodologies, replication and benchmarking of previous immunofluorescence imaging was carried out using the HCV subgenomic replicon system, which does not generate infectious particles and therefore allows investigation under less stringent biocontainment conditions. A cell line was constructed that contained the strain JFH-1 replicon (SGR-JFH1) (Figure 1 [B]) which encoded the neomycin resistance gene for selection of cells that constitutively replicated subgenomic RNA (Huh-7/SGR-JFH1) (Kato et al,2003;Targett-Adams et al,2005). To complement this system and overcome the limitations of certain antibody combinations, the study also took advantage of a GFP-tagged NS5A fusion protein based on the aforementioned JFH-1 replicon system which was developed by Jones *et al* (Jones et al,2007) (SGR-JFH1$_{NS5AGFP}$; Figure 1 [C]). To create subgenomic replicon cells, naive Huh-7 cells were electroporated with RNA transcribed *in vitro* by T7 RNA polymerase from SGR-JFH1$_{NS5AGFP}$ and selected for neomycin resistance. From this process, the Huh-7/ SGR-JFH1$_{NS5AGFP}$ cell line was produced, which constitutively replicated viral RNA, and also expressed GFP-tagged NS5A.

Huh-7/ SGR-JFH1$_{NS5AGFP}$ cells were grown on coverslips and fixed using the fixation methodologies stated in Materials and Methods 2.2.7. These samples were used to confirm the previously established relationship between both NS5A/dsRNA and NS3/dsRNA (Targett-Adams et al,2008) using indirect immunofluorescence and imaged by CLSM. Figure 2 [A] and [B] show the close relationship between the three targets, seen as signal overlap at both magnifications provided by CLSM, the results of which are in agreement

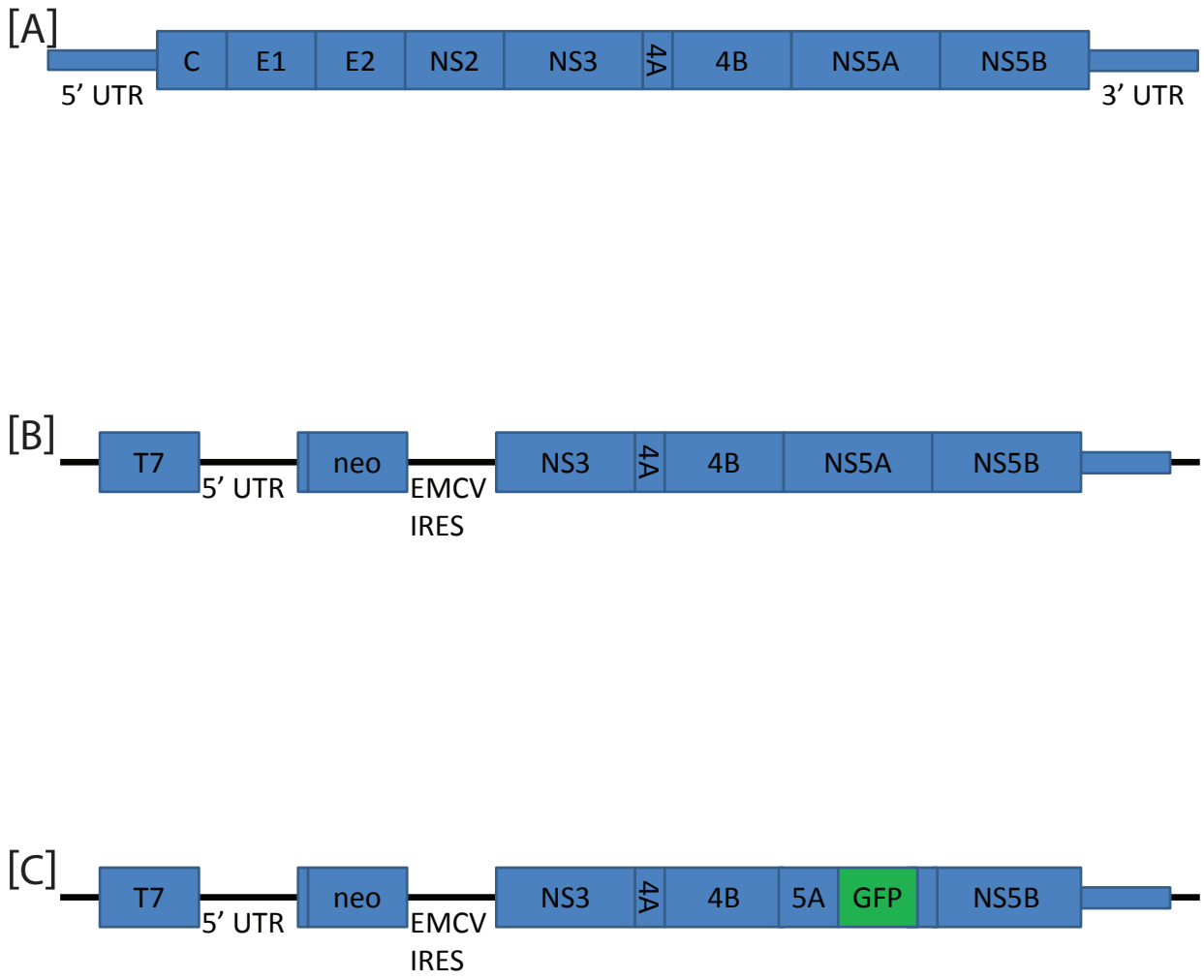

Figure 1. Subgenomic replicon structures SGR-JFH1 and SGR-JFH1$_{NS5AGFP}$
[A] Organisation of the infectious full length JFH-1 genome including the structural proteins C, E1 and E2. Structural proteins p7 and NS2 are removed and replaced with the Neomycin resistance gene (neo) and EMCV IRES inserted upstream of NS3 coding sequences to produce the subgenomic replicon SGR-JFH1 [B], GFP ORF was inserted between amino acids 418 and 419 of NS5A to produce the subgenomic replicon SGR-JFH1$_{NS5AGFP}$ [C]

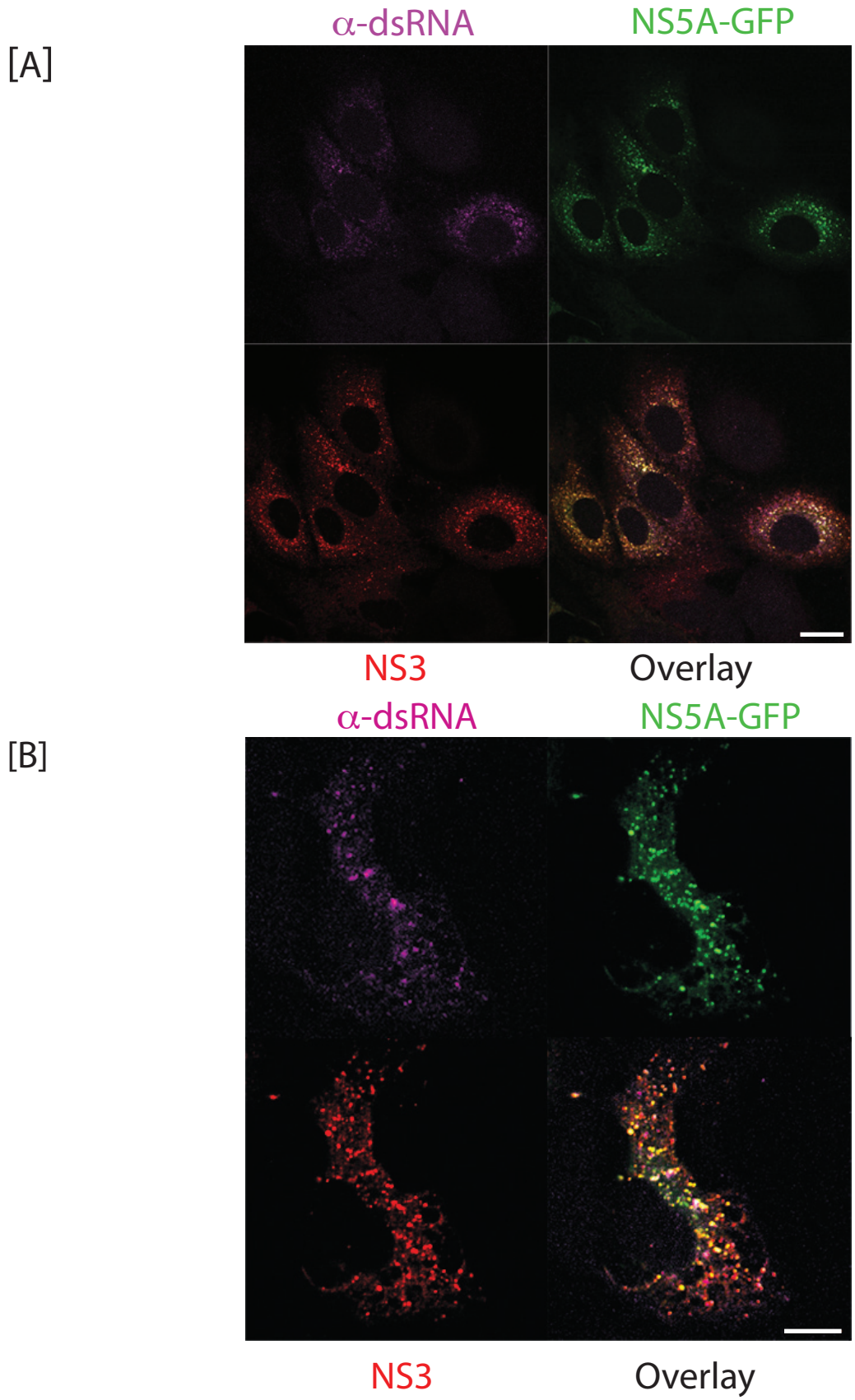

Figure 2. Visualisation of NS5A-GFP, NS3 and dsRNA in cells actively replicating SGR-JFH1$_{NS5AGFP}$ RNA

Huh-7 cells consitutively replicating RNA from SGR-JFH1-NS5A$_{GFP}$ were fixed and stained for NS3 using NS3 antisera and dsRNA using J2 [A] and [B]. Scale bar represents 10μm.

with previously published studies (Targett-Adams et al,2008). Similar results were obtained for Huh7/SGR-JFH1 (data not shown).

3.4. Selection of Optimal Parameters for CLSM

To evaluate data collected by CLSM in greater detail, images were acquired by serial optical sectioning through cells (Z-stacks). HCV NS5A and the viral RNA genome were interrogated as test subjects for methodology optimisation. Fluorophores were chosen to prevent cross talk between channels, allowing multitrack acquisition and samples were mounted in an antifade media of appropriate refractive index. For deconvolution purposes frame size and pixel sampling rate was determined using Nyquist-Shannon sampling theorem, as twice the highest frequency component of the image {Nyquist, 1928 509 /id}{Bracewell, 1999 364 /id;Shannon, 1949 510 /id}. Nyquist-Shannon sampling theorem allows the determination of the minimum number of pixels required to accurately represent and therefore reconstruct the imaging data acquired by the microscope. Given that the minimum resolution of the optical microscope is governed by the Abbe limit, the digital imaging device must be capable of sampling at an interval half that of the resolution limit to prevent any loss of information.

$$d_{DAPI} = \frac{0.61\lambda}{NA} \therefore \frac{0.61(460)}{1.4} = 200nm$$

$$d_{Alexa488} = \frac{0.61\lambda}{NA} \therefore \frac{0.61(510)}{1.4} = 222nm$$

$$d_{Alexa594} = \frac{0.61\lambda}{NA} \therefore \frac{0.61(594)}{1.4} = 258nm$$

$$\therefore \text{Minimum Sampling Rate} = \frac{\text{Shortest Resolvable Distance}_{\text{DAPI}}}{2}$$

$$= \frac{200\text{nm}}{2} = 100nm$$

Equation 4. Calculation of Minimum Resolvable Distance (d) and Minimum (Nyquist-Shannon) Sampling Rate

Calculation of axial resolution is complicated by the hourglass diffraction pattern generated when imaging in the x-z or y-z plane. However this pattern still exhibits the central maxima and periodicity similar to the airy disk seen in the x-y plane, as shown by

Linfoot and Wolf (Linfoot et al,1956). Therefore the axial resolution δ for the system was taken as one quarter of the distance between the first axial minimum and the central maximum within the Airy pattern. Distance from the centre of the 3-D diffraction pattern to the first order axial minimum is determined using the following equation (Pawley,2006).

$$\zeta_{\min DAPI} = \frac{2\lambda\eta}{(NA)^2} = \frac{2(460)1.47}{1.4} = 690nm$$

$$\delta_{DAPI} = \frac{1}{4}(\zeta_{min+} - \zeta_{min-}) = \frac{1}{4}\big(690 - (-690)\big) = 345nm$$

$$\therefore \text{Minimum Sampling Rate} = \frac{\text{Shortest Resolvable Distance}_{\text{DAPI}}}{2}$$

$$= 172.5nm$$

Equation 5. Calculation of axial resolution and sampling rate

Where λ is the emission wavelength and η is the refractive index of the immersion media. It is worth noting that the $\zeta_{minDAPI}$ shrinks inversely proportional to the square of the NA of the objective in contrast to the lateral resolution limit which shrinks with the first power of the NA. Therefore while both lateral and axial resolution are improved by increasing numerical aperture, z-axis resolution improves more dramatically (Pawley,2006).

Data was captured in 12-bit mode throughout the project for greater accuracy during post capture quantitative analysis and scan speed was automatically optimised using the LSM 710 control software. Optimal pinhole size for each individual channel was 1AU, providing the best resolution and depth discrimination. However to achieve equal optical slice thicknesses pinhole size was altered to attain equal z-depth between channels. Using the Range Indicator palette, amplifier offset and detector gain were adjusted to ensure appropriate dynamic range and prevent saturation of the image (Figure 3).

3.5. Deconvolution of CLSM Imaging Data

Following image acquisition, CLSM datasets underwent deconvolution to reverse the degradative blurring effects found within diffraction-limited microscopy systems, a mathematical process known as convolution. This process was carried out using Media Cybernetics Autoquant software in a 3-D Adaptive Blind Deconvolution mode. Blind deconvolution methods were utilised over non-blind methods using a measured PSF due to the low signal to noise ratios of the images and time constraints within the project Adaptive blind deconvolution utilises maximum likelihood estimation and constrained

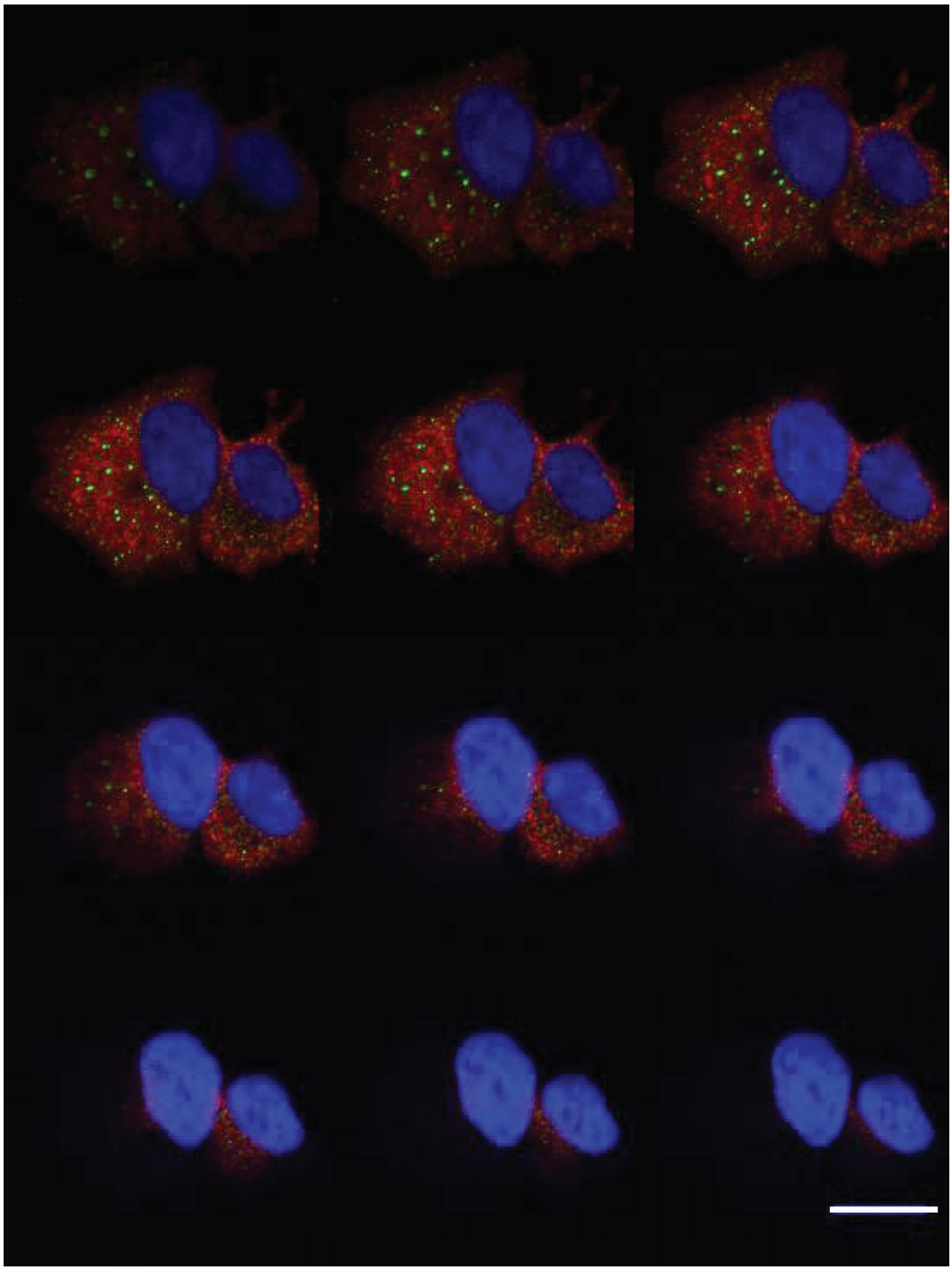

Figure 3. Z-stack montage of CLSM data prior to deconvolution
Huh7/SGR-JFH1 cells were fixed and stained for NS5A using NS5A antisera and dsRNA using J2. Images were captured by CLSM with XY spacing of 46nm and Z of 165nm, full dataset not shown. Scale bar represents 20μm.

iteration to reconstruct the best image solution for the collected dataset rather than the application of a single measured PSF across all images. Classical image restoration processes require the PSF of the system to be explicitly known prior to deconvolution. However, real world optical systems have a number of degenerative non-linear effects which prevent an accurate measurement of the true PSF. Blind deconvolution adapts to this real world PSF which can differ significantly from the theoretical PSF due to variance in biological specimens, thermal expansion and image noise, to provide a more accurate, sample-specific PSF (Campisi et al,2007). One practical advantage of the deconvolution process is the inherent reduction in sample noise, rejecting aberrant noise lying outside the bandwidth of the microscopy system (Anon.,2008).

Datasets were loaded into Autoquant and image acquisition parameters such as sample spacing, emission spectra, objective lens and immersion refractive index were confirmed. 10 rounds of iterative blind deconvolution were then applied to the dataset based on the likelihood function of the deconvolution process. Figure 5[A] demonstrates the improvement in image quality and resolution provided by the deconvolution process. The zoomed area clearly shows a number of distinct punctate sites in green, representing viral genomic intermediates, surrounded by a less distinct red signal (NS5A) representing the convolutions of the membranous web and more general ER staining consistent with the distribution of NS5A (Targett-Adams et al,2008).

3.5.1. Comparison of 3D Models Generated by Autoquant and Imaris Software

3-D modelling capabilities were compared between the Media Cybernetics Autoquant and Bitplane's Imaris software packages. Using the previously deconvoluted dataset from CLSM images, surface modelling was carried out using both packages, each using a similar isosurface-modelling algorithm. The solid surface generated through isosurface modelling represents a constant value within the dataset. Where the values between neighbouring, incrementally examined voxels, transition across this threshold value, a triangle is created between them each transition. Setting of this threshold value differs between software packages; Autoquant is restricted to an automatically selected threshold value based on a "Mexican hat filter" background subtracted histogram. This process allows objects of various intensities within the image to be identified above what maybe a variable background prior to background subtraction. The resultant histogram gives the appearance of the profile of a number of sombreros placed on a surface. The Imaris

package provides a more flexible modelling environment, utilising a number of user defined variables during the surface modelling process

Threshold values in Imaris can be defined based on the absolute values within the histogram or a background subtraction algorithm similar to Autoquant. Selection of either method is dependent on the signal to noise ratio within the dataset. Background subtraction methods are more suitable for the inherently noisy CLSM images. In both packages a Gaussian filter is used to estimate the background intensity of each voxel before subtracting the variable background from every voxel within the dataset.

Discrimination of the object background threshold is based on the algorithm of Ridler and Calvard (Ridler et al,1978). This threshold selection method attempts to extract object data from the image using an iterative process, based on background sampling. Background "patch" samples are selected far from the object, i.e. the corners of the image and utilised as a switching function against which the rest of the image is compared. The switching function itself is a grey value of the mean density the patch sample taken previously. Image signals that match the switching function value are defined as background while those above the switch are defined as object and processed through one of two integrators. Upon processing the final element of the image, the integrator elements are averaged to find a threshold, L_0. The dataset is then defined as black or white dependent on the pixel or voxel value relative to this threshold and the resulting silhouette used as the new switching function for the following iteration (Ridler et al,1978).

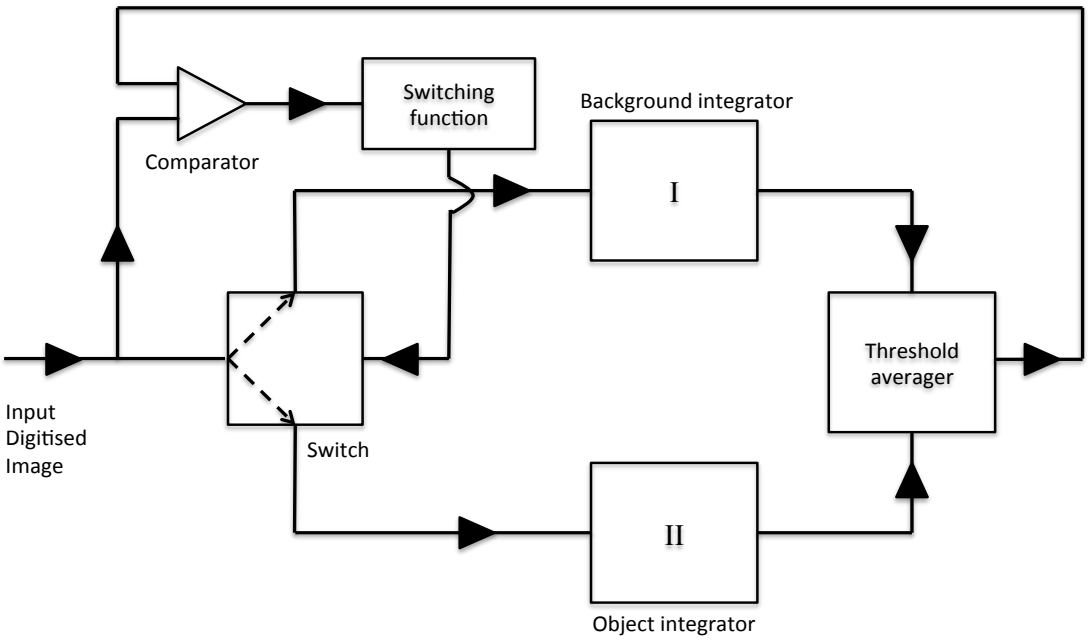

Figure. Imaris thresholding process used to identify objects within the image through iterative integration of the selected background.

It was assumed that the Autoquant automatic threshold operated on a similar principle. Figure 5 [B] shows the isosurface generated using the Autoquant automated process; similar results were achieved using the Imaris automated function. While brighter regions of the image have been successfully rendered, such as the ROI, it is apparent that a number of lower intensity regions have been calculated as background by the system. This could result from the manner in which the automated algorithm selects background. The low intensity of the fluorescence coupled with the punctate nature of the replication sites may, taken out of context during comparison with the switching function, be classed as background, thereby yielding a far lower percentage of surface modelling than would be expected. Figure 5 [C] and [D] show the manually thresholded modelling process available in Imaris, resulting in a far higher and more realistic textured percentage of the image.

Comparison of the two modelled ROI, Figure 5 [B] & [D] demonstrates the similarity between the two systems in brighter regions of the image. While scaling was identical within the xy plane of the model, changes to the CLSM dataset through Autoquant deconvolution resulted in compression of the model on the xz and yz axis. It was found

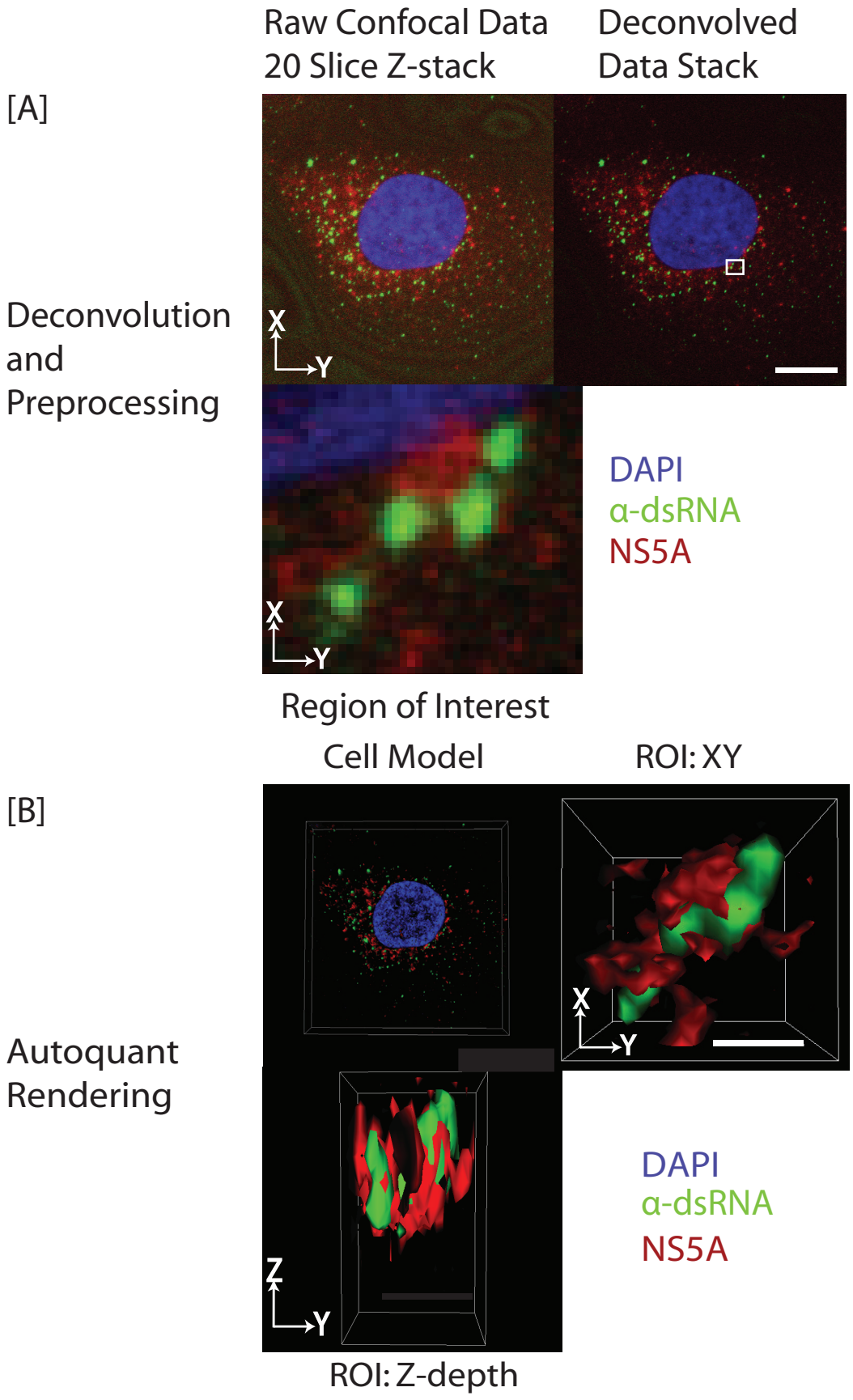

Figure 5. Comparison of deconvolution and volume rendering software and methodologies

Huh-7/SGR-JFH1 cells [A] and [C] were fixed and stained for NS5A using NS5A antisera and dsRNA using J2. x63 CLSM images [A] were deconvolved using Autoquant software. Deconvolved data was used to generate surface rendered models [B] based on maximum intensity projections using Autoquant [B] and Imaris [C] [D] . Cell Nuclei were stained using DAPI. Scale bar represents 10μm [A],[C] and 500nm[B], [D] .

[C]

Deconvolved Data Stack

Imaris Model

Deconvolved CLSM Image

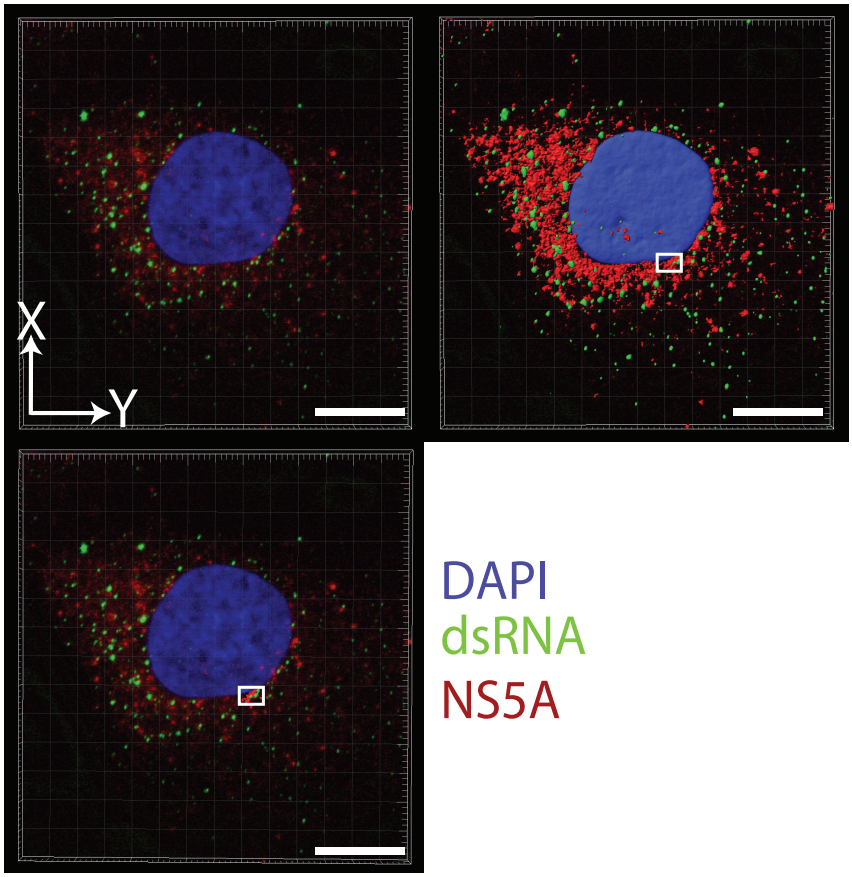

DAPI
dsRNA
NS5A

ROI

[D]

ROI: XY

ROI: Z-Depth

Imaris ROI Rendering

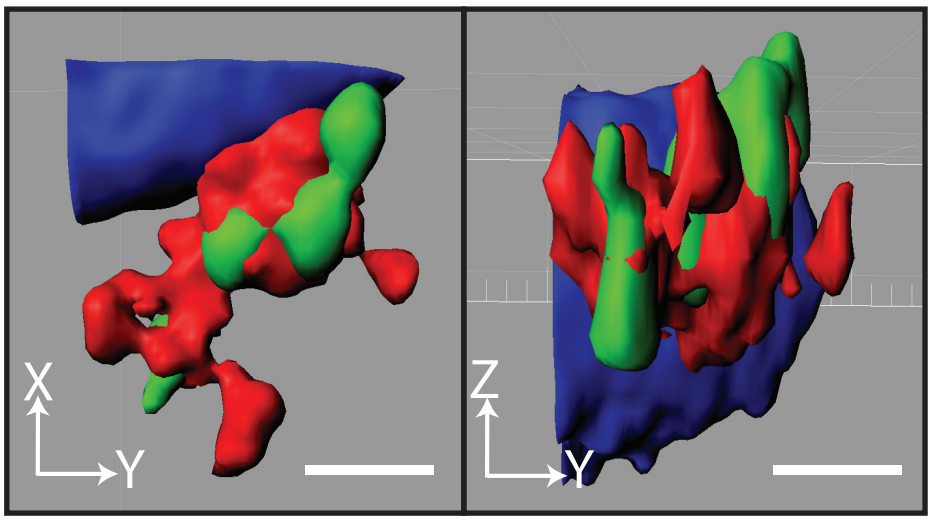

DAPI dsRNA NS5A

that the automated transfer of image data within the pipeline from Autoquant to Imaris resulted in the misreading of scale values within the dataset, from μm to nm, This required manual comparison and correction of file metadata prior to modelling or analysis using Imaris this difficulty was only noted in the TIFF file format.

Given the previously identified limitations of the automatic thresholding process in detecting lower intensity replication sites within the image, Imaris was chosen as the preferred modelling software due to its manual thresholding function. Despite the increased risk of operator bias it was felt that this was the most appropriate methodology to adopt, especially due to the increased resolution and therefore small replication site size, provided by SIM.

3.6. Optimisation of OMX Microscopy Parameters

SIM imaging was initially carried out using the SGR-JFH1$_{NS5AGFP}$ cell line, utilising the previously described dsRNA antibody J2 and acquired using the API OMX Blaze microscope system.Images were captured on three, channel specific back illuminated 16 bit scientific CMOS cameras with a 512x512 pixel chip size. Images were captured using SIM with a pixel resolution of 0.08μm. Prior to super-resolution acquisition, cells of interest were imaged using the LMX widefield microscopy system and the spatial co-ordinates recorded for transfer to OMX. SIM imaging mode was selected and channel exposure settings were adjusted to provide a mean intensity count value of approximately 50-100. Z-depth was manually determined by visual identification of the upper surface of the cell and the lower coverslip/cell interface and automatically adjusted from this the optical section spacing. 488 and 594nm channels were captured simultaneously followed by the 405nm channel. Subsequent imaging of the 405nm channel was carried out to limit non-specific photobleaching of the fluorophore due to the higher energy excitation laser.

Raw data was transferred to the processing workstation for reconstruction. Using a previously acquired Optical Transfer Function (OTF) file, data was processed to produce the reconstructed image. OTF files contain the fourier transform of a measured PSF representing the radial (XY) frequency and axial (Z) frequency of the microscope system for a point source of light. This is acquired for each channel through imaging of 100nm single fluorescent bead. Reconstruction was carried out on both the 488-594nm file and the separate 405nm file before the two were merged to create a single three channel file. Finally, channels were corrected for alignment errors. It is worth noting that this procedure

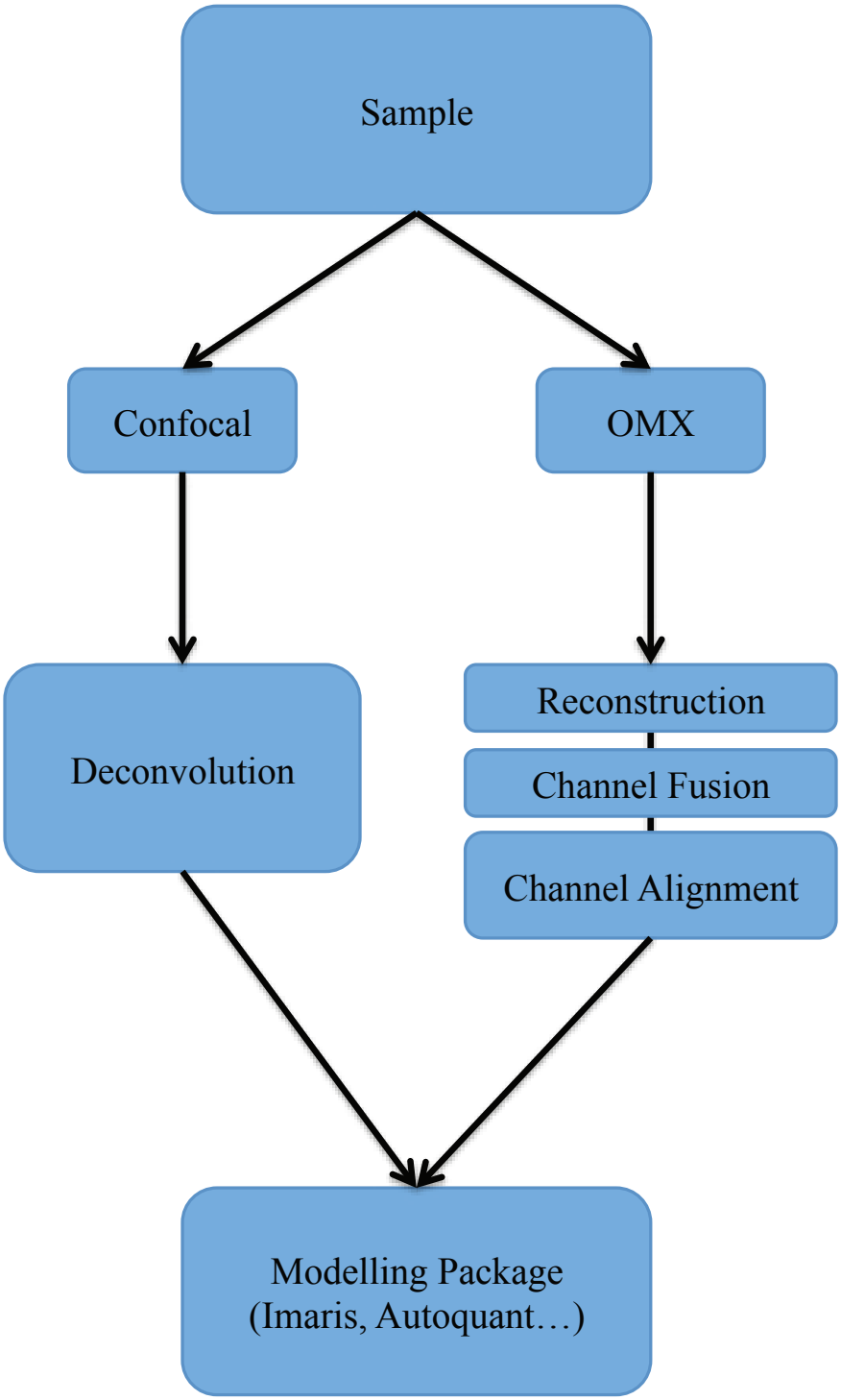

Figure 6. Image acquisition and preprocessing workflow for Confocal and SIM microscopy

was not optimised; manual correction of z-axis correction is discussed later (Section 3.9). A comparison of the CLSM and OMX image processing procedures is shown in Figure 6.

3.7. Interaction of NS5A with dsRNA at Putative HCV Replication Sites

Using Huh7/SGR-JFH1$_{NS5AGFP}$ cells, the location of HCV NS5A at foci containing dsRNA was examined as these were deemed to be putative sites of HCV RNA replication. Cells were grown overnight prior to fixation and stained for dsRNA. Coverslips were mounted using antifade reagent prior to SIM imaging (Materials and Methods 2.2.7.7.). Previous analysis of dsRNA/GFP-NS5A distribution, as demonstrated in Figure 2 [A] and [B] show colocalisation at the maximum resolution afforded by CLSM. Using OMX imaging, it was possible to determine the relative distribution of these moieties at a resolution approximately twice that of CLSM. Following acquisition and preprocessing of raw OMX data, datasets were processed to remove any remaining background noise and the punctate sites were modelled using the process described in 3.6 above and in Figure 6. A ROI was selected which centred around an individual dsRNA/NS5A focus that was representative of the foci detected.

Figure 7 shows the 3-D model of a predicted replication focus. The reconstruction illustrates differences from similar data obtained by CLSM. Rather than presenting as colocalised signals, a distinct sub-population of the dsRNA and GFP-NS5A signals exist in a nested configuration, with the dsRNA residing within a scaffold formed by NS5A. This configuration was observed from visual examination of 5 OMX datasets acquired during the imaging process. The GFP-NS5A protein existed in two discernible structural forms. The first had little or no apparent structure, was less than 300nm in size and showed no colocalisation with dsRNA, Such data were interpreted to represent immature or partially formed replication site debris, making up a large portion of the signal distal to the nucleus (data not shown). The second form of NS5A possessed a discrete and relatively uniform barrel structure of approximately 300nm, centred around a core dsRNA signal (Figure 7). Such sites were relatively few in number, roughly 10-20 per cell with a somewhat perinuclear distribution, visible either as single structures, or as shown in Figure 7, larger multinucleated structures, with each internal space having a diameter of approx 300nm. In each case, this gap was filled by the signal for dsRNA, which mapped precisely within the space created by GFP-NS5A. The elongated nature of the reconstruction is a result of the 2x difference in lateral and axial resolution (Gustafsson,2000). It is highly probable that

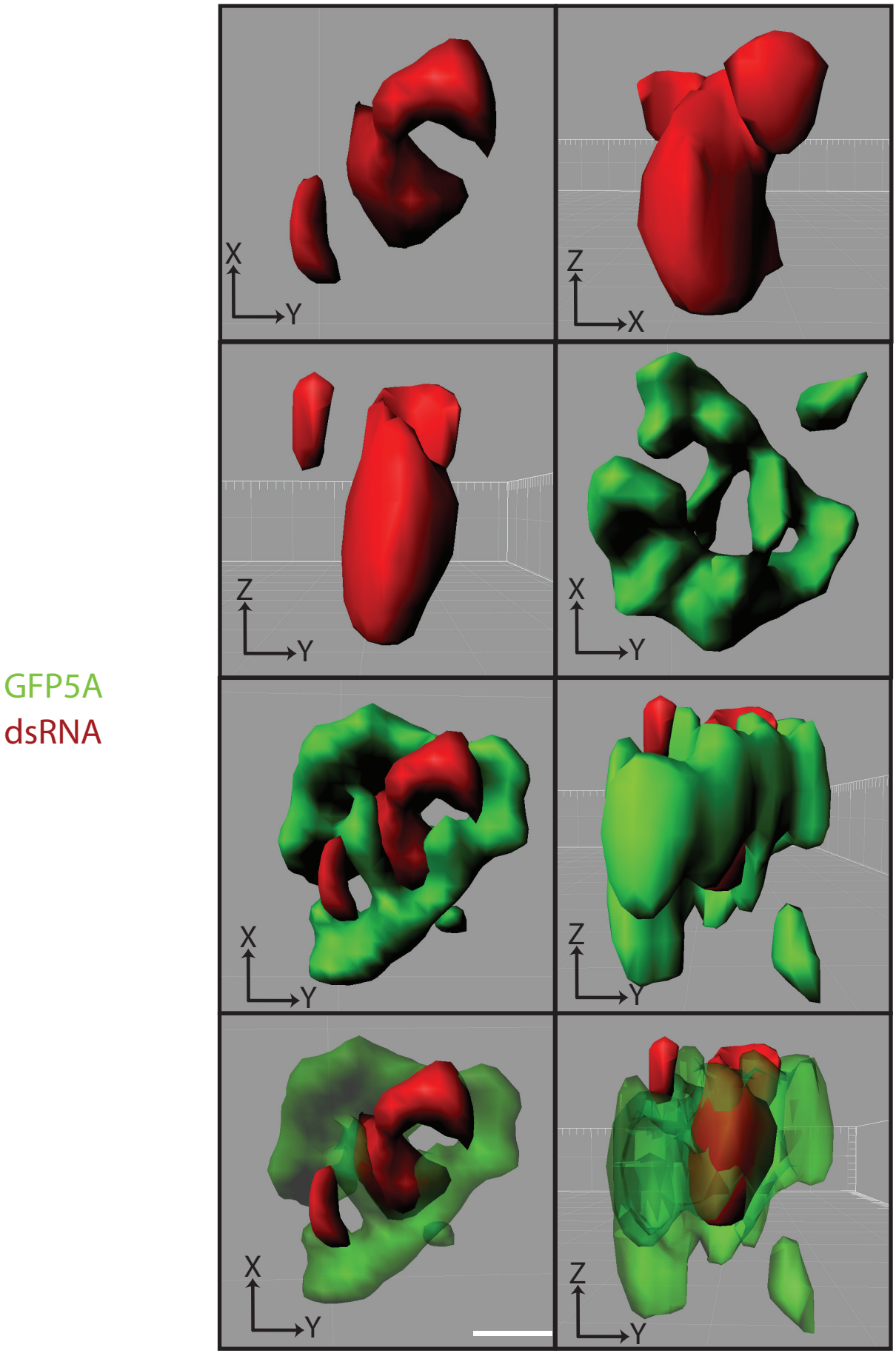

Figure 7. Modelling of OMX data showing hollow structure interaction of the GFP-NS5A protein complex with dsRNA at putative replication sites
Huh-7/SGR-JFH1-NS5AGFP cells were fixed and stained for dsRNA using J2 antibody. Images were acquired by OMX miroscopy while surface modelling was performed on structures of interest using Imaris. Scale bar represents 300nm

the dsRNA signal is more spherical than linear in nature. Increasing the transparency of the GFP-NS5A model towards 50% allowed better visualisation of the spatial relationship between the two components as seen in the bottom right panel of Figure 7.

3.8. Automated Quantification of Putative Replication Sites Using Imaris

Given the ability to discriminate between different forms of NS5A, a more rigorous approach was attempted for quantitative analysis of putative replication sites. To validate the results with a non-tagged form of NS5A, Huh-7/SGR-JFH1 cells were used for the following analysis. To limit the effects of truly random non-specific background staining, Imaris software was applied to evaluate the dataset for significant colocalisation between HCV NS5A and NS3. The J2 dsRNA antibody was replaced with NS3 due to the nested configuration of the NS5A/dsRNA signals observed in the above studies, which yielded reduced colocalisation by OMX. NS3 and NS5A exhibit a high degree of colocalisation, as evidenced from previous studies (Gosert et al 2003) and as shown in Figure 8a [A]. This colocalisation was then analysed using single cell images generated by OMX (Figure 8a [B]). From this evaluation a third channel based on the colocalised signal from the two proteins, identified using the scatterplot in Figure 8b [C] (see Section 3.10 for a description of Scatterplot analysis), was generated and the resultant signal was employed for surface rendering (Figure 8b [D]). The Imaris MeasurementPro sphere detection feature was then utilised on the rendered model in Figure 8b [D], to identify and quantify all individual structures with a roughly spherical structure of any size (Figure 8b [F]). As the colocalisation channel had already undergone Costes thresholding, (Section 3.11.1) background subtraction or thresholding was unnecessary at this stage.

Following quantification of modelled objects within the colocalised channel, the sphere detection feature of Imaris was again reapplied to the colocalised dataset. In this instance a number of filters were applied to the data, removing all objects below the 300nm diameter threshold previously observed, identified in [E]. Subtracting the number of ≥300nm objects from the original count provided a quantification of the two distinct populations being investigated. This methodology was applied to a number of OMX datasets and the data plotted in Figure 8c.

Results revealed a significant difference in population sizes across the 6 samples analysed in this manner. From the mean number of total objects quantified (n≈1000) approx. 60 objects had a diameter of ≥300nm. Although there is significant variation between

individual samples, there is an approximately 100-fold difference between the two populations.

There are a number of factors which affect the accuracy of this analytical method. The most obvious factor is the inclusion of other cells or parts thereof within the image area which could skew the quantitation results. This form of error is even more important given the non-homogeneous distribution of the two populations within the cell. Inclusion of distal regions of other cells will result in an increase in quantity of <300nm objects. This issue can be avoided through the selection of an ROI within the dataset, excluding extraneous data from other cell components. Unfortunately automatic ROI selection, utilised to prevent user bias, was not possible given the complexity of the datasets being examined.

One of the more complex causes of error lies with the manner in which the software determines the centre and size of spherical objects and the nature of the objects being studied. Imaris software selects and identifies spheres by the "quality" of an object's sphericity from a central point of maximal intensity, in other words the software examines the dataset for solid spherical objects. This poses a problem for comparative analysis of HCV replication sites. As stated above, the ≥300nm structures of interest appear to have a hollow spherical nature, resulting in a central minimum instead of a central maximum, akin to an inverse PSF. When such an object is analysed using the MeasurementPro package, the quantitation algorithm fails to recognise some of the hollow spherical, or multinucleated structures described in Figure 7. Instead, the software selects high intensity regions within the structure, ostensibly the walls or surface of the RC being quantified, utilising these as seeding points from which to determine spherical regions for quantification. This can result in a number of error variations, from multiple spheres assigned to single objects through to multinucleated regions being recognised as single spheres.

Although the unique nature of the data being analysed can result in such errors, the characteristic signal intensities of hollow structures should allow customised algorithms to identify these regions with far greater accuracy than the current package filters available. Identifying spherical objects of maximal intensity with a diameter of 300nm with a central minimum is a computationally simple task. While the development of such an algorithm lay outside the remit of the project, the ability to link the Imaris package with an alternative numerical computation and visualisation package, such as Matlab could allow scope for further work within this area.

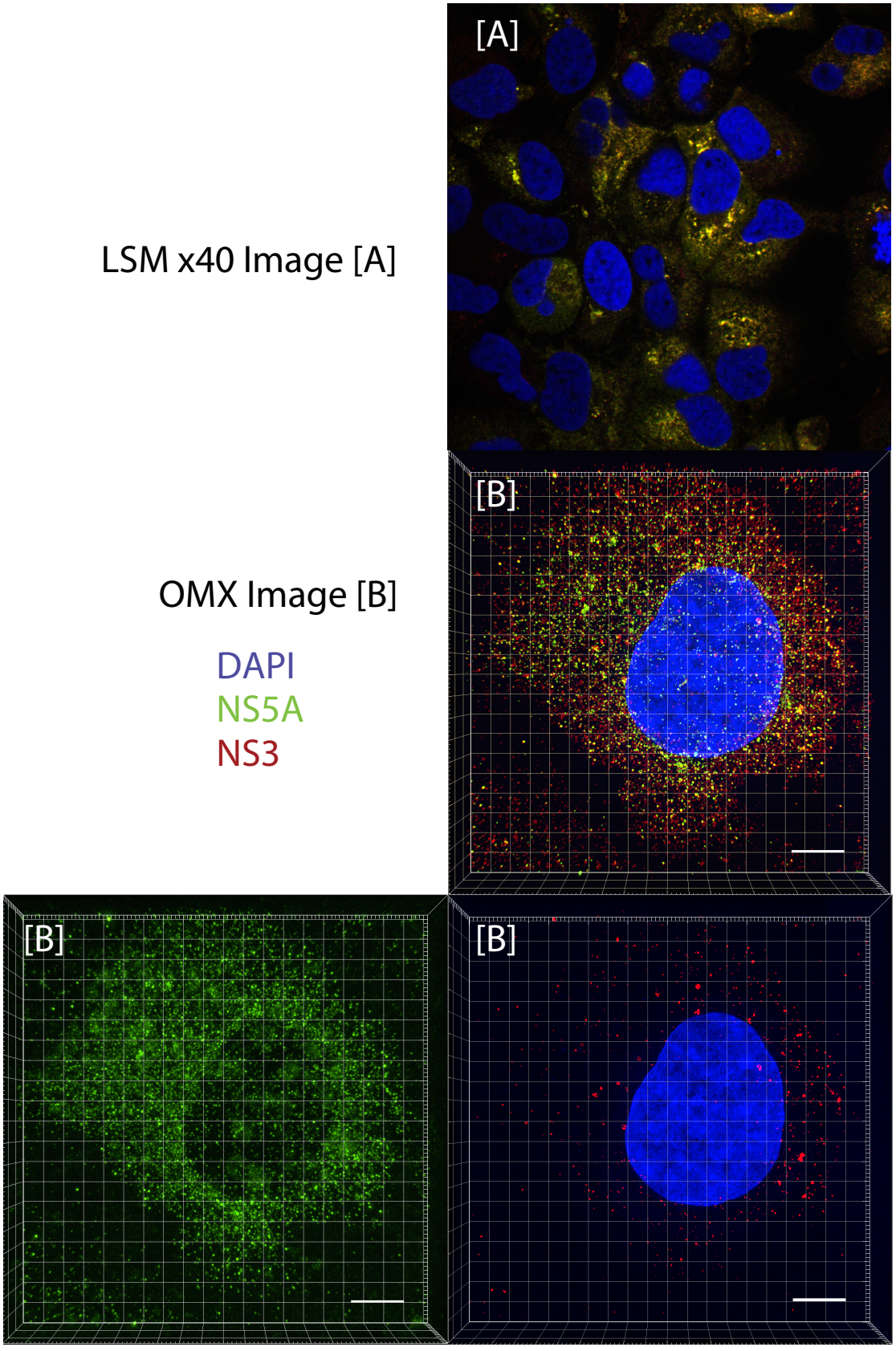

Figure 8a.Colocalisation of replication sites identified by the NS3 and NS5A proteins for quantification using Imaris MeasurementPro

Huh-7/SGR-JFH1 cells [A] [B] were fixed and stained for NS5A using anti-NS5A antibody and NS3 using anti-NS3 antibody. Image [A] captured using confocal microscopy at x40 magnification. Cell Nuclei were stained using DAPI. Scale bar represents 10μ m.

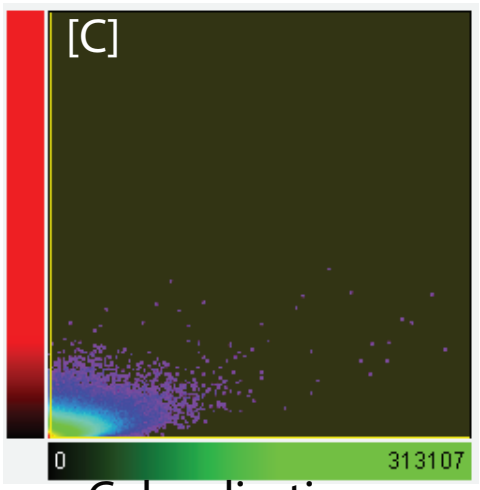

Colocalisation Histogram

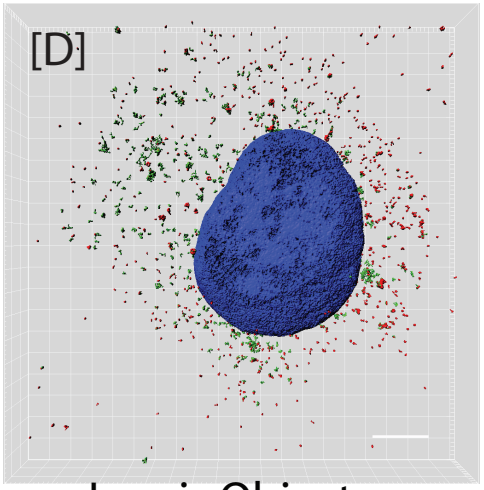

Imaris Object Identification

Colocalisation Channel

Spheres >300nm diameter

Sphere >300nm diameter

Objects with <300nm diameter

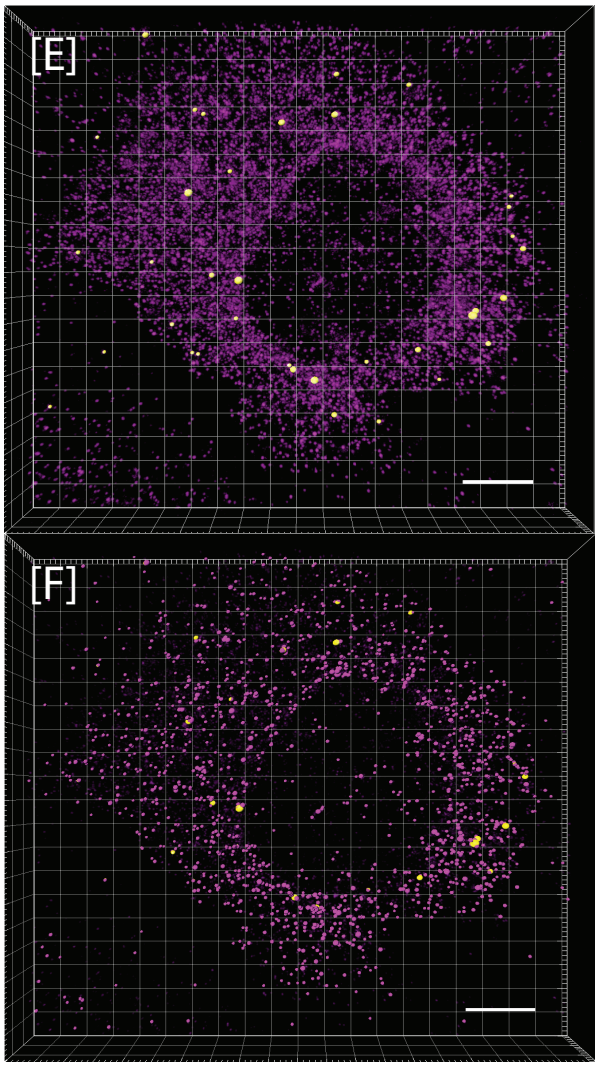

Figure 8b. Quantification of identified replication sites using Imaris MeasurementPro

Single cell images captured by OMX microscopy (Shown in Figure 7a) were used to produce colocalisation channel histogram [C] and the resultant surface rendering [D]. Spherical structures were separated by size and identified using Imaris MeasurementPro [E] and [F]. Cell Scale bar represents 10μ m.

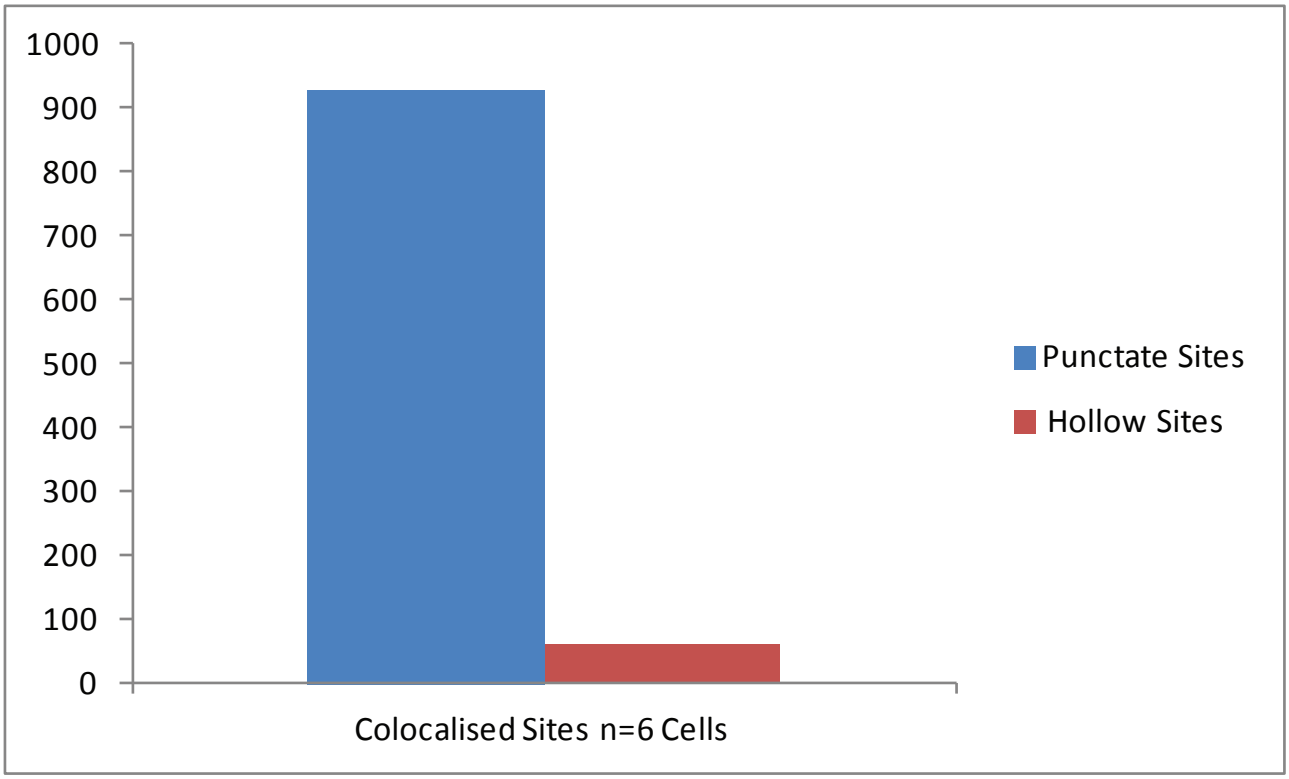

Figure 8c. Quantification of replication sites

3.9. The Affect of Channel Alignment on Statistical Colocalisation

During analysis of the OMX data it became apparent that the automated alignment process did not accurately correct an apparent shift between channels. Unlike single detector systems such as the photomultiplier detection unit employed in CLSM, the use of individual cameras and optical trains with the OMX system can result in significant shifts, rotation and magnification errors. To confirm and adjust alignment, multi-colour fluorescent 100nm TetraSpeck Beads, dried onto a coverslip were utilised for camera calibration.

Despite the care taken to ensure channel alignment it became obvious that the datasets acquired still continued to display a degree of channel shift, most noticeable between the green 488nm and red 594nm channels. Figure 9a [A], shows the apparent lateral colocalisation of the GFP-NS5A and NS3 signals, which demonstrate a high level of colocalisation by CLSM. By contrast Figure 9a [B] shows the lack of colocalisation within the axial domain for OMX images taken with Huh7/SGR-JFH1$_{NS5AGFP}$ cells.. The uncorrected image [B] shows the GFP-NS5A and NS3 signal, colocalised within the xy-plane but a uniform disparity within the z-plane. The resultant effects on colocalisation statistics are clearly visible in a scatterplot derived from the uncorrected image (Figure 9a [D]) which indicates a random distribution of voxels. Using Imaris, the 594nm channel was shifted by -2 voxels relative to the 488 and 405nm channel (corrected image in Figure 9a [C]). Standard channel alignment methodology utilises correction of the 594nm and 405nm channels relative to the 488nm reference channel. The inability to perform half voxel shifts of the data set within the software package prevented complete channel alignment. The validation of this shift was confirmed both visually through merging of xy-aligned voxels and through analysis of the colocalisation scatterplot (Figure 9a [E]). Comparison of the original (Figure 9a [D]) with the corrected version (Figure 9a [E]) shows the shift from randomised signals towards a more linear dispersion indicative of greater colocalisation of NS3 and NS5A.

3.10. Scatterplot Analysis

Having defined and confirmed the axial correction shift required for correcting channel alignment a comparative study of the effects of increased resolution on colocalisation values was performed. Similar 3-D CLSM and OMX datasets of SGR-JFH1$_{NS5AGFP}$ cells

XY Overview

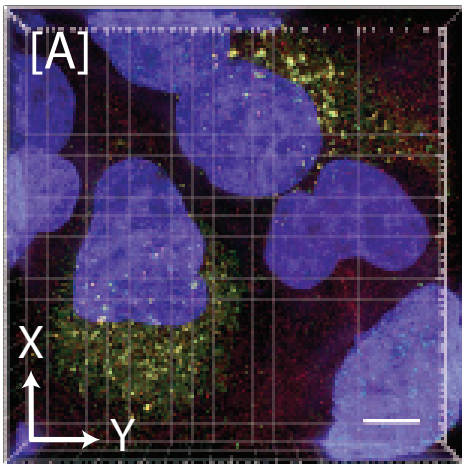

OMX Image
GFP5A NS3

Colocalisation
Scatterplot

Original Z-axis
Data

Z-axis Data
Corrected

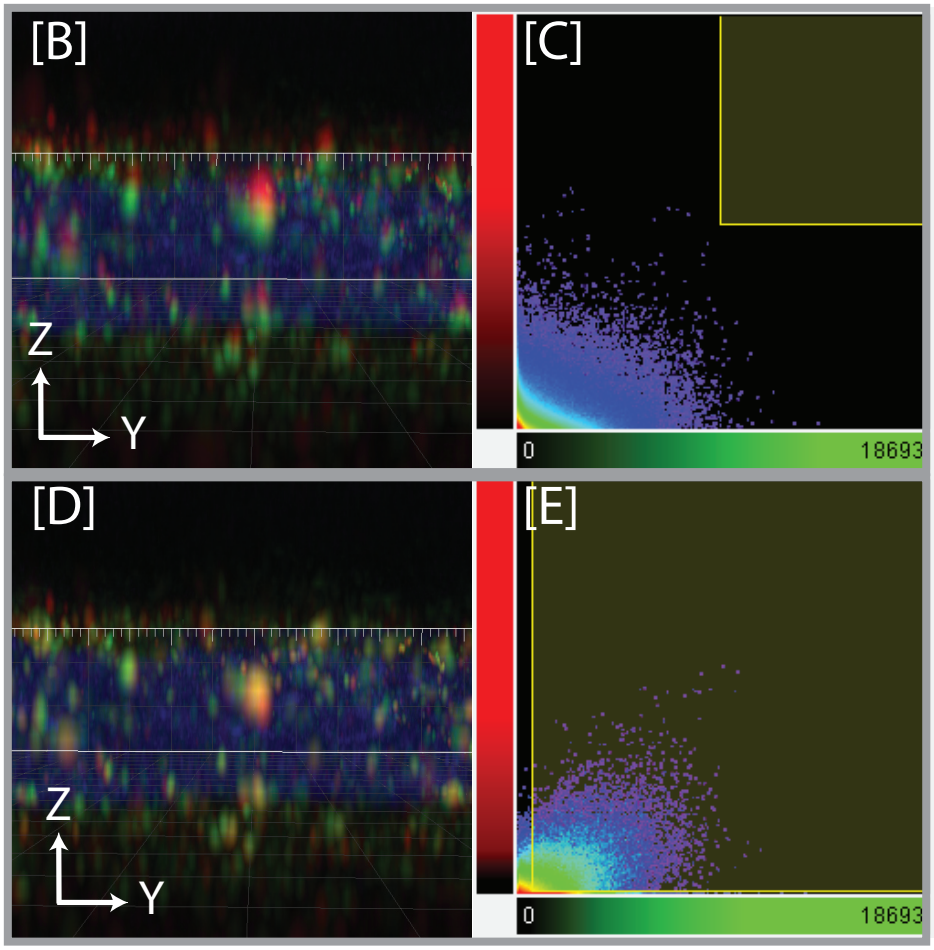

Figure 9a. Correction of channel alignment within the Z-plane leads to an increase in colocalisation between channels

Huh7/SGR-JFH1$_{NS5AGFP}$ cells were fixed and stained for NS3 using NS3 antisera. Panel [A] shows expected XY colocalisation by OMX microscopy. Panel [B] shows misalignment of the 594nm channel relative to the 488nm channel along the Z-axis and the resultant decrease in channel colocalisation shown in panel [C] . Realignment of the 594nm channel was carried out using a 2 voxel shift applied to the Z-axis shown in panel [D] resulting in an increase in scatterplot colocalisation seen in panel [E].

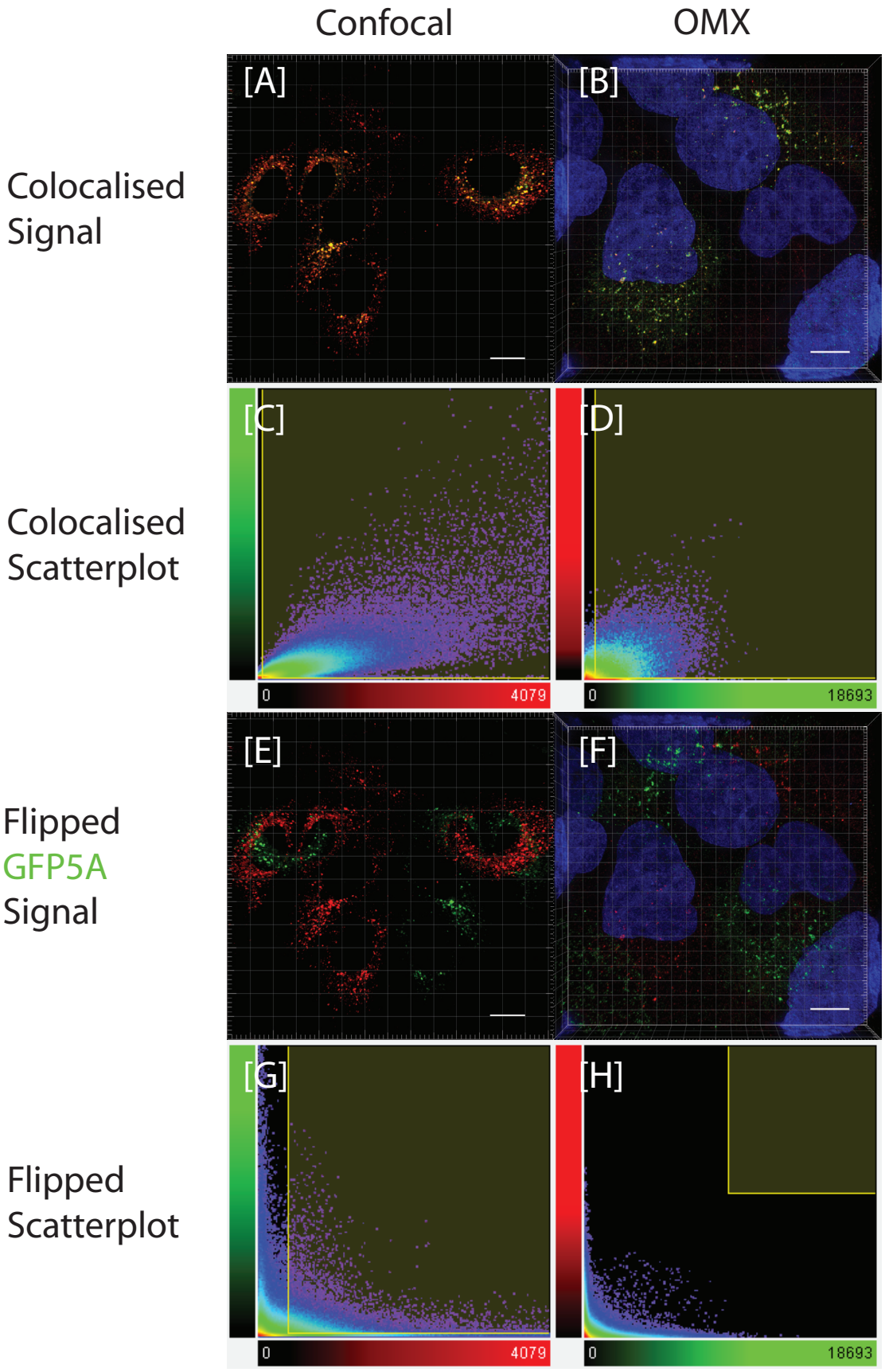

Figure 9b. Variation in colocalisation values dependent on image resolution. **Huh7/SGR-JFH1$_{NS5AGFP}$ cells were fixed and stained for NS3 using NS3 antisera. Images were captured using either CLSM (Zeiss, LSM710) [A] [E], or OMX [B] [F]. Colocalisation analysis was carried out using Imaris and comparative results plotted [I]. Scale bar represents 10**µm.

[I]

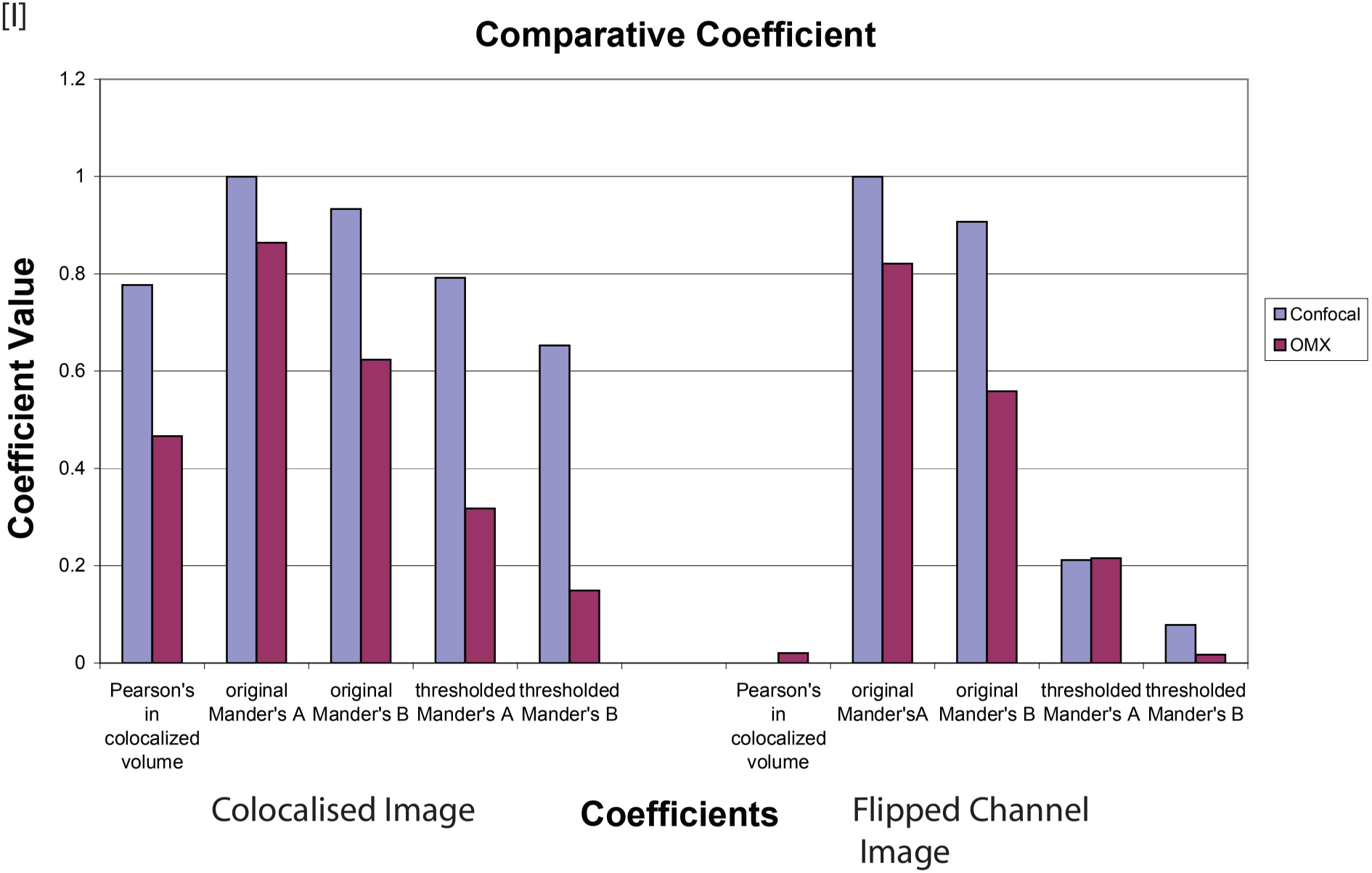
Comparative Coefficient
Coefficient Value
1.2
1
0.8
0.6
0.4
0.2
0
Pearson's in colocalized volume
original Mander's A
original Mander's B
thresholded Mander's A
thresholded Mander's B
Pearson's in colocalized volume
original Mander'sA
original Mander's B
thresholded Mander's A
thresholded Mander's B
Confocal
OMX
Colocalised Image
Coefficients
Flipped Channel Image

were processed in the manner described above. Colocalisation analysis was performed using the Imaris Coloc module, which generates the scatterplots displayed in Figures 8a and 9a.

Scatterplot analysis was used frequently throughout the project to provide an easily understood visual representation of colocalisation within the datasets. Each pixel or "bin" within the plot represents a voxel with the intensity values matching that particular co-ordinate based on a Cartesian coordinate system.

$$Bin\ Value = [IntRed_{x,y}, IntGreen_{x,y}]$$

Using this method, voxels with maximum intensity in the red channel but 0 in the green will lie at the maximum of the y axis, while those with maximum intensity in the green channel will lie on the x axis. Therefore a voxel with equal intensity in both the red and the green channels will be plotted in a linear manner equidistant from both axes. Where voxels share the same intensity values and scatterplot coordinates, the values are summed and the colour of the representative bin altered as a heat map ranging from blue for bins with single voxel values to red for those with maximum summed values. In this way the manner and distribution of colocalisation can be visualised. The ideal "perfect" colocalised dataset is presented as a linear dispersion at a 45^{o} angle from the origin with tight clustering of bins around this line of regression resulting in a low R^2 value. Image background is visualised as a hot spot near the origin, where low intensity (0,0) coordinates cluster.

Real world sampling however rarely provides such datasets; uneven labelling between targets, background noise, photobleaching (especially given the high intensity lasers utilised in OMX) and miscalibrated acquisition channels during microscopy can all significantly alter datasets to result in skewed colocalisation plots. Where the intensity of one channel dominates over another, this may be seen as a tilt of the linear dispersion towards that axis. However this may also arise from high background within that channel or poor/unapplied background subtraction.

The nature of the images being analysed also presented a number of challenges. For larger targets, there is greater accuracy in colocalisation plotting, with small errors in channel alignment chromatic aberration and staining being averaged out. Moreover, greater numbers of antibody targets or GFP molecules increase the intensity of each PSF which will be evident therefore as a higher signal to noise ratio and voxel intensity. The accuracy required for any experiment and the resolving power of the microscopy system also play an

important part in the distributions within the plot. There are a number of challenges associated with increasing microscope resolution and in particular SIM. As resolution increases, the effect of spatial errors and optical train on colocalisation increases also. Hence, an optical system such as the OMX will be affected twice as much as CLSM. This is compounded by imaging and modelling replication sites of a size at or beyond the diffraction limit. While a 1 voxel shift error may not have a noticeable effect on colocalization of diffuse targets within a large structure, such as mitochondria, the effects on colocalisation of proteins within a punctate site of 300nm can be significant.

By way of an example the colocalisation scatterplot from CLSM data (Figure 9b panels [C] and [A] respectively) reveals a distinct but skewed level of colocalisation within the dataset. As mentioned previously, in an ideal dataset with perfect colocalisation, the majority of bins within the scatterplot would exist as a straight diagonal line. Such a graphical representation requires signal intensities of the two channels to essentially be identical. Deviation from the ideal can be seen in Figure 9b [C] with the difference in maximal signal intensity between the 594nm and 488nm channels resulting in the line of regression being heavily weighted towards the higher intensity red channel. While such skewing may be the effect of intense background signal, observation of the original image Figure9b [A] suggests this is not the case and that the diagonal for the colocalised is generated by the higher intensity fluorophores of the NS3 (red) signal as compared to that of GFP-NS5A.

The OMX colocalisation scatterplot Figure 9b [D] shows a distribution distinct from that of the lower resolution CLSM dataset. Signal intensity is more even between the two channels however the distribution of voxels lacks the narrow linear dispersion seen in the lower resolution CLSM dataset. Given the differences in the intensity maximum between the CLSM and OMX data, this distribution is more likely the result of compression of the intensity values within the dataset. This can be caused by a divergence in actual maximum values within the image and those recorded in the image file metadata. This divergence seems to be caused by an isolated number of noisy pixels with high intensity captured during imaging which are then lost during image processing.

Given the lack of a clearly defined line of regression and the low level of signal intensity within the scatterplot in Figure 9b [D], the datasets in [A] and [B] were compared and validated with a randomised image of similar signal intensity and voxel quantity. To construct such randomised imaging data, an artificially randomised version of the dataset was created through inversion of the 488nm channel. This image shown in Figure 9b [F].

was then utilised to generate a colocalisation scatterplot (Figure 9b [H]) by applying the same parameters as the original analysis. Given the non-diffuse, punctate nature of signals detected for the HCV NS proteins, any colocalisation within the image should be random. This randomising process was repeated for the CLSM dataset for comparative purposes (Figure 9b [E] and [G]).

The results of this randomisation process on the OMX data are apparent (Figure 9b [H]), where exclusion between the two channels is clearly evident in the two distinct bin populations. The low intensity correlated pixels close to the xy intersect are the result of background noise and 0 value voxels. Again, given the punctate nature and high resolution, this level of clustering around the origin when compared to the CLSM scatterplot (Figure 9b [G]) is to be expected.

Comparing the original and flipped scatterplots highlights the clear difference between randomised data and the colocalised voxels of the original image. Therefore while there is a significant difference between the two scatterplots themselves (Figure 9b [C] and [D]) each plot when examined in the correct context can be regarded as representative of colocalisation within the respective datasets.

3.11. Quantification of Colocalisation Data

Based on the colocalisation scatterplots described above, the Imaris Coloc analysis module was used to yield quantitative analysis of the precise colocalisation values with the intention of limiting operator error and bias during interpretation. The aim was to develop a standardised protocol and algorithm for comparison of multiple datasets in a more meaningful manner. To achieve such an objective required a more detailed understanding of the processes and parameters applied by Imaris, especially for OMX datasets as there has been limited application of this software to interpret super-resolution images.

The following four subsections describe some of the underlying mathematical approaches and other considerations that contribute to the generation of quantitative analysis by Imaris and its interpretation.

3.11.1. Costes Threshold

Several approaches have been developed for the quantitative analysis of colocalisation, either through cross correlation (Akner et al,1991) or cluster analysis of the generated histogram (Demandolx et al,1997). However the majority of these methodologies are either

qualitative or subjective, requiring manual identification of clusters within the histogram. Two correlation algorithms are now widely utilised for quantitative estimation of correlation, the Pearsons Correlation Coefficient (PCC) {Pearson, 1896 374 /id}{Manders, 1992 371 /id;Pearson, 1895 511 /id} and the more biologically relevant coefficients produced by the Manders Overlap Coefficient (MOC)(Manders et al,1993). Importantly, both the PCC and MOC require a threshold to be set for each value, acting as a cutoff between specific staining and non-specific background. Colocalisation is then analysed based on the overlapping signal between both channels that are above this threshold. The greatest problem with these methods is the manner in which the thresholds are set, usually through visual estimation, resulting in inconsistent and irreproducible results (Costes et al,2004).

To overcome this limitation, Costes *et al* developed an automated threshold estimation system based on the correlation within different regions of the two-dimensional histogram. Costes' approach uses a statistical test developed from Lifshitz (Lifshitz,1998) to determine the probability (P-value) of the correlation coefficient *r,* from the two channels being significantly greater than would be calculated from random overlap. Comparisons are made between random scrambled images generated from one of the channels; through iterations of channel scrambling and comparison, a probability distribution of the random overlap of the two signals can be determined. By comparing the correlation of the unscrambled channels against the correlation distribution of the scrambled images (usually 200 generated images) determines whether significant colocalisation can be drawn from a predefined probability for significance, usually >95% (Costes et al,2004).

The Costes approach is applied as follows. Randomly generated scrambled images generated from the original data are produced as a Poisson distribution in a spatially random manner, i.e. 1) a pixel is equally likely to be placed anywhere within the image and 2) a pixel's placement is independent of the placement of all other pixels (Lifshitz,1998). This process assumes that the intensity of each pixel is also independent and uncorrelated from its neighbouring pixel when determining random overlap. However, such an approach does not hold true for images captured by an optical system, as the point spread function of the system will result in correlation between neighbouring pixels, in the form of the Airy disk. To compensate for this effect, images are broken down, not into the smallest unit available for scrambling, but independent blocks of a size defined by the PSF of the optical system (Costes et al,2004). This results in significantly fewer data points

within the scrambled image which in turn leads to a significantly broader distribution of overlap patterns.

The threshold search and estimation is completed through analysis of the 2-D colocalisation scatterplot. Starting with the highest intensity values, the algorithm incrementally reduces the threshold value along a line of regression obtained from a linear least-square fit of the two channels. The correlation coefficient, *r* is calculated using pixels of intensity below the threshold value. This process occurs in an iterative manner until the coefficient reaches 0, and at this point the overall correlation of pixels below this value is on average non-colocalised. It is of note that some dim colocalized pixels, lying close to the line of regression and the origin will be lost as background. However these pixels tend to represent a small contribution to the total amount of colocalisation. This methodology has been shown to accurately quantify colocalisation at as little as 3% while providing an unbiased and reproducible method for threshold estimation (Costes et al,2004).

Costes' method for automatic threshold estimation was applied to datasets to limit user bias and increase reproducibility. Following this threshold process, a new colocalisation channel was produced based on the summed intensity of colocalised voxels within any dataset. Pearsons (Section 3.11.2) and Manders (Section 3.11.4) coefficients were then calculated for both CLSM and OMX approaches (Figure 9b [I]).

3.11.2. Pearsons Correlation Coefficient

The PCC, developed by Pearson in 1896 (Pearson,1896;Stigler,1989) and introduced to biological microscopy by Manders in 1992, measures the linear dependence between two patterns, independent of the average value of the signal, as a value r_p ranging from +1 showing complete colocalisation, through 0, showing random colocalisation, to -1 showing complete exclusion of the two channels (Manders et al,1993).

$$r_p = \frac{\Sigma_i(\mathrm{ChR_i} - \mathrm{ChR_{Ave.Coloc}}) * (\mathrm{ChG_i} - \mathrm{ChG_{Ave.Coloc}})}{\sqrt{\Sigma_i(\mathrm{ChR_i} - \mathrm{ChR_{Ave.Coloc}})^2 * (\mathrm{ChG_i} - \mathrm{ChG_{Ave.Coloc}})^2}}$$

Equation 6. Pearsons Correlation Coefficient

Equation 6 shows the algorithm utilised by the Imaris software to determine the degree of overlap between the two channels within the colocalised volume. ChR_i and ChG_i represent the intensitites of the red and green pixels respectively being analysed while $ChR_{Ave.\ Coloc.}$ and $ChG_{Ave.\ Coloc.}$ represent the average intensity value of the red and green pixels

within the thresholded colocalisation channel. This can be simplified by considering a channel average subtraction to produce Equation 7.

$$r_p = \frac{\Sigma_i(\mathrm{ChR_i}) * (\mathrm{ChG_i})}{\sqrt{\Sigma_i(\mathrm{ChR_i})^2 * (\mathrm{ChG_i})^2}}$$

Equation 7. Channel Average subtracted PCC

The value of the coefficient in Eq. 7 ranges from 0 to 1, the product in the numerator of the equation ($\Sigma_i(\mathrm{ChR_i}) * (\mathrm{ChG_i})$) returns a significant value only when both R_i and G_i belong to a voxel within the colocalizing channel with a value >0. This simplified equation highlights the importance of effective Costes thresholding and background subtraction prior to analysis. The PCC algorithm calculates colocalisation on all pixels within the image. However the subtraction of the mean channel intensity from each pixel's intensity value renders the results independent of signal intensity (Dunn et al,2011). Therefore each pixel within the image, contributes an equal and unweighted value to the final coefficient value. This has important ramifications when considering the dramatic differences in coefficient values between the two modes of image capture. For the purposes of clarity, it was assumed that both the CLSM and OMX capture devices operate in an equivalent manner with similar pixel size and number and that the resolution of the OMX capture system was exactly twice that of the confocal system. Examining a single point source fluorophore by CLSM may result in a 4x4 matrix of pixels registering positive values based on the PSF of the optical system Figure 10 [B]. This same source when imaged using the increased resolution of the OMX system would be expected to resolve this same point to a 2x2 matrix of pixels, representative of the smaller OMX PSF, double the resolution of the confocal system Figure 10 [A] This can be assumed to hold true for both channels being imaged.

3.11.3. Effects of imaging system on colocalisation

While investigating the mechanism of the PCC algorithm it became apparent that the differing optical properties of the CLSM and OMX microscopy systems may have an effect on the correlation values generated using Imaris. Therefore the various characteristics of the two systems were studied to identify factors affecting correlation values.

If the optical trains of both channels are perfectly aligned then the PCC values of both will be 1, i.e. perfect colocalisation. However as previously discussed, there are significant differences in the manner of image capture between the two systems. The CLSM system

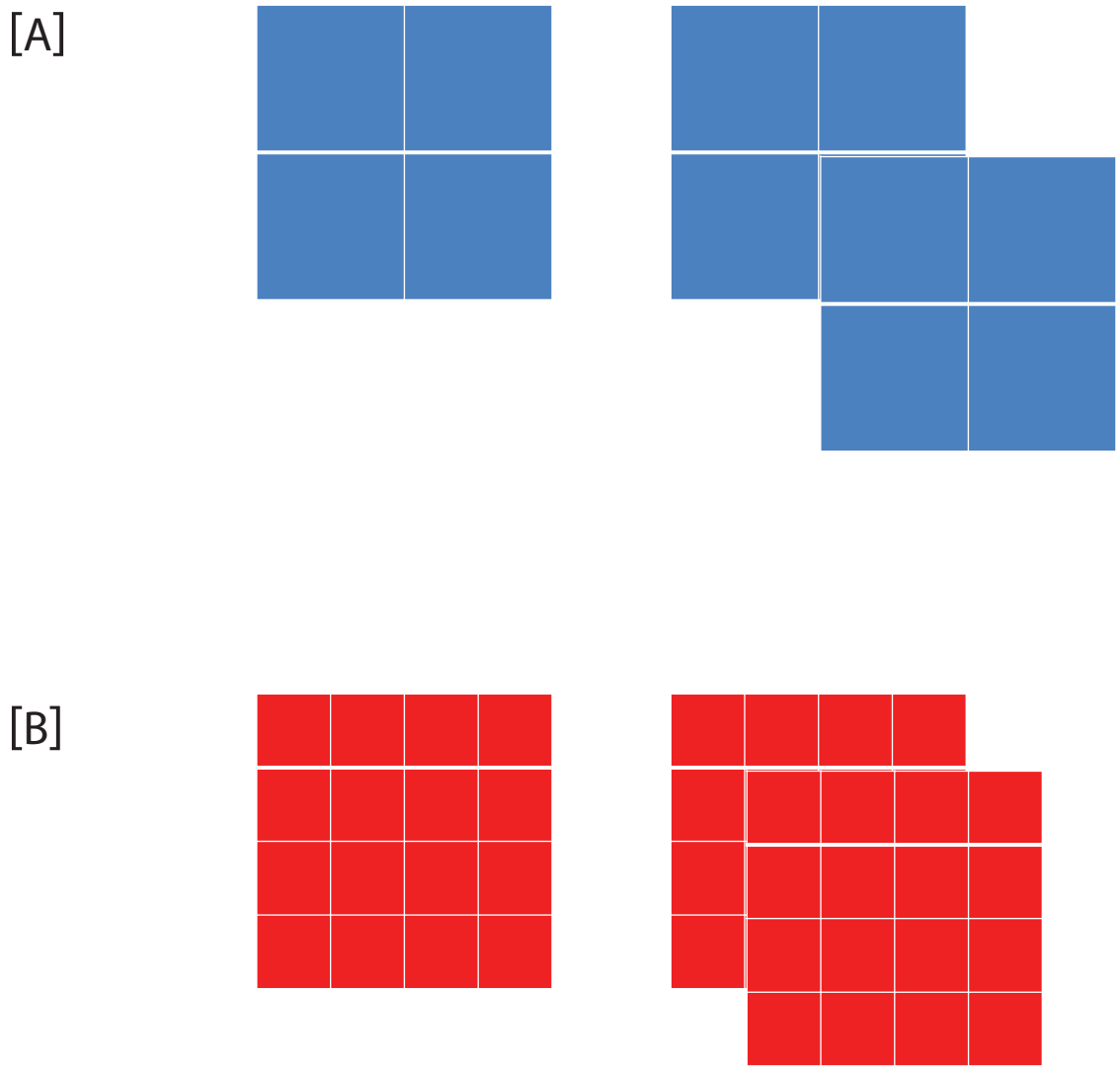

Figure 10. Pixel Overlap CLSM [A] and OMX [B] Imaging Systems.

utilises a single optical train and capture device, limiting calibration errors between the channels. The multiple optical paths within the OMX require careful calibration and alignment to ensure image fidelity. Complications with channel alignment and correction have been discussed in Section 3.9, however the channel shift applied did not entirely correct this problem within the z-axis, mainly due to the sub-voxel shift required. The Imaris package is only capable of +/- whole voxel corrections, preventing absolute correction. This, coupled with the small, yet unavoidable alignment problems caused by chromatic and spherical aberrations, results in imperfectly superimposed channels. Therefore although the OMX system produces higher resolution images, it is still affected by the imaging errors found in all forms of microscopy.

Given this systemic error, a 1 pixel shift can be applied to both CLSM and OMX systems along the x-axis and y axis. In this instance the number of correlated pixels within the 4x4 matrix of the confocal image drops from 16 to 12, while the 2x2 matrix of the OMX image drops from 4 to 1. Hence, as a percentage, CLSM maintains a 56% correlation from the original 100%, whereas the OMX correlation drops to 25%.

This effect is again exacerbated by the nature of the replication sites being studied; while "single pixel" errors may be lost when examining larger subcellular components such as mitochondria, the punctate nature of replication foci only serves to increase the impact of image error on coefficient values. As a consequence, there is an overall decrease in correlation as defined by the PCC. Despite the unexpected differences in values between microscopy modes, both suggest a reasonably significant colocalisation between the two NS proteins. Such unexpected results highlight the need for care when analysing quantitative data from novel imaging techniques.

3.11.4. Manders Overlap Coefficient

The other colocalisation values in Figure 9b [I]. are based upon the closely related Manders Overlap Coefficient (MOC) described by Equation 8:

$$k_R = \frac{\Sigma_i ChR_i * ChG_i}{\Sigma_i (ChR_i)^2}$$

$$k_G = \frac{\Sigma_i ChR_i * ChG_i}{\Sigma_i (ChG_i)^2}$$

Equation 8. Manders Overlap Coefficient

The MOC, named after Erik Manders, is a derivation of the PCC developed in 1993 to overcome some of the ambiguity caused by the -1 to 1 coefficient range. Unlike the PCC, there is no subtraction of mean signal intensity, and therefore the MOC algorithm only returns values between 0 and 1, which may be less confusing than the negative values that can be generated using the PCC. Moreover, although the PCC is independent of signal intensity it is strongly influenced by the ratio of the number of objects within both channels, an important consideration for sample preparation. Differences in antibody affinity and non-specific binding can result in an object offset from a 1:1 target ratio within the sample.

To overcome this effect, the overlap coefficient *r* can be divided into two separate coefficients k_R and k_G, used to express the degree of colocalisation relative to each channel. Unlike the PCC, k_R and k_G are both affected by the signal intensity of the channels. Therefore, two further coefficients can be defined that are independent of intensity (Equation. 8) (Manders et al,1993).

$$M_R = \frac{\Sigma_i ChR_{i\ coloc}}{\Sigma_i ChR_i}$$

Where $R_{i\ coloc} = R_i$ if $G_i>0$ and $R_{i\ coloc} = 0$ if $G_i=0$

$$M_G = \frac{\Sigma_i ChG_{i\ coloc}}{\Sigma_i ChG_i}$$

and $G_{i\ coloc} = G_i$ if $R_i>0$ and $G_{i\ coloc} = 0$ if $R_i = 0$.

Following these algorithms, the signal intensity of each voxel within the channel is summed where it colocalises with a voxel of the other channel with a value greater than threshold. This is then divided by the total fluorescence value within that channel. Through this method the coefficients of both channels' relative colocalisation can be determined even when the signal intensities differ greatly (Manders et al,1993).

As with the PCC, MOC values are heavily influenced by background values, therefore Costes threshold estimation is a valuable preprocessing step. Unlike the PCC, the Manders coefficient is far less affected by non-colocalising pixels providing a greater understanding of the interaction between the two image components. The MOC results in Figure 9b [I] show a clear difference in signal overlap between the two channels; the original Manders results show values taken before thresholding, i.e. across all voxels, while the thresholded coefficients display the values after threshold estimation. The original Manders A confocal

data shows the extent of colocalisation of the GFP-NS5A signal within the area of the 594nm NS3 stain, with values close to 1 showing almost complete colocalisation with the NS3 signal. Comparing this with the confocal image used to derive these values in Figure 8b [A] shows the cause of such values. The GFP-NS5A signal displays a higher S/N-R with fewer punctate sites than the colocalising NS3 component. The high colocalisation values of the original Manders A coefficient are in contrast to the decreased values of original Manders B, measuring the colocalisation of NS3 against that of GFP-NS5A. In this instance, the colocalisation coefficient is decreased due to decreased specificity of the NS3 stain, leading to higher background values.

The original Manders values produced by the Imaris software are limited in their usage, since without a preprocessing threshold step, any voxel with a value greater than 0 in both channels will be regarded as colocalised. Therefore, large regions of background volume will be regarded as positively correlated voxels of interest. Consequently, attention was focused on the thresholded MOC values generated. Compared to the original values, there is a significant decrease in colocalisation values, after application of thresholding especially so with the OMX values (Figure 9b [I]). This is to be expected, as the MOC values are affected (albeit to a lesser extent) by the same spatial errors that influence the PCC. The low values generated from the OMX data are, taken on their own, inconclusive or suggestive of random colocalisation between the channels. However, from a subjective viewpoint of the imaging data, this is obviously not the case.

3.11.5. Validation of Coefficient Values

Given the divergent correlation values between the CLSM and OMX system further investigation was carried out into the effects of correlation analysis using a negative control. Therefore colocalisation analysis was carried out on the same images with the green (GFP-NS5A) component inverted. The same preprocessing and threshold estimation steps were applied prior to generation of colocalisation values as shown in Figure 8b [I]. The PCC values from these images show an almost complete lack of colocalisation from both the CLSM and OMX data. When viewing the initial image PCC values in light of the negative control data (Figure 9b [E and F]) , colocalisation is perhaps more specific than previous considered, especially for the OMX-derived data.

Negative control values of the original Manders A&B coefficients provide an interesting insight into the influence of background intensities on correlation values (Figure 9b [I]) Both A&B coefficients for the randomised CLSM image show complete or extremely high

colocalisation between the two channels despite the inversion. This is again caused by the lack of threshold estimation resulting in colocalisation of all voxels >0 in value. Therefore, drawing any conclusions from such values would be erroneous. The higher colocalisation values of the original CLSM Manders values compared to OMX are an effect of the higher background noise levels within the CLSM system. The OMX images have a higher ratio of background voxels with a true 0 value resulting in lower colocalisation values than those produced by the higher CLSM background values.

Thresholded Manders A and B values of the randomised images present a more realistic view of colocalisation between the channels. Values trending towards 0 for both channels and imaging modes strongly suggest random colocalisation between the two signals, as would be expected from such manipulated images. When comparing the relative change between inverted and colocalised images however, the OMX values appear to have less significance above that of the negative control compared to CLSM images.

3.11.6. Analysis of Colocalisation Results

From these results, it seems apparent that the CLSM system provides a more accurate measure of colocalisation between the images. Discounting the unthresholded original Manders values, the CLSM system consistently generated higher values within the colocalisation images combined with lower negative control values for both thresholded PCC and MOC values. In comparison, values generated from the OMX images were less definitive. Comparing both imaging systems based burely on colocalisation it seems clear that CLSM offers a more robust platform for the production of valid statistical data.

Such results seem at odds with the distinct improvements in resolution and signal to noise ratio provided by the OMX system over that of CLSM. It stands to reason that the system which would increase spatial resolution and yield a higher signal to noise ratio would also provide the most accurate measure of colocalisation between two proteins. Indeed when combined with the analysis of the replication complex with dsRNA genomic intermediates as seen in Figure 7 the increased resolution of the OMX system offers a hitherto unseen level of accuracy in both structure and interaction between the two components. There appear to be a number of factors that act in a synergistic manner to reduce the quantitative colocalisation values while still providing high quality, subjectively accurate images. The first is the nature of the sites of interest themselves. Current literature examining the replication sites of other positive-strand RNA viruses postulate a size of 200-400nm (den Boon et al,2010), which is supported by the results obtained here. Replication site

quantification by microscopy and based on consistent structural features suggest only small numbers of actively replicating complexes within each cell. Given the small number of such sites relative to the high ratio of background voxels within the image, any calibration or optical errors will have a far greater effect on the statistical values than if those same errors were applied to larger subcellular structures such as mitochondria, endosomes etc. Therefore the nature of the structure being analysed serves to exacerbate any errors within the system.

Differences in image capture methods may also contribute to errors in estimating the extent of colocalisation. The independent optical paths of the OMX system were developed to provide the highest resolution possible for each individual channel. However such design requires significant post-capture processing to accurately realign each channel with the next. In this study, channel alignment was a significant source of error. Such axial error influenced colocalisation when analysed via a 2-D histogram (Figure 9a [C-D]). However, as previously noted, limitations within the software environment prevent accurate realignment of the image components beyond the +/- 1 voxel channel shift. From an entirely subjective viewpoint, there appears to be alignment and correction errors within the xy plane in the form of uncorrected spherical lens aberration. Such problems were encountered at early stages in the study; assuming the centre of the image to be the origin of the axis (0,0) spatial errors between the channels was found to occur as a non-linear function of the distance from this point. Therefore differences in spatial colocalisation were significantly increased at the edge of an image compared to the origin. While this error was corrected through an API softWorX software update, a small but significant spatial error affecting the imaging system may remain within the data. Given the complexity and various steps of image reconstruction within the OMX, confirming the existence of such error was outside the scope of this study. However comparison and calibration of the channels using multi-colour fluorescent beads across the entire field of view may give some indication of any errors affecting the system.

One other possible source of error may result from the difference in diffraction and PSF size as a result of the different emission wavelengths of the two fluorophore components. The longer emission wavelengths of the red 594nm channel will give a larger 3-D PSF than the shorter wavelength green 488nm channel. Even if perfect overlap and alignment is assumed, the larger red PSF will generate a differential in colocalisation coefficients which would be evident as a decrease in value of the thresholded Manders Red value and PCC.

There is currently a dearth of research within the area of quantitative analysis using super-resolution microscopy; therefore comparison with other independent datasets was unavailable. However, from the results presented here it was clear that the resolution benefits afforded by such new techniques may not necessarily translate to increased accuracy in quantitative methodologies. Super-resolution microscopy and the API OMX system in particular is in its infancy as well understood and defined imaging systems. The utilisation of a super-resolution microscopy platform undergoing continued development, while at the cutting edge of imaging is far more susceptible to unforeseen errors than the well understood and defined commercial CLSM systems. It may be that with future updates, channel alignment errors may be more effectively corrected for as the limits of the systems are better understood. Correction of non-linear channel alignment errors is a perfect example of such a problem. It may be that a systematic review of currently utilised correlation coefficients is required viewed in the light of increasing resolution beyond the physical barriers for which they were conceived. Both the PCC and MOC were developed at a time when the diffraction limit was expected to be an absolute limit to microscopy.

3.12. Interaction of Replication Sites with the ER membrane

Having evaluated and defined the relative distribution and colocalisation of individual viral NS proteins, the interaction of predicted replication sites with the host ER membrane was investigated. As described earlier, viral RNA synthesis is thought to occur at replication foci found on morphologically altered ER membrane surfaces (Gosert et al,2003;Moradpour et al,2004). These membrane alterations are induced by the viral NS proteins, specifically NS4B, to form complex multi-component structures termed the membranous web (Moradpour et al,2007). Previous analysis of these replication sites revealed resistance to protease and nuclease treatment and a partial sensitivity to detergent. This suggested that the foci may exist as invaginations within the ER membrane (Quinkert et al,2005).

3.12.1. Utilisation of ER markers

To investigate the juxtaposition of components of viral replication sites with host membranes, two markers for the ER, reticulon-4a (Rtn4a) and Sec61β were evaluated for OMX imaging. Rtn4a was tagged with a Myc epitope (Rtn4a-Myc) while Sec61β was fused to GFP (Sec61β-GFP). Rtn4a is one of a number of the reticulon family of proteins, that are targeted to the peripheral ER where they aid membrane curvature allowing the formation of tubular structures (Hu et al,2008). Despite the flexibility in staining afforded

by Myc-tagged Rtn4a, difficulty in achieving effective staining with the protocols required for viral proteins prevented further use within the project, this may be the result of epitope shielding by the ER membrane, kept largely intact by the soft permeabilisation techniques utilised. Greater success was found with Sec61β-GFP, which did not require any antibody for detection and therefore was compatible with the antibodies used to detect the viral components. The heteromeric Sec61 complex forms the core of the mammalian translocon, comprised of three subunits, alpha, beta and gamma. Oligomerisation of these subunits results in formation of a closed pore complex through which proteins are transported and integrated into the ER membrane (Greenfield et al,1999). As such the various subunits are distributed throughout both the nuclear envelope and the peripheral reticular system (Voeltz et al,2006).

Initial experiments revealed that transfection of the Sec61β-GFP plasmid into Huh-7 and Huh-7/SGR-JFH1 cells gave high fluorescence; some time-dependent cell toxicity beyond 16 hours was noted, most likely due to overexpression of the tagged protein. Following time course analysis of up to 24 hours of combined Sec61β-GFP and viral protein expression a fixation protocol was developed to enable both efficient detection of the ER marker and viral RCs without any observable differences in cell morphology or RC distribution and quantity as seen in Figure 11 [A].

Optimisation of staining protocols was carried out initially by CLSM. This also enabled further comparison between diffraction and sub-diffraction imaging systems. OMX imaging and processing of transfected samples was carried out using the protocol as set out in Section 2.2.5. Structural and colocalisation analysis was performed using Bitplane Imaris software.

3.12.2. Interaction of the ER membrane and HCV dsRNA

For the following analysis, Huh-7/SGR-JFH1 cells were stained with the J2 antibody, to identify viral dsRNA at replication sites. In terms of juxtaposition with the ER membrane, it was assumed that the viral dsRNA could localise with Sec61β-GFP in two possible manners, either as an embedded and colocalised signal within the membrane which would support the notion of viral replication sites existing as invaginations within the membrane. Alternatively, any relative distribution that indicated viral dsRNA existed as an independent signal, in close association but excluded from the GFP-tagged protein could suggest protrusion of the viral replication sites from the membrane. Based on the evidence above which describes difficulties with establishing colocalisation between signals by

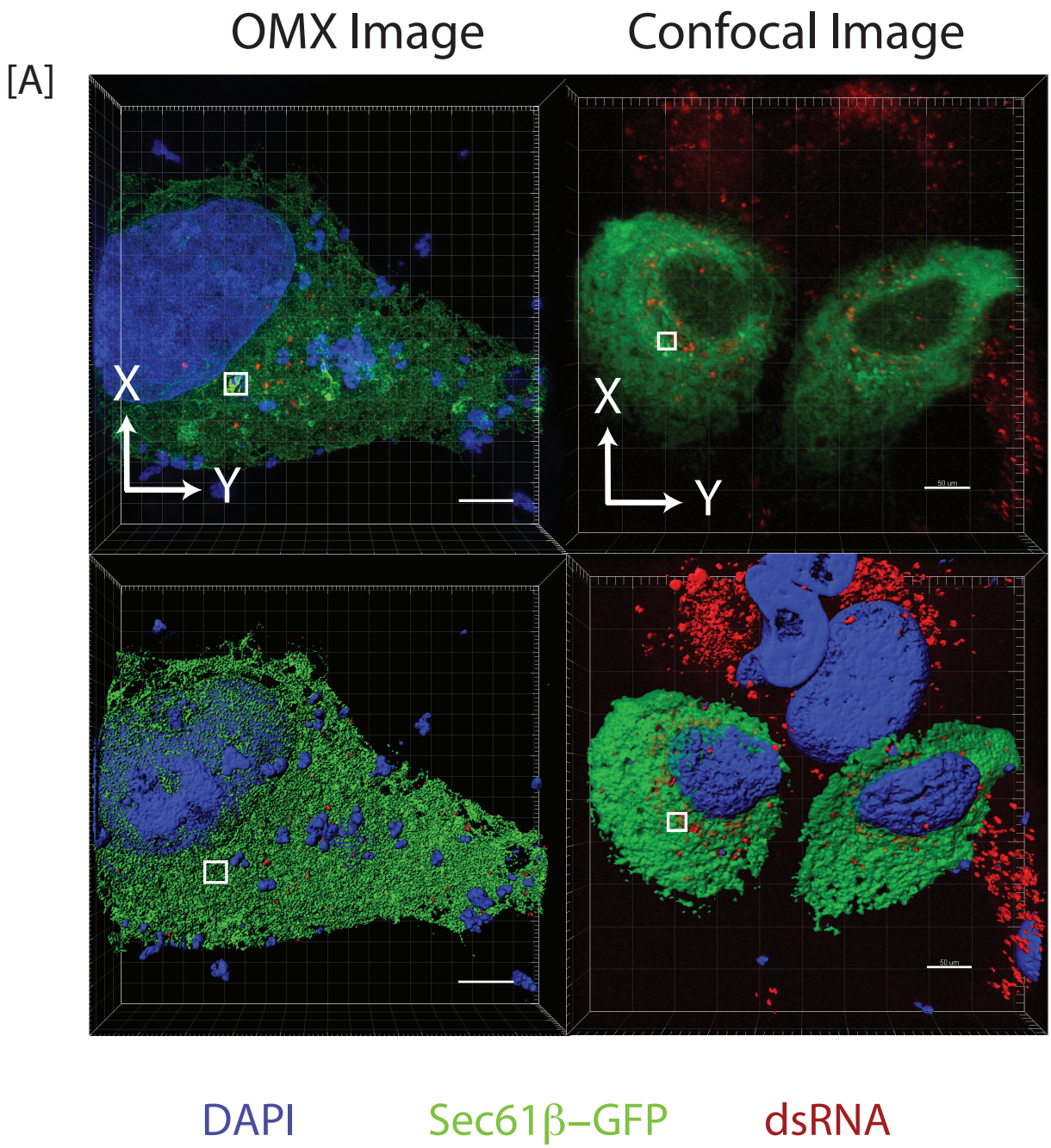

Figure 11a. Visualisation and surface rendering of dsRNA localised to ER membrane by both confocal and super resolution microscopy.

Huh-7/SGR-JFH1 cells transfected with Sec61b$_{GFP}$ were fixed and stained for dsRNA using J2 antibody. Images were then captured by either confocal microscopy or OMX super resolution microscopy. Surface rendering was carried out using Imaris. Region highlighted in white [A] Scale bar represents 10μm.

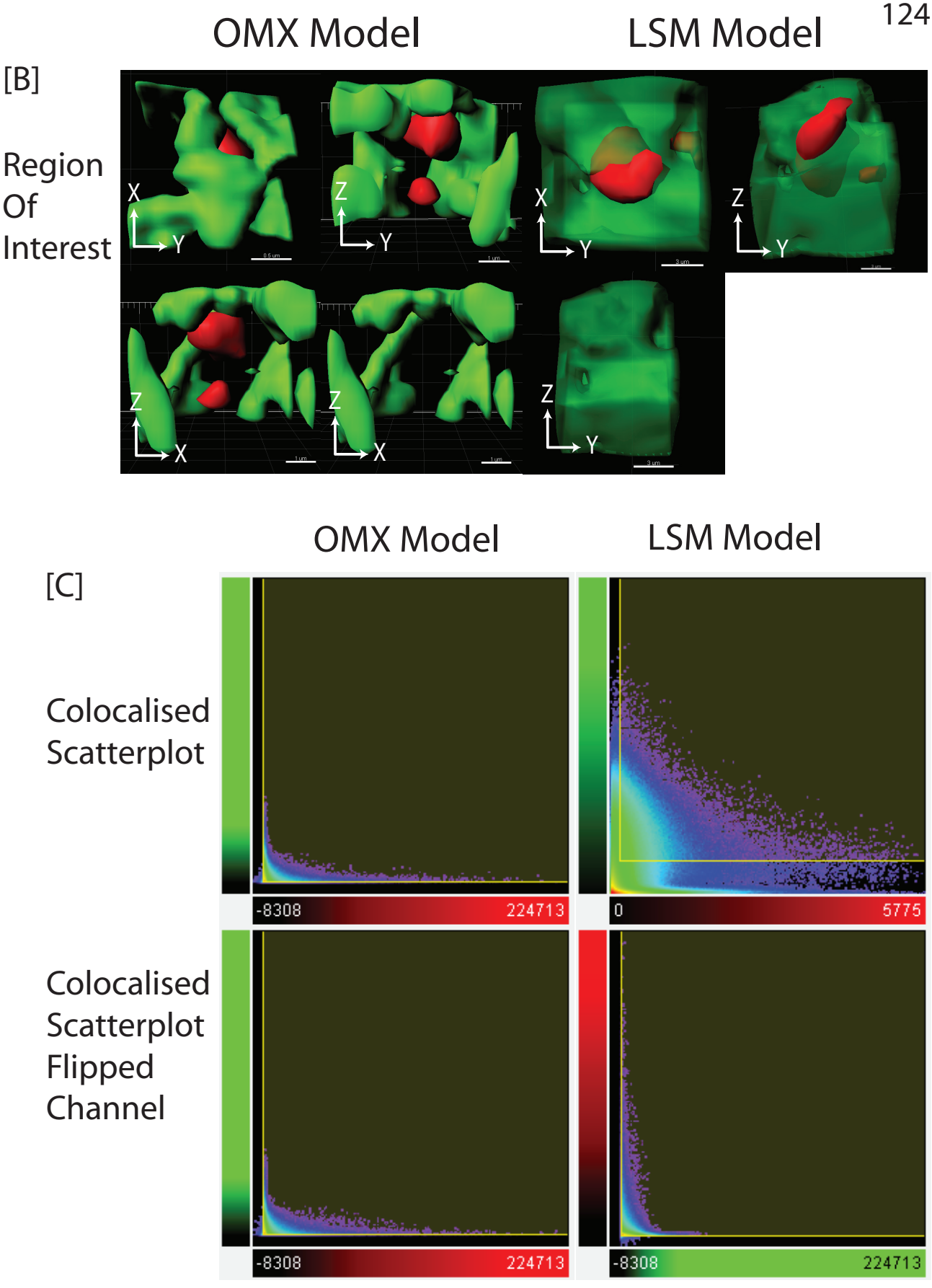

Figure 11b. Visualisation of ROI highlighting differences in imaging resolution on surface rendering and Colocalisation Scatterplots

Region Of Interest (ROI) identified in Figure 10a [A]. Panel [B] shows the effects of increasing resolution within the ROI. Colocalisation scatterplots [C] were carried out using Imaris MeasurementPro.

OMX imaging, analysis for the relative distribution of ER proteins and viral components at replication sites employed scatterplot analysis and image modelling for interpreting the data.

Figure 11a [A] presents a typical cell image following transfection of the Sec61β-GFP construct into Huh-7/SGR-JFH1 cells. Cells were fixed and stained with the J2 antibody using standard protocols. Firstly, channel misalignment within the OMX datasets was corrected by Imaris software using a two voxel shift on the z-axis, identified and confirmed visually before being applied across the entire dataset. Both OMX and CLSM images show the complexity and extensive distribution of the reticular ER network within the cells (shown in green). Sites of genome replication are indicated by red punctate sites detected by antibody J2. Of note is the extranuclear DAPI staining, seen in Figure 11a [A] as blue speckles surrounding the cell. This is likely to be liposomes carrying Sec61β-GFP DNA as such a pattern was found only in cells exposed to the transfection reagents combined with DNA (data not shown) thereby excluding the possibility of mycoplasma infection, a common cause of such staining. The structural complexity of such images prevents an effective qualitative understanding of the relative distributions of the host ER membranes and viral dsRNA from the original image data. However application of surface rendering techniques to the dataset gives a clearer view of their interactions within cells.

Differences in spatial resolution are also evident following the surface rendering applied to the cells shown in Figure 11a [A]. Reticular structures are more obvious from the OMX dataset compared to the amorphous and ill-defined ER generated from the CLSM dataset. There are difficulties in observing any meaningful interactions within such a model, thereby limiting any insight into the location and relationship between viral replication sites and host membranes. Further analysis was carried out on Regions Of Interest (ROI) containing punctate dsRNA signals indicative of active viral RNA replication.

The ROIs from OMX and CLSM data give a clearer indication of the differences in resolving power and target localisation between the two systems (Figure 11b [B]). The CLSM image shows the punctate dsRNA signal partially embedded within the ER, supporting invagination of replication sites into the membrane. By contrast, the OMX data reveals the dsRNA as a separate and distinct signal sitting distal to the membrane surface. The reticular structure of the ER apparently surrounds the immediate area of the replication focus, suggestive of the alternative hypothesis in which replication sites protrude into the cytosol. While previous CLSM data has shown the dsRNA signal to protrude from the ER membrane, the limited resolution afforded by such a technique is equivocal as to the true

relationship between the viral components and membrane surface. Through the use of super-resolution techniques, it becomes possible to resolve the fine structural detail of the tubular ER and identify the juxtaposition of the two targets.

The results of colocalisation analysis show the effect of increased resolution on the associated 2-D scatterplot (Figure 11b [C]). In the OMX scatterplot, there is clear exclusion of the two image components with any colocalisation arising close to the origin and therefore attributable to background intensities. The lack of colocalisation is further demonstrated by comparison to the flipped channel random image scatterplot, which yields an identical distribution of voxels. By contrast, the CLSM scatterplot reveals lower levels of exclusion between the two image components, than the corresponding OMX data and greater colocalisation distal from the origin, suggestive of low level colocalisation. Thus, there appears to be greater colocalisation with the CLSM system, ostensibly a result of the lower resolution achieved with this approach.

3.12.3. Imaging of ER and Viral RC components

Having observed differences in the colocalisation of dsRNA with the ER by OMX compared to CLSM data, the relationship between other components of the viral RC and the ER membrane was investigated. To this end, labelling with other components of the RC along with the ER membrane was explored. Antibodies against several targets (NS3, NS4B and NS5A) were tested for their compatibility of staining with Sec61β-GFP. Although conditions for detecting both NS3 and NS5A had already been optimised, the opportunity to localise NS4B, another of the NS proteins required for replication, was examined since antibodies specific to the protein were available (Gretton et al,2005). The ability to expand analysis to NS4B was of particular interest in relation to the barrel-like structures identified in the previous section since this viral protein can induce distinct membrane alterations independent of other viral proteins (Egger et al,2002). A number of NS4B specific antibodies (R1061, R1063 and R1152) have been raised for immunofluorescence or Western blot analysis of the subgenomic replicon. Previous attempts to utilise these antibodies under a limited set of conditions for detecting NS4B by immunofluorescence in Huh-7/SGR-JFH1 cells had been unsuccessful (Gretton,2006). Therefore, a more extensive series of parameters, including a variety of fixation, permeabilisation and antigen retrieval methodologies commonly used in the field of immunohistochemistry to unmask fixative crosslinked epitopes were attempted to develop a protocol capable of detecting NS4B in Huh-7/SGR-JFH1 cells. Soft permeabilisation and

staining of live cells with the glycoside digitonin was attempted since epitope blocking can arise through use of fixatives such as PFA and GLA. Antigen retrieval of fixed samples was also tried utilising a heated sodium citrate antigen retrieval buffer. However, neither method proved effective in providing an acceptable fluorescent signal with any of the NS4B antibodies for confident examination of the protein by either CLSM or OMX (data not shown).

Having failed to optimise conditions for NS4B detection, protein targets were limited therefore to NS3 and NS5A for colocalisation studies with Sec61β-GFP. Since detection of fluorescent signals was limited to 3 channels with the OMX, the DAPI nuclear stain was replaced with an Alexafluor 405nm secondary antibody for detecting the NS3 antibody, while the NS5A antibody was identified with an Alexafluor 594nm secondary antibody. Initial experiments with this combination of fluorophores gave significant deterioration of the 405nm signal, especially when exposed to the high laser intensity needed for OMX image capture even in the presence of free radical scavenging mounting media such as ProLong Gold (Invitrogen). Comparison of the decay in signal for a number of blue fluorophores following exposure to a suitable excitation laser revealed a significant difference in bleaching between fluorophores of the same wavelength. Indeed, Alexafluor 405 gave poor photobleaching resistance (data not shown). Hence, AlexaFluor 405 was replaced with the fluorophore Atto 425, which gave greater resistance to photobleaching (data not shown) (M. Posch, personal communication). Although the excitation laser wavelength was not optimal and the fluorophore gave a lower quantum yield compared to AlexaFluor 405nm, the increased photobleaching resistance of Atto 425 yielded an overall improvement in image quality.

Samples were reanalysed by OMX using this more optimal set of imaging conditions and processed as described earlier, including corrections for channel alignment. Results are shown in Figure 12 [A], where the punctate nature of the NS proteins is visible within the reticular ER signal.

Despite difficulty in interpreting the blue NS3 signal on the black background of the original dataset, the image components were surface rendered to generate a 3-D model upon a grey background (Figure 12 [B]). This provided greater contrast and a somewhat clearer view of the NS3 signal, showing it's predominantly perinuclear distribution. Increasing the transparency of the ER signal also gave an improved impression of the localisation between the two viral proteins within the complex signal given by

[A]

NS3
Sec61βGFP
NS5A

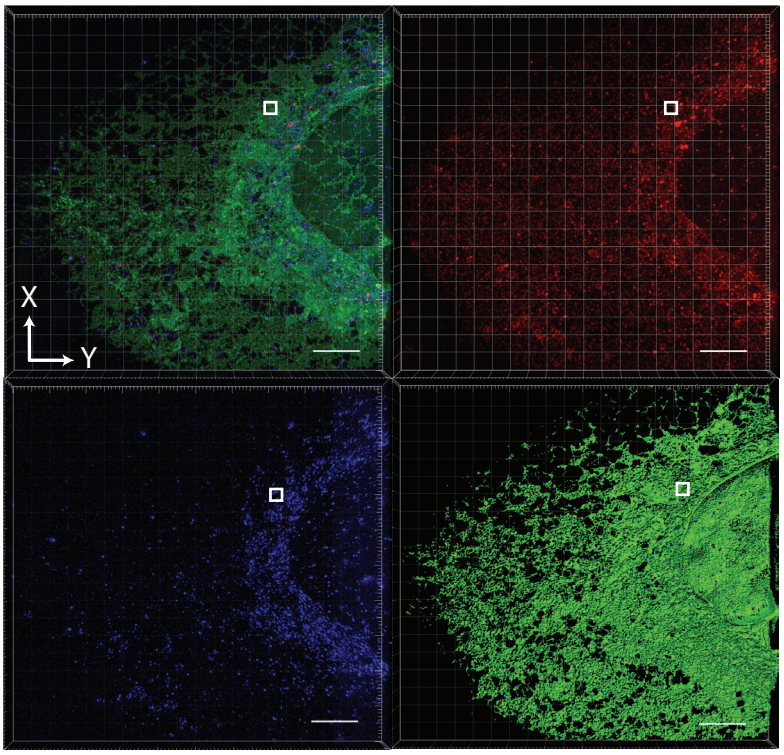

[B]

Imaris
Model

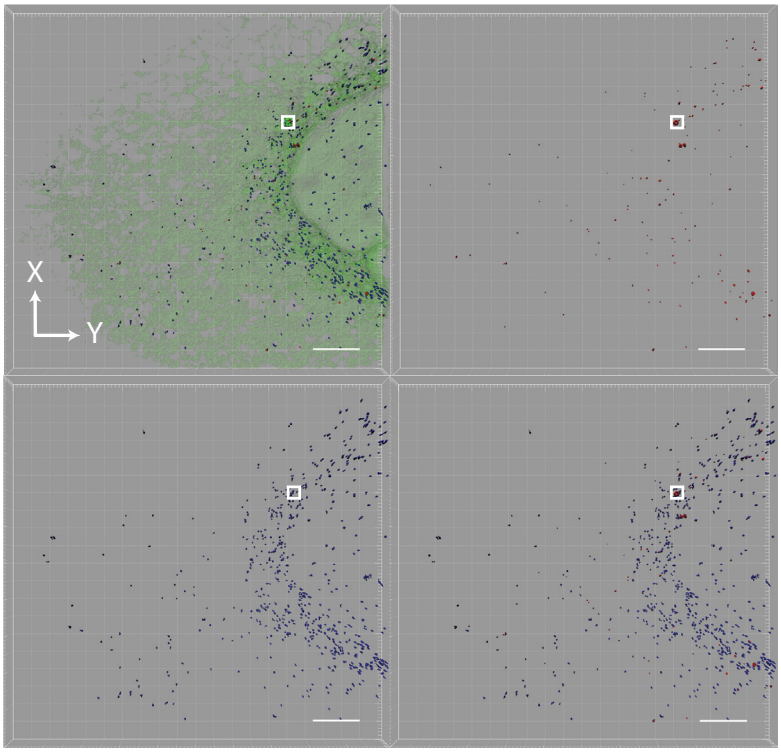

Figure 12a. Visualisation of NS5A, NS3 localised to ER in cells actively replicating HCV RNA

Huh-7/SGR-JFH1 cells were transfected with Sec61β_{GFP}. Cells were fixed and stained for NS3 using NS3 antisera and NS5A using NS5A antisera. Three channel images were captured by OMX and used to generate a surface rendered model of the membrane and viral structure shown in panel [A]. Model clarity was increased through utilisation of a grey background [B]. ROI marked in white [A] and [B] . Colocalisation analysis was carried out using Imaris [D]. Scale bar represents 10μm.

[C]

Region
Of
Interest

NS3
Sec61βGFP
NS5A

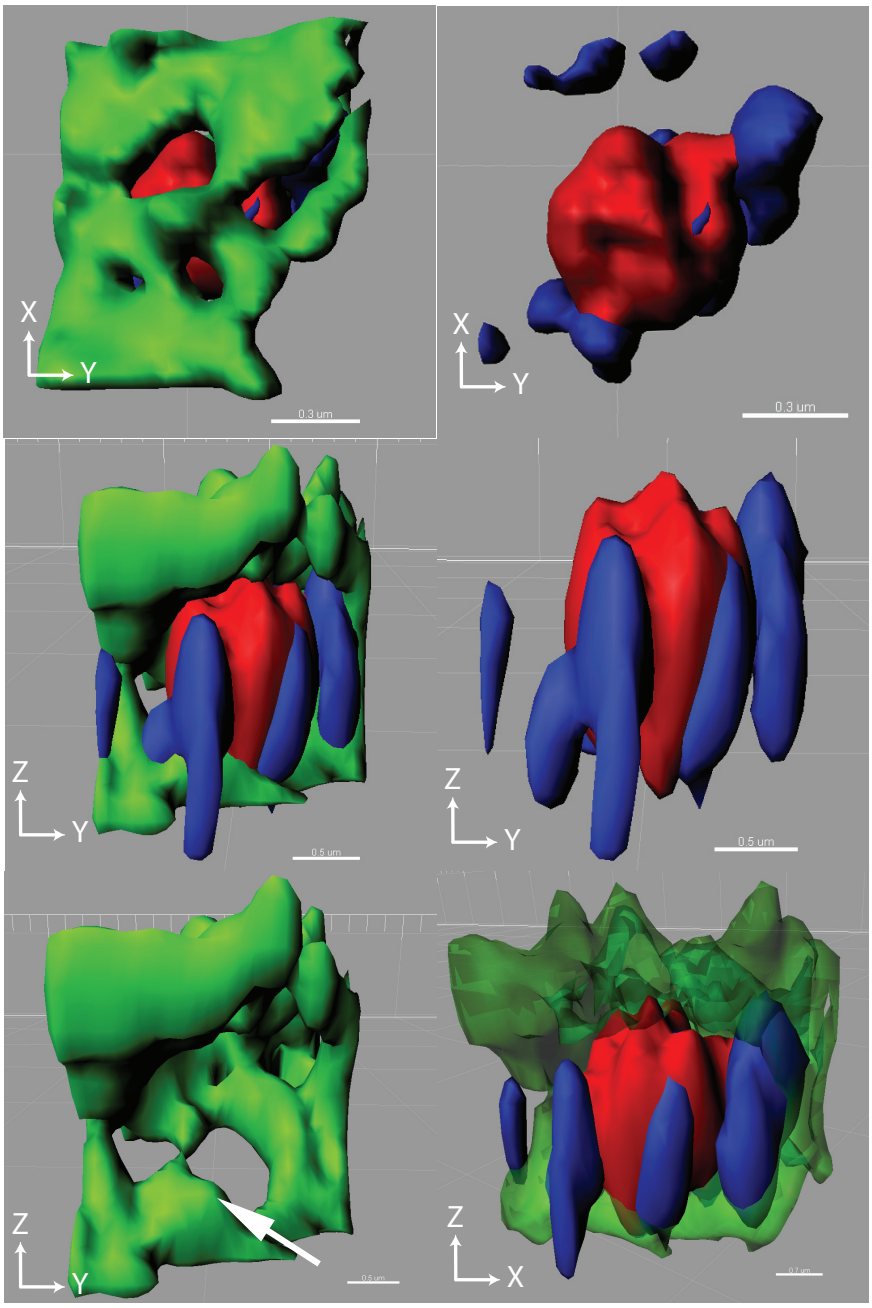

[D]

Channel
Colocalisation

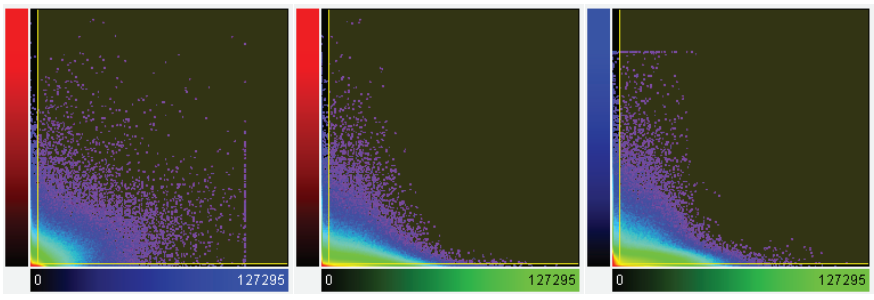

Figure 12b. Visualisation of ROI showing connecting membrane structures to the viral replication complex, identified by NS5A, NS3 in cells actively replicating HCV RNA

ROI identified in Figure 11a. is shown in various orientations showing the interaction and location of the viral replication complex relative to host peripheral ER. "Neck like connection" identified by white arrow. Colocalisation analysis of image components was carried out using Imaris [D].

Sec61β-GFP. From this image, a ROI, which contained a putative replication site of similar size and structure to those identified earlier, was selected for further analysis (Figure 12 [C]).

The selected ROI contained a replication site with an approximate internal diameter of 300nm. Although modelling of the structure did not reveal an entirely hollow structure, the region showed a central depression, indicative of the decreased intensity that would be expected from a similar, albeit less well-resolved hollow structure. The lower quality of the blue Atto 425 signal, representative of the NS3 protein, resulted in a reduced signal to noise ratio than would be expected for other fluorophores (e.g. those excited at 488nm and 594nm), which are more fade resistant. The result of this photobleaching was a colocalised NS3/NS5A signal (Figure 12 [B]) but with diminished structural detail within the NS3 (Atto425) signal.

Assuming that the NS3 and NS5A signals represent a single replication site, it is possible to consider their distribution compared to Sec61β-GFP. Viewed from a number of angles, the viral RC apparently existed within the cytosolic space between the various tubular structures of the ER identified by Sec61β-GFP. From these data, it was concluded that components of the ER were excluded from the replication site. This interpretation is supported by scatterplots (Figure 12 [D]), which suggest some limited overlap in the NS3 and NS5A signals but much less for scatterplots that compare colocalisation between either of the viral proteins and the Sec61β-GFP ER marker. Nevertheless, the modelled RC shown in Figure 12 [C] does suggest close juxtaposition with the ER, with a narrow elongated prominence from the membrane (indicated by white arrow) connecting the replication focus to the reticular network.

3.13. Discussion

All positive-strand RNA viruses replicate within distinct membranous compartments induced during infection which are formed from remodelling of host intracellular membranes (Miller et al,2008). Orchestration of viral RNA replication in these “replication factories” offers a number of benefits including, i) localised concentrations of viral components, ii) physical scaffolding and organisation of the RNA replication complex and, iii) evasion of the host immune response to the dsRNA replication intermediates which could otherwise be recognised by innate immune sensors such as RIG-I or MDA5 (Saito et al,2008).

The existing paradigm of HCV replication centres around the oft described “membranous web”, a complex of tightly associated double- and single-membrane vesicles and vacuoles surrounded by the ER membrane(Merz et al,2013). Similar structures have previously been described in the liver of a HCV-infected chimpanzee (Pfeifer et al,1980). However, the large multicomponent multi-membrane replication complexes described within such animal studies are found in the later stages of infection, most likely the result of cellular stress responses, in a manner similar to the autophagic response (Ferraris et al,2010).

From these findings and the modelling of related Flaviviridae replication sites, it is assumed that the “membranous web” formed by HCV consists of ER membrane invaginations encapsulating the replication complex (Welsch et al,2009). Prior to the initiation of this study, little was known about the 3-D architecture of the membranous web. Here, we have taken advantage of the increased spatial resolution provided by SIM to investigate and model the structure of proposed sites of replication.

Due to the relatively novel nature of the OMX system this study initially set out to compare and define similarities and differences with the CLSM system. Validation of published imaging data was utilised as a baseline from which to compare the improvements in image quality and optimise sample preparation techniques. Such comparisons showed no significant difference in image quality, cellular distribution or size of fluorescent signal except for the improved resolution expected of the OMX system. Analyses of the respective workflow methodologies highlighted issues with image fidelity during transfer between software packages, resulting in a scaling error between axes. This was identified as an error in image metadata reading and corrected prior to final image analysis and modelling.

Having confirmed the fidelity of data generated using the OMX, this approach was utilised to reanalyse the structure and localisation of the various components of viral replication complexes. Utilising the $NS5A_{GFP}$ construct and the α-dsRNA antibody J2, the relationship between a viral replicase protein and HCV dsRNA genomic intermediates necessary for replication were examined at higher resolution than previously possible by light microscopy. By employing the 3-D modelling capabilities of the Imaris software, the relationship of the two image components could be examined as an interaction between two solid objects, as shown in Figure 7. These data showed that the dsRNA genomic intermediates existed within a “barrel-like” structure formed by NS5A. Previous imaging investigations into HCV replication have noted the close relationship between HCV dsRNA and NS5A, however the limited resolution of such systems could merely suggest

colocalisation between the two viral components. With increased resolution, it was possible to discern that the two components exhibited close association and indeed an intimate relationship, however they were not colocalised in the manner that had previously been reported (Targett-Adams et al,2008). This interaction was visible not just as a single replication site but as a multi-nucleated complex with multiple dsRNA copies existing within the hollow interior of the replication site(s). It is perhaps worth noting the largely perinuclear localisation of the fully-formed replication sites; while there was staining throughout the cytoplasm, those sites exhibiting structure and dsRNA association were found relatively close to the nucleus, in support of previous studies (Targett-Adams et al,2008). The structure and interaction between the components supports previous interpretations of the replication complexes of the related flaviviruses, dengue and West Nile virus. In these cases, it has been shown that viral RNA is most likely replicated within membrane invaginations originating from the endoplasmic reticulum membrane (Welsch et al,2009;Gillespie et al,2010). The barrel structure and internally localised dsRNA could feasibly be the invaginated replication complex seen in other flaviviridae, with one or other ends of the structure opening into the cytosol for RNA release.

It was noted that colocalisation appeared to occur only with the small number of NS5A structures of ~300nm diameter within the cell, alongside a larger population of non-colocalised unstructured sub-300nm diameter objects. The colocalisation of HCV dsRNA with a population of structures with a discrete size was not unexpected, since the energetic requirements of membrane curvature will likely contribute to the optimum dimensions needed to sustain replication (Zimmerberg et al,2006). Previous investigations into replication site size have suggested values of between 80-150nm per vesicle, compared to the 70-400nm range of the picornaviridae (Miller et al,2008). The results of this study suggest that replication of the HCV genome likely occurs within vesicles of approximately 300nm in diameter as defined by the highest resolution OMX data. These results are based on measurements between adjacent maximum intensity points at predicted replication sites and therefore do not provide a truly accurate measurement of site size; the minimum OMX resolution is 120nm on the optical plane, suggesting that the site size can be assumed to be more likely between 120-300nm.

Having elucidated the physical size and structure of the HCV replication site and its similarity to other flaviviridae replication sites, the study then sought to investigate the relationship between the viral components and host ER membranes. Beforehand, we sought to utilise and validate previously described quantitative methods to investigate the

relationship between the various viral and host components of interest in an unbiased manner. To this end, a comparison of the two principle colocalisation methodologies utilised in image and pattern analysis, the PCC and the MOC, were performed.

It was immediately apparent that there were issues regarding channel alignment within the OMX system, resulting in displacement of the data from the 488nm and 594nm channels along the optical axis. This misalignment could be adjusted through a 2-voxel channel shift correction within the Imaris software package. It was noted though that this shift did not entirely correct the misalignment since a sub-voxel correction was unavailable. The effects of this correction were shown in the model in Figure 8a and 2-D scatterplots which presented pre-correction and corrected colocalisation data.

Contrary to predictions, comparison of the CLSM and OMX data showed that the higher resolution data gave lower PCC and MOC colocalisation coefficients. This result seems counterintuitive to the general assumption that a higher resolution system would produce a colocalisation coefficient greater than that afforded by the lower resolution. Given the relative novelty of SIM techniques, very little published data exists relating to its use with quantitative colocalisation techniques. In-depth analysis of the equations utilised in producing these values highlighted the effects of increasing resolution on degradation of coefficient fidelity and accuracy. Channel alignment errors, as previously discussed, caused by the different optical trains of the OMX system, also were exacerbated by the relatively small size of the punctate sites being investigated. Cumulatively, this generated a lower colocalisation coefficient for the OMX data as compared to the CLSM data.

Nonetheless, correlation was still higher than that of randomly-generated signals. Overall, further work is required to explore such limitations of super-resolution techniques with regards to quantitative analysis. Until such a time as more data is available on the subject, or a systematic study focused solely on colocalisation utilising OMX is carried out, all colocalisation values should be viewed critically and perhaps more weight given to the data provided by CLSM.

This aspect of the project also highlighted the need to analyse data generated from the various coefficients in a holistic and critical manner and not as a sole indicator of colocalisation. Utilising any one of the values generated during the analysis it was possible to derive, i) complete colocalisation of both channels, ii) entirely random localisation or iii) any number of intermediates through selective analysis of the data. Only through careful

analysis and understanding of the limits to each value can a true picture of interdependency and interaction be generated.

Having investigated and defined some of the limitations of the OMX system for quantitative analysis, the study continued with the examination of the relationship between the host ER membrane and the viral replication complex. Following current literature on ER membrane involvement in HCV replication, our study initially focused on this organelle surface (Moradpour et al,2007;Egger et al,2002). To this end, a GFP-tagged construct of the peripheral ER transmembrane transport protein Sec61β was utilised as a fluorescent marker to locate the membrane.

To investigate this interaction, the study initially examined the relationship between the ER membrane and dsRNA genomic intermediates. Based on the two possible relationships to the organelle, the dsRNA signal would be visible either embedded within the ER itself as suggested by the related flavivirus replication complex, or as a distinct and independent signal distal to the membrane surface.

Figure 11 compares the data generated by both OMX and CLSM systems. The most striking aspect is the very obvious difference in resolution between the two imaging methods. While CLSM data only provides a generalised outline of the ER network, the OMX data allows a far more detailed and intricate model of the convoluted network of tubules that comprise the ER. The two levels of resolution also display different interactions between HCV dsRNA and the ER. Examination of the CLSM model suggests that the dsRNA is heavily embedded within the ER membrane, in a manner suggestive of the flavivirus replication complex. Increasing the transparency of the model combined with examination of the colocalisation scatterplot in Figure 11b [C] would suggest that there is a strong colocalisation and embedding of the replication site within the ER membrane.

Examining the interactions with the higher resolution OMX model revealed a different picture to that provided by CLSM. Here, HCV dsRNA resides in a position distal to the membrane surface, surrounded by the tubular ER network with a gap of approximately 100nm between the two signals. This qualitative data is supported by 2-D scatterplots (Figure 11b [C]) in which the two signals show almost complete exclusion from each other. When compared to the randomly generated colocalisation scatterplot, there was no observable difference suggestive of little specific interaction between the viral and host components.

Having established an exclusionary relationship between the ER membrane surface and HCV dsRNA by OMX imaging, the study then investigated the relationship between HCV replicase proteins and the ER surface. Figure 12 [A] and [B] show the colocalised signal of HCV NS3 and NS5A within the ER structure marked by Sec61β. Examining a region of interest containing a structurally-defined RC in detail (Figure 12 [C]) shows the interaction between the replication site and ER membrane mirrors that of the dsRNA/ER interaction.

In Figure 12 [C] the replication complex resides within the cytosolic space between the network of ER tubules, outside of the membrane surface as suggested from the dsRNA localisation. There does appear to be some interaction between the viral proteins and host membrane in the form of "neck-like" protrusions connecting to the replication complex, similar to those described by Merz *et al* (Merz et al,2013). Based on reconstruction of the OMX data, it would appear that the membrane is displaced around the replication complex, leading to the formation of holes and gaps within the ER that are filled by the viral components.

By examining the 2-D scatterplots (Figure 12 [D]), there is a low level of colocalisation between the two viral components, whereas the colocalisation between the viral proteins and the host membrane is significantly lower. There may be some low level interaction between the proteins of the replication complex and the ER surface, with the two moieties connected by the narrow "neck like" protrusions discussed earlier. Colocalisation between the viral proteins is higher, presumably due to the multicomponent nature of the replication site and the need for close cooperation and interaction between the replicase proteins (Gosert et al,2003). The protruding, evidently non-invaginated nature of such a site supports the Bartenschlager hypothesis that viral replication occurs in protuberances from the ER membrane itself, connected by a narrow "neck" of host membrane (Merz et al,2013).

The alteration of host membranes is induced by both the viral proteins, NS4B and NS5A, forming Single Membrane Vesicles (SMV) and Double Membrane Vesicles (DMV)s respectively suggesting that formation of a successful replication complex requires the actions of several HCV replicase proteins (Egger et al,2002;Ferraris et al,2010;Merz et al,2013). Late stage infection results in the formation of multi-membrane formations, possibly the result of a stress-induced reaction. In this respect, the mechanism of HCV infection closely resembles the membrane rearrangements seen in the distantly related picornaviridae and coronaviridae (Gosert et al,2002).

Combining all of the data from this chapter, it is possible to propose a model of the viral replication sites. Formation of the viral replication site occurs on the ER membrane surface. As has been shown previously, expression of the NS4B and NS5A proteins, induce morphological changes at this membrane, forming what has been termed the membranous web (Egger et al,2002). Unlike the other closely related flaviviruses such as dengue and West Nile Virus, the evidence in this study suggests that the HCV replication complex does not replicate within membrane invaginations but instead from membrane protrusions in a manner more reminiscent of other positive-strand RNA viruses such as the prototype member, poliovirus (Welsch et al,2009). The maturation of these membrane exvaginations, results in the formation of hollow single- and multi-nucleated barrel structures, attached to the membrane and organelle through neck-like structures from which they were formed. It is expected that replication of the viral genome through the formation of dsRNA intermediates occurs within these hollow structures before packaging of positive strands of the genome into immature virions. The number of sites that actively participates in replication and assembly is unknown but is expected to be relatively low given the low yields of virus from infected cells. It is possible that the sites composed of barrel-like structures identified by OMX are more likely to contribute to active replication and virion assembly. Such analysis was beyond the scope of the project but could be tackled for example by examining the effect of direct-acting antivirals on the number and characteristics of the proposed replication sites with structural features. This type of study may also shed light on the anti-viral function of some agents such as daclatasvir, which targets NS5A through an unknown mechanism (Targett-Adams et al,2008;Targett-Adams et al,2011).

4. Requirement for Targeting of NS5A to Sites of HCV RNA Replication

4.1. Introduction

The pipeline described in Chapter 3 identified a systematic approach for image capture, post-image processing and unbiased mathematical analysis for evaluating colocalisation of fluorescent signals by CLSM and OMX. Further validation of the pipeline was pursued using CLSM, in light of the issues associated with applying statistical methods to OMX data. Therefore, the methods outlined in Chapter 3 were extended to a project examining the ability of HCV NS5A expressed either as an individual protein or as a component of a NS3-5A polyprotein to locate to sites of HCV RNA replication. This project formed part of a collaborative study with Dr Chris McCormick (University of Southampton).

The existing literature on the ability to complement non-functional HCV replicase components by co-expressing a wild-type, functional counterpart has demonstrated that NS5A is the only protein for which complementation is possible to any significant level (Appel et al,2005;Graziani et al,2004;Tong et al,2006;Jones et al,2009). However, these reports do not agree on whether NS5A requires expression as part of the HCV polyprotein to enable complementation. One hypothesis is that complementation requires efficient targeting and integration of functional NS5A with defective replication complexes in order to participate in restoring replication competence. It is possible that the context of NS5A expression, either as part of a polyprotein or as an individual polypeptide, plays an important role in targeting.

To examine whether the context of NS5A expression influenced targeting to replication sites, two subgenomic replicons, SGR/NS5A[V5]/NS3-5B[FLAG] and SGR/NS3-5A[V5]/NS3-5B[FLAG], were constructed (Figure 1 [A] and [B]). Both constructs expressed the NS3-5B polyprotein in the second cistron, which directs replication of the subgenomic replicon. In addition, NS5A in this polyprotein was tagged with a FLAG epitope. For SGR/NS5A[V5]/NS3-5B[FLAG], NS5A was expressed in the first cistron and was tagged with the V5 tag from the paramyxovirus, simian virus-5 (C McCormick, personal communication). In the case of SGR/NS3-5A[V5]/NS3-5B[FLAG], NS5A in the first cistron was generated by NS3/4A cleavage of a NS3-5A polyprotein precursor and was also tagged with the V5 epitope. Finally, upstream of NS5A and NS3-5A, the first cistron expresses the Renilla luciferase gene as a reporter for HCV RNA replication.

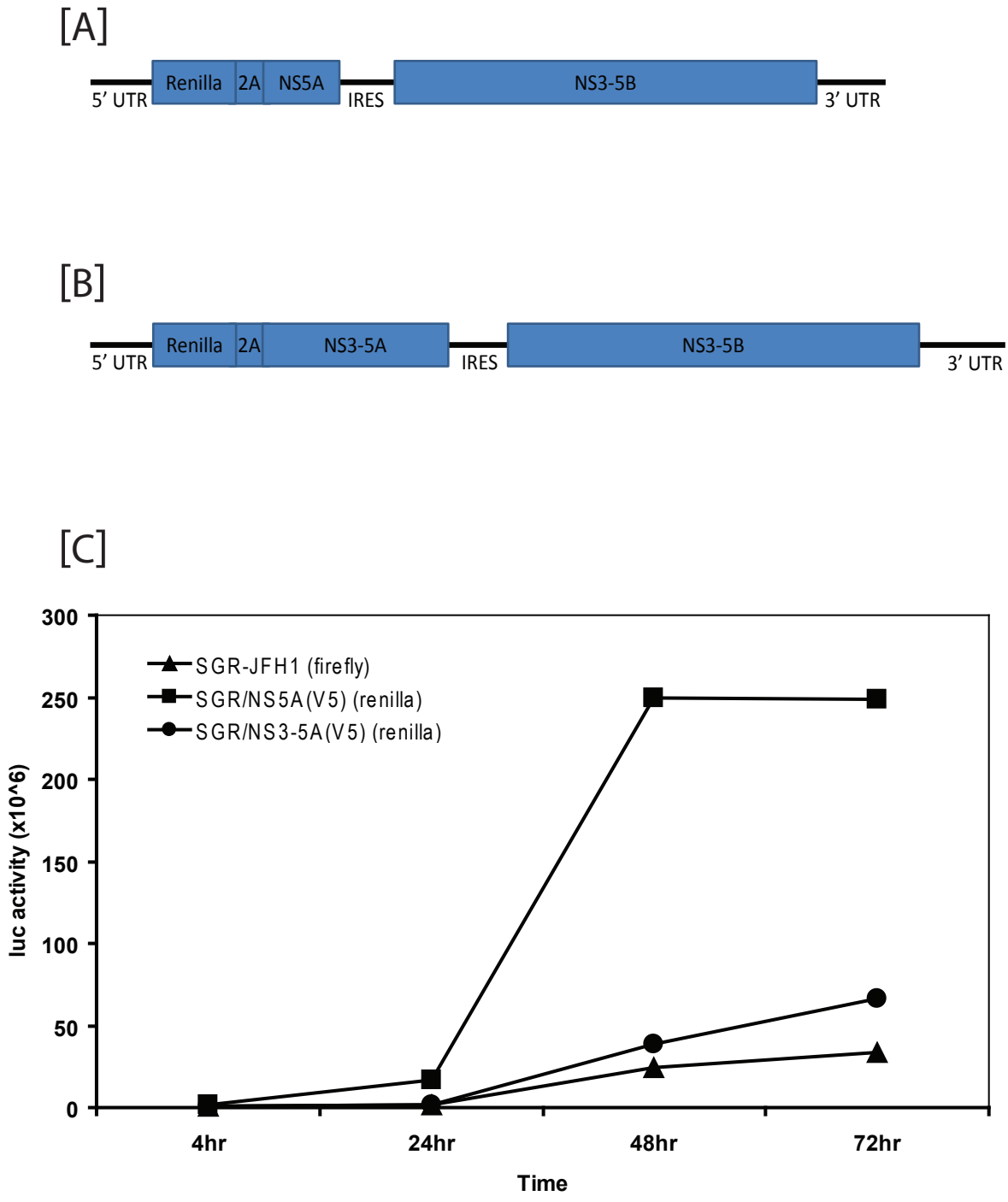

Figure 1. Subgenomic Replicon Structures used for analysis of NS5A localisation.
Construct SGR-NS5A[V5]/NS3-5B[FLAG] shown in panel [A] and SGR-NS3-5A[V5]/NS3-5B[FLAG] panel [B] were expressed in following electroporation into Huh-7 cells used to examine the effects of the Non Structural proteins on NS5A distribution. Replication efficiency was determined by luciferase assay [C].

Separating the luciferase and NS5A/NS3-5A sequences is a short FMDV 2A element, which directs intraribosomal cleavage at its C-terminus (de Felipe et al,2003).

4.2. Transient HCV RNA Replication by SGR/NS5A[V5]/NS3-5B[FLAG] and SGR/NS3-5A[V5]/NS3-5B[FLAG]

Huh-7 cells were electroporated with RNA transcribed *in vitro* from both constructs at 3µg per $1x10^6$, RNA quality was assessed by gel electrophoresis. Luciferase activity was measured at 4 hours post-electroporation and subsequently at 24, 48 and 72 hours. Results revealed that luciferase activities increased over time and were significantly higher than at the 4 hour time point (Figure 1 [C]). For comparison, cells were also electroporated with SGR-JFH1$_{NS5AGFP}$ RNA, which produces Firefly luciferase. Luciferase activity for this replicon was lower than that for SGR/NS5A[V5]/NS3-5B[FLAG] and SGR/NS3-5A[V5]/NS3-5B[FLAG]. However, this was due to the reduced activity typically seen for Firefly luciferase as compared to its Renilla equivalent. These data indicated that both replicons expressing the Renilla luciferase produced replicating HCV RNA although it was evident that the level of replication for SGR/NS3-5A[V5]/NS3-5B[FLAG] was somewhat less as compared to that for SGR/NS5A[V5]/NS3-5B[FLAG]. At 72 hours after electroporation, cells were fixed with methanol at -20oC and then probed with antibodies against the V5 and FLAG tags.

Analysis by CLSM showed that there were fewer cells expressing NS5A for SGR/NS3-5A[V5]/NS3-5B[FLAG] compared to SGR/NS5A[V5]/NS3-5B[FLAG], which explained the reduced levels of Renilla luciferase activity for this replicon. To determine the extent of colocalisation between the two forms of NS5A, Z-stacks were taken from a series of cells expressing the replicons (n=2 coverslips per sample). Stacks consisted of 30 slices with pixel and Z-step size determined for appropriate Nyquist-Shannon sampling rates as discussed in Chapter 3. Imaging was carried out on a Carl Zeiss LSM 710 Meta confocal microscope using settings to maintain signal intensity within the dynamic range of the microscope. The stacks were then deconvolved using the AutoQuant software in the manner described in Section 3.5.

4.3. Comparative Quantitative Analysis of NS5A Colocalisation

Deconvolved data was transferred to the Imaris software package for colocalisation analysis using the Coloc module and processed as described in Section 3.12 to produce the colocalisation dataset shown in Figure 2a and b. Visualisation of the SGR/NS3-

5A[V5]/NS3-5B[FLAG] dataset reveal approximately equal levels of expression of the 2 copies of NS5A from the SGR (Figure 2a, [A]-[C]) and colocalisation between the signals for the two proteins. By evaluating the colocalisation of the two NS5A species using the Coloc module, a fourth channel comprised of all colocalised voxels was generated and added to the dataset as shown in [D]. This derived channel is shown also in [E] in greyscale to illustrate the similar distributions of the V5- and FLAG-tagged NS5A moieties.

The 2-D histogram in [F] presents the comparison in intensity between red and green voxels and demonstrates the extent of colocalisation. The histogram reveals an almost perfect linear relationship between the two channels, with each voxel within the image having an equal fluorescent intensity in both channels, leading to the 45^{o} slope of the graph. The low levels of background signal can be seen in the restriction of voxels along the axis to a region near the origin. This extremely high level of linear correlation between the two channels was observed in all other SGR/NS3-5A[V5]/NS3-5B[FLAG] samples imaged (data not shown).

Visualisation of the SGR/NS5A[V5]/NS3-5B[FLAG] dataset in Figure 2b [A]-[C], again shows roughly equivalent expression of both tagged NS5A species. Merged channels (Figure 2b [A]) suggest reduced colocalisation, particularly in punctuate areas (identified by white arrows). Examination of the individual channels [B] and [C] further illustrates lesser colocalisation of the two proteins in punctae. This reduced colocalisation in foci is apparently a consequence of greater diffuse staining of V5-tagged NS5A compared to the FLAG-tagged species.

The 2-D histogram in Figure 2b [F] shows the extent of colocalisation is different for SGR/NS5A[V5]/NS3-5B[FLAG] as compared to SGR/NS3-5A[V5]/NS3-5B[FLAG]. In Figure 2a [F], voxels do display a linear relationship at low to medium intensity values but almost complete exclusion for the highest intensity voxels. The correlation between low to medium intensity voxels suggests that there is little background staining within the sample. Those voxels that do correlate close to the origin are most likely the low levels of fluorescence seen within the ER of the cell in both samples.

Of greater interest is the pattern for the highest intensity voxels (highlighted in the histogram). For the high intensity green voxels (circle 1) representing FLAG-tagged NS5A, it would appear that there is some colocalisation with the V5-tagged protein, albeit with low and medium intensity voxels in the red channel. This does not represent exclusion

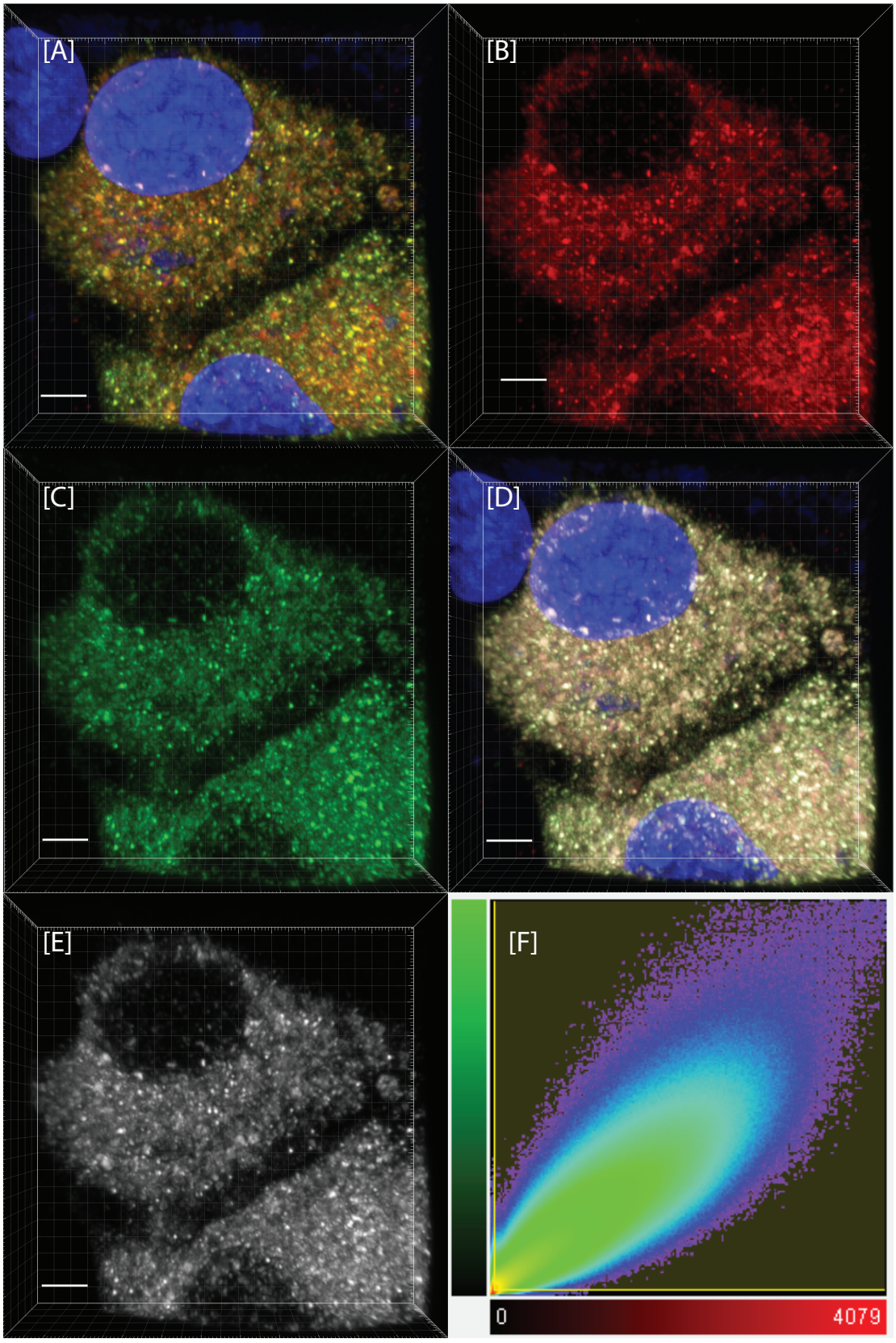

Figure 2a. Data processing validation SGR-NS3-5A[V5]/NS3-5B[FLAG] data and histogram

[A] Merged image of original data, [B] NS3-5A[V5] signal (594nm), [C] SGR-NS3-5B[FLAG] signal (488nm), [D] Merged image including generated colocalisation signal [E]. 2D Histogram generated using Imaris Coloc [F]. Scale Bar Represents 20mm.

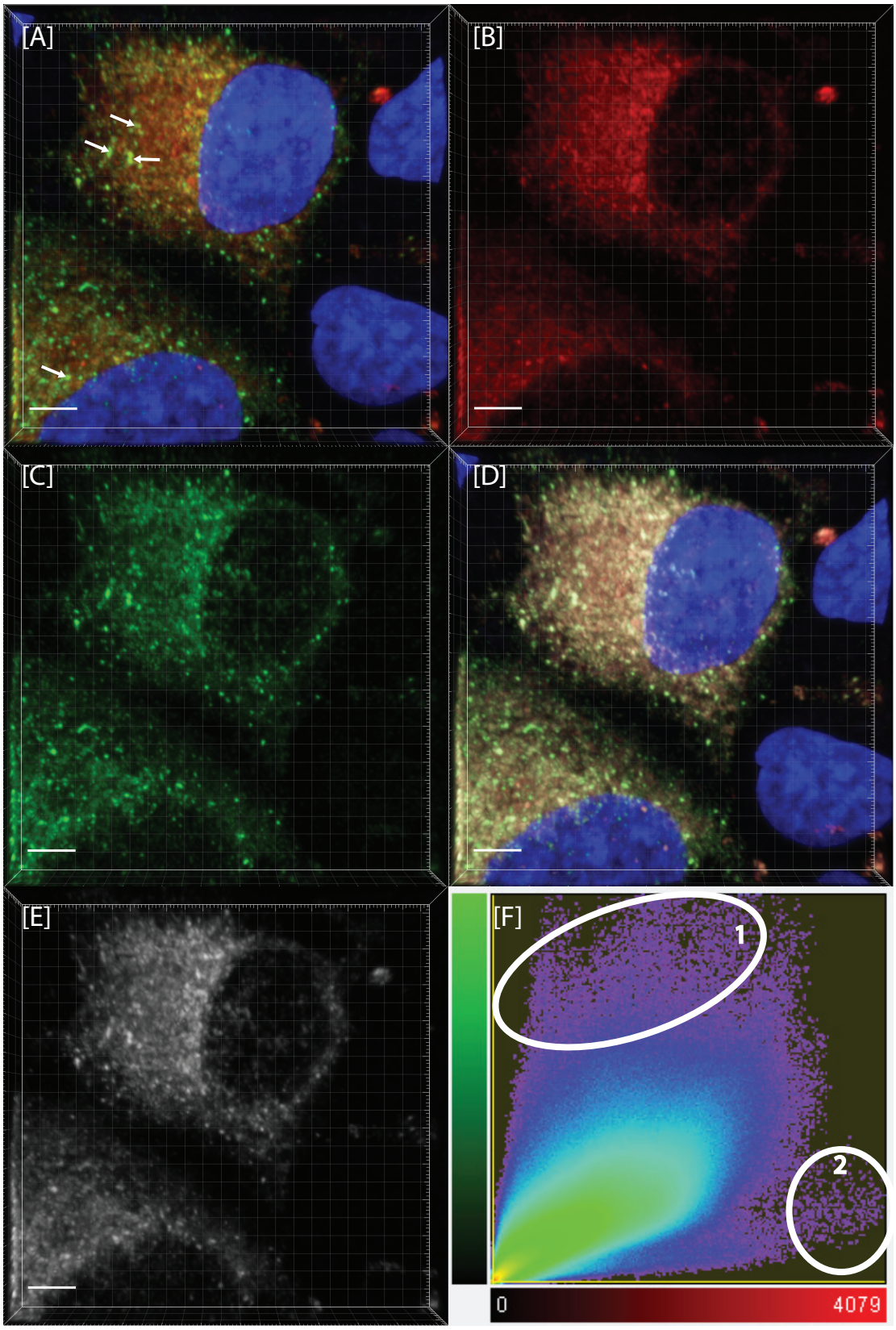

Figure 2b. Data processing validation SGR-NS5A[V5]/NS3-5B[FLAG] data and histogram

[A] Merged image of original data, [B] NS5A[V5] signal (594nm), [C] SGR-NS3-5B[FLAG] signal (488nm), [D] Merged image including generated colocalisation signal [E]. 2D Histogram generated using Imaris Coloc [F]. Scale Bar Represents 20mm.

[A]

	SGR/NS3-5A[V5]/NS3-5B[FLAG]			SGR/NS3-5A[V5]/NS3-5B[FLAG]		
Sample	PCC	MOC A	MOC B	PCC	MOC A	MOC B
1				0.8834	0.9565	0.9548
2	0.9459	0.9688	0.9737	0.8813	0.882	0.9439
3	0.9509	0.9383	0.8924	0.8908	0.9345	0.8809
4	0.8634	0.9454	0.9408	0.8952	0.9659	0.9794
5	0.9255	0.9713	0.9423	0.731	0.8939	0.7269
6	0.9368	0.9874	0.9896			
7	0.9327	0.9717	0.9853			
8	0.9594	0.9437	0.9258			
9	0.9433	0.9674	0.9772			
Average	0.9322375	0.96175	0.9533875	0.849575	0.919075	0.882775
StDev	0.02976133	0.01720789	0.0339565	0.07926253	0.03846577	0.1116142

[B]

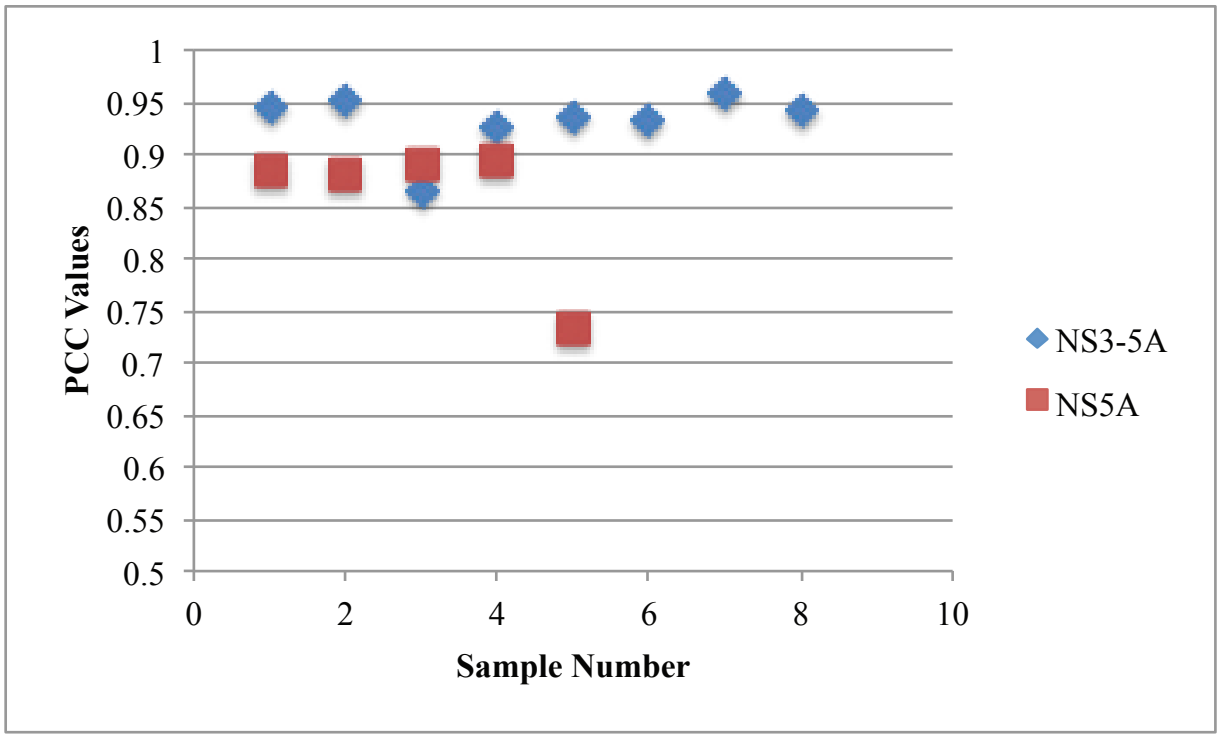

Figure 2c. Data processing validation of SGR-NS3-5A[V5]/NS3-5B[FLAG] Vs SGR-NS5A[V5]/NS3-5B[FLAG] colocalisation analysis

[A] Results of Pearsons Correlation Coefficient (PCC) and Manders Overlap Coefficient (MOC) generated using Imaris Coloc. PCC values were plotted showing the small but significant difference between the two cell populations examined [B].

as the highest intensity voxels in the green channel (FLAG-tagged NS5A) would lie closer to the y-axis. There is some evidence of exclusion of green voxels for the highest intensity red voxels (circle 2) which possibly arises from apparent non-specific staining in the upper right section of the image in Figure 2b [B]. Moreover, there are a lower number of high intensity voxels within the red channel, which may indicate reduced staining at punctate sites. Discounting the highest intensity voxels of the red V5-NS5A channel as non-specific staining, it was concluded that there was some colocalisation between the two channels, principally for the high-mid intensity FLAG-tagged NS5A with the medium intensity V5-tagged NS5A, resulting in upwards skewing of the graph.

Additional images were collected for each replicon and correlation coefficients for the datasets were calculated following Costes thresholding to derive significance of the data generated through the Imaris Coloc module (Figure 2c [A]). Examination of the MOC A_{Red} and B_{Green} coefficients for SGR/NS3-5A[V5]/NS3-5B[FLAG] show no significant differences between coefficients, and average values of 0.96 and 0.95 for A_{Red} and B_{Green} respectively indicating extremely high levels of colocalisation between the NS5A proteins made from this replicon. The PCC for this sample (0.93) mirrors the results of MOC A_{Red} and B_{Green}, thereby confirming and validating the near identical distribution of the two NS5A species. For SGR/NS5A[V5]/NS3-5B[FLAG], the average MOC A_{Red} and B_{Green} values are slightly different. The lower value of MOC B_{Green} (0.88) compared to MOC A_{Red} (0.91) suggests that although there is a high level of colocalisation between the two channels, there are also regions where V5-NS5A is excluded from FLAG-NS5A. A larger sample size is necessary to determine whether this difference is statistically significant, but the limited data available could suggest that the decrease in colocalisation results from exclusion of V5-NS5A from the replication complexes formed by FLAG-NS5A. The PCC value for SGR/NS5A[V5]/NS3-5B[FLAG] is lower (0.85) than that for SGR/NS3-5A[V5]/NS3-5B[FLAG]. Examination of the PCC values in the scatterplot in Figure 2c. [B] show that this decrease is a trend between the two NS5A sample populations evaluated.

4.4. Discussion

These results illustrate the value of a detailed analysis of the extent of colocalisation using the pipeline developed in the study. The near perfect colocalisation values for V5- and FLAG-NS5A expressed from SGR/NS3-5A[V5]/NS3-5B[FLAG] suggests that expressing two copies of the protein, both of which are produced in the context of a polyprotein, does

not lead to the formation of two distinct populations of foci. Two distinct populations might have been expected, and formed by the two polyproteins expressed by the replicon. Instead the perfect linear relationship in colocalisation indicates that the recruitment of NS proteins to foci is stoichiometrically equal for the two polyproteins expressed from the SGR/NS3-5A[V5]/NS3-5B[FLAG] replicon.

Compared to the results with SGR/NS5A[V5]/NS3-5B[FLAG], it is clear that expression of the NS3-NS4B proteins is required for targeting and integration of the NS5A protein into sites of viral replication. Examination of the distribution of V5-NS5A shows a similar diffuse, low intensity staining of the ER membrane matching that of FLAG-NS5A generated from NS3-5B[FLAG]. However, V5-NS5A is underrepresented at replication foci, indicating that expressing V5-NS5A alone does allow targeting of the protein to the ER membrane but not integration at replication sites. Thus, replication foci generated by SGR/NS5A[V5]/NS3-5B[FLAG] reside as complex "islands"produced by NS3-5B[FLAG] within an ER-bound "sea" of V5-NS5A protein. This model would explain the lower MOC_{Green} values seen in the sample set. In conclusion therefore, NS5A requires components from the NS3-4B polyprotein for targeting to replication sites.

While both NS3 and NS5A have been shown to be essential for the formation of viral RCs, the proteins themselves have no known direct interactions {Blight, 2000 110 /id}{Lam, 2005 513 /id}. There is evidence to suggest though that there is a direct action between NS3 and NS5A with tubulin and actin respectively mediating the movement of RCs within the cell, this interaction is most likely vital to the interaction of viral RCs with the lipid droplets necessary for effective viral replication {Lai, 2008 514 /id}.

The model system and data analysis pipeline presented provides a novel platform for further investigation into formation of the viral replication sites and targeting of the various HCV NS proteins. It would be interesting to explore the effects of the individual NS proteins on NS5A localisation. NS4B has been identified as playing a critical role in the formation and recruitment of viral proteins into replication complexes. Therefore, evaluating a NS4B-NS5A precursor in the replicon system described could be informative. Production of the individual NS4B and NS5A components from a NS4B-NS5A polyprotein would require the NS3/NS4A protease, which would be provided by the NS3-5B[FLAG] polyprotein in the second cistron. Combined with the detailed confocal analysis presented here, this would be a powerful approach to understand targeting of NS proteins to replication sites.

5. Development of Quantum Dot Technologies for Correlative Light and Electron Microscopy (CLEM)

5.1. Introduction

In the previous chapters, super-resolution imaging was deployed to investigate HCV replication sites and their relationship to the host ER membrane. The results achieved using this approach prompted an investigation into combining the specificity afforded by light microscopy with the ultrastructural detail of EM.

As discussed in the Chapter 3, all positive-strand RNA viruses induce distinct membrane alterations, which result from viral non-structural protein expression that provide the scaffold for RNA replication. Candidate viral replication complexes have previously been imaged utilising EM techniques, however there has been limited data to suggest specificity (Egger et al,2002). Recent studies have employed GFP-tagged HCV NS5A protein to identify and model the replication site utilising Electron Tomography (ET) {Romero-Brey, 2013 377 /id}.

In recent years, Correlative Light and Electron Microscopy (CLEM) has become increasingly attainable as a methodology for combining imaging modalities. Light and laser-based microscopy techniques provide rich detail on the subcellular localisation and interaction of specific proteins (Giepmans et al,2005). Despite the versatility and depth of information provided by light microscopy, there remains a significant limitation in the spatial resolution afforded even by super-resolution methods when analysing protein interactions (Schermelleh et al,2010). To investigate the supramolecular detail of the viral replication complex, Transmission Electron Microscopy (TEM) is the current methodology of choice, eschewing photons for the 100,000 times shorter wavelength of high energy electrons, to achieve spatial resolution of 50pm (Rolf et al,2009). It is clear that the advantages of light and electron microscopy are highly additive, however the methodological differences have long prevented an efficient use of single samples for imaging under both modalities.

A number of whole cell labelling methods can be applied for CLEM, either immuno-labelling or genetically coded tags to identify targets of interest. However, the permeabilisation by detergents that is required for immunolabelling often results in damage to the delicate ultrastructure of interest during delivery of reagents (Giepmans,2008). The discovery and development of GFP and its derivatives as imaging tags in the early 1990s

provided a number of novel genetically coded immunofluorescence probes compatible with EM methodologies without the need for destructive permeabilisation techniques (Giepmans et al,2006).

While both immuno- and genetic labelling of targets provide a suitable label for light microscopy, the organic nature of most fluorescent probes lacks the intrinsic electron dense nature required to scatter the electron beam rendering them visible by EM (Giepmans et al,2005). Therefore probes must be modified with an electron dense particle, either through sequential labelling with gold and fluorescent labelled antibodies, or silver enhancement of fluoronanogold (Takizawa et al,1998). These multistep methodologies can be unreliable and limited in compatibility for multiplexing of labels (Giepmans et al,2005). The ideal CLEM probe marries the fluorescence afforded by traditional organic fluorophores with an intrinsic electron dense structure (Giepmans,2008).

Recently, colloidal semiconductor nanocrystals, termed Quantum Dots (QDs) have emerged as prime candidates for CLEM probes. Quantum dots are single, uniform nanometre-sized crystals of cadmium selenide or related material coated in a passivating layer of zinc sulphide (Giepmans et al,2005). The high quantum yield (approaching 90%) and electron dense core make them ideal for visualisation through CLSM and TEM (Reiss et al,2002;Nisman et al,2004). The target specificity of the QD can be altered and defined through functionalisation of the surface with any number of biomolecules (Giepmans et al,2005).

In this part of the project, the potential for use of QDs as probes to detect viral RNA and protein was examined. Moreover, the study sought to expand on the structural detail achieved in Chapter 3 by combining QDs with CLEM techniques.

5.2. Investigation of Viral Genome Replication

Previous visual investigation into the nature of viral genomic replication was based solely on the existence of dsRNA, identified using the J2 antibody. This monoclonal antibody possesses sequence- and nucleotide-independent specificity to the helix formed by dsRNA Replicative Intermediates (RIs). Therefore any targets identified with this antibody are not virus specific and only indicative of this RI stage, not the individual positive and negative ssRNA strands.

Given the lack of any sequence specificity, initial development of QDs as CLEM probes focussed on targeting specific sequences in viral RNA. A short ssRNA probe with

sequence specificity to the 5' UTR of HCV strain JFH1 was chemically synthesised, and included a biotin linker molecule attached to the 3' end. This probe was designed to anneal to the positive strand of HCV RNA between nucleotides 315 to 333 in the 5' UTR region. Huh-7/SGR-JFH1 cells were grown overnight on sterilised coverslips and fixed with 4% PFA prior to permeabilisation with 0.25% Triton X-100. Cells were then incubated and blocked using Endogenous Biotin Blocking Kit (Invitrogen), to prevent non-specific binding of the biotin tag during probe incubation. RNA probe concentrations were titrated from 0.1µg RNA to 0.5µg diluted in Saline Sodium Citrate (SSC) and incubated overnight at 37^{o}C (Chaumeil et al,2008). Following RNA probe conjugation, secondary staining was carried out utilising 605nm ITK Streptavidin Quantum Dots diluted to 20nM in the supplied secondary incubation buffer for 1 hour at room temperature (Invitrogen,2007). The resulting probe structure is shown in Figure 1 [A].

Cells were imaged via CLSM and the results are shown in Figure 2[A]. Initial imaging appeared to identify punctate sites normally associated with detection of dsRNA in cells bearing the HCV JFH1 subgenomic replicon. However, examination of naïve Huh-7 cells, seen in Figure 2 [B] revealed a pattern and level of staining similar to that in Huh-7/SGR-JFH1 cells. This similarity in staining between samples suggested non-specific binding possibly as a result of insufficient blocking of endogenous biotin epitopes within the cell, most likely within mitochondria (Coone et al,2008).

A number of attempts were made to optimise the approach through various blocking steps and antibody/QD titrations. Despite further attempts at optimisation, it was not possible to develop a successful staining protocol using the combination of RNA and QD probes (Figure 3 [A] and [B]). Given that the number of copies of positive-sense viral RNA per cell varies between approximately 60-150 genomes (Leitch et al,2013), it was possible that the system would not achieve the sensitivity required without intensive development and hence this approach was not pursued further. Since viral proteins are produced in far greater excess compared to viral RNA, attention was directed at using QDs to detect viral protein.

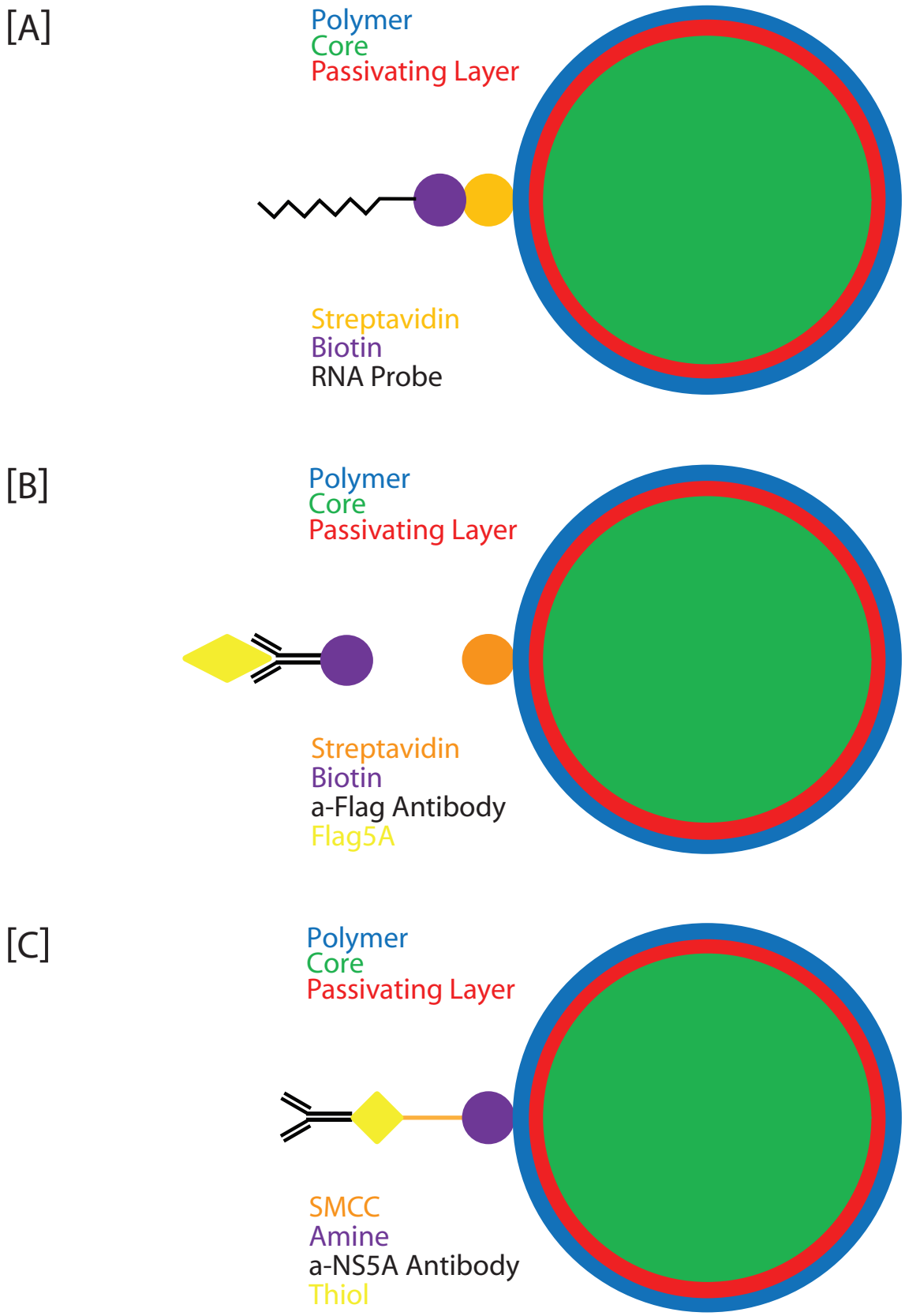

Figure 1. Quantum Dot Conjugation and Functionalisation Methodologies

Conjugation Methodologies utilised within the study. Invitrogen Qdot 605nm ITK Streptavidin conjugated to RNA probe [A] and secondary staining of biotin tagged α-FLAG antibody. Invitrogen Qdot 585nm direct conjugation to 9E10 antibody [C].

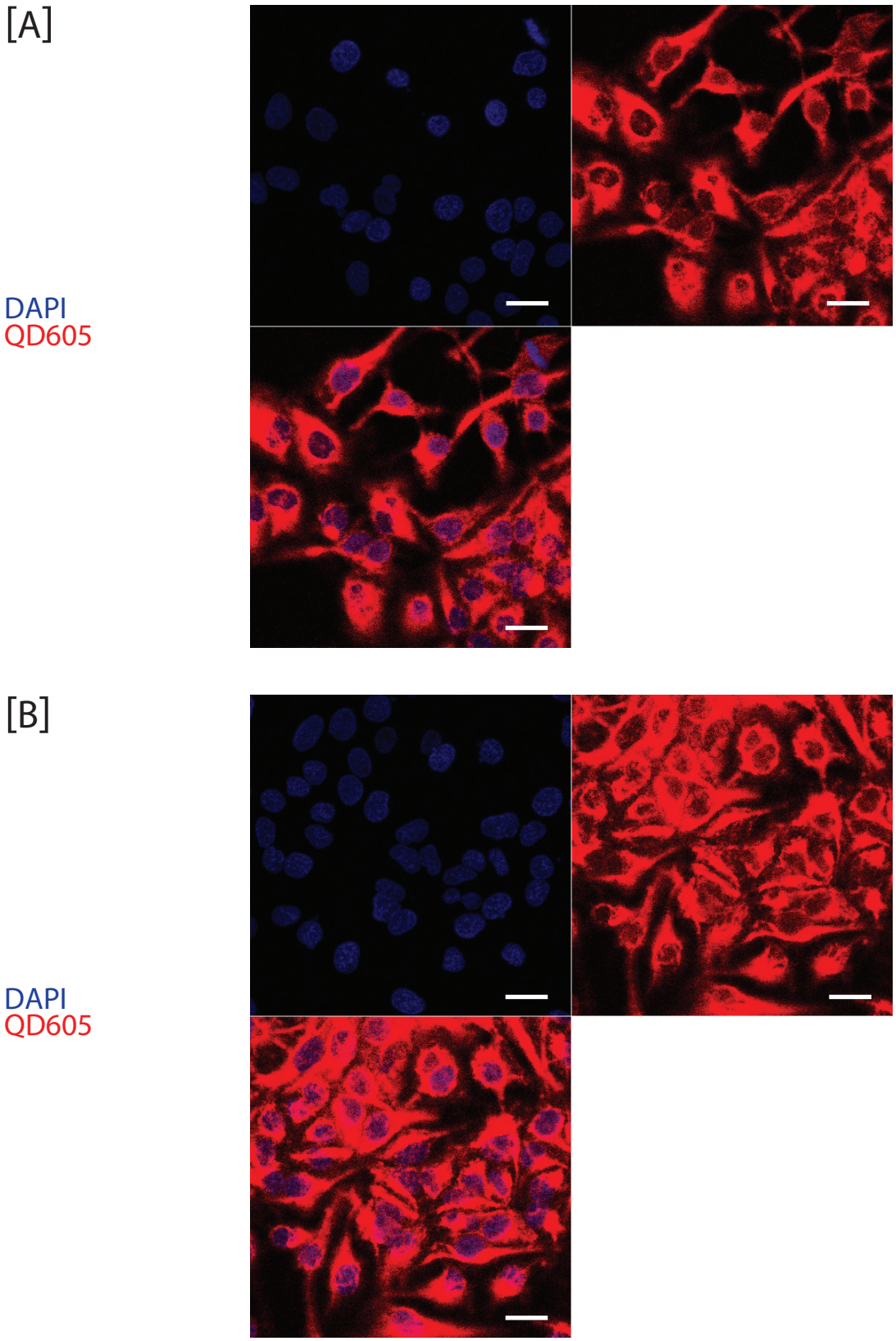

Figure 2. Visualisation of SGR-JFH1 genomic RNA utilising 5'UTR targeted RNA probe conjugated to 605nm quantum dots
Huh-7/SGR-JFH1 cells were fixed and stained for the 5' UTR region of the viral genome utilising 605nm quantum dots conjugated to specific RNA probe [A]. Huh-7 negative controls were fixed and stained using the same protocol [B]. Scale bars represent 20µm

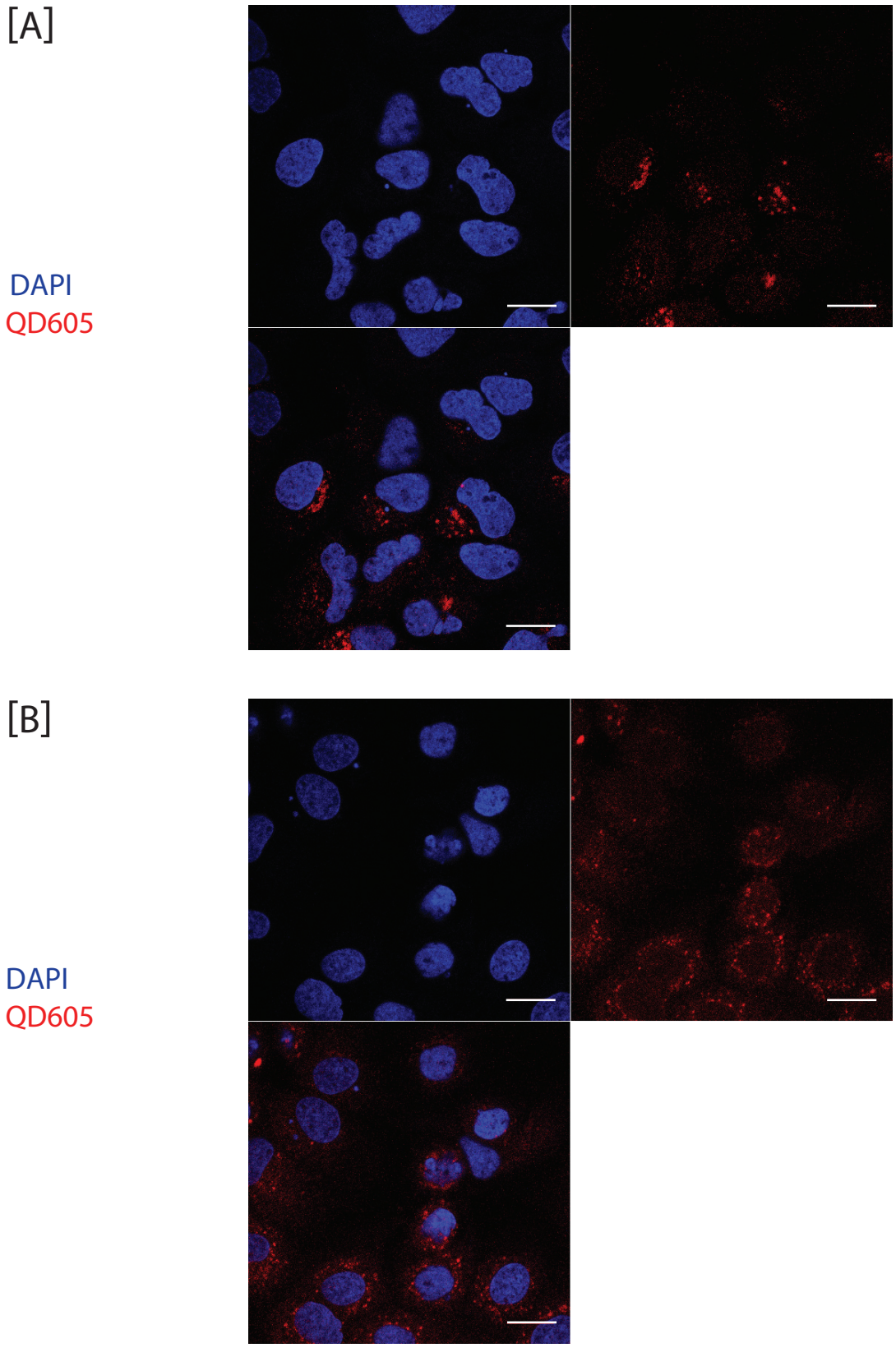

Figure 3. Visualisation of Huh-7 SGR genomic RNA utilising 5'UTR targeted RNA probe conjugated to 605nm quantum dots

Huh-7/SGR-JFH1 cells were fixed and stained for the 5' UTR region of the viral genome utilising 605nm quantum dots conjugated to a 5'UTR specific RNA probe [A]. Huh-7 negative controls were fixed and stained using the same protocol [B]. Scale bars represent 20μm

5.3. Quantum Dot Targeting Using FLAG-NS5A

To simplify the imaging protocol, the use of RNA sequence-specific probes was replaced with an antibody-based immunofluoresence approach to enable comparison of the QD technique with a traditional primary-secondary staining method. Therefore it was decided to target proteins at replication sites, specifically the NS5A protein studied in Chapter 3. Due to the lack of a biotin-tagged α-NS5A antibody, a novel SGR construct containing a FLAG tag within the NS5A protein (SGR-JFH1$_{NS5AFLAG}$, Materials and Methods 2.1.10, kindly provided by Chris McCormick and shown in Figure 4 [B]) was utilised; the FLAG tag in this construct was inserted at the same position as GFP in NS5A (Figure 4 [C]). This enabled utilisation of a commercially produced biotin-tagged α-FLAG antibody allowing detection of NS5A protein while providing a linker molecule for secondary conjugation to streptavidin-coated QD.

A cell line was constructed containing the SGR-JFH1$_{NS5AFLAG}$ replicon, encoding the neomycin resistance gene to allow selection of cells constitutively replicating subgenomic RNA. Naïve Huh-7 cells were electroporated with RNA transcribed *in vitro* using T7 RNA polymerase from the SGR-JFH1$_{NS5AFLAG}$ and selected for neomycin resistance. Through this process a stable Huh-7/SGR-JFH1$_{NS5AFLAG}$ cell line was produced, constitutively replicating viral RNA and FLAG-tagged NS5A.

Huh-7/SGR-JFH1$_{NS5AFLAG}$ cells were grown on coverslips, fixed and permeabilised with Triton X-100 as described above. Non specific binding sites were blocked using Endogenous Biotin Blocking Kit (Invitrogen) prior to application of primary α-FLAG antibody followed by incubation for 1 hour at room temperature. Samples were rinsed to remove unbound primary antibody followed by blocking of non-specific binding sites utilising Endogenous Biotin Blocking Kit ((Invitrogen). 605nm ITK Streptavidin Quantum Dots were added to cells at a concentration of 20nM diluted in secondary conjugation buffer and incubated for 1 hour at room temperature. As with standard immunofluorescence protocols, samples were rinsed with PBS and mounted using Invitrogen ProLong Gold antifade reagent. Samples were then imaged using the appropriate laser and filter combinations.

Initial results failed to detect any fluorescence within the samples stained with QDs (data not shown). Validation of NS5A detection was carried out using the α-FLAG antibody combined with a standard secondary AlexaFluor antibody. Utilising this traditional staining methodology, punctate foci indicative of FLAG-NS5A at replication sites were

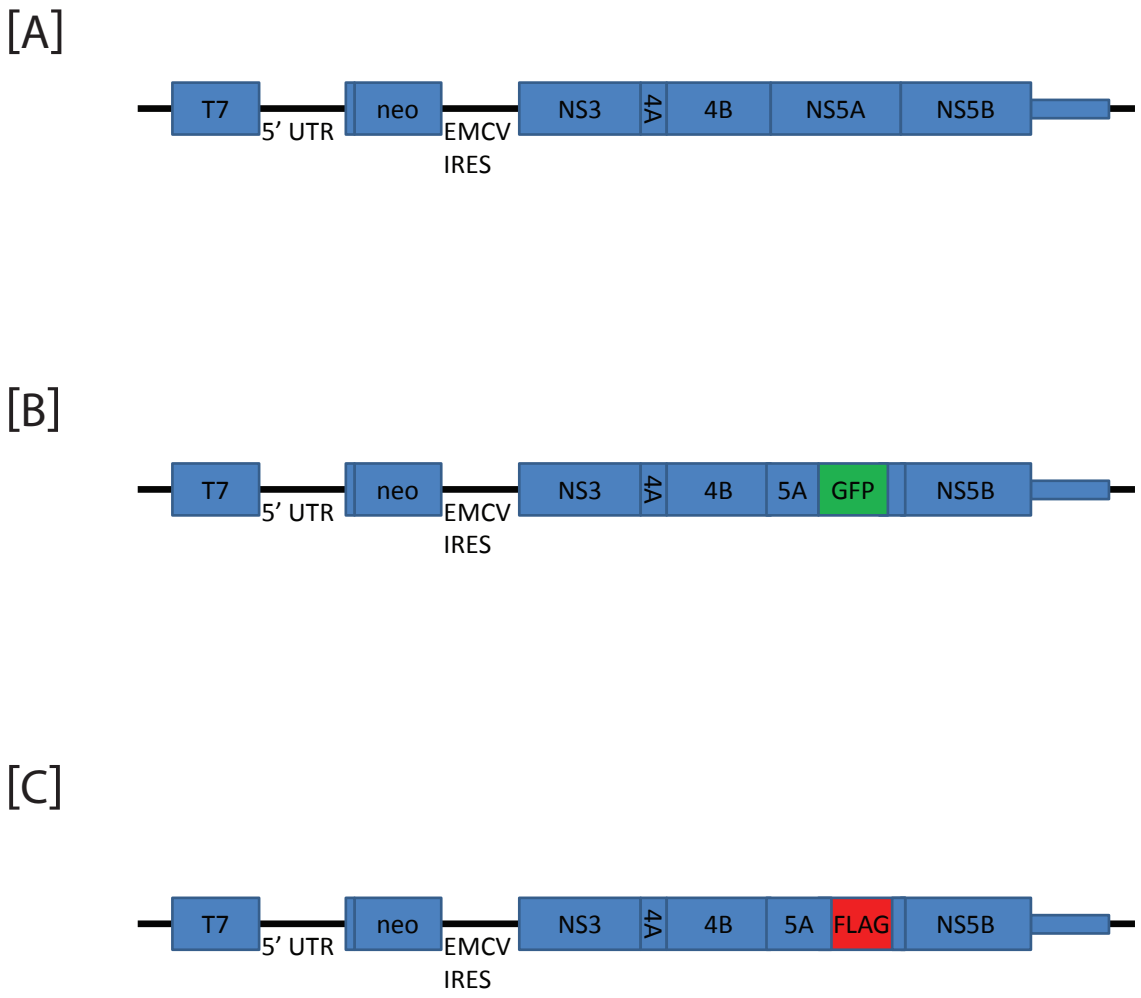

Figure 4. Subgenomic Replicon Structures SGR-JFH1, SGR-JFH1$_{NS5AGFP}$ and SGR-JFH1$_{NS5AFLAG}$

Structural proteins are removed and replaced with the Neomycin resistance gene neo and T7 RNA promoter region to produce the subgenomic replicon SGR-JFH1 [A]. GFP was introduced into the C-terminus of NS5A [B]. This same region was also utilised for the insertion of a FLAG tag [C].

visible in the Huh-7/SGR-JFH1$_{NS5AFLAG}$ cell line. Specificity of the α-FLAG antibody was also confirmed further through counter-staining with a NS5A-specific sheep antibody (Materials and Methods 2.1.7.1), kindly provided by Mark Harris shown in Figure 5 [A].

Therefore, failure of QD- based staining most likely occurred after application of the primary antibody. Fluorescence of the probe itself was validated through visual inspection of diluted quantum dot probe using a UV illuminator (data not shown). Having narrowed the reason for failure of QDs to detect FLAG-NS5A, a literature search was carried to identify possible problems associated with secondary quantum dot conjugation and imaging. One possible cause of experimental failure lay in the use of mounting media containing antifade reagents specific to organic fluorophores, such as ProLong (Ignatius,2010;Whaley,2011)

This quenching effect appears to result from the addition of antioxidants such as p-Phenylenediamine (PPD). When used with traditional organic fluorophores, the antioxidant properties of PPD prevent the formation of free radicals, the main cause of fluorescence photobleaching. When applied to semiconductor-based nanocrystals, PPD acts as an electron acceptor or hole,, trapping the previously excited confined electrons in the excited state within it's valence band thereby preventing them from returning to the ground state with subsequent photon release (Sharma et al, 2003).

Having identified the mounting media as a possible cause of QD quenching, Prolong reagent was replaced with a 9:1 PBS/glycerol as mounting media and the previous experiment repeated. Figure 5 [B] shows the results of this change in mounting media on fluorescent signal in Huh-7/SGR-JFH1$_{NS5AFLAG}$ cells. Restoration of this signal revealed a number of punctate sites with a staining pattern and dispersion similar to previous NS5A results. When counterstained using the alternative NS5A antibody however, the colocalisation seen in Figure 5 [A] between the NS5A and FLAG antibodies was not evident. Despite numerous attempts to optimise this methodology through verification of antibody specificity and mounting media, it was not possible to achieve the specificity required for accurate staining of the NS5A protein.

The failure to develop a specific staining methodology utilising either the RNA probe or FLAG-tagged immunofluorescence techniques against viral proteins suggested that incompatibility lay not with the probe itself but with the streptavidin QDs used for labelling. It was felt that perhaps the streptavidin biotin linker may contribute to the inconsistent results. The relatively high concentrations of endogenous biotin within

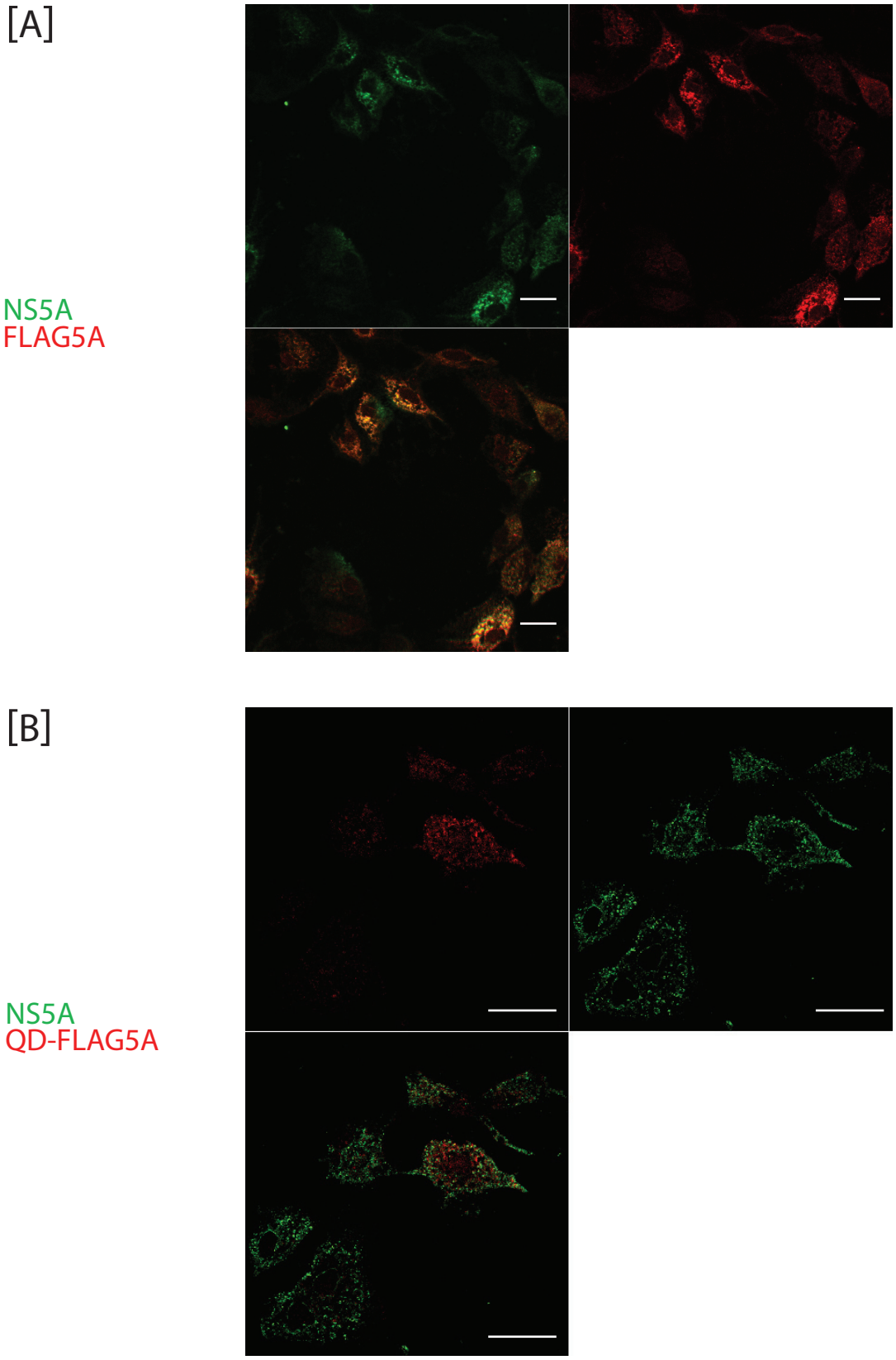

Figure 5. Visualisation of NS5A expressed by SGR-JFH1$_{NS5AFLAG}$ cells
Huh-7 /SGR-JFH1$_{NS5AFLAG}$ cells were fixed and stained for the FLAG tag using a-FLAG antibody and NS5A using NS5A antisera[A]. This was repeated utilising a-FLAG conjugated quantum dots and NS5A antisera [B]. Scale bars represent 20μm

metabolically active cells such as hepatocytes may also be the cause (Wood et al,1981). Therefore alternative methods of conjugation were sought which may prove more suitable to the cell lines being investigated.

5.4. CLEM Imaging using GFP as a Detector

Given the lack of success in developing an optimised QD staining methodology that could be further used for CLEM, the focus of probe development shifted to utilising GFP in place of nanocrystal technology. Unlike QDs, use of encoded GFP constructs has been well characterised as a localisation technique for use in CLEM with a number of robust protocols available for application in both EM and cryo-EM modalities (Luby-Phelps et al, 2003). Utilising the Huh-7/SGR-JFH1$_{NS5AGFP}$ cells, results in Chapter 3 had shown it was possible to localise predicted replication sites using the GFP-NS5A protein and examine the underlying ultrastructure and altered membranes associated with the membranous web.

Having characterised the fluorescent signal of GFP-NS5A by OMX imaging described in the Chapter 3, it was noted that the percentage of cells expressing GFP-NS5A was approximately 50%. While the differences in replicon expression were of limited significance for CLSM imaging, such variation decreases the likelihood of locating cells expressing the fluorescent tagged protein by EM. In an effort to increase the probability of visualising GFP-NS5A within samples, Huh-7/SGR-JFH1$_{NS5AGFP}$ cells were selected for GFP expression by Fluorescence Activated Cell Sorting (FACS). This increased the proportion of cells in monolayers that expressed GFP-NS5A to about 95%.

FACS-purified cells were transferred to MatTek live cell imaging dishes containing a number of sterilised sapphire discs submerged in DMEM and incubated for 24 hours at 37^{o}C to allow cell adhesion. Expression of the GFP-NS5A protein was confirmed by CLSM imaging of the discs prior to embedding, as shown in Figure 6 [A]. Sapphire discs with adherent GFP-NS5A were then transferred to sample carriers for High Pressure Freezing (HPF) using a Leica EM PACT2 High Pressure Freezer. The extremely low thermal inertia of sapphire makes it an ideal substrate for rapid freezing of samples (Reipert et al, 2003). Samples were rapidly frozen using a jet of LN_2 and transferred under cryo-conditions to a Leica EM AFS2 for freeze substitution and Lowicryl HM20 resin embedding. Samples were processed as described in Materials and Methods 2.2.12.

Sectioned samples were transferred to EM finder grids for initial fluorescence microscopy by CLSM. One of the difficulties faced in CLEM methodologies is the imaging of resin-

embedded and grid-mounted samples, which may not reside parallel to the focal plane. Physical size of the grids also poses certain technical difficulties, being almost of similar size to the objective lens making manipulation and retention of the sample difficult. To overcome these problems, MatTek dishes were utilised to hold a number of grids simultaneously, placed resin-side down to the glass coverslip base. In order to improve image quality, grids were immersed in ddH_2O, limiting the changes in refractive index between media. Regions of interest within each grid were identified visually and 3D datasets of the fluorescent signal acquired through CLSM using appropriate laser and filter sets.

Figure 6 [B] shows the Maximum Intensity Projection (MIP) of a single grid square harbouring a Huh-7/SGR-JFH1$_{NS5AGFP}$ cell, with alternate views and depth projection shown in [C] and [D]. The depth projection shown in [C] demonstrates the difficulty in successfully imaging target cells using only single focal plane data. The signal can clearly be seen to reside at a significant angle relative to the focal plane; using single image analysis, such a target could be easily missed or misinterpreted as background. Thus, only by collecting 3-D data of the ROI can such cells be accurately detected. Of note, it was somewhat surprising that the GFP signal was readily detected after UV polymerisation for 48 hours. Resistance to photobleaching may be conferred by the resin absorbing the UV energy during polymerisation. The low temperature of the freeze substitution method may also act as a form of cryoprotection, limiting the excitation of electrons to higher energy states which can result in photobleaching (Rost,1992).

Having successfully identified cells expressing GFP-NS5A by CLSM, samples were transferred to TEM. Despite successfully identifying and imaging the GFP-NS5A signal by fluorescence microscopy, TEM analysis failed to detect any clear structures that could be attributed to the signal itself. Further progress was hampered due to technical problems with curing of Lowicryl resin. While it was not possible to achieve accurate correlation between the two imaging modalities within the timescale of this project, in principle, the technical barriers should be surmountable in time.

[A]

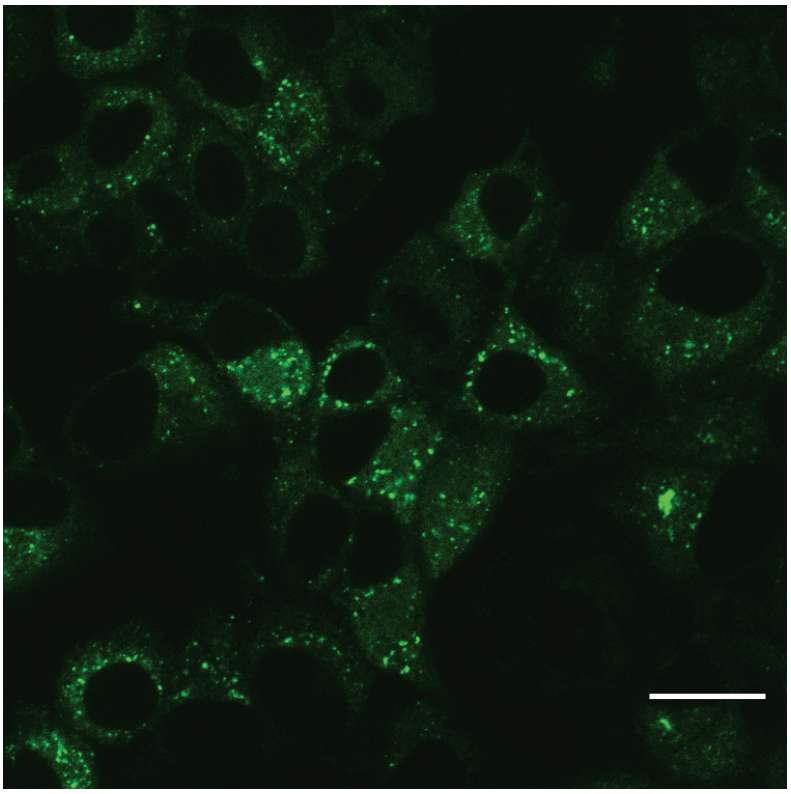

[B]

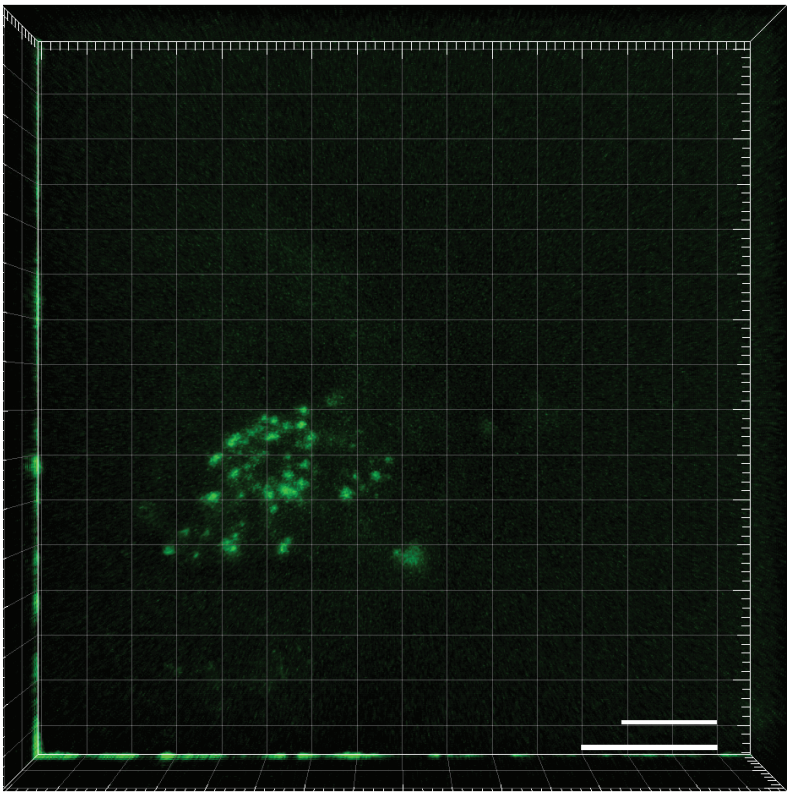

Figure 6 Visualisation of NS5A from SGR-JFH1$_{NS5AGFP}$ cells prepared for correlative Microscopy. Visualisation of NS5A from SGR-JFH1$_{NS5AGFP}$ cells prepared for correlative Microscopy

Huh-7/SGR-JFH1$_{NS5AGFP}$ cells were grown on sapphire discs and imaged by CLSM prior to embedding [A]. Embedded samples were sectioned and mounted on finder grids and visualised through 3D CLSM. Imaris software was utilised to generate a Maximum Intensity Projection (MIP) of the Z-stack data [B] [C] [D]. Scale bars represent 20µm

[C]

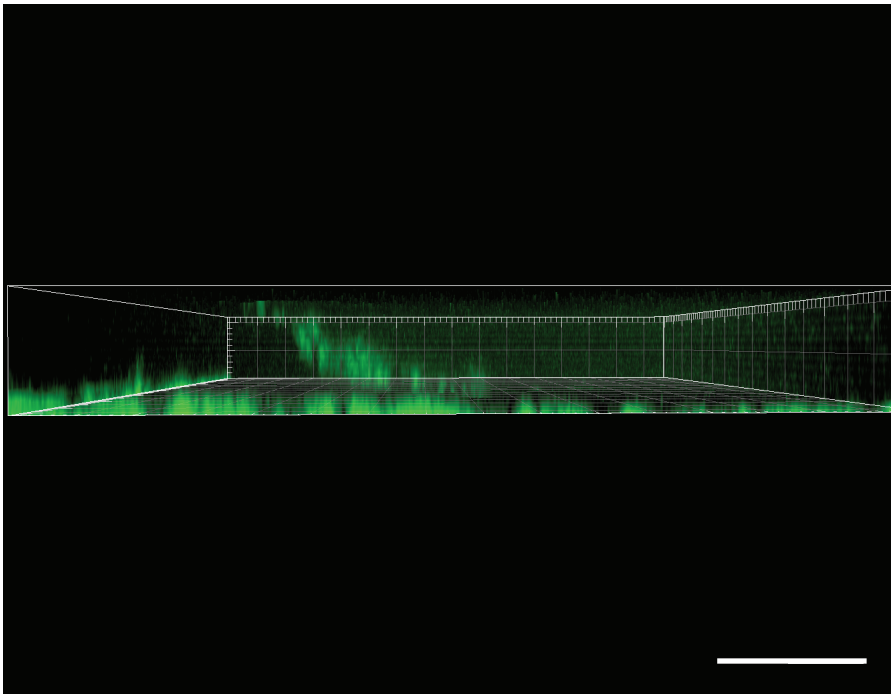

[D]

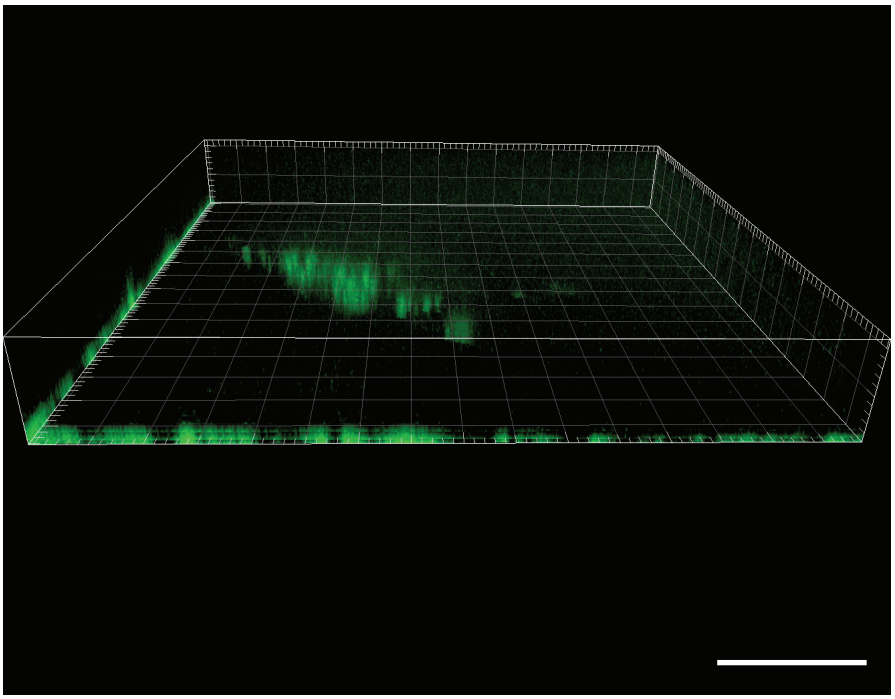

Thus, by this stage, a number of problems had been encountered in the project including:

a) Difficulties with sensitivity to detect viral RNA with QDs.

b) Lack of specificity for detecting viral protein by attempts to recognise viral NS5A using a traditional primary/secondary sandwich antibody approach.

c) Technical problems with curing of Lowicryl resin.

In the final part of the study, the experiences from the above problems were applied in an attempt to detect NS5A using QDs.

5.5. NS5A Antibody Quantum Dot Conjugation

During investigation of the GFP tag for CLEM, a novel commercial product became available allowing the direct conjugation of primary antibody to QDs (Qdot Antibody Conjugation Kit [Invitrogen]). It was considered that such a reagent could circumvent the problems previously encountered through the use of streptavidin/biotin-based secondary conjugation. However, one major limitation for use of this kit was the large quantity of antibody required for accurate stoichiometry during the conjugation reaction. Given the limited availability of the polyclonal α-NS5A an alternative source of antibody was sought. We were able to access milligram quantities of purified monoclonal antibody 9E10 (kindly provided by Dr T Tellinghuisen), which is highly specific for NS5A and was employed for crystallisation studies on Domain 1 of the protein (Tellinghuisen et al,2005).

Specificity of 9E10 for NS5A expressed by the SGR-JFH1 replicon was confirmed through indirect immunofluorescence with Huh-7/SGR-JFH1 cells (data not shown). Having established the specificity of 9E10 with subgenomic replicon cells, conjugation of QDs to the monoclonal antibody was carried out as described in Materials and Methods 2.2.8.2. to form the probe conjugate shown in Figure 1 [C]. Given the previous problems encountered with secondary antibody conjugation, newly synthesised 9E10/QD conjugates were verified through colocalisation testing with the anti-NS5A polyclonal antibody. Huh-7/SGR-JFH1 cells were fixed, permeabilised following the method described by Giepmans et al (2005) and probed with 9E10/QDs and α-NS5A polyclonal antibody (Figure 7 [A]). The 9E10/QD conjugated probe gave a signal that largely colocalised with the polyclonal NS5A antibody, in particular detecting punctate sites; by contrast, no such signals were detected in control Huh-7 cells (data not shown). Examination of cells prepared and stained

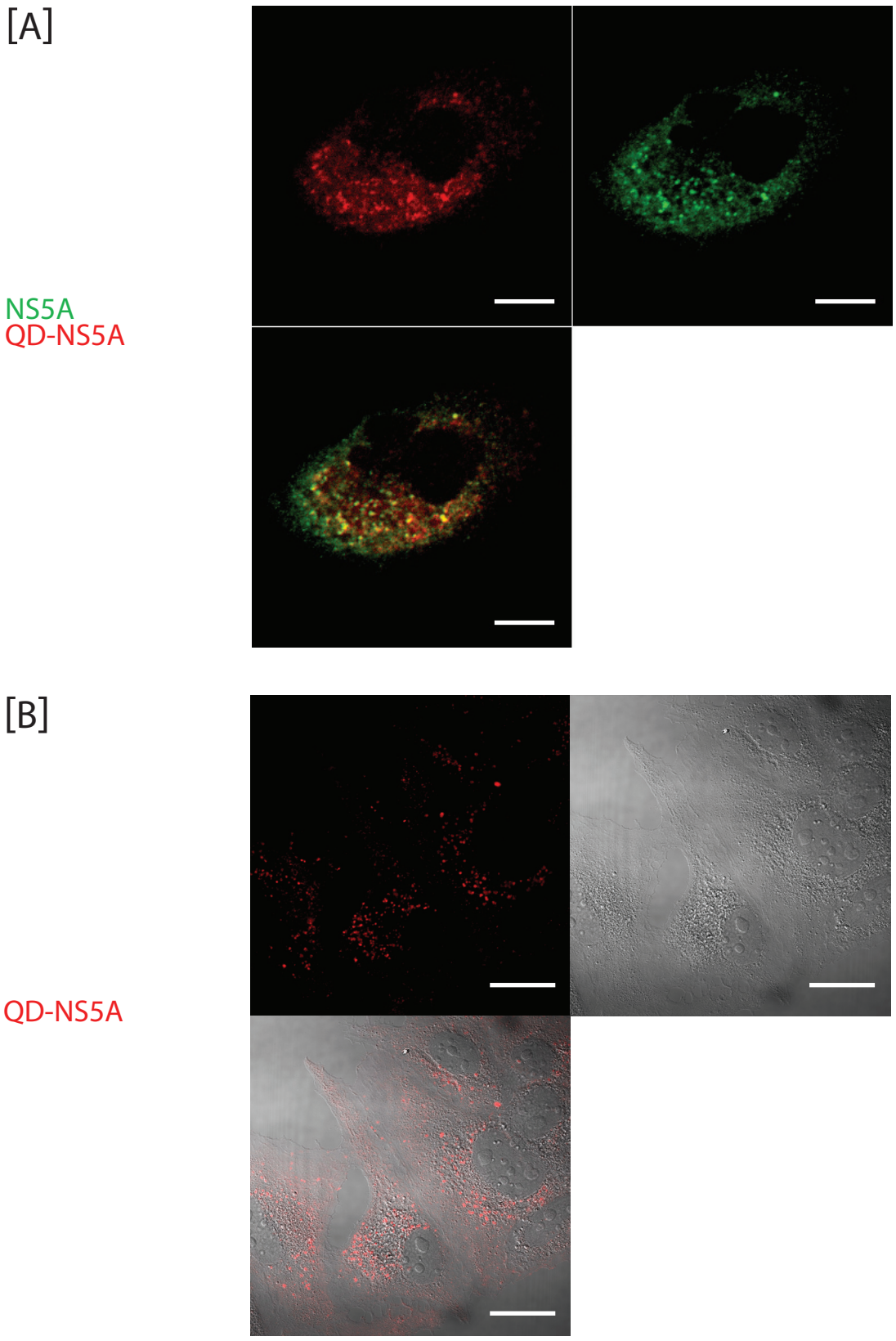

Figure 7. Visualisation of NS5A expressed by SGR-JFH1 cells utilising functionalised quantum dots.

Huh-7/SGR-JFH1 cells were fixed and stained for the NS5A tag using quantum dot functionalised with the NS5A monoclonal anitbody 9E10, counterstained with a-**NS5A antisera [A]. QD were visualised with DIC [B]. Scale bars represent 20**μm

using this methodology showed no obvious disruption of cell structure or morphology when examined by fluorescence microscopy combined with Differential Interference Contrast (DIC) microscopy (Figure 7 [B]). Based on these data, samples were then prepared and embedded for EM imaging.

Given the technical problems associated with curing of resin with the sapphire disc HPS-FS method, samples were chemically fixed, scraped from cell culture flasks and pelleted by centrifugation prior to EM staining. Unlike the planar methodology described previously, pelleting of the sample provides a greater density of cells, increasing the likelihood of identifying sample fluorescence. Following embedding in Epon resin, samples were trimmed to produce a planar surface. Trimmed samples were mounted in a custom holder and the entire block face imaged by CLSM.

CLSM imaging of the resin blockface revealed that the fluorescence signal observed in cell monolayers had been entirely quenched. Cells were visible through the microscope as dark silhouettes devoid of any fluorescence including any typical background autofluorescence caused by the resin itself. The experiment was repeated with fluorescence imaging prior to embedding, which confirmed the existence of a fluorescence QD signal prior to embedding. However, analysis of the block after processing showed no fluorescence. Therefore it was concluded that the observed fluorescence quenching was a result of sample preparation for EM.

Post-fixation processing included use of osmium tetroxide to provide contrast to the lipid components of the cell. A literature search identified osmium tetroxide as a possible causative agent for fluorescence quenching since it can interact with QDs, resulting in instantaneous and irreversible quenching (Deerinck, 2008). It should be noted that this observation contradicts the method published by Giepmans that had been followed previously. Hence, staining steps that incorporated both osmium tetroxide and uranyl acetate were removed from the protocol and the experiment repeated to assess their impact on QD fluorescence.

An image of an unstained section prepared for EM is shown in Figure 8 [A]. Removal of osmium tetroxide yielded high numbers of punctate fluorescence evident in the grid square. Grids were imaged as described previously, utilising the MatTek dishes to allow immersion of the grid in ddH_2O for CLSM imaging. To accurately capture the non-planar orientation of the grid within the dish, Z-stack datasets were acquired and a MIP of the grid was generated for the image in Figure 8 [A]. This experiment unequivocally demonstrated

[A]

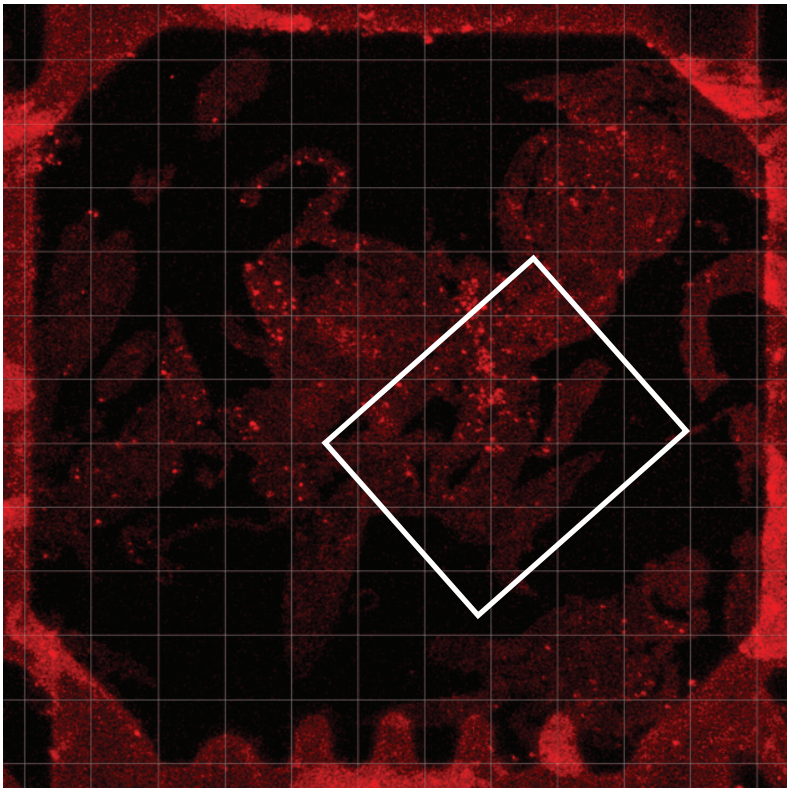

[B]

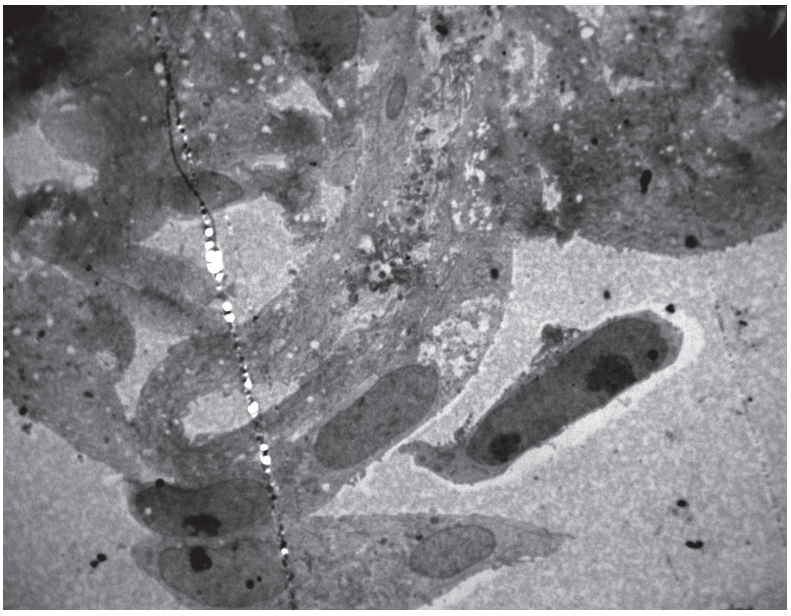

Figure 8. Correlative Imaging of NS5A utilising targeted 585nm QDs on 100nm sections.

Huh-7/SGR-JFH1 cells were fixed and embedded in Epon resin, cut into 100nm sections and stained for NS5A using 9E10 Ab conjugated to 585nm QDs [A]. ROI were identified (shown by white box) [A] and [C] and examined by TEM at a number of magnifications, x3k [B] and x5k [E]. The appropriate region of fluoresence was selected [D] and overlayed upon the TEM image to generate a combined CLSM/TEM image showing structural detail within regions of fluoresence [F]. Scale bars represent 20µm

[C]

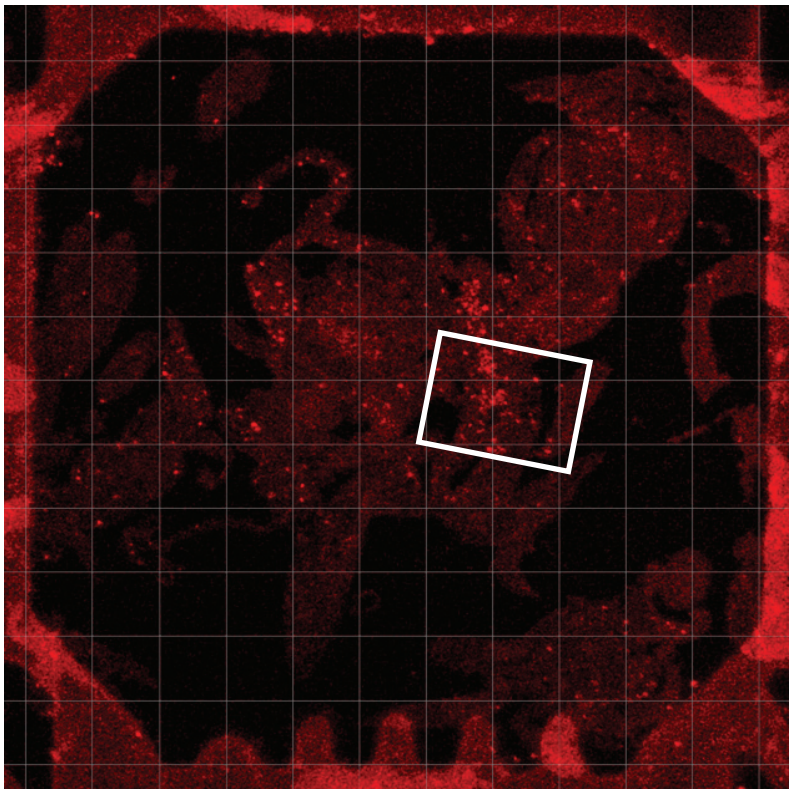

[D]

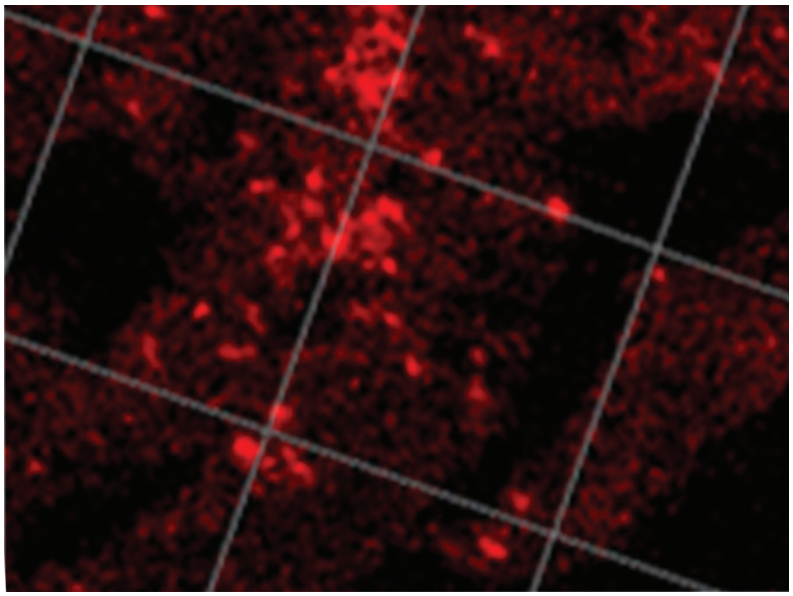

[E]

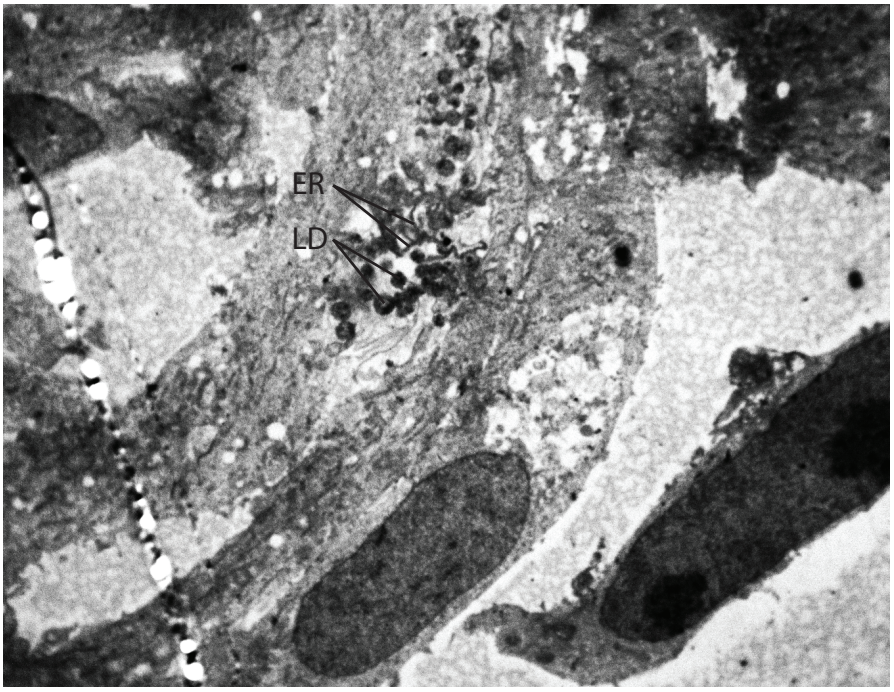

[F]

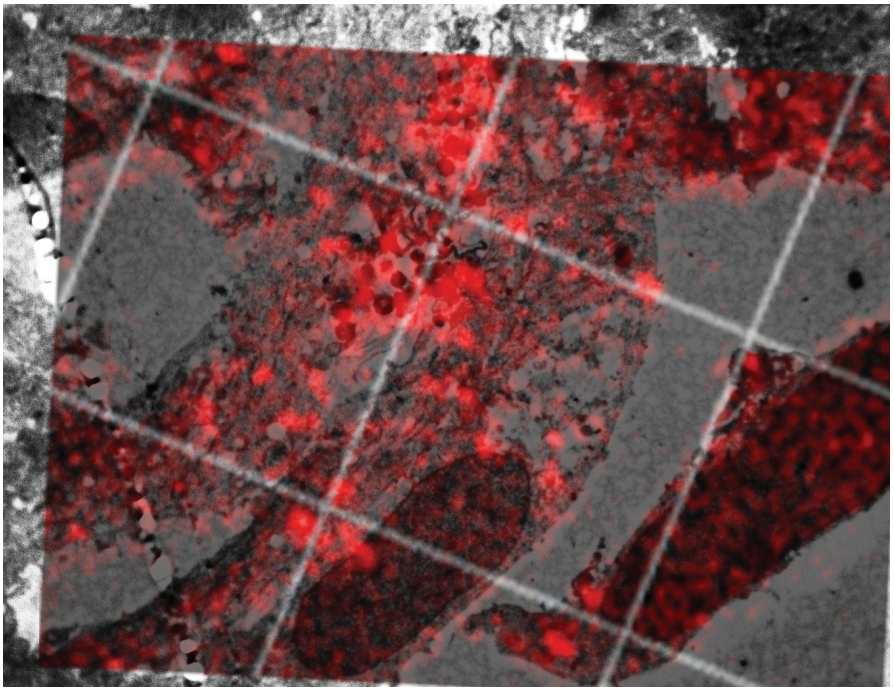

that heavy metal staining was incompatible with retaining QD fluorescence. However, staining of the individual grids post image capture by CLSM remained possible and was a simple alteration to the method. Thus, samples were stained after CLSM imaging and transferred to the Transmission Election Microscope (TEM). All electron microscopy described below was carried out by Dr Frazer Rixon (MRC-UoG Centre for Virus Research). Resultant EM images are shown in Figure 8 [B] and [E]. The final protocol therefore resulted in a modified version of Giepmans' protocol, utilising embedding, sectioning and CLSM imaging followed by staining with osmium tetroxide and uranyl acetate prior to EM imaging The major incompatibility found with the Giepmans' protocol may be due to differences in the quantum dot properties used in both experiments. Given the proprietary nature of the quantum dots used in this project it may be that the bio-compatible coating varies in permeability to osmium tetroxide, resulting in the differences described here.

The region highlighted in Figure 8 [A] was selected as an area of interest due to the levels of complexity and signal intensity shown in the fluorescence image. Having identified this region, EM imaging was carried out at a number of magnifications. The lowest magnification of x3000 [B] was used to align the coarse outline of cells and structures to that of the optical image, confirming the similarity and accuracy of regions imaged. Following this identification, a higher magnification (x6000, image [E]) was aligned to a smaller region of interest within the optical image shown in [C] and magnified in [D]. Figure 8 [D] shows a tight collection of punctate sites and unstained regions, which were aligned to image [E]. By increasing the transparency of the optical component [D] overlayed on the corresponding EM image [E] it was possible to observe in greater detail the correlation between the NS5A signal upon the structural details of the cell (Figure 21 [F]).

Examination of this region by EM microscopy showed an extremely complex ultrastructural interaction between a number of cellular components. Central to this region was a number of black spheres, the dark osmium tetroxide stain indicative of lipid dense organelles, most likely lipid droplets (labelled LD). Interwoven between the aggregated lipid droplets was the convoluted ER membrane (labelled ER) and surrounding both of these components are a number of unidentifiable dark grey regions. Overlaying the fluorescence data onto this EM data gives a greater level of detail to the complexity of the region. The fluorescent signal seems to be attributed to the outside of the lipid droplets and

along the ER membrane. Unfortunately it was not possible to directly identify the quantum dots themselves as electron dense regions within the sample, attempts to image unbound stock of the quantum dots failed(?) suggesting that the dots may have been significantly smaller and less dense than expected.

Having successfully identified sites of replication by CLEM/QD methodology for standard TEM imaging of 100nm thick sections, the study progressed to investigation of the 3D architecture of putative replication sites. This was achieved using electron tomography of 250nm sections, taken from the same sample as seen in Figure 21. Thicker sections were utilised to provide greater 3D depth of information of replication sites. ROI were identified in the same manner as 100nm using the LSM 710 meta, prior to deconvolution and generation of MIP using Autoquant and Imaris (Figure 9 [A]). A slight decrease in optical image quality was noted at this point, most likely down to the increased thickness of the resin being imaged. After a ROI (Figure 9 [A] White Box) was imaged and identified using the co-ordinate system of the finder grid, the sample was then transferred to a JEOL JEM-2200FS for electron microscopy.

Prior to tomography, 2D micrographs of the ROI were captured at a number of magnifications to allow alignment of the subsequent high magnification tomogram (Figure 9 [B]). Although the image resolution afforded by the thicker sample is somewhat lower than the previous 100nm section seen in Figure 8 [B], it is still possible to identify a complex alteration within the cell with similarity to previously identified membrane perturbations that could be replication sites (Identified by white arrow).

Tomograms were then generate at 5000x magnification as a +/- 55^{o} tilt series, imaged at 2^{o} increments, using 200kV accelerating voltage and energy-filtered image capture to exclude inelastically scattered electrons and enhance image contrast. Alignment of the tilt series was carried out using 15nm nanogold fiducial markers, pipetted onto the surface of the section prior to tomography. The region captured is identified by the black box in Figure 9 [C], the tomogram itself shown in Figure 9 [D] (Full tilt series presented as a movie in accompanying material). Tomograms were then aligned to the previous generated CLEM image using coarse cellular landmarks visible at lower magnification. Using the aligned tomogram and CLEM image (Figure 9 [E]) the fluorescent signal was applied to generate a correlated fluorescence/tomogram (Figure 9 [F]). The fluorescent component of the correlated tomogram was then adjusted to show the region of highest intensity fluorescence to enable more accurate identification of structures within the tomogram (Figure 9 [G]).

[A]

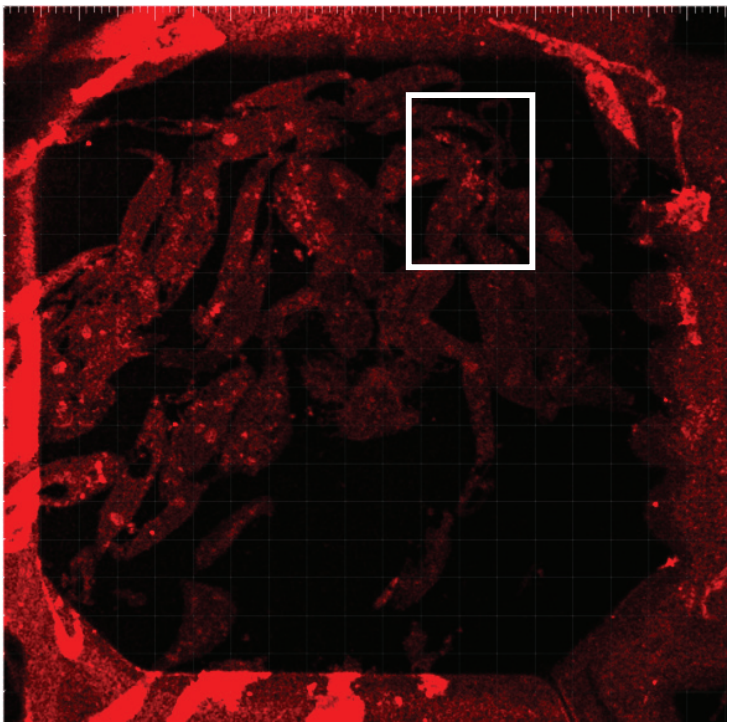

[B]

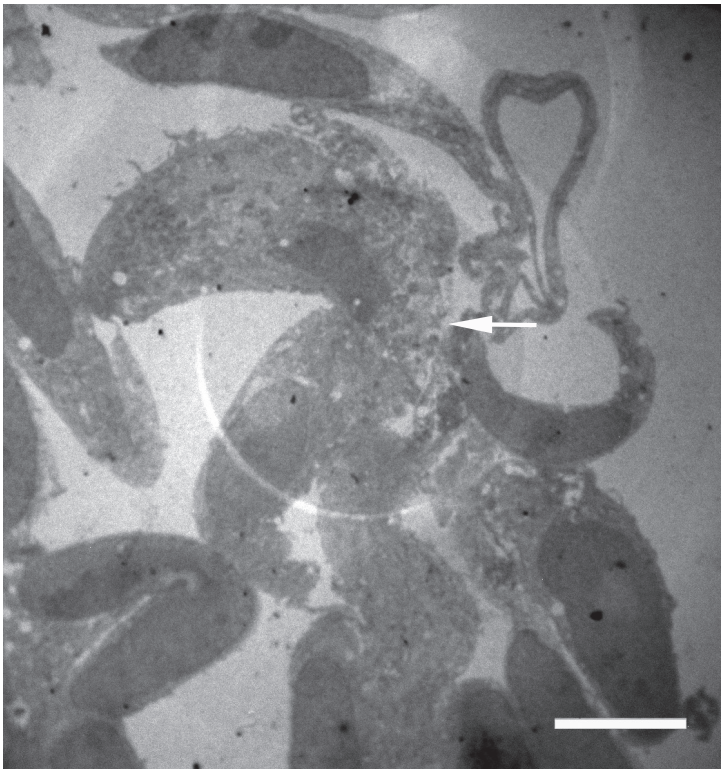

Figure 9a. Correlative Tomography of viral replication complexes identified by the NS5A protein tagged using 585nm QDs on 250nm thick resin sections.

Huh-7/SGR-JFH1cells were fixed, stained for NS5A using 9E10 Ab conjugated to 585nm QDs and embedded in Epon resin prior to sectioning. Confocal microscopy was carried out on sections mounted on reference grids [A]. ROI were identified (shown by white box) in [A] and examined by TEM at x3000magnification prior to tomography [B]. Fluorescence was found to correlate to regions of altered cellular structure identified by white arrow.

Scale bar: [B] 2μm

[C]

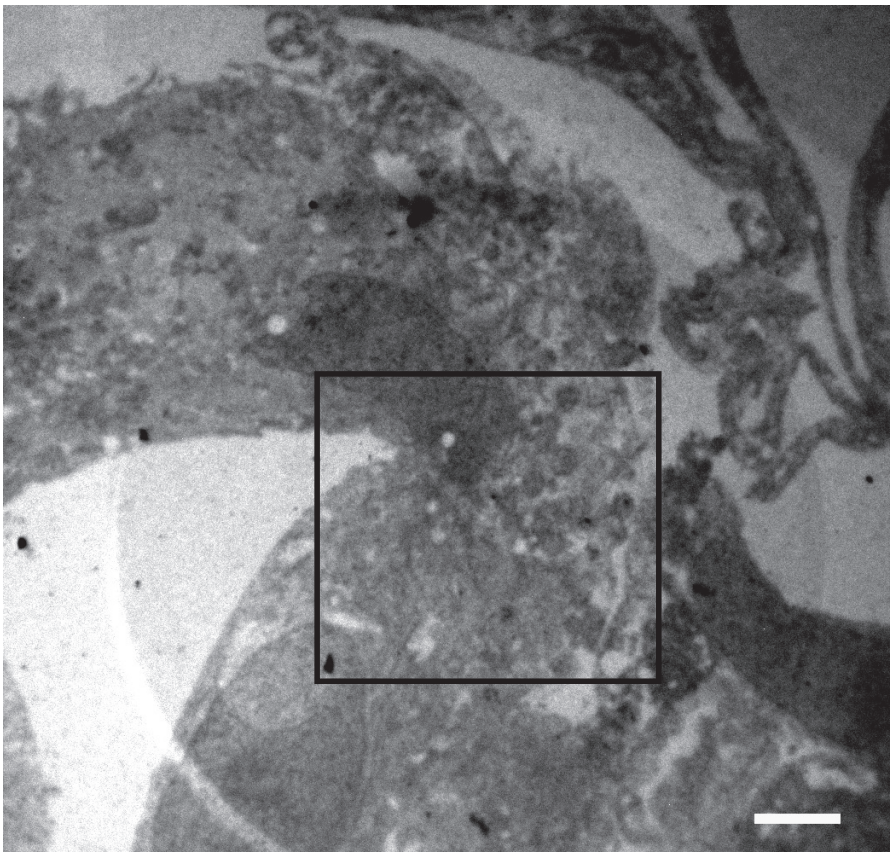

[D]

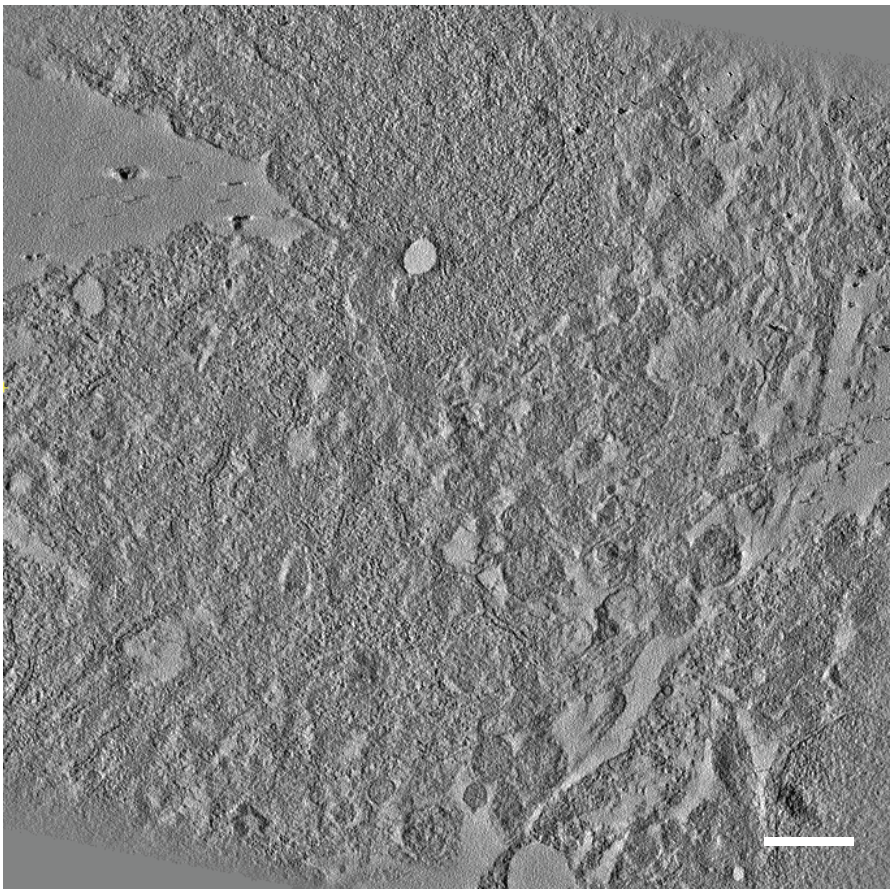

Figure 9b. Identification of regions for Correlated Tomography
ROI identified in Figure 22a. were imaged with increasing magnification up to x6000 by TEM [C] to select ROI, shown by black box, for further investigation by tomography at x5000 magnification shown in panel [D].
Scale Bars: [C] 2μm, [D] 1μm

[E]

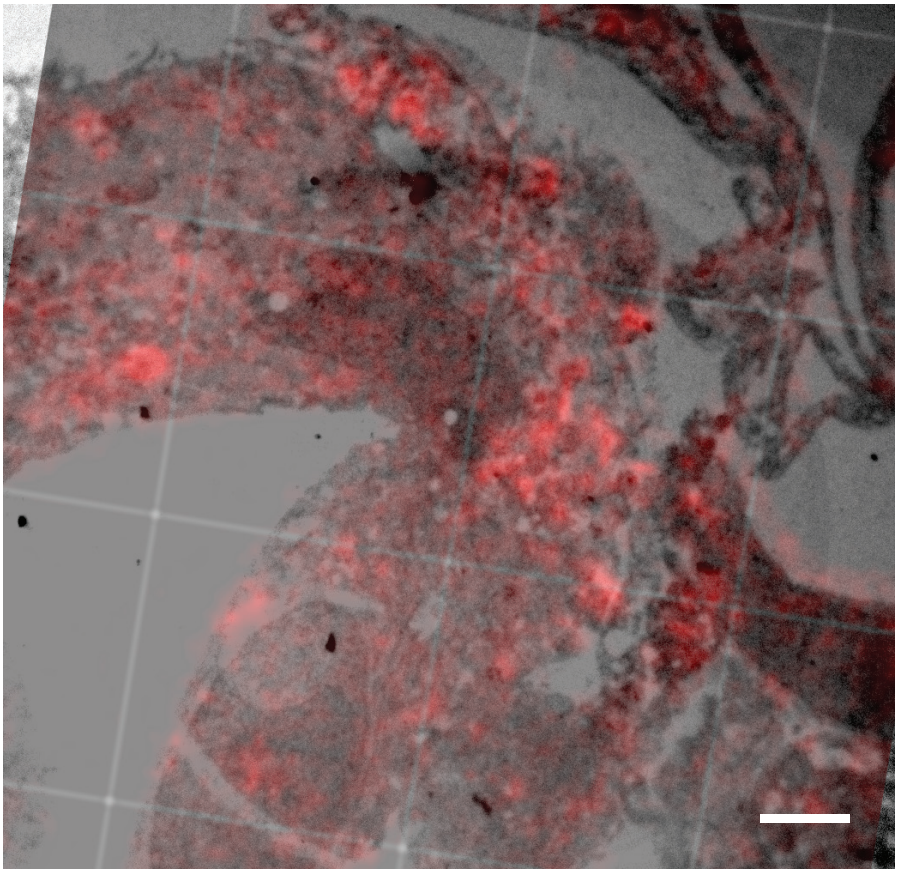

[F]

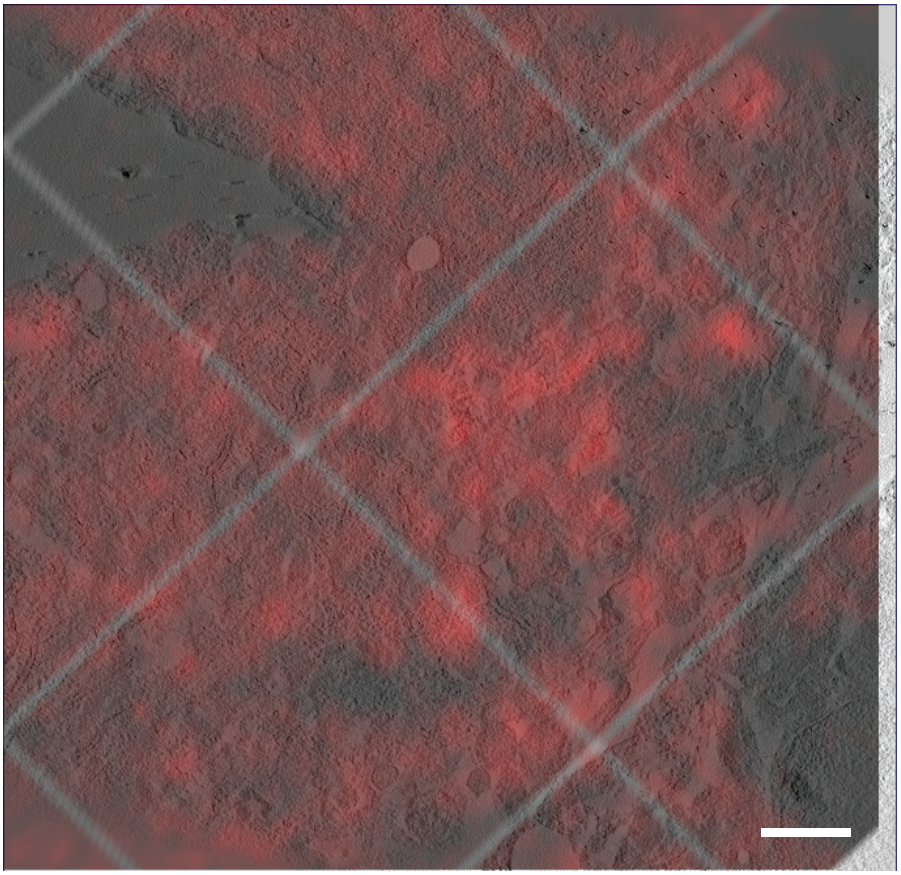

Figure 9c. Correlation of Fluorescence signal with TEM images and Tomograms.
TEM image and Tomogram shown in Figure 22b were then overlayed with the correlating region of fluorescence from Figure 22a [A] to produce the correlated TEM image [E] and correlated Tomogram [F].
Scale bars: [E] 2μm, [F] 1μm.

[G]

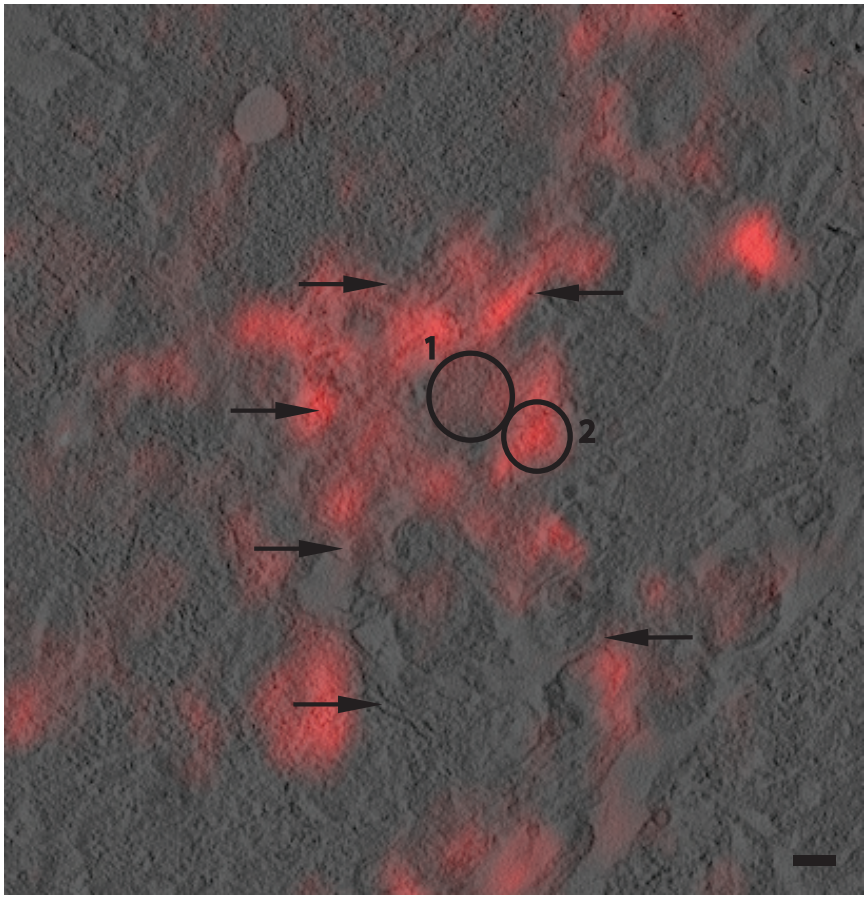

[H]

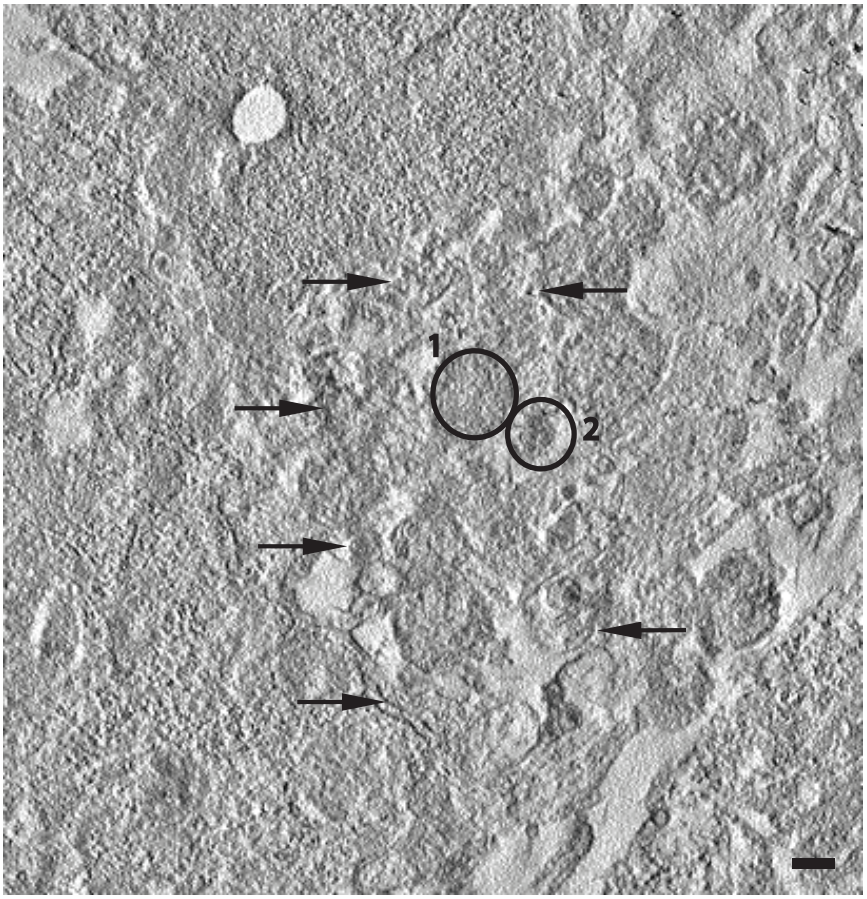

Figure 9d. Magnified ROI of Tomogram with annotated cellular structures.

Magnified region of captured Tomogram shown in Figure 22b & c with cellular structures identified, convoluted ER membrane marked by black arrows. Spherical structures identified by black circles 1&2.

Scale bars: [G] [H] 300nm.

From this overlay a number of structures were identified within the tomogram and plotted in Figure 9 [H].

Figure 9 [H] shows a magnified region of the tomogram, centred on the high intensity fluorescence shown in Figure 9[G]. Compared to the surrounding cellular structure on the left-hand side of the image, there is a significant change in cell architecture and structure in the region detected by the NS5A-QD probe. Examining the location of the fluorescent signal indicates that it surrounds a large vesicle of at least 700nm in diameter (black circle 1) with a number of other identifiable spherules or vesicles in close proximity. The ER membrane (identified by black arrows) can be seen interwoven throughout this region, surrounding the areas of highest intensity fluorescence. It should be noted that the regions of highest intensity fluorescence do not correlate with the vesicles themselves but are instead juxtaposed to their surface. The region identified by circle 2 is or particular interest, correlating with the highest intensity fluorescence within the image. It appears to be a complex, roughly spherical structure of approximately 300nm in diameter. The correlation in both fluorescent signal and structure size with those seen in Chapter 3 suggests that this may be a putative replication site. Its juxtaposition to the central vesicle (indicated by circle 1) lends weight to the possibility it could be a lipid droplet, associating through NS5A with the replication complex (Shi et al,2002). Given the number of punctate fluorescent sites within the boundings of the identified ER membrane, it may be that each signal represents a putative replication unit bound to vesicles to generate the membranous web.

5.6. Discussion

Through both 2D and 3D TEM imaging, a unique and unusual cellular architecture correlated with a fluorescent signal specific for NS5A which is located at viral replication sites. This identified structure of numerous vesicles held together in a tightly woven network or matrix of membranous materials, termed the membranous web, has been described previously as a cellular alteration caused by expression of the viral proteins (Egger et al,2002). Such images also bear striking similarity to the EM images revealing membrane alterations caused by infection by poliovirus (Dales et al,1965). Until now, there has been limited data on the architecture of these membrane perturbations. The use of CLEM methodologies provides an unprecedented level of fidelity, not just to confirm that such sites harbour viral proteins, but also to extend the structural detail of replication sites.

Here, it has been possible to show that the NS5A protein can be found at punctate sites, juxtaposed to organelles likely to be lipid droplets.

A similar methodology to that used in section 5.4 has recently been employed to identify membranous web structures within Huh-7 Lunet cells transfected with SGR-JFH1$_{NS5AGFP}$ RNA (Romero-Brey, 2013). Unlike the method described above, fluorescence imaging was carried out on samples prior to HPF and FS, allowing imaging of cells upon the sapphire discs themselves. There are a number of benefits associated with this method: i) photobleaching during polymerisation is removed as a inhibitory factor, ii) the clarity of the fluorescent image is greatly increased due to the greater integrity of the cell prior to sectioning and, iii) the less complex optical pathway available through the imaging medium. However there are also pitfalls with this approach. Firstly, there is a lack of certainty in reacquiring the same cell post-EM processing and sectioning. While the quality of fluorescence imaging of the resin section may be decreased compared to the sapphire disc method, there is no doubt as to the accuracy of the acquisition of the same cell at higher magnification due to the coordinates etched into each grid square. Identifying single cells upon removal of such a reference pattern makes location of a specific cell extremely difficult. The overlaying of widefield fluorescent images upon 60nm resin sections is also a cause for concern. Given the very different depths of field for both images, interpretation of the correlated signals is far more difficult. Only through fluorescent imaging of the section itself can the signal be definitively attributed to that particular region of the cell.

Although limited by time constraints, the successful acquisition of 3D tomograms of putative HCV replication sites provides the foundation for further ultrastructural modelling of this region through tracing of the tomographic reconstructions to produce 3D representations such as those shown for optical imaging in Chapters 3 and 4. The methods developed in this chapter demonstrate that it is now possible to accurately determine the structural detail and location of fluorescent targets alongside the ultrastructural resolution provided by TEM. Moreover, the studies presented provide proof-of-concept for detecting viral antigens using QDs directly conjugated to a virus-specific antibody. This offers opportunities for other exploratory studies, not just in HCV but also with other viral pathogens. For example, there is scope to employ QDs with other spectral properties to enable multiplexing for detection of other viral or host cell factors. In addition, the ability to combine CLEM with EM tomography is a powerful method to expand the structural detail of sites where replication and virus assembly occurs.

6. Quantitative Proteomics of Naive Cell Lines by SILAC Mass Spectrometry

6.1. Introduction

Following on from the success of the genomics, there has been a significant trend in the life sciences towards the investigation of organisms at the systems level, methodologies collectively known as 'omics technologies (Joyce et al,2006). Each specialises in the analysis of the pool of biomolecules within a particular organism, producing large-scale datasets which provide an unprecedented view of the inner workings of the cell (Tyers et al,2003). The proteomics branch of the 'omics family examines the entire complement of proteins coded by the genome, including their modifications and structures to elucidate the metabolic pathways of the cell.

The simplistic examination of protein expression as a binary present/not present function within the cell is in itself, limited in value. Of greater interest is the quantitative analysis of protein expression between two separate cell states, either as an absolute measure of protein quantity or the relative change between the two states (Mann,2006). Early quantitative techniques utilising fluorescence and radioactivity combined with 2-D gel electrophoresis provided excellent sensitivity and dynamic range but limited depth of proteome coverage, constrained to only the most abundant proteins within the sample (Tyers et al,2003;Bantscheff et al,2007). The application of Liquid Chromatography-Mass Spectrometry (LC-MS), has rapidly increased the depth of analysis available in proteomics, however it is not an inherently quantitative technique due to the complex relationship between analyte quantity and signal intensity, which can be affected by size, charge and hydrophobicity of the peptide (Bantscheff et al,2007;Aebersold et al,2003).

While not a quantitative method *per se,* observed isotopic peak ratios are highly accurate, due to the lack of chemical differences between species. Consequently, a number of methods have been developed, based around the incorporation of isotopically labelled references into the sample, either as metabolic or chemical tags or as an external standard of a spiked synthetic peptide (Bantscheff et al,2007). Stable-Isotope Labelling by Amino Acid Composition (SILAC) is one such recently developed metabolic labelling technique, incorporating isotopically heavy- and light-labelled amino acids into amino acid deficient cell culture media to ensure incorporation of labels directly into the cell proteome. By labelling one cell population with light amino acids and another with heavy amino acids, the two cell extracts can be mixed and proteomes analysed. By mixing populations at an

early stage in processing, losses occurring during extraction through to analysis will affect both samples equally, ensuring accuracy in relative quantification (Ong et al,2002). During analysis both heavy- and light-labelled peptides are detected simultaneously and identified by their relative mass shifts.

As already described in this study, the Huh-7 cell line provides a cellular environment permissive for replication of the JFH-1 subgenomic replicon SGR-JFH1 (Targett-Adams et al,2005). Treatment of Huh-7 cells harbouring SGR-JFH1, or any other HCV subgenomic replicon, with IFN-α can eliminate the self replicating RNA creating a cured cell line. Cured cells have increased permissiveness to HCV infection. To further develop this permissiveness, a number of cured Huh-7 cell lines were cloned and tested for replication competence. From such an approach, Huh-7.5 cells were found to support a significantly higher (3-fold increase) level of replication than the parental Huh-7 cell line (Blight et al,2002).

To investigate the possible cause of increased permissiveness, the study described in this chapter sought to compare the proteomes of Huh-7 and Huh-7.5 cells through SILAC analysis. With this aim, SILAC methodology was developed to enable stable maintenance of the two cell populations in SILAC media. Utilising these SILAC-maintained cell lines, it was hoped to identify differences in levels of protein expression which may affect HCV permissiveness.

6.2. Cell Culture Development

6.2.1. Foetal Calf Serum Testing

Central to any SILAC investigation is the effective and sustained maintenance of the cell line in isotopically labelled SILAC media. Stable growth of the cell line under such conditions is critical to the success of the experiment as 5 rounds of cell division must be accomplished to ensure complete integration of the labelled amino acids, L-lysine and L-arginine into the entire proteome. Failure to integrate heavy-labelled tags into the cell population results in a shift in relative expression towards light-labelled amino acids.

To ensure complete integration of labelled lysine and arginine, all other sources of amino acids within the growth media must be removed or limited. Although SILAC DMEM media is deficient in both amino acids, the supplemental Foetal Calf Serum (FCS), containing a variety of undefined growth factors necessary for effective cell growth, is a source of unlabelled amino acids at unknown concentrations. To prevent contamination of

the media through supplementation, FCS utilised in any SILAC experiments must be thoroughly dialysed to remove free amino acids prior to use.

Several commercially available dialysed media were tested for compatibility with Huh-7 and Huh-7.5 cell lines. Due to the lack of availability of a dialysed variant of Gibco FCS typically used for Huh-7 maintenance, alternatives from Dundee Cell Products (DCP) and BioSera were tested. In addition, SILAC DMEM from DCP was used at this stage of the project. Sequential adaptation of the cells to dialysed FCS from these companies was employed to limit cell stress using the following method.

Passage 1: 75% Standard FCS/25% Dialysed FCS

Passage 2: 50% Standard FCS/50% Dialysed FCS

Passage 3: 25% Standard FCS/75% Dialysed FCS

Passage 4: 100% Dialysed FCS

Despite the application of a sequential adaptation process during FCS testing, cell mortality increased with passage number rising to complete death of the cell population before passage 5. In an effort to lessen the effects of dialysed FCS on cell mortality rates during passaging, fresh media was supplemented with 25% conditioned media from the previous passage in an effort to reintroduce any low molecular weight (MW) growth factors excreted by the cells which may otherwise be lost. Unfortunately, even with sequential adaptation and supplementation with conditioned media, cell mortality continued to occur by passage 5.

Commercially available dialysed FCS was therefore disregarded as a viable media supplementation method. As an alternative, Gibco FCS was dialysed, thereby minimising the adaptation requirements of the cell line for successful growth. Dialysis was carried out as described in Materials and Methods 2.2.13.1. This form of dialysed FCS failed to improve the growth and longevity of cell lines in SILAC DMEM media.

6.3. Analysis and Comparison of SILAC Media Compositions

Having failed to sustain cell growth using SILAC-modified DMEM supplied by DCP, a comparison was carried out of the constituent components of the media provided by the company with standard Gibco $DMEM_{COMPLETE}$ normally used for culturing of Huh-7/Huh-7.5 cell lines. Comparing the two base media formulations, it became apparent that the DCP SILAC media was deficient in 20mM HEPES buffer found in Gibco $DMEM_{COMPLETE}$. This was a significant alteration from the expected formulation. HEPES buffer has an important role providing extra buffering capacity for metabolically active cells such as hepatocyte-derived cell lines. It was concluded that this lack of buffering resulted in a decrease in media pH values caused by excretion of metabolic by-products and the aforementioned cell mortality.

Having identified the most likely cause of cell death during adaptation, a replacement SILAC DMEM formulation was sourced from Thermo matching that provided by Gibco. Testing of the Thermo SILAC DMEM in same manner as described above showed efficient cell growth during sequential adaptation through to continual passaging of both cell lines using 100% self-dialysed Gibco FCS. Cell viability was assessed and found to reach 92%.

6.4. Huh-7/Huh-7.5 Comparative Proteome Analysis Using SILAC

Establishment of stable cell growth in the SILAC media allowed progression to analysis of samples by mass spectrometry (MS). Huh-7 samples were grown in the “light” non-isotopically labelled media, while the Huh-7.5 cell line was grown in media containing “heavy” labelled 13C lysine and arginine. Cells were harvested and proteins extracted for SDS-PAGE fractionation, followed by In-gel tryptic digestion and extraction of resultant peptides (Materials and Methods, Section 2.2.13.4). SILAC analysis was carried out in duplicate by Robin Antrobus (Cambridge Institute for Medical Research) using a Thermo Scientific LTQ Orbitrap and results processed using MaxQuant 1.3.0.2. As shown in Figure 1 [A], integration of the heavy labelled isotope tags was 97% efficient; the remaining 3% of light-labelled peptides can be accounted for during analysis, limiting its effects on quantitative accuracy.

Processing of resultant data generated a list of peptides detected during MS analysis and their associated heavy and light ratios for both samples. From this list, it was possible to allocate each peptide to its associated parent protein. These data were then used to generate

[A]

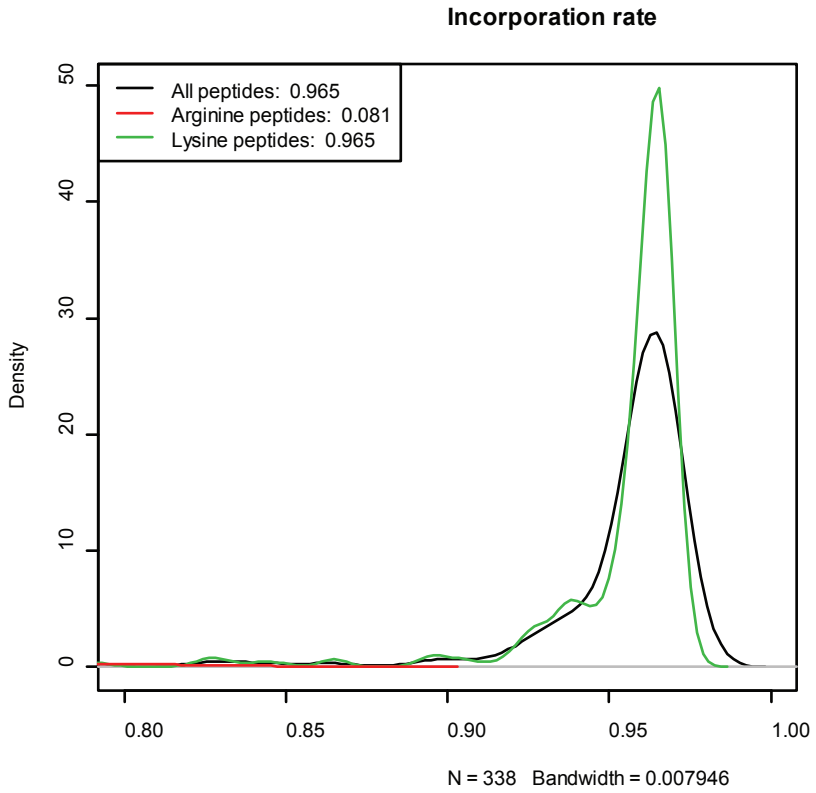

[B]

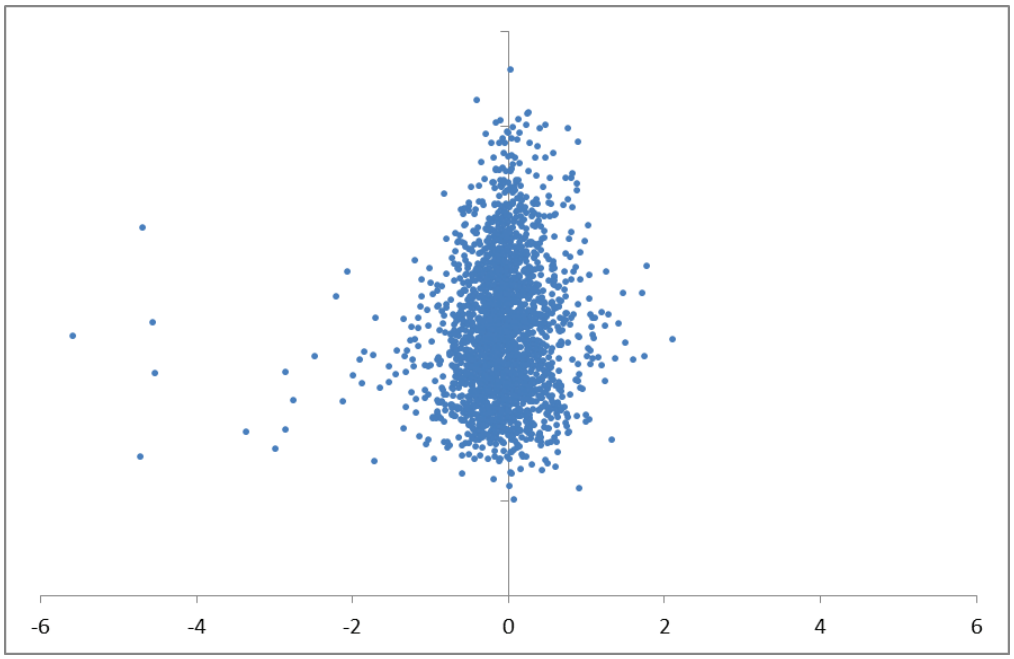

Figure 1. SILAC Comparative Analysis of Huh-7 Vs Huh7.5 Proteomes

[A] Integration analysis of heavy isotope labelled Lysine [B]Scatteplot showing log2 normalised Heavy (Huh-7.5)/Light (Huh-7) (H/L) ratios plotted against log10 intensity values. [C] Protein outliers with statistically significant values showing relative ratio between H/L samples.

[C]

Protein names	Gene names	Ratio H/L normalized	Intensity
FRAS1-related extracellular matrix protein 2	FREM2	-5.57787	6.76171
Keratinocyte proline-rich protein	KPRP	-4.718464	5.470072
Keratin, type II cytoskeletal 6B	KRT6B	-4.559724	6.899717
Saitohin	STH	-4.531423	6.357954
Dehydrogenase/reductase SDR family member 7B	DHRS7B	-3.35872	5.737383
Pro-MCH	PMCH	-2.983703	5.553834
CAP-Gly domain-containing linker protein 2	CLIP2	-2.860295	5.759381
Protein broad-minded	BROMI	-2.856528	6.371972
Pyruvate Dehydrogenase Phosphatase Regulatory Subunit	PDPR	-2.757794	6.077586
Exportin-5	XPO5	-2.483339	6.546703
Aldo-keto reductase family 1 member C1	AKR1C1	-2.209361	7.177738
Equilibrative nucleoside transporter 2	SLC29A2	-2.11904	6.066214
Protein S100-P	S100P	-2.062987	7.439932
Integrin alpha-5	ITGA5	-1.98633	6.342561
Filamin-C	FLNC	-1.90498	6.508853
Dual specificity mitogen-activated protein kinase kinase 3	MAP2K3	-1.869544	6.259068
Arylacetamide deacetylase	AADAC	-1.840888	6.59608
Histone H1.1	HIST1H1A	-1.725565	6.553859
LIM domain-containing protein 2	LIMD2	-1.707312	5.425094
Sequestosome-1	SQSTM1	-1.6997	6.950443
SNARE-associated protein Snapin	SNAPIN	-1.639804	6.205231
Multidrug resistance protein 1	ABCB1	-1.531156	6.269326
APOBEC1 complementation factor	A1CF	-1.529406	6.440657
Tubulin-folding cofactor B	TBCB	-1.442654	6.348052
Iron-sulfur protein NUBPL	NUBPL	-1.334753	6.934332
Prolow-density lipoprotein receptor-related protein 1	LRP1	-1.244104	6.858224
Integrin beta-1	ITGB1	-1.191458	7.563932
Integrin alpha-V	ITGAV	-1.11416	7.361293
Dihydrolipoyllysine-residue acetyltransferase component of pyruvate dehydrogenase complex, mitochondrial	DLAT	-1.01249	7.480007
NAD(P)H dehydrogenase [quinone] 1	NQO1	-0.9953045	7.3235
Alpha-fetoprotein	AFP	1.244887	6.871608
Dihydrofolate reductase	DHFR	1.245678	6.282984
Farnesyl pyrophosphate synthase	FDPS	1.264837	7.442464
Methylsterol monooxygenase 1	MSMO1	1.290955	6.982755
Ladinin-1	LAD1	1.332565	5.651879
Bile salt sulfotransferase	SULT2A1	1.369327	6.52106
Estradiol 17-beta-dehydrogenase 2	HSD17B2	1.420078	6.897424
Peptidyl-prolyl cis-trans isomerase FKBP11	FKBP11	1.47415	7.210479
Microsomal glutathione S-transferase 3	MGST3	1.505942	6.690701
Ubiquitin-conjugating enzyme E2 D3	UBE2D3	1.608242	6.512217
Anterior gradient protein 2 homolog	AGR2	1.720541	7.214923
F-box only protein 2	FBXO2	1.750392	6.545121
Hydroxymethylglutaryl-CoA synthase, cytoplasmic	HMGCS1	1.771548	7.505313
Arginase-1	ARG1	2.107219	6.722659

a scatterplot (Figure 1 [B]) of log2 heavy/light ratios of protein against the log10 of intensity values, yielding a “teardrop”-shaped cluster with a number of outliers. The slightly diffuse nature of the central cluster is expected to be general minor differences between the two cell lines (R. Antrobus, Personal Communication). Outliers with statistical significance are identified in Figure 1 [B]. Positive values within the Ratio H/L normalized column represent an upregulation of the specific protein while negative values represent a down-regulation of the associated protein within Huh-7.5 compared to Huh-7 cells.

Unfortunately, it was not possible to identify any variations in protein expression that may help elucidate the difference in viral replication permissiveness. The three targets identified with the greatest variation between cell lines are associated with epithelial skin cells and are therefore most likely contamination of the sample during processing (Smyth et al,2005). This downregulation is also an example of the effects of unlabelled protein on the skewing of results towards the unlabelled sample.

6.5. Discussion

Despite the failure to identify any targets, the methodology for establishing growth of Huh-7 cells in SILAC media provides a novel platform for further investigation into identifying the determinants for increased permissiveness of Huh-7.5 cells to HCV RNA replication. In the context of the study described, it is perhaps unsurprising that it was not possible to identify significant differences in protein expression between the two cell lines given the filial relationship of Huh-7.5 to Huh-7 cells and the global proteomic analysis carried out. Proteins that were identified represent the tip of a proteome iceberg, the dynamic range of protein levels within any sample, a combination of both protein abundance within the cell and efficiency of extraction from the lysate will usually be outside the capabilities of most MS systems, preventing full coverage of the cellular proteome{Thakur, 2011 512 /id}..

Adapting processing methodologies to enhance extraction of membrane-bound proteins might yield more in-depth results for that particular class of protein. Such an approach may yield more promising data since HCV RNA replication occurs at the ER membrane. Thus, there may be quantitative differences in host protein composition at sites of viral replication that could help to explain the differences in permissiveness between Huh-7 and Huh-7.5 cells. Separate from cell line comparisons, SILAC methodologies may be more suitable for the analysis of protein expression changes during viral infection or establishment of cells harboring subgenomic replicons. Preliminary experiments with this

objective using Huh-7/SGR-JFH1 cells failed due to an inability to establish stable cell growth in SILAC media. Indeed, the rapid cell mortality described above was accelerated in cells harbouring SGR-JFH1. With hindsight, this increased mortality may have been caused by the addition of G418 as the selection antibiotic in HEPES-deficient media; G418 is acidic and would cause an even greater decrease in pH. Re-evaluation using the protocol established at the end of the study with the appropriate suppliers of media may be more productive for identifying the proteins that could be involved in promoting HCV RNA replication.

7. Conclusions and Further Perspectives

7.1. Summary

By developing novel approaches to light and electron microscopy, this study has produced a number of findings which contribute to the understanding of the structure and location of sites of HCV RNA replication. The work described addresses the current paradigm of the architecture of replication sites, presenting evidence that is in support of recently published findings (Merz et al,2013;Ferraris et al,2010).

Chapter 3 focussed on developing super-resolution microscopy as an approach to further investigate the nature of viral replication sites and their relationship with cellular membranes. Firstly, an evaluation of current diffraction-limited microscopy methods examined the achievable resolution and deconvolution processing methods available to improve the quality of imaging datasets. Volume rendering methods were evaluated to ensure data fidelity throughout the processing pipeline and to identify possible sources of error.

Using the Huh-7/SGR-JFH1$_{NS5AGFP}$ cell line, examination of the GFP-NS5A signal revealed that previously observed punctate sites formed by NS5A were resolved to hollow, often multinucleated barrel-shaped structures. The dsRNA signal, employed as a marker for replicating viral RNA, which appears to colocalise with NS5A by CLSM microscopy, exhibited a nested configuration, residing within the hollow barrel structures resolved by OMX. Multinucleated structures apparently interacted with a number of dsRNA moieties residing within each of the spaces. The structure and localisation of these two viral components are indicative of viral replication sites, common to all positive-strand RNA viruses, typically characterised as membrane invaginations or spherules.

It was noted that there appeared to be two distinct populations of NS5A at putative replication foci, a small population of 300nm barrel structures alongside a larger population of smaller-sized indistinct objects. Utilising the modelling and quantification capabilities of the Imaris software package, these objects were identified, filtered based on diameter and the two populations quantified. However limitations in the sphere identification algorithms obviated accurate quantification of the two populations.

Channel alignment issues with the OMX dataset were identified during comparative analysis of quantitative signal correlation in CLSM and OMX datasets. Correction of this misalignment led to increased colocalisation within the dataset, although contrary to

expectation, colocalisation values were found to decrease with the increase in resolution. An in-depth investigation and comparison of the CLSM and OMX image capture and colocalisation methodologies highlighted a number of factors leading to this difference in correlation value. Through this analytical process, it became clear that differing values during OMX and CLSM imaging were not necessarily a decrease in colocalisation of the target proteins but instead the increased effects of inherent variation of the imaging technology combined with the correlation algorithms.

Having determined the particular characteristics of OMX microscopy datasets relative to current technologies, the study sought to re-evaluate the interaction of the hollow barrel-shaped structures with the surface of the ER membrane. Using the GFP-tagged Sec61β to visualise the ER membrane, the data revealed that the replication complex appears to sit distal to the membrane surface, as a spherule connected by a narrow "neck" of membrane. This result does not support the widely held view that HCV replication foci reside within membrane invaginations, a characteristic of other flaviviridae replication sites (Gillespie et al,2010;Welsch et al,2009;Paul et al,2013). By contrast, the data support recently published evidence suggesting that HCV replication foci mirror the membrane protrusions seen in the prototype RNA virus, poliovirus (Belov et al,2012;Merz et al,2013).

The data processing pipeline developed for evaluating the CLSM and OMX imaging data was also used to provide a quantitative analysis of the extent of colocalisation between two tagged forms of NS5A expressed from different cistrons in subgenomic replicons. Through quantitative colocalisation analysis, it was shown that the NS3-4B proteins were required for targeting and integration of the NS5A protein into sites of viral replication. The validation of the approach to evaluate colocalisation by a more robust statistical and non-subjective analysis opens opportunities for further studies on the cell biology of HCV RNA replication and assembly as well as for applications in studies on other viruses.

In addition to the super-resolution optical microscopy techniques developed in this study, a method for bridging the gap between optical and electron microscopy was investigated. A number of CLEM techniques were examined to combine the specificity of optical immunofluorescence with the ultrastructural detail provided by TEM.

Quantum dots (QDs) were investigated as a novel dual modality probe for use with CLEM microscopy, their high quantum yield and electron dense core making them ideal for both imaging modalities. Initial development failed to produce a probe conjugate and staining process which provided accurate and specific targeting of HCV replication sites. However,

the availability of new conjugation methods combined with access to a highly purified primary antibody allowed the production of a novel probe specific for the viral NS5A protein. Using this QD-NS5A antibody probe it was possible to accurately identify replication sites through CLSM imaging and correlate these with the same region by EM. Such images revealed that regions of high intensity fluorescence mapped to a complex region of lipid droplets and interwoven ER membrane.

As an adjunct to the imaging analysis, proteomic studies were conducted on Huh-7 and Huh-7.5 cells to try to determine whether the greater permissiveness of Huh-7.5 cells for viral replication could arise from differential expression of proteins. The approach utilised SILAC methods for differential labelling of proteins in the two cell lines. Testing of SILAC media identified a number of factors which affected maintenance of Huh-7/Huh-7.5 cells, allowing successful development of a protocol for the stable growth and labelling of both cell lines during cell culture. Although SILAC analysis of fractionated proteome samples failed to identify any significant differences between cell lines, the successful maintenance of cell lines within the media provides the opportunity for further analysis of both cell lines under a variety of conditions (e.g infection or treatment with agents that modulate expression such as IFN-α).

7.2. Applications of Imaging Technology to Examine the HCV Lifecycle

The level of detail provided by super-resolution could prove invaluable in further elucidating not just the fine structure and cellular interactions of the HCV replication complex but other aspects of the viral lifecycle. In this study, OMX imaging techniques were applied to re-evaluate the previously published confocal microscopy data that has formed the basis of the current structure and location paradigm of the replication stage of the lifecycle. Application of the OMX has provided the highest resolution images by light microscopy of replication sites and supports the emerging body of evidence questioning the membrane invaginations induced by replication complex formation.

While investigation of the entire life cycle of infectious virus was not possible due to the current facility restrictions on handling a Hazard Group 3 pathogen, in principle there are no limitations to the use of OMX with the HCVcc system. Without these limitations the infectious model system could be explored by super-resolution microscopy.

Considering the unique insight provided by super-resolution to our understanding of the architecture of the viral replication complex, there is a case for a systematic review of the observed optical imaging data for the different stages of HCV infection using this approach. One aspect of the replication process not addressed in this study is the role and sequestration of lipid droplets to sites of viral RNA replication. Previous reports have indicated a high level of qualitative colocalisation and interaction between the core and NS proteins with the surface of lipid droplets. CLSM has shown NS5A associates with regions of the surface of lipid droplets that also stain for core protein, exhibiting a diameter slightly greater than that of the core signal itself. The close proximity of such core/NS5A-lipid droplets to the ER membrane has prompted suggestions that core recruits both free NS proteins and the replication complex itself to lipid droplet-associated membranes (Miyanari et al,2007;Boulant et al,2006). While current optical imaging data of the core/NS5A/lipid droplet interaction merely show a level of colocalisation, determining the juxtaposition of the components sites at the edge of current CLSM resolution (Miyanari et al,2007). Re-examining the juxtaposition of the viral proteins at replication sites and on the surface of lipid droplets may give greater insight into the possible location of sites of assembly. For example, the data presented here suggests that there are 2 populations of structures targeted by NS5A with the larger barrel-shaped entities considered to possibly represent active replication sites. It would be of interest to determine whether lipid droplets are found associated at a higher frequency with the barrel-shaped structures compared to the non-structured sites. If so, this could indicate a selective process in the positioning of lipid droplets to sites of replication. Indeed, it may be the case that there are direct connections between lipid droplets and replication sites to aid transfer of viral RNA to sites where virion assembly initiates. In this regard, it has been shown recently that MAVS, an adaptor protein for RIG-I, the pathogen recognition receptor, is targeted to a synapse between mitochondria and the ER membrane, which has been termed the mitochondrial-associated membrane (Horner et al,2011). MAVS is cleaved by the NS3/4A protease, thereby disrupting RIG-I signalling. Current evidence suggests that this synapse is a ‘bridge’ connecting mitochondria and the ER rather than direct contact between the two organelles (M. Gale, personal communication). Identification of this structure was only possible through higher resolution imaging by both light and electron microscopy. Similar studies using the power of immunofluorescence with super-resolution, allied to the correlative EM methods described here, would enable more detailed examination of possible links between sites of viral RNA replication and lipid droplets.

Another area not addressed by this study is the involvement and function of host factors in HCV RNA replication. Of particular interest is the membrane-bound lipid kinase, phosphatidylinositol 4-kinase, subtype III alpha (PI4KIIIα) which is critical for formation of the membranous web from previous studies (Berger et al,2009). PI4KIIIα binds to NS5A, which in turn stimulates its kinase activity, thereby generating phosphatidylinositol 4-phosphate (PI4P) (Reiss et al,2011;Reiss et al,2013).The levels of PI4P are increased approximately 3-fold and accumulate at cytoplasmic punctuate foci. These foci only partially overlap with NS5A and hence the proximity of PI4P to sites of viral RNA replication remains unclear. Similarly, HCV RNA replication induces cytoplasmic foci containing polyubiquitin but their relationship to the membranous web is not known (V Schregel, personal communication). Using the approaches developed here, for example with super-resolution and statistical analysis, would help to unravel the nature of the interactions between these cellular pathways and replication sites. More broadly, the pipelines from this study could be employed for any virus system and potentially shed new light on virus-host interactions.

A further application would be to apply the live cell capability of OMX to cells harbouring the subgenomic replicon that expresses GFP-tagged NS5A. This could give greater insight into the formation and dynamics of replications sites. Currently, the greatest limitation to live cell imaging is the temporal sampling rate available for 3-D multichannel analysis. Standard CLSM techniques are restricted to approximately 1 3-D image/sec, thus any process occurring on a subsecond timescale lies outside the temporal resolution of most systems. While advances such as resonant scanning may increase the temporal resolution of CLSM systems, the non linearity of scanning velocity, however the ultra short pixel dwell times in these systems result in poor signal to noise ratios and are ill suited to the work carried out within this project. While spinning disc systems provide high speed capture of thin optical sections similar to CLSM, the low level of light transmission through the disc, combined with the high levels of light reflected by the disc again result in a poor signal to noise ratio for low fluorescence samples. By contrast, the OMX system achieves between 2 and 10 3-D images/sec while still maintaining an excellent signal to noise ratio. Combined with the greater spatial resolution, OMX could therefore be an ideal platform for investigations into trafficking of viral proteins and the dynamics of their attachment to the membranous web (Dobbie et al,2011).

From the results described previously it is clear that the major benefits of OMX technology may lie in its live cell imaging capabilities, while there is a significant increase in

resolution over CLSM systems there are a number of other super resolution techniques which may provide higher resolution and more accurate spatial correlation. REversible Saturable Optical Fluorescence Transitions (RESOLFT) methodologies use photoswitchable fluorescent probes that can be reversibly switched between a fluorescent on state and fluorescent dark off state {Huang, 2009 515 /id}. Techniques such as PhotoActivated Localization Microscopy (PALM) and stochastic optical reconstruction microscopy (STORM) use low level laser intensities to ensure any given fluorophore has a low probability of being activated, the image collected at this stage should therefore be a small number of spatially distributed airy discs. The centroid of each airy disc can be identified accurately. By repeating this process a number of images are collected, each with a stochastically unique subset of fluorophores, the position of the individual molecules can be identified and a summed image generated from this dataset {Hofmann, 2005 516 /id}. The accuracy of the location of each molecule is determined by the number of photons that can be collected from each emitter, therefore a large series of images must be combined to generate an accurate image. In this manner, resolution of 50-100nm in the XY plane can be achieved, significantly higher than that of OMX microscopy. Due to the long acquisition times necessary to acquire the image numbers required for this methodology, combined with the specialised media required for quenching make these techniques suitable only for fixed cell imaging. Unfortunately such methodologies were unavailable for use during this project but may provide the accuracy and resolution required to investigate the viral replication complex further.

7.3. Applications for Quantum Dots as Intracellular Probes

This study undertook an ambitious project to develop QDs as intracellular probes using HCV RNA replication sites as a model system. The justification for selecting QDs for this purpose was 2-fold. Firstly, QDs offer advantages over organic fluorophores in terms of their spectral properties and secondly, the possibility of detecting them as objects by EM. Combining both properties would then potentially make them ideal for CLEM.

7.3.1. Development of Quantum Dots as Detectors of Intracellular Viral Components

Investigating the numerous host and viral factors involved in HCV RNA replication through standard immunofluorescence methodologies is hindered by the spectral overlap of the various organic fluorophores currently available. Such issues can be overcome with QDs as they possess an extremely narrow emission spectra and single excitation wavelength that is an inherent property of nanocrystal technology. This property opens the possibility for multiplexing, enabling a range of probes with distinct spectral characteristics conjugated to different antibodies to be used for investigating multiple factors in the same cell (Deerinck,2008). The one barrier to developing such a toolkit is the ready availability of antibody reagents for conjugation. However, the study presented here provides proof-of-concept that purified antibodies with high specificity can be ideal probes following conjugation to QDs. The added advantage of QDs is that they can avoid difficulties with probing cells using multiple antibodies raised against the same species. For example, the antibodies that detect the viral NS3 protein and viral dsRNA are both monoclonal antibodies, this presents problems with indirect immunofluorescence as any secondary antibody (raised in mouse) would detect both primary antibodies. It would be possible to conjugate either antibody to QDs with different spectral properties to enable such combinations and indeed use other monoclonal antibodies to multiplex for other factors. Thus, there is significant potential for probing cells for multiple factors, which would avoid the current limitations of indirect immunofluorescence.

Another possible use for QDs is for internalisation and probing intracellular events by live cell imaging. In the study presented here, the fixed nature of the samples limit our understanding of replication dynamics. During the course of the study, digitonin permeabilisation was investigated as a method for delivery of QDs into live cells for long-term study. Preliminary results were promising, showing staining in live cells after 72hrs. Although the QDs used were non-specific, it would have been interesting to attempt such experiments with the QD-NS5A probe that was produced towards the end of the project. The low toxicity, high quantum yield and resistance to photobleaching could make QDs preferable candidates for the real-time examination of events in live cells compared to GFP. Following on from the application set out above, the ability to insert functionalised QDs into live cells without any observable deleterious effects may then be combined with their multiplexing capability so that a number of target proteins could be simultaneously imaged in the same cell.

7.3.2. Quantum Dots for Detecting Intracellular Structures by CLEM

One of the reasons for the development of QDs as CLEM probes was their ability to be visualised by EM. Although this aim was not achieved with the available microscope, it is feasible that failure to identify the nanocrystals by EM could be due to the limited information available for commercial probes. An alternative approach could be to custom-manufacture QDs with pre-defined physical properties required for any particular project.

Despite the inability to directly visualise QDs, their use with CLEM did demonstrate it was possible to overlay fluorescence images collected by light microscopy onto EM tomograms. This approach did identify the convoluted and complex structures that make up the membranous web. While attempts to model the replication site using tomography were limited by time constraints, there are now few technical hurdles to build on the experimental strategy that has been developed.

One possible extension of the QD/CLEM methodology would exploit the long-term physical and photochemical stability of the nanocrystals to tag virus particles *in situ* during release from infected cells. For example, QDs can be targeted to a number of membranes in live cells, bound using chitosan-coated probes to produce positively-charged nanoparticles. During assembly and release of infectious virions, QDs attached to host membranes would be recruited to form the viral envelope, thereby producing a population of infectious QD-tagged virus (Chen et al,2010). QD-coated virus particles could then be analysed to elucidate the mechanisms underlying particle trafficking during virus entry. In a similar manner to previous investigations utilising the HCV_{PP} system, harvested virus can be applied to naive Huh-7 cells grown on live cell dishes and the fluorescent signal of the QD-labelled virions particle tracked by live cell microscopy. By following virus particles in real time, it should be possible to image virions at various stages of attachment and entry using fluorescence microscopy. The infected cell can then be mapped with the grid reference system used in CLEM and the sample fixed using chemical or cryo-techniques.

Traditional sample processing for EM imaging of biological samples would then require a form of sectioning to produce thin samples for TEM. However, identifying the particular region of the cell or sample containing tagged virions becomes more difficult as the number of processing steps increases. One method to circumvent this particular problem is the utilisation of Focused Ion Beam Scanning Electron Microscopy (FIB-SEM) to generate a 3-D “Z-stack” of the sample in a manner similar to 3-D CLSM. FIB-SEM uses a raster scanning electron beam to interact with the surface atoms of the sample, creating an image

composed of the secondary incident electrons released from the surface. Following image acquisition, a focused beam of ions, typically Ga^{+}, is used to ablate the surface of the sample to a depth of several nanometres. This process of imaging/ablation is then repeated throughout the sample to produce a number of image slices that can be reconstructed to provide a 3-D model of the sample (Volkert et al,2007;Earl et al,2013).

Having identified the regions of virus binding and trafficking within the cell, the particle and surrounding cellular ultrastructure can be identified by the electron dense QDs coating the virion. By applying this method to a time course analysis of the various stages of binding, entry and trafficking, identified by CLSM, it should be possible to provide a level of temporal resolution or "snapshots" of the various stages of the virus lifecycle at an ultrastructural level. Proof of concept for applying QDs to label virions has been successfully demonstrated for influenza virus and the approach has enabled studies on the dynamic trafficking of labelled virions at the single particle level (Liu et al,2013). There has been success with labelling the core protein in HCV virions using a tetracysteine tag to examine trafficking of the protein during the early stages of infection (Coller et al,2012). Combining this approach with labelling the virion envelope with QDs would offer the possibility for new insight into the relative dynamics of the viral envelope and the protein that forms the nucleocapsid. Clearly, this could have wider applications in virology aside from HCV.

References

2002 National institutes of health consensus development conference statement: Management of Hepatitis C Hepatology **36** 3-20

FEI, 2006 All you wanted to know about Electron Microscopy http://web.pdx.edu/~pmoeck/pdf/all%20you%20wanted%20to%20know%20about%20electron%20microscopy.pdf [31 August 2013]

Media Cybernetics 2008 AutoDeblur User Manual http://www.bitplane.com/download/manuals/ADX210/AutoDeblurUserGuideX.pdf [2 February 2013]

University of Dundee 2010 SULSA OMX Dundee Sample Preparation, http://microscopy.lifesci.dundee.ac.uk/docs/DundeeOMX_SamplePreparation.pdf [4 June 2013]

The British Museum 2012 The Nimrud lens/ the Layard lens Collection Database.The British Museum. http://www.britishmuseum.org/research/collection_online/collection_object_details.aspx?objectId=369215&partId=1 [12 Januray 2013]

Microscopy Society of America 2012 Otto Scherzer: The father of aberration correction http://www.microscopy.org/images/posters/Scherzer.pdf [23 March 2013]

Adrian, M., Dubochet, J., Lepault, J., and McDowall, A. W. 1984 Cryo-electron microscopy of viruses Nature **308** 32-36

Aebersold, R. H. and Mann, M. 2003 Mass spectrometry-based proteomics Nature **422** 198-207

Afdhal, N. H. 2002 Supporting the patient with chronic hepatitis during treatment Clin.Gastroenterol.Hepatol. 211-232

Akner, G., Mossberg, K., Wirkstrom, A-C., Sundqvist, K-G., and Gustafsson, J-A. 1991 Evidence for colocalization of glucocorticoid receptor with cytoplasmic microtubules in human gingival fibroblasts, using two different monoclonal anti-gr antibodies, confocal laser scanning microscopy and image analysis. J.Steroid.Biochem.Mol.Biol. **39** 419-432

Alter, H. J., Purcell, R. H., Holland, P. V., and Popper, H. 1978 Transmissible agent in non-A, non-B hepatitis Lancet **8062** 459-463

Alter, H. J. and H. G. Klein. 2008. The hazards of blood transfusion in historical perspective. Blood **112**:2617-2626.

Alter, H. J., Purcell, R. H., Shih, J. W., Melpolder, J. C., Houghton, M., Choo, Q, and Kuo, G. 2010 Detection of antibody to hepatitis C virus in prospectively followed transfusion recipients with acute and chronic non-A, non-B hepatitis N.Eng.J.Med. **321** 1494-1500

Alter, M. J. 2007 Epidemiology of hepatitis C virus infection World J.Gastroenterol. **13** 2436-2441

Amako, Y., Sarkeshik, A., Hotta, H., Yates, J. R., and Siddiqui, A. 2009 Role of Oxysterol Binding Protein in Hepatitis C Virus Infection J.Virol **83** 9237-9246

Andre, P., Komurian-Pradel, F., Deforges, S., Perret, M., Berland, J. L., Sodoyer, M., Pol, S., Bréchot, C., Paranhos-Baccalà, G., and Lotteau, V. 2002 Characterization of low- and very-low-density hepatitis C virus RNA-containing particles J.Virol **76** 6919-6928

Appel, N., Herian, U., and Bartenschlager, R. 2005 Efficient rescue of hepatitis C virus RNA replication by trans-complementation with nonstructural protein 5A J.Gen.Virol. **79** 896-909

Appel, N., Zayas, M., Miller, S., Krijnse-Locker, J., Schaller, T., Friebe, P., Kallis, S., Engel, U., and Bartenschlager, R. 2008 Essential Role of Domain III of Nonstructural Protein 5A for Hepatitis C Virus Infectious Particle Assembly PLOS Pathogens **4** 1-14

Ashfaq, U. A., Khan, S. N., Nawaz, Z., and Riazuddin, S. 2011 In-vitro model systems to study Hepatitis C Virus Genet.Vaccines.Ther. **9** 7

Aston, F. W. 1919 A positive ray spectrograph Philos.J. **38** 707-714

Ball, G., Parton, R. M., Hamilton, R. S., and Davis, I 2012 Chapter Two - A Cell Biologist's Guide to High Resolution Imaging Methods Enzymol. **504** 29-55

Bandeira, N., Pham, V., Pevzner, P., Arnott, D., and Lill, J. R. 2008 Beyond Edman Degradation: Automated *De novo* Protein Sequencing of Monoclonal Antibodies Nat.Biotechnol. **12** 1336-1338

Bantscheff, M., Schirle, M., Sweetman, G., Rick, J., and Kuster, B. 2007 Quantitative mass spectrometry in proteomics: a critical review Anal.Bioanal.Chem. **389** 1017-1031

Bartenschlager, R., Penin, F., Lohmann, V., and Andre, P. 2011 Assembly of infectious hepatitis C virus particles. Trends Microbiol. **19** 95-103

Bartosch, B., Dubuisson, J., and Cosset, F-L. 2003 Infectious Hepatitis C Virus Pseudo-particles Containing Functional E1-E2 Envelope Protein Complexes J.Exp.Med **197** 633-642

Bartosch, B., Vitelli, A., Granier, C., Goujon, C., Dubuisson, J., and Pascale, S. 2003 Cell entry of hepatitis C virus requires a set of co-receptors that include the CD81 tetraspanin and the SR-BI scavenger receptor. J.Biol.Chem. **278** 41624-41630

Batschelet, E., Domingo, E., and Weissmann, C. 1976 The proportion of revertant and mutant phage in a growing population as a function of mutation and growth rate. Gene **1** 27-32

Baumert, T. F., Ito, S., Wong, D. T., and Liang, T. J. 1998 Hepatitis C Virus Structural Proteins Assemble into Viruslike Particles in Insect Cells Am.Soc.Micro. **72** 3827-3836

Belov, G. A., Nair, V., Hansen, B. T., Hoyt, F. H., Fischer, E. R., and Ehrenfeld, E. 2012 Complex dynamic development of poliovirus membranous replication complexes J.Virol **86** 302-312

Benga, W. J. A., Krieger, S. E., Dimitrova, M., Zeisel, M. B., Parton, R. M., Lupberger, J., Hildt, E., Luo, G., McLauchlan, J., Baumert, T. F., and Schuster, C. 2009 Apolipoprotein E Interacts with Hepatitis C Virus Nonstructural Protein 5A and Determines Assembly of Infectious Particles Hepatology **51** 43-53

Berenguer, M. and Wright, T. L. 1999 Hepatitis C and liver transplantation Gut **45** 159-163

Berger, K. L., Cooper, J. D., Heaton, N. S., Yoor, R., Oakland, T. E., Jordan, T. X., Mateu, G., Grakoui, A., and Randall, G. 2009 Roles for endocytic trafficking and phosphatidylinositol 4-kinase III alpha in hepatitis C virus replication Proc.Natl.Acad.Sci.USA **106** 7577-7582

Berman, M., H. J. Alter, K. G. Ishak, R. H. Purcell, and E. A. Jones. 1979. The Chronic Sequelae of Non-A, Non-B Hepatitis. Ann.Int.Med. **91**:1-6.

Bienz, K., Egger, D., and Pasamontes, L. 1987 Association of polioviral proteins of the P2 genomic region with the viral replication complex and virus-induced membrane synthesis as visualized by electron microscopic immunocytochemistry and autoradiography

Binder, M., Quinkert, D., Bochkarova, O., Klein, R., Kezmic, N., Bartenschlager, R., and Lohmann, V. 2007 Identification of Determinants Involved in Initiation of Hepatitis C Virus RNA Synthesis by Using Intergenotypic Replicase Chimeras J.Virol **81** 5270-5283

Binder, M., Kochs, G., Bartenschlager, R., and Lohmann, V. 2007 Hepatitis C virus escape from the interferon regulatory factor 3 pathway by a passive and active evasion strategy Hepatology **46** 1365-1374

Binder, M., Sulaimanov, N., Clausznitzer, D., Schulze, M., Hüber, C. M., Lenz, S. M., Schlöder, J. P., Trippler, M., Bartenschlager, R., Lohmann, V., and Kaderali, L. 2013 Replication vesicles are load- and choke-points in the hepatitis C virus lifecycle PLOS Pathogens **9**

Blaising, J. and Pecheur, E-I. 2012 Lipids - A key for hepatitis C virus entry and a potential target for antiviral strategies Biochimie 1-7

Blanchard, E., Belouzard, S., Goueslain, L., Wakita, T., Dubuisson, J., and Wychowski, C. 2006 Hepatitis C virus entry depends on clathrin-mediated endocytosis. J.Virol **80** 6964-6972

Blasiole, D. A., Davis, R. A., and Attie, A. D. 2007 The physiological and molecular regulation of lipoprotein assembly and secretion Mol.Biosyst **9** 608-619

Blight, K. J., Kolykhalov, A. A., and Rice, C. M. 2000 Efficient Initiation of HCV RNA Replication in Cell Culture Science **290** 1972-1974

Blight, K. J., McKeating, J. A., and Rice, C. M. 2002 Highly Permissive Cell Lines for Subgenomic and Genomic Hepatitis C Virus RNA Replication J.Virol **76** 13001-13014

Blight, K. J., McKeating, J. A., Marcotrigiano, J., and Rice, C. M. 2003 Efficient replication of hepatitis C virus genotype 1a RNAs in cell culture J.Virol **77** 3181-3190

Bolte, S. and Cordelières, F. P. 2006 A guided tour into subcellular colocalization analysis in light microscopy J.Microsc **224** 213-232

Born, M. and Wolf, E. 1999 Principles of Optics

Boulant, S., Montserret, R., Hope, G., Ratinier, M., Targett-Adams, P., Lavergne, J-P., Penin, F., and McLauchlan, J. 2006 Structural Determinants That Target the Hepatitis C Virus Core Protein to Lipid Droplets J.Biol.Chem. **281** 22236-22247

Boulant, S., Targett-Adams, P., and McLauchlan, J. 2007 Disrupting the association of hepatitis C virus core protein with lipid droplets correlates with a loss in production of infectious virus J.Gen.Virol. **88** 2204-2213

Bozzola, J. J. and Russell, L. D. 1999 Electron Microscopy: Principles and Techniques for Biologists

Bracewell, R. N. 1999 The Fourier Transform and It's Applications

Bradley, D. W., Maynard, J. E., and Popper, H. 1981 Persistent non-A, non-B hepatitis in experimentally infected chimpanzees J.Inf.Dis. **143** 210-218

Bradley, D. W., McCaustland, K. A., Cook, E. H., Schable, C. A., Ebert, J. W., and Maynard, J. E. 1985 Posttransfusion non-A, non-B hepatitis in chimpanzees. Physicochemical evidence that the tubule-forming agent is a small, enveloped virus. Gastroenterology **88** 773-779

Bradley, D. W., McCaustland, K. A., Krawczynski, J., Spelbring, C., Humphrey, C., and Cook, E. H. 1991 Hepatitis C Virus: Buoyant Density of the Factor VIII-Derived Isolate in Sucrose J.Med.Virol. **34** 206-208

Brass, V., Bieck, E., Montserret, R., Wolk, B., Hellings, J. A., Blum, H. E., Penin, F., and Moradpour, D. 2001 An Amino-terminal Amphipathic α−Helix Mediates Membrane Association of the Hepatitis C Virus Nonstructural Protein 5A J.Biol.Chem. **277** 8130-8139

Braun, F. 1897 Ueber ein Verfahren zur Demonstration und zum Studium des zeitlichen Verlaufes variabler Strome [On a technique for the demonstration and for the study of the course of variable currents] Annalen der Physik und Chemie **60** 552-559

Brönstrup, M. 2004 Absolute quantification strategies in proteomics based on mass spectrometry Expert Rev.Proteomics. **1** 503-512

Brönstrup, M. 2004 Absolute quantification strategies in proteomics based on mass spectrometry Expert Rev.Proteomics. **1** 503-512

Brunnée, C. 1987 The Ideal Mass Analyser Int.J.Mass.Spectrom. **76** 125-237

Buseck, P., Cowley, J. M., and Eyring, E. 1988 High-Resolution Transmission Electron Microscopy: And Associated Techniques

Campisi, P. and Egiazarian, K. 2007 Blind Image Deconvolution: Theory and Applications

Carlsson, K., Danielsson, P. E., Lenz, R., Liljeborg, A., Majlof, L., and Aslund, N. 1985 Three-dimensional microscopy using a confocal laser scanning microscope Opt.Lett. **10** 53-55

Carrasco, L. 1995 Modification of membrane permeability by animal viruses Adv.Virus.Res. **45** 61-112

Carrere-Kremer, S., Montpellier-Pala, C., and Cocquerel, L. 2002 Subcellular Localization and Topology of the p7 Polypeptideof Hepatitis C Virus J.Virol **76** 3720-3730

Catanese, M. T., Ansuini, H., Graziani, R., Huby, T., Moreau, M., and Ball, J. K. 2010 Role of scavenger receptor class B type I in hepatitis C virus entry: kinetics and molecular determinants. J.Virol **84** 34-43

Catanese, M. T., Uryu, K., Kopp, M., Edwards, T. J., Andrus, L., Rice, W. J., Silvestry, M., Kuhn, R. J., and Rice, C. M. 2013 Ultrastructural analysis of hepatitis C virus particles Proc.Natl.Acad.Sci.USA **110** 9505-9510

Chalfie, M., Tu, Y., Euskirchen, G., Ward, W. W., and Prasher, D. C. 1994 Green Fluorescent Protein as a Marker for Gene Expression Science **263** 802-805

Champness, P. E. 2001 Electron Diffraction in the Transmission Electron Microscope

Chang, K-S, Jiang, J., Cai, Z., and Luo, G. 2007 Human Apolipoprotein E is Required for Infectivity and Production of Hepatitis C Virus in Cell Culture J.Virol **81** 13783-13793

Chaumeil, J., Augui, S., Chow, J. C., and Heard, E. 2008 Combined Immunofluorescence, RNA Fluorescent In Situ Hybridisation, and DNA Fluorescent In Situ Hybridisation to Study Chromatin Changes, Transcriptional Activity, Nuclear Organization, and X-Chromosome Inactivation Methods.Mol.Biol. **463** 297-308

Chen, H., Swedlow, J. R., Grote, M., Sedat, J. W., and Agard, D. A. 1995 The Collection, Processing, and Display of Digital Three-Dimensional Images of Biological Specimens Handbook of Biological Confocal Microcsopy 197-210

Chen, Y-H., Wang, C-H., Chang, C-W, and Peng, C-A. 2010 *In Situ* formation of viruses tagged with quantum dots Integr.Biol. **2** 258-264

Chernushevich, I. V., Loboda, A. V., and Thomson, B. A. 2001 An introduction to quadrupole-time-of-flight mass spectrometry J.Mass Spectrom. **36** 849-865

Choo, Q, Weiner, A. J., Overby, L. R., Kuo, G., Houghton, M., and Bradley, D. W. 1990 Hepatitis C virus: The major causative agent of viral non-A, non-B hepatitis Br.Med.Bull. **46** 423-441

Choo, Q, Richman, K. H., Han, J., Berger, K., Lee, C., Dong, C., Gallegos, C., Coit, D., Medina-Selby, A., Barr, P. J., Weiner, A. J., Bradley, D. W., Kuo, G., and Houghton, M.

1991 Genetic organization and diversity of the hepatitis C virus Proc.Natl.Acad.Sci.USA **88** 2451-2455

Choo, Q., Kuo, G., Weiner, A. J., Overby, L. R., Bradley, D. W., and Houghton, M. 1989 Isolation of a cDNA clone Derived from a Blood-Borne Non-A, Non-B Viral Hepatitis Genome Science **244** 359-362

Claude, A. 1948 Studies on cells: Morphology, chemical constitution of and distribution of biochemical functions. Harvey Lecture **43** 1921-1964

Cocquerel, L., Voisset, C., and Dubuisson, J. 2006 Hepatitis C virus entry: potential receptors and their biological functions J.Gen.Virol. **87** 1075-1084

Coller, K. E., Berger, K. L., Heaton, N. S., Cooper, J. D., Yoon, R., and Randell, G. 2009 RNA interference and single particle tracking analysisof hepatitis C virus endocytosis PLOS Pathogens **5** 1-14

Coller, K. E., Heaton, N. S., Berger, K., Cooper, J. D., Saunders, J. L., and Randall, G. 2012 Molecular determinants and dynamics of hepatitis C virus secretion PLOS Pathogens **8**

Comisarow, M. B. and Marshall, A. G. 1974 Fourier Transform Ion Cyclotron Resonance Spectroscopy Chem.Phys.Lett. **25** 282-283

Coone, E. D., Shaw, M. K., and Vaux, D. J. 2008 Anti-biotin antibodies offer superior organelle-specific labelling of mitochondria over avidin or streptavidin Methods.Mol.Biol. **418** 157-170

Cormier, E. G., Durso, R. J., Tsamis, F., Boussemart, L., Manix, C., Olson, W. C., Gardner, J. P., and Dragic, T. 2004 L-SIGN (CD209L) and DC-SIGN (CD209) mediate transinfection of liver cells by hepatitis C virus Proc.Natl.Acad.Sci.USA **101** 14067-14072

Cormier, E. G., Tsamis, F., Kajumo, F., Durso, R. J., Gardner, J. P., and Dragic, T. 2004 CD81 is an entry coreceptor for hepatitis C virus Proc.Natl.Acad.Sci.USA **101** 7270-7274

Cortese, K., Diaspro, A., and Tacchetti, C. 2009 Advanced Correlative Light/Electron Microscopy: Current Methods and New Developments Using Tokuyasu Cryosections J.Histochem.Cytochem. **57** 1103-1112

Costella, A. 2008 "Hepatitis C in the UK" The Health Protection Agency Annual Report 2008 Health Protection Agency Centre for Infections

Costes, S. V., Daelemans, D., Cho, E. H., Dobbin, Z., and Pavlakis, G. 2004 Automatic and Quantitative Measurement of Protein-Protein Colocalization in Live Cells Biophysics **86** 3993-4003

Counihan, N. A., Rawlinson, S. M., and Lindenbach, B. D. 2011 Trafficking of Hepatitis C Virus Core Protein during Virus Particle Assembly PLOS Pathogens **7** 1-14

Dabbousi, B. O., Rodriguez-Viejo, T., Mikulec, F. V., Heine, J. R., Mattoussi, H., Ober, R., Jensen, K. F., and Bawendi, M. G. 1997 (CdSe)ZnS Core-Shell Quantum Dots:

Synthesis and Characterization of a Size Series of Highly Luminescent Nanocrystallites J.Phys.Chem. **101** 9463-9475

Dales, S., Eggers, H. J., Tamm, I., and Palade, G. E. 1965 Electron microscopic study of the formation of poliovirus Virology **26** 379-389

Dane, D. S., C. H. Cameron, and M. Briggs. 1970. Virus-Like Particles In Serum Of Patients With Australia-Antigen-Associated Hepatitis. Lancet **295**:695-698. doi:doi: DOI: 10.1016/S0140-6736(70)90926-8.

Daumas, M. 1989 Scientific Instruments of the Seventeenth and Eighteenth Centuries and Their Makers

Davidson, M. W. 2003 Molecular Expressions: Science, Optics and You -Timeline - Zacharias Janssen

de Broglie, L. 1925 *Recherches sur la theorie des quanta* (Researches on the Theory of Quanta), Thesis Ann.de Phys. **10**

de Felipe, P., Hughes, L. E., Ryan, M. D., and Brown, J. D. 2003 Co-translational, Intraribosomal Cleavage of Polypeptides by the Foot-and-mouth Disease Virus 2A Peptide J.Biol.Chem. **278** 11441-11448

Dean, J. A. 1992 Lange's Handbook of Chemistry

Deerinck, T. J. 2008 The Application of Fluorescent Quantum Dots to Confocal, Multiphoton and Electron Imaging Toxicol.Pathol. **36** 112-116

Demandolx, D. and Davoust, J. 1997 Multicolor analysis and local image correlation in confocal microscopy J.Microsc **185** 21-36

Dempster, A. J. 1918 A New Method Of Positive Ray Analysis Phys.Rev. **11** 316-325

den Boon, J. A. and Ahlquist, P. 2010 Organelle-Like Membrane Compartmentalization of Positive-Strand RNA Virus Replication Factories Annu.Rev.Microbiol. **64** 241-256

Dienstag, J. L. 1983 Non-A, non-B hepatitis. Recognition, epidemiology, and clinical features. Gastroenterology **85** 439-462

Dienstag, J. L. and Alter, H. J. 1986 Non-A, non-B hepatitis: evolving epidemiological and clinical perspective. Semin.Liver Dis. **6** 67-81

Dobbie, I. M., King, E., Parton, R. M., Carlton, P. M., Sedat, J. W., Swedlow, J. R., and Davis, I 2011 OMX: A New Platform for Multimodal, Multichannel Wide-Imaging Cold.Spring.Harb.Prot. 899-909

Domingo, E., Martinez-Salas, E., Sobrino, F., de la Torre, J. C., Portela, A, Ortin, J., Lopez-Galindez, C., Perez-Brena, P., Villanueva, N., Najera, R., VandePol, S., Steinhauer, D. A., DePolo, N., and Holland, J. J. 1985 The quasispecies (extremely heterogeneous) nature of viral RNA genome populations: biological relevance - a review Gene **40** 1-8

Domingo, E. 1989 RNA virus evolution and the control of viral disease Prog.Drug.Res. **33** 93-133

Domon, B. and Aebersold, R. H. 2006 Mass Spectrometry and Protein Analysis Science **312** 212-217

Dubochet, J. and McDowall, A. W. 1981 Vitrification of pure water for electron microscopy J.Microsc **124** 3-4

Dubuisson, J., Hsu, H. H., Cheung, R. C., Greenberg, H. B., Russell, D. G., and Rice, C. M. 1994 Formation and Intracellular Localization of Hepatitis C Virus Envelope Glycoprotein Complexes Expressed by Recombinant Vaccinia and Sindbis Viruses J.Virol **68** 6147-6160

Dubuisson, J., Penin, F., and Moradpour, D. 2002 Interaction of hepatitis C virus proteins with host cell membranes and lipids Trends.Cell.Biol. **12** 517-523

Dunn, K. W., Kamocka, M. M., and McDonald, J. H. 2011 A practical guide to evaluating colocalization in biological microscopy

Dykstra, M. J. 1993 A manual of Applied Techniques for Biological Electron Microscopy

Earl, L. A., Lifson, J. D., and Subramaniam, S. 2013 Catching HIV 'in the act' with 3D electron microscopy Trends Microbiol. **21** 397-404

Egger, D., Wolk, B., Gosert, R., Bianchi, L., Blum, H. E., Moradpour, D., and Bienz, K. 2002 Expression of Hepatitis C Virus Proteins Induces Distinct Membrane Alterations Including a Candidate Viral Replication Complex Am.Soc.Micro. **76** 5974-5984

Ekimov, A. I. and Onushchenko, A. A. 1981 Quantum size effect in three-dimensional microscopic semiconductor crystals J.Exp.Theo.Phys.Letts. **34** 345-348

El-Hage, N. and Luo, G. 2003 Replication of hepatitis C virus RNA occurs in a membrane-bound replication complex containing nonstructural viral proteins and RNA J.Gen.Virol. **84** 2761-2769

Elazar, M., Cheong, K. H., Liu, P., Greenberg, H. B., Rice, C. M., and Glenn, J. S. 2003 Amphipathic Helix-Dependent Localization of NS5A Mediates Hepatitis C Virus RNA Replication J.Virol **77** 6055-6061

Elazar, M., Liu, P., Rice, C. M., and Glenn, J. S. 2004 An N-Terminal Amphipathic Helix in Hepatitis C Virus (HCV) NS4B Mediates Membrane Association, Correct Localization of Replication Complex Proteins and HCV RNA Replication Am.Soc.Micro. **78** 11393-11400

Enomoto, N., Sakuma, I., Asahina, Y., Kurosaki, M., Murakami, T., Yamamoto, C., Izumi, N., Marumo, F., and Sato, C. 1995 Comparison of Full-length Sequences of Interferon-sensitive and Resistant Hepatitis C Virus 1b J.Clin.Invest. **96** 224-230

Evans, M. J., von Hahn, T., Tscheme, D. M., Syder, A. J., Panis, M., and Wolk, B. 2007 Claudin-1 is a hepatitis C virus co-receptor required for a late step in entry Nature **446** 801-805

Ezzell, C. 1988 Candidate cause identified of non-A, non-B hepatitis. Nature **333**

Failla, C., Tomei, L., and Francesco, R. D. 2013 Both NS3 and NS4A Are Required for Proteolytic Processing of Hepatitis C Virus Nonstructural Proteins J.Virol **86** 3753-3760

Fara, P. 2009 A microscopic reality tale Nature **459** 642-644

Feinstone, S. M., Kapikian, A. Z., and Purcell, R. H. 1973 Hepatitis A detection by immune electron microscopy of a virus-like antigen associated with acute illness. Science **182** 1026-1028

Feinstone, S. M., A. Z. Kapikian, R. H. Purcell, H. J. Alter, and P. V. Holland. 1975. Transfusion-associated hepatitis not due to viral hepatitis type A or B. N.Eng.J.Med. **292**:767-770.

Feinstone, S. M., K. B. Mihalik, T. Kamimura, H. J. Alter, W. T. London, and R. H. Purcell. 1983. Inactivation of hepatitis B virus and non-A, non-B hepatitis by chloroform. Infect.Immun. **41** :816-821.

Fenn, J. B., Mann, M., Meng, C. K., Wong, S. F., and Whitehouse, C. M. 1989 Electrospray Ionization for Mass Spectrometry of Large Biomolecules Science **246** 64-71

Ferraris, P., Blanchard, E., and Roinegeard, P. 2010 Ultrastructural and biochemical analyses of hepatitis C virus-associated host cell membranes J.Gen.Virol. **91** 2230-2237

Fishman, J. A., Rubin, R. H., Koziel, M. J., and Periera, B. J. G 1996 Hepatitis C Virus and Organ Transplantation Transplantation **62** 147-154

Flint, M., Thomas, J. M., Maidens, C. M., Shotton, C., Levy, S., Barclay, W. S., and McKeating, J. A. 1999 Functional Analysis of Cell Surface-Expressed Hepatitis C Virus E2 Glycoprotein J.Virol **73** 6782-6790

Flint, M., Maidens, C. M., Loomis-Price, L. D., Shotton, C., Dubuisson, J., and Monk, P. 1999 Characterization of hepatitis C virus E2 glycoprotein interaction with a putative cellular receptor CD81 J.Virol **73** 6235-6244

Flors, C., Ravarani, C. N. J., and Dryden, D. T. F. 2009 Super-Resolution Imaging of DNA Labelled with Intercalating Dyes Chem.Phys.Chem **10** 2201-2204

Flynn, B. O. and Davidson, M. W. 2012 Chromatic Aberration Nikon MicroscopyU

Ford, B. J. 1996 Antony Van Leeuwenhoek (1632-1723)

Forns, X., Bukh, J., and Purcell, R. H. 2002 The challenge of developing a vaccine against hepatitis C virus Hepatology **37** 684-695

Fox, C. H., Johnson, F. B., Whiting, J., and Roller, P. P. 1985 Formaldehyde Fixation J.Histochem.Cytochem. **33** 845-853

Fraenkel-Conrat, H. and Olcott, H. S. 1948 The Reaction of Formaldehyde with proteins. V. Cross-linking between Amino and Primary Amide or Guanidyl Groups J.Am.Chem.Soc. **70** 2673-2684

Freitag, B., Kujawa, S., Mul, P. M., Ringnalda, J., and Tiemeijer, P. C. 2005 Breaking the spherical and chromatic aberration barrier in transmission electron microscopy Ultramicroscopy **102** 209-214

Fricker, M., Runions, J., and Moore, I. 2006 Quantitative Fluorescence Microscopy: From Art to Science Annu.Rev.Plant Biol. **57** 79-107

Friebe, P., Lohmann, V., Krieger, N., and Bartenschlager, R. 2001 Sequences in the 5' Nontranslated Region of Hepatitis C Virus Required for RNA Replication J.Virol **75** 12047-12057

Fried, M. W. 2002 Side Effects of Therapy of Hepatitis C and Their Management Hepatology **36** 237-244

Friedlander, M., Moore, D. H., and Koprowski, H. 1955 Studies with the electron microscope of virus-host relationships in Ehrlich ascites tumor cells II. The localization and possible development of Anopheles A virus within the endoplasmic reticulum of the host cells. J.Exp.Med **102** 371-378

Furuse, M., Fujita, K., Hiiragi, T., Fujimoto, K., and Tsukita, S. 1998 Claudin-1 and -2: novel integral membrane proteins localizing at tight junctions with no sequence similarity to occludin J.Cell Biol. **1998** 1539-1550

Gale, M., Korth, M. J., Tang, N. M., Tan, S-L., Hopkins, D. A., Dever, T. E., Polyak, S. J., Gretch, D. R., and Katze, M. G. 1997 Evidence That Hepatitis C Virus Resistance to Interferon Is Mediated through Repression of the PKR Protein Kinase by the Nonstructural 5A Protein Virology **230** 217-227

Gane, E. J., Portmann, B. C., Naoumov, N., Smith, H. M., Underhill, J. A., Donaldson, P. T., Maertens, G., and Williams, R. 1996 Long-Term Outcome Of Hepatitis C Infection After Liver Transplantation N.Eng.J.Med. **334** 815-820

Gardner, J. P., Durso, R. J., Arrigale, R. R., Donovan, G. P., Maddon, P. J., and Dragic, T. 2003 L-SIGN (CD209L) is a liver-specific capture receptor for hepatitis C virus Proc.Natl.Acad.Sci.USA **100** 4498-4503

Gevaert, K. and Vandekerckhove, J. 2000 Protein identification methods in proteomics Electrophoresis **21** 1145-1154

Gibbons, G. F., Wiggins, D., and Hebbachi, A. M. 2004 Synthesis and function of hepatic very-low-density lipoprotein Biochem.Soc.Trans. **32** 59-64

Giepmans, B. N. G., Deerinck, T. J., Smarr, B. L., Jones, Y. Z., and Ellisman, M. H. 2005 Correlated light and electron microscopic imaging of multiple endogenous proteins using Quantum dots Nat.Methods. **2** 743-749

Giepmans, B. N. G., Adams, S. R., Ellisman, M. H., and Tsien, R. Y. 2006 The Fluorescent Toolbox for Assessing Protein Location and Function Science **312** 217-224

Giepmans, B. N. G. 2008 Bridging fluorescence microscopy and electron microscopy Histochem.Cell Biol. **130** 211-217

Gillespie, L. K., Hoenen, A., Morgan, G., and Mackenzie, J. M. 2010 The endoplasmic reticulum provides the membrane platform for biogenesis of the flavivirus replication complex J.Virol **20** 10438-10447

Giloh, H. and Sedat, J. W. 1982 Fluorescence Microscopy: Reduced Photobleaching of Rhodamine and Fluorescein Protein Conjugates by n-Propyl Gallate Science **217** 1252-1255

Goffard, A., Callens, N., Bartosch, B., Wychowski, C., Cosset, F-L., Montpellier-Pala, C., and Dubuisson, J. 2005 Role of N-Linked Glycans in the Functions of Hepatitis C Virus Envelope Glycoproteins J.Virol **79** 8400-8409

Gofieau, A., Barrell, B. G., Bussey, H., Davis, R. W., Dujon, B., Feldmann, H., Galibert, F., Hoheisel, J. D., Jacq, C., Johnston, M., Louis, E. J., Mewes, H. W., Murakami, Y., Philippsen, P., Tettelin, H., and Oliver, S. G. 1996 Life with 6000 Genes Science **274** 546-567

Goldsmith, C. S. and Miller, S. E. 2009 Modern Uses of Electron Microscopy for Detection of Viruses Clin.Microbiol.Rev. **22** 552-563

Goldstein, J., Joy, D. C., and Romig, A. D. 1986 Principles of Analytical Electron Microscopy

Gondeau, C., Pichard-Garcia, L., and Maurel, P. 2009 Cellular models for the screening and development of anti-hepatitis C virus agents Pharmacol.Ther. **124** 1-22

Gosert, R., Kanjanahaluethai, A., Egger, D., Bienz, K., and Baker, S. C. 2002 RNA replication of mouse hepatitis virus takes place at double-membrane vesicles J.Virol **8** 3697-3708

Gosert, R., Egger, D., Lohmann, V., Bartenschlager, R., Blum, H. E., Bienz, K., and Moradpour, D. 2003 Identification of the Hepatitis C Virus RNA Replication Complex in Huh-7 Cells Harboring Subgenomic Replicons J.Virol **77** 5487-5492

Grakoui, A., McCourt, D. W., Wychowski, C., Feinstone, S. M., and Rice, C. M. 1993 A second hepatitis C virus-encoded proteinase Proc.Natl.Acad.Sci.USA **90** 10583-10587

Grakoui, A., McCourt, D. W., Wychowski, C., Feinstone, S. M., and Rice, C. M. 1993 Characterization of the Hepatitis C Virus-Encoded Serine Proteinase: Determination of Proteinase-Dependent Polyprotein Cleavage Sites J.Virol **67** 2832-2843

Graziani, R. and Paonessa, G. 2004 Dominant negative effect of wild-type NS5A on NS5A-adapted subgenomic hepatitis C virus RNA replication J.Gen.Virol. **85** 1867-1875

Greenfield, J. J. and High, S. 1999 The Sec61 complex is located both in the ER and the ER-Golgi intermediate compartment J.Cell Sci. **112** 1477-1486

Greiner, W. 2001 Quantum Mechanics: An Introduction

Gretton, S. N., Taylor, A. I., and McLauchlan, J. 2005 Mobility of the hepatitis C virus NS4B protein on the endoplasmic reticulum membrane and membrane associated foci. J.Gen.Virol. **86** 1415-1421

Gretton, S. N. 2006 Topology and biophysical characterisation of the hepatitis C virus NS4B protein

Griffin, S. D., Beales, L. P., Clarke, D. S., Worsfold, O., Evans, S. D., Jaeger, J., Harris, M. P., and Rowlands, D. J. 2003 The p7 protein of hepatitis C virus forms an ion channel that is blocked by the antiviral drug, Amantidine. FEBS Lett. **535** 34-38

Gruska, M., Medalia, O., Baumeister, W., and Leis, A. 2008 Electron tomography of vitreous sections from cultured mammalian cells. J.Struct.Biol. **161** 384-392

Gu, M. and Sheppard, C. J. R 1992 Confocal fluorescent microscopy with a finite-sized circular detector J.Opt.Soc.Am. **9** 151-153

Gustafsson, M. G. L. 2000 Surpassing the lateral resolution limit by a factor of two using structured illumination microscopy J.Microsc **198** 82-87

Gygi, S. P., Rist, B., Gerber, S. A., Turecek, F., Gelb, M. H., and Aebersold, R. H. 1997 Quantitative analysis of complex protein mixtures using isotope-coded affinity tags Nat.Biotechnol. **17** 994-999

Haider, M., Rose, H., Uhlemann, S., Schwan, E., Kabius, B., and Urban, K. 1998 A Spherical-aberration-corrected 200kV transmission electron microscope Ultramicroscopy 53-60

Hall, C. E. 1955 Electron Densitometry of Stained Virus Particles J.Biophysic.Biochem.Cytol. **1** 1-12

Han, Q., Xu, C., Wu, C., Zhu, W., Yang, R., and Chen, X. 2009 Compensatory mutations in NS3 and NS5A proteins enhance the virus production capability of hepatitis C reporter virus Virus Res. **145** 63-73

Han, X., Aslanian, A., and Yates, J. R. 2008 Mass Spectrometry for Proteomics Curr.Opin.Chem.Bio. **12** 483-490

Harris, H. J., Farquhar, M. J., Mee, C. J., Davis, C., Reynolds, G. M., and Jennings, A. 2008 CD81 and claudin1 coreceptor association: role in hepatitis C virus entry. J.Virol **82** 5007-5020

He, LF., Alling, D., Popkin, T., Shapiro, M., Alter, H. J., and Purcell, R. H. 1987 Determining the Size of Non-A, Non-B Hepatitis Virus by Filtration J.Inf.Dis. **156** 636

Heintzmann, R. and Cremer, C. 1998 Laterally Modulated Excitation Microscopy: Improvement of resolution by using a diffraction grating Proc.SPIE **3568** 185-196

Helle, F., Goffard, A., Morel, V., Duverlie, G., McKeating, J. A., and Keck, Z. Y. 2007 The neutralizing activity of anti-hepatitis C virus antibodies is modulated by specific glycans on the E2 envelope protein. J.Virol **81** 8101-8111

Hertz, H. 1883 Miscellaneous Papers Wiedmann's Annalen **19** 782

Hezode, C., Lonjon, I., Roudot-Thoraval, F., Pawlotsky, J-M., and Zafrani, E-S. 2003 Impact of moderate alcohol consumption on histological activity and fibrosis in patients with chronic hepatitis C, and specific influence of steatosis: a prospective study Aliment.Pharmacol.Ther. **17** 1031-1037

Honda, M., Ping, L. H., Rijnbrand, R. C., Amphlett, E., Clarke, B., Rowlands, D. J., and Lemon, S. M. 1996 Structural requirements for initiation of translation by internal ribosome entry within genome-length hepatitis C virus RNA Virology **222** 31-42

Hope, G. and McLauchlan, J. 2000 Sequence motifs required for lipid droplet association and protein stability are unique to the hepatitis C virus core protein J.Gen.Virol. **81** 1913-1925

Hopwood, D. 1967 Some aspects of fixation with glutaraldehyde J.Anatomy **101** 83-92

Horiba, J. Y. 2013 A Guide to Recording Fluorescence Quantum Yields

Horner, S. M., Liu, H. M., Park, H. S., Briley, J., and Gale, M. 2011 Mitochondrial-associated endoplasmic reticulum membranes (MAM) form innate immune synapses and are targeted by hepatitis C virus Proc.Natl.Acad.Sci.USA **108** 14590-14595

Houghton, M., Weiner, A. J., Han, J., Kuo, G., and Choo, Q 1991 Molecular Biology of the Hepatitis C Viruses: Implications for Diagnosis, Development and Control of Viral Disease Hepatology **14** 381-388

Houghton, M. 2010 The hepatitis C virus: A new paradigm for the identification and control of infectious disease Nat.Med. **6** 1084-1086

Hu, J., Shibata, Y., Voss, C., Shemesh, T., Li, Z., Coughlin, M., Kozlov, M. M., Rapoport, T. A., and Prinz, W. A. 2008 Membrane Proteins of the Endoplasmic Reticulum Induce High-Curvature Tubules Science **319** 1247-1250

Hu, Q., Noll, R. J., Li, H., Makarov, A., Hardman, M., and Cooks, R. G. 2005 The Orbitrap: a new mass spectrometer J.Mass Spectrom. **40** 430-443

Huang, L., Hwang, J., Sharma, S. D., Hargittai, M. R., Chen, Y., Arnold, J. J., Raney, K. D., and Cameron, C. E. 2005 Hepatitis C virus nonstructural protein 5A (NS5A) is an RNA-binding protein J.Biol.Chem. **280** 36417-36428

Hugle, T., Fehrmann, F., Bieck, E., Kohara, M., Krausslich, H-G., Rice, C. M., Blum, H. E., and Moradpour, D. 2001 The Hepatitis C Virus Nonstructural Protein 4B Is an Integral Endoplasmic Reticulum Membrane Protein Virology **284** 70-81

Iacovacci, S., Manzin, A., Barca, S., Sargiacomo, M., Serafino, A., Valli, M. B., Macioce, G., Hassan, H. J., Ponzetto, A., Clementi, M., Peschle, C., and Carloni, G. 1997 Molecular

Characterization and Dynamics of Hepatitis C Virus Replication in Human Fetal Hepatocytes Infected *In Vitro* Hepatology **26** 1328-1337

Ignatius, M. 2010 Quantum dots mounting media. Confocal Microscopy List [Online]

Invitrogen 2007 Qdot Conjugates Protocol Handbook Molecular Probes Handbook 1-17

Ito, T., Mukaigawa, J., Zuo, J., Hirabayashi, Y., Mitamura, K., and Yasui, K. 1996 Cultivation of hepatitis C virus in primary hepatocyte culture from patients with chronic hepatitis C results in release of high titre infectious virus

Jaeckel, E., Cornberg, M., Wedemeyer, H., Santantonio, T., Mayer, J., Zankel, M., Pastore, G., Dietrich, M., Trautwein, C., and Manns, M. P. 2001 Treatment of Acute Hepatitis C With Interferon Alfa-2b N.Eng.J.Med. **345** 1452-1457

Jaiswal, J. K., Mattoussi, H., Mauro, J. M., and Simon, S. M. 2002 Long-term multiple color imaging of live cells using quantum dot bioconjugates Nat.Biotechnol. **21** 47-51

JI, H., Fraser, C. S., Yu, Y., Leary, J., and Doudna, J. A. 2004 Coordinated assembly of human translation initiation complexes by the hepatitis C virus internal ribosome entry site RNA Proc.Natl.Acad.Sci.USA **101** 16990-16995

Johnson, F. H., Shimomura, O., Sajga, Y., Gershman, L. C., Reynolds, G. M., and Waters, J. H. 1962 Quantum Efficiency of Cypridina Luminescence, With a Note on That of Aequorea J.Cell Comp.Phys. **60** 85-103

Jones, C. T., Murray, C. L., Eastman, D. K., Tassello, J., and Rice, C. M. 2007 Hepatitis C Virus p7 and NS2 Proteins are Essential for Production of Infectious Virus J.Virol **81** 8374-8383

Jones, D. M., Gretton, S. N., McLauchlan, J., and Targett-Adams, P. 2007 Mobility analysis of an NS5A-GFP fusion protein in cells actively replicating hepatitis C virus subgenomic RNA J.Gen.Virol. **88** 470-475

Jones, D. M., Patel, A. H., Targett-Adams, P., and McLauchlan, J. 2009 The hepatitis C virus NS4B protein can trans-complement viral RNA replication and modulates production of infectious virus J.Virol **85** 2163-2177

Jones, D. M., Domingues, P., Targett-Adams, P., and McLauchlan, J. 2010 Comparison of U2OS and Huh-7 cells for identifying host factors that affect hepatitis C virus RNA replication J.Gen.Virol. **91** 2238-2248

Jonschen, K. R. and Yates, J. R. 1997 The Quadrupole Ion Trap Mass Spectrometer - A Small Solution to a Big Challenge Anal.Biochem. **244** 1-15

Joyce, A. R. and Palsson, B. Ø. 2006 The model organism as a system: integrating "omics" data sets Nat.Rev.Mol.Cell.Biol. **7** 198-210

Karnovsky, M. J. 1965 A formaldehyde-glutaraldehyde fixative of high osmolarity for use in electron microscopy J.Cell Biol. **27** 137-138A

Kato, N., Hijikata, M., Ootsuyama, Y., Nakagawa, M., Ohkoshi, S., Sugimura, T., and Shimotohno, K. 1990 Molecular cloning of the human hepatitis C virus genome from Japanese patients with non-A, non-B hepatitis Proc.Natl.Acad.Sci.USA **87** 9524-9528

Kato, T., Date, T., Miyamoto, M., Furusaka, A., Tokushige, K., Mizokami, M., and Wakita, T. 2003 Efficient Replication of the Genotype 2a Hepatitis C Virus Subgenomic Replication Gastroenterology **125** 1808-1817

Kato, T., Date, T., Miyamoto, M., Zhao, Z., Mizokami, M., and Wakita, T. 2005 Nonhepatic cell lines HeLa and 293 support efficient replication of the hepatitis C virus genotype 2a subgenomic replicon J.Virol **79** 592-596

Katze, M. G., He, Y., and Gale, M. 2002 Viruses and Interferon: A Fight For Supremacy Nat.Rev.Immunol. **2** 675-687

Kausche, G., Pfankuch, E., and Ruska, H. 1939 Die Sichtbarmachung von pflanzlichem Virus im Übernikroskop Naturwissenschaften **27** 292-299

Kelleher, N. L., Nicewonger, R. B., Begley, T. P., and McLafferty, F. W. 1997 Identification of Modification Sites in Large Biomolecules by Stable Isotope Labeling and Tandem High Resolution Mass Spectrometry. The active site nucleophile of thiaminase I J.Biol.Chem. **272** 32215-32220

Khare, A., Wills, A. W., Ammerman, L. M., Norris, D. J., and Aydil, E. S. 2011 Size control and quantum confinement in Cu_2ZnSnS_4 nanocrystals Chem.Commun. **47** 11721-11723

Kim, J. L., Morgenstern, K. A., Lin, C., Fox, T., Dwyer, M. D., Landro, J. A., Chambers, S. P., Markland, W., Lepre, C. A., O'Malley, E. T., Harbeson, S. L., Rice, C. M., Murcko, M. A., Caron, P. R., and Thomson, J. A. 1996 Crystal Structure of the Hepatitis C Virus NS3 Protease Domain Complexed with a Synthetic NS4A Cofactor Peptide Cell **87** 343-355

Kim, J. L., Lee, D., and Choe, J. 1999 Hepatitis C virus NS5A protein is phosphorylated by casein kinase II Biochem.Biophys.Res.Commun. **257** 777-781

Kingdon, K. H. 1923 A Method for the Neutralization of Electron Space Charge by Positive Ionization at Very Low Gas Pressures Phys.Rev. **21** 408-418

Klose, J. and Kobalz, U. 1995 Two-dimensional electrophoresis of proteins: An updated protocol and implications for a functional analysis of the genome Electrophoresis **16** 1034-1059

Knockenmuss, R. 2006 Ion formation mechanisms in UV-MALDI Analyst **131** 966-986

Kobayashi, S., Serizawa, Y., Fujita, T., and Coupland, R. E. 1978 SGC (small granule chromaffin) cells in the mouse adrenal medulla: light and electron microscopic identification using semi-thin and ultra-thin sections Endocrinol.Jpn. **25** 467-476

Kolykhalov, A. A., Agapov, E. V., Blight, K. J., Mihalik, K. B., Feinstone, S. M., and Rice, C. M. 1997 Transmission of hepatitis C by intrahepatic inoculation with transcribed RNA Science **277** 570-574

Kopek, B. G., Perkins, G., Miller, D. J., Ellisman, M. H., and Ahlquist, P. 2007 Three-dimensional analysis of a viral RNA replication complex reveals a virus-induced mini-organelle PLOS Biology **5** 2022-2034

Korn, E. E. 1967 A Chromatographic and Spectrophotometric Study of the Products of the Reaction of Osmium Tetroxide with Unsaturated Lipids J.Cell Biol. **34** 627-638

Koutsoudakis, G., Kaul, A., Steinmann, E., Kallis, S., Lohmann, V., Pietschmann, T., and Bartenschlager, R. 2006 Characterization of the Early Steps of Hepatitis C Virus Infection by Using Luciferase Reporter Viruses J.Virol **80** 5308-5320

Krey, T., d'Alayer, J., Kikuti, C. M., Saulnier, A., Damier-Piolle, L., Petitpas, I., Johansson, D. X., Tawar, R. G., Baron, B., Robert, B., England, P., Persson, Mats. A. A., Martin, A., and Rey, F. A. 2010 The Disulfide Bonds in Glycoprotein E2 of Hepatitis C Virus Reveal the Tertiary Organization of the Molecule PLOS Pathogens **6**

Krieger, M. 2001 Scavenger receptor class B type I is a multiligand HDL receptor that influences diverse physiologic systems J.Clin.Invest. **108** 793-797

Krieger, N., Lohmann, V., and Bartenschlager, R. 2001 Enhancement of hepatitis C virus RNA replication by cell culture-adaptive mutations J.Virol **75** 4614-4624

Krugman, S. 1975 Viral Hepatitis: Overview and Historical Perspectives Yale.J.Biol.Med. **49** 199-203

Kumar, D., Farrell, G. C., Fung, C., and George, J. 2002 Hepatitis C Virus Genotype 3 Is Cytopathic to Hepatocytes: Reversal of Hepatic Steatosis After Sustained Therapeutic Response Hepatology **36** 1266-1272

Kuo, G., Choo, Q, Alter, H. J., Gitnick, G. L., Redeker, A. G., Purcell, R. H., Miyamura, T., Dienstag, J. L., Alter, M. J., Stevens, C. E., Tegtmeier, G. E., Bonino, F., Colombo, M., Lee, W.-S, Kuo, G., Berger, K., Shuster, J. R., Overby, L. R., Bradley, D. W., and Houghton, M. 1989 An Assay for Circulating Antibodies to a Major Etiologic Virus of Human Non-A Non-B Hepatitis Science **244** 362-364

Kwong, A. D., McNair, L., Jacobson, I., and George, S. 2008 Recent progress in the development of selected hepatitis C virus NS3-4A protease and NS5B polymerase inhibitors Curr.Opin.Pharm. **8** 522-531

Lagging, L. M., Meyer, K., Owens, R. J., and Ray, R. 1998 Functional Role of Hepatitis C Virus Chimeric Glycoproteins in the Infectivity of Pseudotyped Virus J.Virol **72** 3539-3546

Lamarre, D., Anderson, P. C., Bailey, M., Beaulieu, P., Bolger, G., Bonneau, P., Bos, M., Cameron, D. R., Cartier, M., Cordingley, M. G., Faucher, A-M., Goudreau, N., Kawai, S. H., Kukolj, G., Lagace, L., LaPlante, S. R., Narjes, H., Poupart, M-A., Rancourt, J., Sentjens, R. E., St George, R., Simoneau, B., Steinmann, G., Thibeault, D., Tsantrizos, Y.

S., Weldon, S. M., Yong, C-L., and Llinas-Brunet, M. 2003 An NS3 Protease inhibitor with antiviral effects in humans infected with hepatitis C virus Nature **426** 186-189

Landmann, L. 2002 Deconvolution improves colocalization analysis of multiple fluorochromes in 3D confocal data sets more than filtering techniques J.Microsc **208** 134-147

Landmann, L. and Marbet, P. 2004 Colocalization Analysis Yields Superior Results After Image Restoration Microsc.Res.Tech. **64** 103-112

Lee, M. D. 1977 Hepatitis B Virus Infection N.Eng.J.Med. **337** 1733-1745

Leitch, E. C. McW. and McLauchlan, J. 2013 Determining the cellular diversity of HCV quasispecies by single-cell viral sequencing J.Virol 01-27

Lesburg, C. A., Cable, M. B., Ferrari, E., Hong, Z., Mannarino, A. F., and Weber, P. C. 1999 Crystal structure of the RNA-dependent RNA polymerase from hepatitis C virus reveals a fully encircled active site Nat.Struct.Biol. **6** 937-943

Li, X-D., Sun, L., Seth, R. B., Pineda-Tamondong, G., and Chen, Z. J. 2005 Hepatitis C virus protease NS3/4A cleaves mitochondrial antiviral signaling protein off the mitochondria to evade innate immunity Proc.Natl.Acad.Sci.USA **102** 17717-17722

Lifshitz, L. M. 1998 Determining Data Independence on a Digitized Membrane in Three Dimensions IEEE Trans.Med.Image. **17** 299-303

Lin, C., Pragai, B. M., Grakoui, A., Xu, J., and Rice, C. M. 1994 Hepatitis C Virus NS3 Serine Proteinase: Trans-Cleavage Requirements and Processing Kinetics Am.Soc.Micro. **68** 8147-8157

Lindenbach, B. D. and Rice, C. M. 2005 Unraveling hepatitis C virus replication from genome to function Nature **436** 933-938

Lindenbach, B. D., Evans, M. J., Syder, A. J., Wolk, B., Tellinghuisen, T. L., Liu, C. C., Maruyama, T., Hynes, R. O., Burton, D. R., McKeating, J. A., and Rice, C. M. 2005 Complete Replication of Hepatitis C Virus in Cell Culture Science **309** 623-626

Lindenbach, B. D. 2011 Understanding How Hepatitis C Virus Builds It's Unctuous Home Cell Host Microbe **9** 1-2

Lindsay, K. L., Trepo, C., Heintges, T., Shiffman, M., Gordon, S. C., Hoefs, J. C., Schiff, E. R., Goodman, Z. D., Laughlin, M., Yao, R., and Albrecht, J. K. 2001 A Randomized, Double-Blind Trial Comparing Pegylated Interferon Alfa-2b to Interferon Alfa-2b as Initial Treatment for Chronic Hepatitis C Hepatology **34** 395-403

Linfoot, E. H. and Wolf, E. 1952 Diffraction Images in Systems with an Annular Aperture Proc.Phys.Soc. **66** 145-149

Linfoot, E. H. and Wolf, E. 1956 Phase Distribution near Focus in an Aberration-free Diffraction Image Proc.Phys.Soc. **69** 823-832

Lippincott-Schwartz, J., Herman, B., and Davidson, M. W. 2013 Fluorophores for Confocal Microscopy

Liu, S., Yang, W., Shen, L., Turner, J. R., Coyne, C. B., and Wang, T. 2009 Tight Junction Proteins Claudin-1 and Occludin Control Hepatitis C Virus Entry and Are Downregulated during Infection To Prevent Superinfection J.Virol **83** 2011-2014

Liu, S. L., Li, J., Zhang, Z. L., Wang, Z. G., Tian, Z. Q., Wang, G. P., and Pang, D. W. 2013 Fast and high-accuracy localization for three-dimensional single-particle tracking Sci.Rep. **3**

Lohmann, V., Korner, F., Koch, J.-O, Herian, U., Theilmann, L., and Bartenschlager, R. 1999 Replication of Subgenomic Hepatitis C Virus RNAs in a Hepatoma Cell Line Science **285** 110-113

Lohmann, V., Korner, F., Dobierzewska, A., and Bartenschlager, R. 2001 Mutations in Hepatitis C Virus RNAs Conferring Cell Culture Adaptation Am.Soc.Micro. **75** 1437-1449

Long, G., Hiet, M. S., Windisch, M. P., Lee, J. Y., Lohmann, V., and Bartenschlager, R. 2011 Mouse hepatic cells support assembly of infectious hepatitis C virus particles Gastroenterology **141** 1057-1066

Love, R. A., Brodsky, O., Hickey, M. J., Wells, P. A., and Cronin, C. N. 2009 Crystal Structure of a Novel Dimeric Form of NS5A Domain I Protein from Hepatitis C Virus J.Virol **83** 4395-4403

Luby-Phelps, K., Ning, G., Fogerty, J., and Besharse, J. C. 2003 Visualization of identified GFP-expressing cells by light and electron microscopy J.Histochem.Cytochem. **51** 271-274

Ludwig, J. 2007 Image Convolution 1-8

Macdonald, A., Crowder, K., Street, A., McCormick, C. J., Saksela, K., and Harris, M. P. 2003 The hepatitis C virus non-structural NS5A protein inhibits activating protein-1 function by perturbing ras-ERK pathway signaling J.Biol.Chem. **278** 177775-177784

Major, M. E. and Feinstone, S. M. 1997 The Molecular Virology of Hepatitis C Hepatology **25** 1527-1538

Makarov, A. 2000 Electrostatic Axially Harmonic Orbital Trapping: A High-Performance Technique of Mass Analysis Anal.Chem. **72** 1156-1162

Manders, E. M. M., Stap, J., Brakenhoff, G. J., van Driel, R., and Aten, J. A. 1992 Dynamics of three-dimensional replication patterns during the S-phase, analysed by double labelling of DNA and confocal microscopy J.Cell Sci. **103** 857-862

Manders, E. M. M., Verbeek, F. J., and Aten, J. A. 1993 Measurement of co-localization of objects in dual-colour confocal images J.Microsc **169** 375-382

Mann, M. 2006 Functional and quantitative proteomics using SILAC Nat.Rev.Mol.Cell.Biol. **7** 952-958

Manns, M. P., McHutchison, J. G., Gordon, S. C., Rustgi, V. K., Shiffman, M., Reindollar, R., Goodman, Z. D., Koury, K., Ling, M-H., and Albrecht, J. K. 2001 Peginterferon alfa-2b plus ribavirin compared with interferon alfa-2b plus ribavirin for initial treatment of chronic hepatitis C: a randomised trial Lancet **358** 958-965

Marcellin, P., Asselah, T., and Boyer, N. 2002 Fibrosis and Disease Progression in Hepatitis C Hepatology **36** 547-556

Marsh, M. and Helenius, A. 2006 Virus entry: open sesame Cell **124** 729-740

Marshall, A. G., Hendrickson, C. L., and Jackson, G. S. 1998 Fourier Transform Ion Cyclotron Resonance Mass Spectrometry: A Primer Mass.Spectrom.Rev. **17** 1-35

Martell, M., Esteban, J. I., Quer, J., Genesca, J., Weiner, A. J., Esteban, R., Guardia, J., and Gomez, J. 1992 Hepatitis C Virus (HCV) Circulates as a Population of Different but Closely Related Genomes: Quasispecies Nature of HCV Genome Distribution J.Virol **66** 3225-3229

Masaki, T., Suzuki, R., Murakami, K., Aizaki, H., Ishii, K., Murayama, A., Date, T., Matsuura, Y, Miyamura, T., Wakita, T., and Suzuki, T. 2008 Interaction of Hepatitis C Virus Nonstructural Protein 5A with Core Protein Is Critical for the Production of Infectious Virus Particles J.Virol **82** 7964-7976

Masters, B. R. 2009 History of the Electron Microscope in Cell Biology Encyclopedia of Life Sciences (ELS). 1-9

McCormick, C. J., Brown, D., Griffin, S., Challinor, L., Rowlands, D. J., and Harris, M. P. 2006 A link between translation of the hepatitis C virus polyprotein and polymerase function; possible consequences for hyperphosphorylation of NS5A J.Gen.Virol. **87** 93-102

McHutchison, J. G., Gordon, S. C., Schiff, E. R., Shiffman, M., Lee, W. M., Rustgi, V. K., Goodman, Z. D., Ling, M-H., Cort, S., and Albrecht, J. K. 1998 Interferon Alfa-2b Alone or in Combination with Ribavirin as Initial Treatment for Chronic Hepatitis C N.Eng.J.Med. **339** 1485-1492

McKeating, J. A., Zhang, J., Logvinoff, C., Flint, M., Zhang, L. Q., and Yu, J. 2004 Diverse hepatitis C virus glycoproteins mediate viral infection in a CD81-dependent manner J.Virol **78** 8496-8505

McLauchlan, J., Lemberg, M. K., Hope, G., and Martoglio, B. 2002 Intramembrane proteolysis promotes trafficking of hepatitis C virus core protein to lipid droplets EMBO J. **21** 3980-3988

McWilliam, E. C. and McLauchlan, J. 2013 Determining the cellular diversity of HCV quasispecies by single-cell viral sequencing

Medintz, I. L, Uyeda, H. T., Goldman, E. R., and Mattoussi, H. 2005 Quantum dot bioconjugates for imaging, labelling and sensing Nat.Mater. **4** 435-446

Meijering, E. and Cappellen, G. v. 2007 Imaging Cellular and Molecular Biological Functions Principles and Practice: Quantitative Biological Image Analysis 45-70

Merz, A., Long, G., Hiet, M. S., Brugger, B., Chlanda, P., Andre, P., Wieland, F., Krijnse-Locker, J., and Bartenschlager, R. 2011 Biochemical and morphological properties of hepatitis C virus particles and determination of their lipidome. J.Biol.Chem. **286** 3018-3032

Merz, A., Romero-Brey, I., Chiramel, A., Lee, J-Y., Chlanda, P., Haselman, U., Santarella-Mellwig, R., Habermann, A., Hoppe, S., Kallis, S., Walther, P., Antony, C., Krijnse-Locker, J., and Bartenschlager, R. 2013 Three-Dimensional Architecture and Biogenesis of Membrane Structures Associated with Hepatitis C Virus Replication

Meyer, J. C., Girit, C. O., Crommie, M. F., and Zettle, A. 2008 Imaging and dynamics of light atoms and molecules on graphene Nature **454** 319-322

Meylan, E., Curran, J., Hofmann, K., Moradpour, D., Binder, M., Bartenschlager, R., and Tschopp, J. 2005 Cardif is an adaptor protein in the RIG-I antiviral pathway and is targeted by hepatitis C virus Nature **437** 1167-1172

Michalet, X., Pinaud, F. F., Bentolila, L. A., Tsay, J. M., Doose, S., Li, J. J., Sundaresan, G., Wu, A. M., Gambhir, S. S., and Weiss, S. 2005 Quantum Dots for Live Cells, in vivo Imaging, and Diagnostics Science **307** 538-544

Miller, R. H. and Purcell, R. H. 1989 Hepatitis C virus shares amino acid sequence similarity with pestiviruses and flaviviruses as well as members of two plant virus supergroups Proc.Natl.Acad.Sci.USA **87** 2057-2061

Miller, S. and Krijnse-Locker, J. 2008 Modification of intracellular membrane structures for virus replication Nat.Rev.Microbiol. **6** 363-374

Minsky, M. 2011 Memoir on inventing the confocal scanning microscope Scanning **10** 128-138

Mironov, A. A., Polishchuk, R. S., and Luini, A. 2000 Visualizing membrane traffic *in vivo* by combined video fluorescence and 3D electron microscopy Trends.Cell.Biol. **10** 349-353

Misteli, T. and Spector, D. L. 1997 Applications of the green fluorescent protein in cell biology and biotechnology Nat.Biotechnol. **15** 961-963

Miyanari, Y., Atsuzawa, K., Usuda, N., Watashi, K., Hishiki, T., Zayas, M., Bartenschlager, R., Wakita, T., Hijikata, M., and Shimotohno, K. 2007 The lipid droplet is an important organelle for hepatitis C virus production Nat.Cell.Biol. **9** 961-969

Mockus, S. M. and Vrana, K. E. 1998 Advances in the Molecular Characterization of Tryptophan Hydroxylase J.Mol.Neurosci. **10** 163-179

Mondelli, M. U., Cerino, A., Meola, A., and Nicosia, A. 2003 Variability or conservation of hepatitis C virus hypervariable region 1? Implications for immune responses J.Biosci **28** 305-310

Moradpour, D., Evans, M. J., Gosert, R., Yuan, Z., Blum, H. E., Goff, S. P., Lindenbach, B. D., and Rice, C. M. 2004 Insertion of Green Fluorescent Protein into Nonstructural Protein 5A Allows Direct Visualization of Functional Hepatitis C Viral Replication Complexes J.Virol **78** 7400-7409

Moradpour, D., Penin, F., and Rice, C. M. 2007 Replication of hepatitis C virus Nat.Rev.Microbiol. **5** 453-463

Morgan, C., Ellison, S. A., Rose, H. M., and Moore, D. H. 1954 Structure and development of viruses as observed in the electron microscope. I. Herpes Simplex Virus. J.Exp.Med **100** 195-202

Mosley, J. W. 1975. The epidemiology of viral hepatitis: an overview. Am.J.Med.Sci. **270**.

Mullins, J. M. 1995 Overview of Fluorophores Immunocytochemical Methods and Protocols **34** 107-116

Mulvey, T. 1962 Origins and historical development of the electron microscope Br.J.App.Phys. **13** 197-207

Mulvey, T. 1989 The electron microscope: the British contribution J.Microsc **155** 327-338

Murphy, R. F., Meijering, E., and Danuser, G. 2005 Special Issue on Molecular and Cellular Bioimaging IEEE Trans.Image.Process. **14** 1233-1236

Murray, C. B. and Kagan, C. R. 2000 Synthesis and Characterization of Monodirperse Nanocrystal Annu.Rev.Mat.Sci. **30** 545-610

Nagler, F. P. and Rake, G. 1948 The Use of the Electron Microscopy in Diagnosis of Variola, Vaccinia, and Variola J.Bacteriol **55** 45-51

Nakabayashi, H., Taketa, K., Miyano, K., Yamane, T., and Sato, J. 1982 Growth of Human Hepatoma Cell Lines with Differentiated Functions in Chemically Defined Medium Cancer Res. **42** 3858-3863

Nakata, T., Terada, S., and Hirokawa, N. 1998 Visualisation of the Dynamics of Synaptic Vesicle and Plasma Membrane Proteins In Living Axons J.Cell Biol. **140** 659-674

Ndongo-Thiam, N., Berthillon, P., Errazuriz, E., Bordes, I., De Sequeira, S., Trepo, C., and Petit, M-A. 2011 Long-Term Propagation of Serum Hepatitis C Virus (HCV) with Production of Enveloped HCV Particles in Human HepaRG Hepatocytes Hepatology **54** 406-417

Nguyen, M. H. and Keeffe, E. B. 2005 Prevalence and Treatment of Hepatitis C Virus Genotypes 4, 5, and 6 Clin.Gastroenterol.Hepatol. **3** 97-101

Nielsen, S. U., Bassendine, M. F., Burt, A. D., Martin, C., Pumeechockal, W., and Toms, G. L. 2006 Association between hepatitis C virus and very-low-density lipoprotein (VLDL)/LDL analyzed in iodixanol density gradients J.Virol **80** 2418-2428

Nisman, R., Dellaire, G., Ren, Y., Li, R., and Bazett-Jones, D. P. 2004 Application of Quantum Dots as Probes for Correlative Fluorescence, Conventional, and Energy-filtered Transmission Electron Microscopy J.Histochem.Cytochem. **52** 13-18

Norris, D. J. and Bawendi, M. G. 1996 Measurement and assignment of the size-dependent optical spectrum in CdSe quantum dots Phys.Rev.B **53** 16338-16346

Nuttal, R. H. 1974 The achromatic microscope in the history of nineteenth century science Philos.J. **11** 71-88

Okamoto, H., Okada, S., Sugiyama, Y., Kurai, K., Iizuka, H., Machida, A., Miyakawa, Y., and Mayumi, M. 1991 Nucleotide sequence of the genomic RNA of hepatitis C virus isolated from a human carrier: comparison with reported isolates for conserved and divergent regions J.Gen.Virol. **72** 2697-2704

Ollis, D. L., Brick, P., Hamlin, R., Xuong, N. G., and Steitz, T. A. 1985 Structure of large fragment of Escherichia coli DNA polymerase I complexed with dTMP Nature **313** 762-766

Ong, S-E, Blagoev, B., Kratchmarova, I., Kristensen, D. B., Steen, H., Pandey, A., and Mann, M. 2002 Stable Isotope Labeling by Amino Acids in Cell Culture, SILAC as a simple and Accurate Approach to Expression Proteomics Mol.Cell.Proteomics **1.5** 376-386

Ong, S-E and Mann, M. 2005 Mass spectrometry -based proteomics turns quantitative Nat.Chem.Biol. **1** 252-262

Oorschot, V., de Wit, H., Annaert, W. G., and Klumperman, J. 2002 A Novel Flat-embedding Method to Prepare Ultrathin Cryosections from Cultured Cells in Their In Situ Orientation J.Histochem.Cytochem. **50** 1067-1080

Op De Beeck, A., Cocquerel, L., and Dubuisson, J. 2001 Biogenesis of hepatitis C virus envelope glycoproteins J.Gen.Virol. **82** 2589-2595

Paeshuyse, J., Dallmeier, K., and Neyts, J. 2011 Ribavirin for the treatment of chronic hepatitis C virus infection: a review of the proposed mechanisms of action Curr.Opin.Virol. **1** 590-598

Parent, R., Marion, M-J., Furio, L., Trepo, C., and Petit, M-A. 2004 Origin and characterization of a human bipotent liver progenitor cell line Gastroenterology **126** 1147-1156

Patterson, S. D. and Aebersold, R. H. 2003 Proteomics: the first decade and beyond Nat.Genet. **33** 311-323

Paul, D., Romero-Brey, I., Gouttenoire, J., Stoitsova, S., Krijnse-Locker, J., Moradpour, D., and Bartenschlager, R. 2011 NS4B self-interaction through conserved C-terminal elements is required for the establishment of functional hepatitis C virus replication complexes J.Virol **85** 6963-6976

Paul, D. and Bartenschlager, R. 2013 Architecture and biogenesis of plus-strand RNA virus replication factories World.J.Virol. **2** 32-48

Pavlovic, D., Neville, D. C., Argaud, O., Blumberg, B., Dwek, R. A., Fischer, W. B., and Zitzmann, N. 2003 The hepatitis C virus p7 protein forms an ion channel that is inhibited by long-alkyl-chain iminosugar derivatives. Proc.Natl.Acad.Sci.USA **100** 6104-6108

Pawley, J. B. 2006 Handbook of Biological Confocal Microscopy (3rd Edition)

Pawlotsky, J-M. 2004 Pathophysiology of hepatitis C virus infection and related liver disease Trends Microbiol. **12** 96-102

Pearson, K. 1896 Mathematical contributions to the theory of evolution III. Regression, heredity and
panmixia Phil.Trans.R.Soc.B **187** 253-318

Penin, F., Dubuisson, J., Rey, F. A., Moradpour, D., and Pawlotsky, J-M. 2004 Structural Biology of Hepatitis C Virus Hepatology **39** 5-19

Penin, F., Brass, V., Appel, N., Ramboarina, S., Montserret, R., Ficheux, D., Blum, H. E., Bartenschlager, R., and Moradpour, D. 2004 Structure and Function of the Membrane Anchor Domain of Hepatitis C Virus Nonstructural Protein 5A J.Biol.Chem. **279** 40835-40843

Perez-Brena, P., Guillen, J., Moreno, M. R., Bernabeu, A., Pabst, G., Laggner, P., and Villalain, J. 2008 Identification of the Membrane-active Regions of Hepatitis C Virus p7 Protein J.Biol.Chem. **283** 8089-8101

Perona, P. and Malik, J. 1990 Scale-Space and Edge Detection Using Anisotropic Diffusion IEEE Transaction on Pattern Analysis and Machine Intelligence **12** 629-639

Peters, M. G. and Terrault, N. A. 2002 Alcohol Use and Hepatitis C Hepatology **36** 220-225

Pfeifer, U., Thomssen, R., Legler, K., Böttcher, U., Gerlich, W., Weinmann, E., and Klinge, O. 1980 Experimental Non-A, Non-B Hepatitis: Four Types of Cytoplasmic Alteration in Hepatocytes of Infected Chimpanzees Virchows Arch.B.Cell.Pathol.Incl.Mol.Pathol. **33** 233-243

Pieroni, L., Santolini, E., Fipaldini, C., Pacini, L., Migliaccio, G., and Monica, N. 1997 In Vitro Study of the NS2-3 Protease of Hepatitis C Virus J.Virol **71** 6373-6380

Pietschmann, T., Kaul, A., Koutsoudakis, G., Shavinskaya, A., Kallis, S., Steinmann, E., Abid, K., Negro, F., Dreux, M., Cosset, F-L., and Bartenschlager, R. 2006 Construction and characterization of infectious intragenotypic and intergenotypic hepatitis C virus chimeras Proc.Natl.Acad.Sci.USA **103** 7408-7413

Plitzko, J. M., Rigort, A., and Leis, A. 2009 Correlative cryo-light microscopy and cryo-electron tomography: from cellular territories to molecular landscapes. Curr.Opin.Biotechnol. **20** 83-89

Ploss, A., Evans, M. J., Gaysinskaya, V. A., Panis, M., You, H., and de Jong, Y. P. 2009 Human occludin is a hepatitis C virus entry factor required for infection of mouse cells. Nature **457** 882-886

Porter, K. R., Claude, A., and Fullam, E. F. 1945 A Study of Tissue Culture Cells by Electron Microscopy J.Exp.Med **81** 233-246

Porter, K. R. and Kallman, F. 1952 The Properties And Effects Of Osmium Tetroxide As A Tissue Fixative With Special Reference To Its Use For Electron Microscopy Exp.Cell.Res. **4** 127-141

Prakash, A., Piening, B., Whiteaker, J., Zhang, H., Shaffer, S. A., Martin, D., Hohmann, L., Cooke, K., Olson, J. M., Hansen, S., Flory, M. R., Lee, H., Watts, J., Goodlett, D. R., Aebersold, R. H., Paulovich, A., and Schwikowski, B. 2007 Assessing bias in experiment design for large scale mass spectrometry-based quantitative proteomics Mol.Cell.Proteomics **6** 1741-1748

Prasher, D. C. 1995 Using GFP to see the light Trends.Genet. **11** 320-323

Prentoe, J. and Bukh, J. 2011 Hepatitis C virus expressing flag-tagged envelope protein 2 has unaltered infectivity and density, is specifically neutralized by flag antibodies and can be purified by affinity chromatography Virology **409** 148-155

Prince, A. B., Grady, G. F., Hazzi, C., Brotman, B, Kuhns, W. J., Levine, R. W., and Millian, S. J. 1974 Long-Incubation Post-Transfusion Hepatitis Without Serological Evidence Of Exposure To Hepatitis-B Virus Lancet 241-246

Prout, W. 1815 On the relation between specific gravities of bodies in their gaseous state and the weights of their atoms. Ann.Phil. **6** 321-330

Purcell, R. H., Alter, H. J., and Dienstag, J. L. 1976 Non-A, Non-B Hepatitis Yale.J.Biol.Med. **49** 243-250

Quinkert, D., Bartenschlager, R., and Lohmann, V. 2005 Quantitative analysis of the hepatitis C virus replication complex J.Virol **79** 13594-13605

Reagan, R. L. and Brueckner, A. L. 1952 Morphological observations by electron microscopy of the Lansing strain of poliomyelitis virus after propagation in the swiss albino mouse Tex.Rep.Biol.Med. **10** 425-428

Reck-Peterson, S. L., Derr, N. D., and Stuurman, N. 2010 Imaging Single Molecules Using Total Internal Reflection Fluorescence Microscopy (TIRFM) Cold.Spring.Harb.Prot.

Reipert, S., Fischer, I., and Wiche, G. 2003 Cryofixation of epithelial cells grown on sapphire coverslips by impact freezing J.Microsc **209** 76-80

Reiss, P., Bleuse, J., and Pron, A. 2002 Highly Luminescent CdSe/ZnSe Core/Shell Nanocrystals of Low Size Dispersion Nano.Lett. **2** 781-784

Reiss, P., Rebhan, I., Backes, P., Romero-Brey, I., Erfle, H., Matula, P., Kaderali, L., Poenisch, M., Blankenburg, H., Hiet, M. S., Longerich, T., Diehl, S., Ramirez, F., Balla, T., Rohr, K., Kaul, A., Bühler, S., Pepperkok, R., Lengauer, T., Albrecht, M., Eils, R., Schirmacher, P., Lohmann, V., and Bartenschlager, R. 2011 Recruitment and activation of

a lipid kinase by hepatitis C virus NS5A is essential for integrity of the membranous replication compartment Cell Host Microbe **9** 32-45

Reiss, S., Harak, C., Romero-Brey, I., Radujkovic, D., Klein, R., Ruggieri, A., Rebhan, I., Bartenschlager, R., and Lohmann, V. 2013 The lipid kinase phosphatidylinositol-4 kinase III alpha regulates the phosphorylation status of hepatitis C virus NS5A PLOS Pathogens **9**

Resch-Genger, U., Grabolle, M., Cavaliere-Jaricot, S., Nitschke, R., and Nann, T. 2008 Quantum dots versus organic dyes as fluorescent labels Nat.Methods. **5** 763-775

Ridler, T. W. and Calvard, S. 1978 Picture Thresholding Using an Iterative Selection Method. IEEE Trans.Syst.Man.Cybern. **8** 630-632

Roinegeard, P. 2008 Viral detection by electron microscopy: past present and future Biol.Cell. **100** 491-501

Rolf, E., Rossell, M. D., Kisielowski, C., and Dahmen, U. 2009 Atomic-Resolution Imaging with a Sub-50-pm Electron Probe Phys.Rev.Lett. **102** 096101-1-096101-4

Rosier, D. J. and Klug, A. 1968 Reconstruction of Three Dimensional Structures from Electron Micrographs Nature **217** 130-134

Rost, F. W. D. 1992 Fluorescence Microscopy **1**

Ruska, E. 1980 The early development of electron lenses and electron microscopy 113-116

Ruska, E. 1986 Nobel Lecture: The Development of the Electron Microscope and of Electron Microscopy Biosci.Rep. **7** 607-629

Ruska, H., von Borries, B., and Ruska, E. 1939 Die bedeutung der ubermikroskopie fur die virusforschung. Arch.Gesamte.Virusforsch. **1** 155-159

Russell, R. S., Meunier, J. C., Takikawa, S., Faulk, K., Engle, R. E., Bukh, J., Purcell, R. H., and Emerson, S. U. 2008 Advantages of a single-cycle production assay to study cell culture-adaptive mutations of hepatitis C virus Proc.Natl.Acad.Sci.USA **105** 4370-4375

Rust, M. J., Bates, M., and Zhuang, X. 2006 Sub-diffraction-limit imaging by stochastic optical reconstruction microscopy (STORM) Nat.Methods. **3** 793-795

Sabatini, D. D., Bensch, K., and Barrnett, R. J. 1963 Cytochemistry and electron microscopy. The preservation of cellular ultrastructure and enzyme activity by aldehyde fixation J.Cell Biol. **17** 19-57

Saeed, M., Scheel, T. K., Gottwein, J. M., Marukian, S., Dustin, L. B., Bukh, J., and Rice, C. M. 2012 Efficient replication of genotype 3a and 4a hepatitis C virus replicons in human hepatoma cells Antimicrob.Agents.Chemother. **56** 5365-5373

Saeed, M., Gondeau, C., Hmwe, S., Yokokawa, H., Date, T., Suzuki, T., Kato, T., Maurel, P., and Wakita, T. 2013 Replication of hepatitis C virus genotype 3a in cultured cells Gastroenterology **144** 56-58

Sainz, B, Jr., TenCate, V., and Uprichard, S. L. 2009 Three-dimensional Huh-7 cell culture system for the study of Hepatitis C Virus infection Virology **6** 103-111

Saito, T., Owen, D. M., Jiang, F., Marcotrigiano, J., and Gale, M. 2008 Innate immunity induced by composition-dependent RIG-I recognition of hepatitis C virus RNA Nature **454** 523-527

Sakamuro, D., Furukawa, T., and Takegami, T. 1995 Hepatitis C Virus Nonstructural Protein NS3 Transforms NIH 3T3 Cells J.Virol **69** 3893-3896

Santolini, E., Pacini, L., Fipaldini, C., Migliaccio, G., and Monica, N. 1995 The NS2 protein of hepatitis C virus is a transmembrane polypeptide J.Virol **69** 7461-7471

Sartori, A., Gatz, R., Beck, F., Rigort, A., Baumeister, W., and Plitzko, J. M. 2007 Correlative microscopy: Bridging the gap between fluorescence light microscopy and cryo-electron tomography J.Struct.Biol. **160** 135-145

Scarselli, E., Ansuini, H., Cerino, R., Roccasecca, R. M., Acali, S., and Filcamo, G. 2002 The human scavenger receptor class B type I is a novel candidate receptor for the hepatitis C virus EMBO J. **21** 5017-5025

Schermelleh, L., Carlton, P. M., Haase, S., Shao, L., Winoto, L., Kner, P., Burke, B., Cardoso, C., Agard, D. A., Gustafsson, M. G. L., Leonhardt, H., and Sedat, J. W. 2008 Subdiffraction Multicolor Imaging of the Nuclear Periphery with 3D Structured Illumination Microscopy Science **320** 1332-1336

Schermelleh, L., Heintzmann, R., and Leonhardt, H. 2010 A guide to super-resolution fluorescence microscopy J.Cell Biol. **190** 165-175

Scherzer, O. 1936 Über einige Fehler von Elektronenlinsen. Zeitschrift für Physik **101** 593-603

Scherzer, O. 1947 Sphärische und chromatische Korrektur von Elektronenlinsen Optik **2** 114-132

Schröder, M. 1980 Osmium Tetroxide Cis Hydrolation of Unsaturated Substrates Chem.Rev. **80** 187-213

Schuppan, D., Ruehl, M., Somasundaram, R., and Hahn, E. G. 2001 Matrix as a modulator of hepatic fibrogenesis. Semin.Liver Dis. **21** 351-372

Schwartz, J. C., Senko, M. W., and Syka, J. E. 2002 A two-dimensional quadrupole ion trap mass spectrometer. J.Am.Soc.Mass Spectrom. **13** 659-669

Senko, M. W., Hunter, K., Sheils, W., and Stresau, D. 2013 Efficient Detection for Linear Traps Using a Single Electron Multiplier

Sharma, S. N., Pillai, Z. S., and Kamat, P. V. 2003 Photoinduced Charge Transfer between CdSe Quantum Dots and p-Phenylenediamine J.Phys.Chem. **107** 10088-10093

Shi, S. T. and Lai, M. M. C. 2001 Hepatitis C viral RNA: challenges and promises Cell.Mol.Life.Sci. **58** 1276-1295

Shi, S. T., Polyak, S. J., Tu, H., Taylor, D. R., Gretch, D. R., and Lai, M. M. C. 2002 Hepatitis C Virus NS5A Colocalizes with the Core Protein on Lipid Droplets and Interacts with Apolipoproteins Virology **292** 198-210

Shih, J. W., Esteban, J. I., and Alter, H. J. 1986 Non-A, non-B hepatitis: advances and unfulfilled
expectations of the first decade Prog.Liver.Dis. **8** 433-452

Shih, J. W., Tsai, T. Y., Chao, C. H., and Wu Lee, Y. H. 2008 Candidate tumor suppressor DDX3 RNA helicase specifically represses cap-dependent translation by acting as an eIF4E inhibitory protein Oncogene **27** 700-714

Shimomura, O., Johnson, F. H., and Saiga, Y. 1962 Extraction, Purification and Properties of Aequorin, a Bioluminescent Protein from the Luminous Hydromedusan, *Aequorea* J.Cell Comp.Phys. **59** 223-239

Shmaefsky, B. 2006 Biotechnology 101 171

Shotton, D. M. 1993 An introduction to digital image processing and image display in electronic microscopy 39-70

Shulla, A. and Randall, G. 2012 Hepatitis C virus - host interactions, replications and viral assembly Curr.Opin.Microbiol. **2** 719-726

Simmonds, P., Holmes, E. C., Cha, T-A., Chan, S-W., McOmish, F., Irvine, B., Beall, E., Yap, P. L., Kolberg, J., and Urdea, M. S. 1993 Classification of hepatitis C virus into six major genotypes and a series of subtypes by phylogenetic analysis of the NS-5 region J.Gen.Virol. **74** 2391-2399

Simmonds, P. 1995 Variability of Hepatitis C Virus Hepatology **21** 570-583

Simmonds, P. 2004 Genetic diversity and evolution of hepatitis C virus - 15 years on J.Gen.Virol. **85** 3173-3188

Sleno, L., Volmer, D. A., and Marshall, A. G. 2005 Assigning product ions form complex MS/MS spectra: The importance of mass uncertainty and resolving power J.Am.Soc.Mass Spectrom. **16** 183-198

Smith, A. E. and Helenius, A. 2004 How Viruses Enter Animal Cells Science **304** 237-242

Smith, D. B., Bukh, J., Kuiken, C., Muerhoff, A. S., Rice, C. M., Stapleton, J. T., and Simmonds, P. 2013 Expanded classification of hepatitis C Virus into 7 genotypes and 67 subtypes: updated criteria and assignment web resource Hepatology 1-39

Smith, F. G. and King, T. A. 2001 Optics and Photonics. An Introduction

Smyth, J. S., Pitera, J. E., Taylor, M. S., van Haelst, M., Bentley, E., McGregor, L., Hopkins, J., Chalepakis, G., Philip, N., Perez Aytes, A., Watt, F. M., Darling, S. M.,

Jackson, I., Woolf, A. S., and Scambler, P. J. 2005 Identification of a new gene mutated in Fraser syndrome and mouse myelencephalic blebs Nat.Genet. **37** 520-525

Solouki, T., Marto, J. A., White, F. M., Guan, S., and Marshall, A. G. 1995 Attomole Biomolecule Mass Analysis by Matrix-Assisted Laser Desorption/Ionization Fourier Transform Ion Cyclotron Resonance Anal.Chem. **67** 4139-4144

Sosinsky, G. E., Giepmans, B. N. G., Deerinck, T. J., Gaietta, G. M., and Ellisman, M. H. 2007 Markers for correlated light and electron microscopy Methods.Cell.Biol. **79** 575-591

Speichinger, K. 2010 Structured Illumination. Physics 598: Optical Microscopy

Spring, K. R., Fellers, T. J., and Davidson, M. W. 2013 Signal-to-Noise Considerations

Steinhauer, C., Forthmann, C., Vogelsang, J., and Tinnefeld, P. 2008 Superresolution Microscopy on the Basis of Engineered Dark States J.Am.Chem.Soc. **130** 16840-16841

Steinhauer, D. A. and Holland, J. J. 1987 Rapid Evolution of RNA Viruses Annu.Rev.Microbiol. **41** 409-433

Steinmann, E., Penin, F., Kallis, S., Patel, A. H., Bartenschlager, R., and Pietschmann, T. 2007 Hepatitis C virus p7 protein is crucial for assembly and release of infectious virions PLOS Pathogens **3**

Stephens, D. J. and Allan, V. J. 2003 Light Microscopy Techniques for Live Cell Imaging Science **300** 82-86

Stigler, S. M. 1989 Francis Galton's Account of the Invention of Correlation Stat.Sci. **4** 73-79

Sumpter, R. Jr., Loo, Y. M., Foy, E., Li, K., Yoneyama, M., Fujita, T., Lemon, S. M., and Gale, M. 2005 Regulating intracellular antiviral defense and permissiveness to hepatitis C virus RNA replication through a cellular RNA helicase, RIG-I J.Virol **79** 2689-2699

Suzich, J. A., Tamura, J. K., Palmer-Hill, F., Warrener, P., Grakoui, A., Rice, C. M., Feinstone, S. M., and Collett, M. S. 1993 Hepatitis C Virus NS3 Protein Polynucleotide-Stimulated Nucleoside Triphosphatase and Comparison with the Related Pestivirus and Flavivirus Enzymes J.Virol **67** 6152-6158

Swedlow, J. R. and Platani, M. 2002 Live Cell Imaging Using Wide-Field Microscopy and Deconvolution Cell.Struct.Funct. **27** 335-341

Szmuness, W., R. Pick, and A. M. Prince. 1970. The Serum Hepatitis Virus Specific Antigen (SH): A Preliminary Report Of Epidemiologic Studies In An Institution For The Mentally Retarded. Am.J.Epidemiol. **92**:51-61.

Tabor, E., Gerety, R. J., Drucker, J. A., Seeff, L. B., Hoofnagle, J. H., Jackson, D. R., April, M., Barker, L. F., and Pineda-Tamondong, G. 1978 Transmission of non-A, non-B hepatitis from man to chimpanzee Lancet **8062** 463-466

Tai, C-L., Chi, W-K, Chen, D. S., and Hwang, L-H. 1996 The Helicase Activity Associated with Hepatitis C Virus Nonstructural Protein 3 (NS3) Am.Soc.Micro. **70** 8477-8484

Takamizawa, A., Mori, C., Fuke, I., Manabe, S., Murakami, S., Fujita, J., Onishi, E., Andoh, T., Yoshida, I., and Okayama, H. 1991 Structure and organization of the hepatitis C virus genome isolated from human carriers J.Virol **65** 1105-1113

Takizawa, T., Suzuki, K., and Robinson, J. M. 1998 Correlative microscopy using FluoroNanogold on ultrathin cryosections. Proof of principle J.Histochem.Cytochem. **46** 1097-1102

Tan, S-L. and Katze, M. G. 2001 How Hepatitis C Virus Counteracts the Interferon Response: The Jury Is Still out on NS5A Virology **284** 1-12

Targett-Adams, P. and McLauchlan, J. 2005 Development and characterization of a transient-replication assay for the genotype 2a hepatitis C virus subgenomic replicon J.Gen.Virol. **86** 3075-3080

Targett-Adams, P., Boulant, S., and McLauchlan, J. 2008 Visualization of Double-Stranded RNA in Cells Supporting Hepatitis C Virus RNA Replication J.Virol **82** 2182-2195

Targett-Adams, P., Graham, E. J. S., Middleton, J., Palmer, A., Shaw, S. M., Lavender, H., Brain, P., Tran, T. D., Jones, L. H., Wakenhut, F., Stammen, B., Pryde, D., Pickford, C., and Westby, M. 2011 Small Molecules Targeting Hepatitis C Virus-Encoded NS5A Cause Subcellular Redistribution of Their Target: Insights into Compound Modes of Action J.Virol **85** 6353-6368

Tellinghuisen, T. L. and Rice, C. M. 2002 Interaction between hepatitis C virus proteins and host cell factors Curr.Opin.Microbiol. **5** 419-427

Tellinghuisen, T. L., Marcotrigiano, J., Gorbalenya, A. E., and Rice, C. M. 2004 The NS5A Protein of Hepatitis C Virus Is a Zinc Metalloprotein J.Biol.Chem. **279** 48576-48587

Tellinghuisen, T. L., Marcotrigiano, J., and Rice, C. M. 2005 Structure of the Zinc binding domain of an essential component of the hepatitis C virus replicase Nature **435** 374-379

Tellinghuisen, T. L., Foss, K. L., and Treadaway, J. 2008 Regulation of Hepatitis C Virion Production via Phosphorylation of the NS5A Protein PLOS Pathogens **4** 1-17

Thimme, R., Oldach, D., Chang, K-M., Steiger, C., Ray, S. C., and Chisari, F. V. 2001 Determinants of Viral Clearance and Persistence during Acute Hepatitis C Virus Infection J.Exp.Med **194** 1395-1406

Thomson, B. J. and Finch, R. G. 2005 Hepatitis C virus infection Clin.Microbiol.Infec. **11** 86-94

Thomson, J. J. 1913 Bakerian Lecture: Rays of Positive Electricity Proc.Royal.Soc. **89** 1-20

Thomssen, R., Bonk, S., Propfe, C., Heermann, K. H., Köchel, H. G., and Uy, A. 1992 Association of hepatitis C virus in human sera with beta-lipoprotein Med.Microbiol.Immunol. **181** 293-300

Tong, X. and Malcolm, B. A. 2006 Trans-complementation of HCV replication by non-structural protein 5A Virus Res. **115** 122-130

Tscheme, D. M., Jones, C. T., Evans, M. J., Lindenbach, B. D., McKeating, J. A., and Rice, C. M. 2006 Time- and temperature-dependent activation of hepatitis C virus for low-pH-triggered entry J.Virol **80** 1734-1741

Tseng, C-T. K. and Klimpel, G. R. 2002 Binding of the Hepatitis C Virus Envelope Protein E2 to CD81 Inhibits Natural Killer Cell Functions J.Exp.Med **195** 43-49

Tsien, R. Y. 1998 The Green Fluorescent Protein Annu.Rev.Biochem **67** 509-544

Tsien, R. Y., Ernst, L., and Waggoner, A. 2006 Fluorophores for Confocal Microscopy: Photophysics and Photochemistry 338-352

Tsukiyama-Kohara, K., Lizuka, N., Kohara, M., and Nomoto, A. 1991 Internal ribosome entry site within hepatitis C virus RNA J.Virol **66** 1476-1483

Tyers, M. and Mann, M. 2003 From Genomics to Proteomics Nature **422** 193-197

van Dam, G. J., Bogitsh, B. J., Fransen, J. A., Kornelis, D., van Zeyl, R. J., and Deelder, A. M. 1991 Application of the FITC-anti-FITC-gold system to ultrastructural localization of antigens J.Histochem.Cytochem. **39** 1725-1728

van Kooyk, Y. and Geijtenbeek, T. B. 2003 DC-SIGN: escape mechanism for pathogens. Nat.Rev.Immunol. **3** 697-709

Vaughan, W. and Weber, G. 1970 Oxygen Quenching of Pyrenebutyric Acid Fluorescence in Water. A Dynamic Probe of the Microenvironment Biochem. **9** 464-473

Venable, J. D., Wohlschlegel, J., McClatchy, D. B., Sung, K. P., and Yates, J. R. 2007 Relative quantification of stable isotope labeled peptides using a linear ion trap-orbitrap hybrid mass spectrometer Anal.Chem. **79** 3056-3064

Venter, J. C. and et al. 2001 The sequence of the human genome Science **291** 1304-1351

Vieyres, G., Thomas, X., Descamps, V., Duverlie, G., Patel, A. H., and Dubuisson, J. 2010 Characterisation of the envelope glycoproteins associated with infectious hepatitis C virus. J.Virol **84** 10159-10168

Voeltz, G. K., Prinz, W. A., Shibata, Y., Rist, J. M., and Rapoport, T. A. 2006 A Class of Membrane Proteins Shaping the Tubular Endoplasmic Reticulum Cell **124** 573-586

Volkert, C. A. and Minor, A. M. 2007 Focused Ion Beam Microscopy and Micromachining MRS Bulletin **32** 389-399

Wakita, T., Pietschmann, T., Kato, T., Date, T., Miyamoto, M., Zhao, Z., Murthy, K., Habermann, A., Krausslich, H-G., Mizokami, M., Bartenschlager, R., and Liang, T. J. 2005 Production of infectious hepatitis C virus in tissue culture from a cloned viral genome Nat.Med. **11** 791-796

Walling, M. A., Novak, J. A., and Shepard, J. R. E. 2009 Quantum Dots for Live Cell and *In Vivo* Imaging Int.J.Mol.Sci. **10** 441-491

Wasley, A. and Alter, M. J. 2000 Epidemiology of Hepatitis C: Geographic Differences and Temporal Trends Semin.Liver Dis. **20** 1-16

Watson, J. T. and Sparkman, O. D. 2008 Introduction to Mass Spectrometry: Instrumentation, Applications and Strategies for Data Interpretation

Watson, M. L. 1958 Staining of Tissue Sections for Electron Microscopy with Heavy Metals J.Biophysic.Biochem.Cytol. **4** 475-478

Wattenberg, B. and Lithgow, T. 2001 Targeting of C-Terminal (Tail)-Anchored Proteins: Understanding how Cytoplasmic Activities are Anchored to Intracellular Membranes Traffic **2** 66-71

Welsch, S., Miller, S., Romero-Brey, I., Merz, A., Bleck, C. K., Walther, P., Fuller, S. D., Antony, C., Krijnse-Locker, J., and Bartenschlager, R. 2009 Composition and three-dimensional architecture of the dengue virus replication and assembly sites Cell Host Microbe **4** 365-375

Whaley, P. 2011 Qdot Conjugates: Sensitive, Multicolor, Stable Fluorescence [Powerpoint]

White, J. C. and Stryer, L. 1987 Photostability studies of phycobiliprotein fluorescent labels Anal.Biochem. **161** 442-452

Wiley, W. C. and McLaren, I. H. 1955 Time-of-flight mass spectrometer with improved resolution Rev.Sci.Instrum. **26** 1150-1157

Wilkins, M. 2009 Proteomics Data Mining Expert Rev.Proteomics. **6** 599-603

Williams, D. B. and Carter, B. C. 1996 Transmission Electron Microscopy: A Textbook for Materials Science, Volume 1

Williams, K. L. 1999 Genomes and proteomes: Towards a multidimensional view of biology Electrophoresis **20** 678-688

Wilson, T. 1989 Optical Sectioning in Confocal Fluorescent Microscopes J.Microsc **154** 143-156

Wolk, B., Sansonno, D., Krausslich, H-G., Dammacco, F., Rice, C. M., Blum, H. E., and Moradpour, D. 2000 Subcellular Localization, Stability, and *trans*-Cleavage Competence of the Hepatitis C Virus NS3-NS4A Complex Expressed in Tetracycline-Regulated Cell Lines Am.Soc.Micro. **74** 2293-2304

Wood, G. S. and Warnke, R. 1981 Suppression of Endogenous Avidin-binding Activity in Tissues and It's relevance to Biotin-Avidin Detection Systems J.Histochem.Cytochem. **29** 1196-1204

World Health Organisation 2000 Hepatitis C Fact Sheet No. 164

Wu, L. and Han, D. K. 2006 Overcoming the dynamic range problem in mass spectrometry-based shotgun proteomics Expert Rev.Proteomics. **3** 611-619

Yanagi, M., Purcell, R. H., Emerson, S. U., and Bukh, J. 1997 Transcripts from a single full-length cDNA clone of hepatitis C virus are infectious when directly transfected into the liver of a chimpanzee Proc.Natl.Acad.Sci.USA **94** 8738-8743

Yates, J. R. 2004 Mass Spectral Analysis in Proteomics Annu.Rev.Biophys.Biomol.Struct. **33** 297-316

Ye, J. 2007 Reliance of Host Cholesterol Metabolic Pathways for the Life Cycle of Hepatitis C Virus PLOS Pathogens **3** 1017-1022

Yi, M., Ma, Y., Yates, J. R., and Lemon, S. M. 2009 Trans-complementation of an NS2 defect in a late step in hepatitis C virus (HCV) particle assembly and maturation PLOS Pathogens **5**

Zeigler, U. 2008 Getting started with image processing using Imaris (Bitplane)

Zeisel, M. B., Koutsoudakis, G., Schnober, E. K., Haberstroh, A., Blum, H. E., and Cosset, F-L. 2007 Scavenger receptor BI is a key host factor for hepatitis C virus infection required for an entry step closely linked to CD81 Hepatology **46** 1722-1731

Zeisel, M. B., Fofana, I., Fafi-Kremer, S., and Baumert, T. F. 2010 Hepatitis C virus entry into hepatocytes: Molecular mechanisms and targets for antiviral therapies J.Hepatology **54** 566-576

Zenobi, R. and Knockenmuss, R. 1998 Ion Formation In MALDI Mass Spectrometry Mass.Spectrom.Rev. **17** 337-366

Zeuzem, S., Schmidt, J. M., Lee, J-H., Ruster, B., and Roth, W. K. 1996 Effect of Interferon Alfa on the Dynamics of Hepatitis C Virus Turnover *In Vivo* Hepatology **23** 366-371

Zhang, J., Randell, G., Higginbottom, A., Monk, P., Rice, C. M., and McKeating, J. A. 2004 CD81 is required for hepatitis C virus glycoprotein-mediated viral infection J.Virol **78** 1448-1455

Zhong, J., Gastaminza, P., Cheng, G., Kapadia, S, Kato, T., Burton, D. R., Wieland, F., Uprichard, S. L., Wakita, T., and Chisari, F. V. 2005 Robust hepatitis C virus infection *in vitro* Proc.Natl.Acad.Sci.USA **102** 9294-9299

Zimmer, M. 2001 Green Fluorescent Protein (GFP): Applications, Structure, and Related Photophysical Behavior Chem.Rev. **102** 759-781

Zimmerberg, J. and Kozlov, M. M. 2006 How proteins produce cellular membrane curvature Nat.Rev.Mol.Cell.Biol. **7** 9-19